The Role of Ferruginous Clay Minerals in the Marine Biogeochemical Cycle of Iron

Doctoral Thesis

to obtain the doctoral degree of natural sciences (Dr. rer. nat.) of Graz University of Technology

Submitted by

M.Sc. Andre Baldermann
Graz, November 2015

Supervisors

Univ.-Prof. Dr. rer. nat. Martin Dietzel
Institute of Applied Geosciences, Graz University of Technology

Univ.-Prof. Ph.D Laurence N. Warr
Department of Geography and Geology, Ernst-Moritz-Arndt-University Greifswald

External Reviewer

Dr. rer. nat. Reiner Dohrmann

Prologue

(I think these citations show how winding and many-faceted science and scientific work is in practice…. and it describes me and my work best!)

Our whole universe was in a hot dense state,
Then nearly fourteen billion years ago expansion started. Wait...
The Earth began to cool,
The autotrophs began to drool,
Neanderthals developed tools,
We built a wall (we built the pyramids),
Math, science, history, unraveling the mysteries,
That all started with the big bang!

"Since the dawn of man" is really not that long,
As every galaxy was formed in less time than it takes to sing this song,
A fraction of a second and the elements were made.
The bipeds stood up straight,
The dinosaurs all met their fate,
They tried to leap but they were late
And they all died (they froze their asses off),
The oceans and Pangea,
See ya, wouldn't wanna be ya,
Set in motion by the same big bang!

It all started with the big BANG!

It's expanding ever outward but one day,
It will cause the stars to go the other way,
Collapsing ever inward, we won't be here, it won't be hurt,
Our best and brightest figure that it'll make an even bigger bang!

Australopithecus would really have been sick of us,
Debating out while here they're catching deer (we're catching viruses),
Religion or astronomy, Encarta, Deuteronomy,
It all started with the big bang!

Music and mythology, Einstein and astrology,
It all started with the big bang!
It all started with the big BANG!

(The Big Bang Theory; 2007 until now)

"Gold is for the mistress, Silver for the maid,
Copper for the craftsman, cunning at his trade,
´Good´ said the Baron, sitting in his hall,
But iron, cold iron, is the master of them all!"

(Rudyard Kipling; 1835-1936)

Statutory Declaration

I declare that I have authored this thesis independently, that I have not used other than the declared sources / resources, and that I have explicitly marked all material which has been quoted either literally or by content from the used sources.

Graz, November 2015

Andre Baldermann

Danksagung

Mein größter Dank geht an Prof. Martin Dietzel (TU Graz) für seine immerwährende Unterstützung, die fachliche Führung, die unermüdliche Bereitschaft und das Engagement mir auch bei schwierigen Fragestellungen stets mit Rat und Tat hilfreich zur Seite gestanden zu haben und natürlich für die Möglichkeit, die Promotion erfolgreich verwirklichen zu können. Seine Kompetenz und sein Vertrauen in meine Arbeit als Universitätsassistent über die letzten Jahre sind mir immer eine große Hilfe gewesen.

Ein besonderer Dank gilt Prof. Laurence N. Warr (Universität Greifswald) für seine Bereitschaft diese Arbeit als zweiter Gutachter zu bewerten, vor allem aber für die stets interessante und erfolgreiche Zusammenarbeit seit nunmehr über sieben Jahren. Seine Anregungen und Ideen und die daraus resultierenden gemeinsamen Projekte und Diskussionen, sowie seine Verbesserungsvorschläge und Korrekturen, waren immer eine Bereicherung für mich.

Ich danke auch Dr. Reiner Dohrmann (BGR Hannover) für seine kollegiale Unterstützung in den letzten Jahren, die zahlreichen Diskussionen, die mir immer wieder neue Impulse und Ideen gegeben haben und natürlich für seine Tätigkeit als externer Begutachter dieser Arbeit.

Allen Mitarbeitern der Angewandten Geowissenschaften der TU Graz (u.a. M. Hierz, J. Jernej, A. Pendl, S. Perchthold, P. Schreiber, D. Sobian und A. Wolf), den langjährigen Kollegen (u.a. R. Boch, M.E. Böttcher, C. Cuadros, A.P. Deditius, V. Fichtner, C. Fischer, G. Grathoff, D. Hippler, D. Höllen, W. Homoky, S. Kaufhold, D. Klammer, A. Leis, I. Letofsky-Papst, F. Mittermayr, H. Strauss und M. Zander), den Mit-Doktoranten (C. Grengg, F. Konrad und J. Stammeier), den „Hiwis“ und den ehemaligen Studenten (u.a. P.M. Frick, R. Fuchs, M. Goger, C. Ortner, M. Spitz und C.P. Stickler) danke ich für die immerwährende Unterstützung bei der Planung und Durchführung von Experimenten, sowie für die Bereitstellung von Daten, ohne die einige Publikationen nicht realisierbar gewesen wären. Ein besonderer Dank gilt insbesondere meinen Büro-Kollegen und Freunden Vasileios Mavromatis und Bettina Purgstaller für ihre stetige Unterstützung und Hilfsbereitschaft.

Zuletzt möchte ich meiner Familie für die emotionale und finanzielle Unterstützung während des Studiums und die vielen guten Ratschläge bedanken. Meiner Frau Claudia Baldermann danke ich für Ihre Liebe und Geduld, die Unterstützung in allen Lebenslagen und Ihre unermüdliche Bereitschaft zur Diskussion auch nach Arbeitsschluss.

Summary

Hydrous phyllosilicates are the most abundant mineral phases found in the various environments of the Earth`s surface. The spatiotemporal distribution and abundance of (FeII+III)-bearing clay minerals in modern marine sediments and ancient sedimentary rocks is closely coupled with the evolution of life forms, climate, and the (biogeo)chemical composition of the past and present global ocean. Most ferruginous clay minerals that form in marine and early diagenetic environments at low-temperatures are only poorly reactive and less bioavailable compared to (nano)particulate Fe-(oxy)hydroxides. Thus, clay minerals are currently believed to play a minor role in the biogeochemical cycle of iron. Moreover, present biogeochemically-coupled ocean circulation models that attempt to quantify mass balance relationships in the marine iron cycle ignore the contribution of ferruginous clay mineral reactions on regulating the benthic Fe fluxes, in particular in the "critical zones" – namely mid-oceanic ridge sites, shallow-shelf sediments, and deep-sea settings. In such settings, the ultimate Fe sequestration associated with the neo-formation of ferrous saponite (~1000 µmol $Fe \cdot cm^{-2} \cdot kyr^{-1}$), nontronite, and glauconite minerals (~80 µmol $Fe \cdot cm^{-2} \cdot kyr^{-1}$), so-called green-clay authigenesis, can by far exceed the global burial rate of Fe related to pyrite (~30 µmol $Fe \cdot cm^{-2} \cdot kyr^{-1}$).

In this doctoral thesis, the ambient (paleo)environmental controls and the underlying reaction mechanisms linked to green-clay authigenesis at the sediment-seawater interface in the critical zones are discussed with recognition of their importance in the past and present marine iron cycle. On the basis of results from combined hydrothermal synthesis experiments and field observations it is shown that green-clay authigenesis can sequester quantitatively important amounts of dissolved Fe^{2+} from the pore water inventory of marine sediments that would otherwise be applicable to be supplied back to the overlying oceanic waters. Ultimate Fe uptake during ferruginous clay mineral reactions is therefore suggested to significantly limit the benthic fluxes of dissolved Fe^{2+} in suboxic sediments and subsequently control a variety of biogeochemical processes on the ocean floor as well as in the deep biosphere.

I suggest that the early diagenetic precipitation of (FeII+III)-bearing clay minerals is a key process that strongly contributes to the biogeochemical, mineralogical, and petrological characteristics of modern and ancient (marine) sediments. The role of ferruginous clay minerals should be considered as a central parameter controlling the global Fe fluxes in the (sedimentary) low-temperature biogeochemical cycle of iron.

Zusammenfassung

Hydrierte Phyllosilikate sind die am Häufigsten vorkommenden Mineralphasen in erdoberflächennahen Bildungsbereichen. Die räumliche und zeitliche Verteilung und die Häufigkeit von (FeII+III)-haltigen Tonmineralen in rezenten marinen Sedimenten, sowie in Sedimentgesteinen, sind unmittelbar an die Entwicklung von Lebensformen, dem Klima und an die (biogeo)chemische Zusammensetzung der vergangenen und modernen Weltozeane gekoppelt. Die meisten Fe-schüssigen Tonminerale bilden sich in marinen und frühdiagenetischen Umfeldern im Niedrigtemperaturbereich; Tone sind aber im Allgemeinen weniger reaktiv and bioverfügbar als (nano)partikuläre Fe-(oxy)hydroxide. Gegenwärtig wird die Rolle der Tonminerale im biogeochemischen Stoffkreislauf von Fe als eher gering angesehen. Als Folge dessen wird der Beitrag von Tonmineralreaktionen am marin-sedimentären Fe-Kreislauf in aktuellen biogeochemisch-gekoppelten Ozeanzirkulationsmodellen nicht berücksichtigt, welcher jedoch in den „kritischen Zonen“ wie beispielsweise an Mittelozeanischen Rücken, in Schelfsedimenten und in der Tiefsee bedeutsam sein kann. In diesen Systemen kann die Deponierung von Fe durch Tonmineralneubildungen von Saponit (~1000 μmol $Fe \cdot cm^{-2} \cdot kyr^{-1}$), Nontronit und Glaukonit-Mineralen (~80 μmol $Fe \cdot cm^{-2} \cdot kyr^{-1}$), besser bekannt als „Grüne Tone“, die globale Fe-Sequestrierungsrate von Pyrit (~30 μmol $Fe \cdot cm^{-2} \cdot kyr^{-1}$) bei weiten überschreiten.

In dieser Doktorarbeit werden die umweltbedingten Kontrollfaktoren und die zu Grunde liegenden Reaktionsmechanismen diskutiert, welche die Genese von Grünen Tonen in den kritischen Zonen an der Meerwasser-Sediment Grenzschicht, sowie deren Bedeutung für den vergangenen und rezenten marinen Fe-Kreislauf, umfassen. Auf der Grundlage der Ergebnisse von hydrothermalen Syntheseexperimenten und Feldbeobachtungen wird gezeigt, dass neugebildete grüne Tone einen quantitativ bedeutsamen Anteil von gelöstem Fe^{2+} aus dem Porenwasserreservoir von marinen Sedimenten sequestrieren können, welcher ansonsten zurück in das überlagernde Meerwasser gespeist werden würde. Die ultimative Deponierung von Fe infolge von Tonmineralreaktionen ist ein wichtiger, limitierender Faktor für den Stofftransport von gelöstem Fe^{2+} in suboxischen Sedimenten und beeinflusst deshalb maßgeblich eine Reihe von biogeochemischen Prozessen auf dem Meeresboden und in der Tiefen Biosphäre.

Die frühdiagenetische Präzipitation von (FeII+III)-haltigen Tonmineralen besitzt eine Schlüsselfunktion in der Regulierung der biogeochemischen, mineralogischen und petrologischen Charakteristika von rezenten (marinen) Sedimenten und Sedimentgesteinen. Die Rolle von Fe-schüssigen Tonmineralen als entscheidender Kontrollfaktor im globalen (sedimentären) Umsatz von Fe sollte deshalb bei der Bewertung des biogeochemischen Stoffkreislaufs von Fe im Niedrigtemperaturbereich besser berücksichtigt werden.

Preface

This doctoral thesis is divided into five main chapters. Here, a summary of the content of the individual chapters is provided, and the most important conclusions from chapters 1 to 7 are presented and briefly discussed in relation to their significance in the low-temperature biogeochemical cycle of iron. Special emphasis lies, in each of the chapters, on the currently underestimated role of ultimate iron sequestration by authigenic clay minerals that form close to the sediment-seawater interface during the early stages of diagenesis. On the basis of experimental work and field observations it is shown that the (neo)formation of ferruginous clays can strongly influence the Fe fluxes in marine, low-temperature settings, covering mid-oceanic ridge sites, deep-water environments, and shallow-shelf regions. All chapters are presented in a way that they can be read separately or are in part subject of published manuscripts.

Chapter 1 provides an overview of the key processes that operate in the past and present biogeochemical iron cycle. The physicochemical conditions and controls on Fe reactivity are highlighted, its transport in aqueous media and multiple mineral sources and sinks for Fe are introduced, and the background provided to understand the biogeochemistry and mineralogy of mineral phases bearing Fe(II+III), *i.e.* Fe-(oxy)hydroxides and Fe-silicates.

Chapter 2 has been published in *Clay Minerals* by Baldermann and co-workers (2014; DOI: 10.1180/claymin.2014.049.3.04) and reports the links between the chemical composition of a synthetic reactive fluid and the mineralogy, composition, structure and stability of precipitated ferruginous clay minerals. A set of hydrothermal experiments was performed at 60°C, 120°C and 180°C and alkaline pH, using reducing experimental solutions with an initial molar Si:Fe:Mg ratio of 4:0:2, 4:1:1, 4:1.5:0.5, 4:1.75:0.25, and 4:1.82:0.18, and reaction times from three to seven days. These conditions were used to simulate weathering of basalt at mid-oceanic ridge sites and to trace the subsequent formation of expandable 2:1 clay minerals bearing Fe(II+III), such as saponite and nontronite. Trioctahedral ferrous saponite and subordinate brucite, opal-CT, ferrihydrite, and dioctahedral nontronite were the experimental products. The chemical composition of synthetic saponite was highly variable and depended mainly on the molar Fe:Mg ratio of the reactive fluid and to some degree on the formation temperature and time of synthesis. Based on the evolution of the solid-phase compositions and experimental solutions, a conceptual reaction sequence for saponite formation is developed. The extent of Fe(II) incorporation in co-precipitating ferrous saponite might be used to trace the chemical composition of hydrothermal fluids generated at mid-oceanic ridge sites.

Chapter 3 has been published in *Clay Minerals* by Baldermann and co-workers (2012; DOI: 10.1180/claymin.2012.047.4.09). This chapter provides an introduction to the environmental conditions leading to glauconite formation (a dioctahedral Fe(III)-rich illite) in fecal pellets, as seen in the ~150 m thick shallow-marine to lagoonal sedimentary rocks from Oker (Central Germany). Using electron microscopy methods, X-ray diffraction, and kinetic modeling as well as trace elemental and $\delta^{18}O$ and $\delta^{13}C$ signatures of carbonates, the micromilieu, precursor phases, temperature range, thermodynamics, and kinetics of the glauconitization reaction are discussed, and a new model for glauconite formation in fecal pellets is presented. It is suggested that the concentration and availability of Fe and K in the modern and ancient ocean play a key role in the entire Fe-smectite to glauconite reaction at low temperature, by fostering the rate of glauconitization compared to that of smectite illitization related to burial diagenesis.

Chapter 4 has been published in *Clays and Clay Minerals* by Baldermann and co-workers (2013; DOI: 10.1346/CCMN.2013.0610307) and provides a detailed overview of the reaction mechanisms and physicochemical controls linked to glauconitization in the modern deep-sea environment of the Ivory Coast–Ghana Marginal Ridge (ODP Site 959). The interplay of the micro-environment, such as foraminifera tests, where glauconite forms, bacterial activity and the chemical composition of the surrounding interstitial solutions being modified during early diagenetic oxidation of organic matter, microbial sulfate reduction, silicate mineral alteration, carbonate dissolution, and Fe redox reactions is discussed, and a revised model for the deep-water glauconitization is presented. It is shown that the net Fe uptake during the burial-driven glauconitization reaction controls the rate of deep-water glauconite formation, which is about five times less than that in shallow-shelf regions but notably higher compared with that of smectite illitization, suggesting that Fe is the rate-limiting factor for glauconitization.

Chapter 5 has been published in *Nature Geoscience* by Baldermann and co-workers (2015; DOI: 10-1038/NGEO2542). In this study, a revised model for the sedimentary cycle of iron at the Ivory Coast–Ghana Marginal Ridge (ODP Site 959) is presented. Using high-resolution transmission electron microscopic methods and sequential sediment extraction techniques, multiple Fe mineral-phase reservoirs in marine sediments are quantified, and for the first time the rates of Fe sequestration attributed to green-clay authigenesis (also known as glauconitization) versus pyrite precipitation are reported. Ultimate Fe uptake by green-clay strongly reduces the pore water inventory of dissolved Fe in modern and ancient pelagic sediments, which calls for a revision of the long-standing view that clay mineral reactions involving Fe(II+III) are of little importance in current biogeochemical models of the marine iron cycle.

Table of Contents

[1] This chapter is published in *Clay Minerals*, **49**, 391-415: Baldermann et al. (2014).

[2]This chapter is published in *Clay Minerals*, **47**, 513-538: Baldermann et al. (2012).
[3]This chapter is published in *Clays and Clay Minerals*, **61**, 258-276: Baldermann et al. (2013).

[4]This chapter is published in *Nature Geoscience*, **8**, 885-889: Baldermann et al. (2015).

Chapter 1

Introduction

1.1 Background on the low-temperature biogeochemical cycle of iron

Iron is the fourth most abundant element in the Earth's present-day crust and due to the high reactivity of most Fe(II+III) minerals that form in Earth's surface environments it also plays a key role in many biogeochemical processes (Raiswell & Canfield, 2012). Although dissolved Fe^{2+} occurs only in trace-level concentrations in modern aqueous systems (Turekian, 1968), it is an essential micro-nutrient for metabolic processes, and Fe redox reactions provide a crucial energy source for microbial activity and growth and related biomineralization processes (Taylor & Konhauser, 2011; Köhler *et al.*, 2013; Posth *et al.*, 2014). Due to the overlapping of the iron cycle with other element cycles, such as the global C, N, P and S cycle, Fe-mineral phase dissolution-precipitation reactions and transformation processes contribute to the biogeochemical, mineralogical, and petrological character of modern and ancient (marine) sediments (Poulton & Raiswell, 2002; Boyd & Ellwood, 2010; Taylor & Macquaker, 2011).

Over the past five decades, advances in the study of Fe biogeochemistry have significantly improved our mechanistic understanding of processes and reaction paths in the marine iron cycle. Today, the complexity of biogeochemical processes linked to the modern cycle of iron are generally considered to be well understood, and global fluxes between multiple sources and sinks of both dissolved and particulate Fe to the oceans are routinely quantified using biogeochemically-coupled ocean circulation models (Parekh *et al.*, 2004; Dale *et al.*, 2015). These models predict that the majority of continental solid-phase Fe(III) input into the oceans is attributed to Fe-(oxy)hydroxides, whereas the formation of pyrite in anoxic pore waters is the most important sink for Fe in modern marine sediments (Canfield *et al.*, 1993; Raiswell & Canfield, 1998; Raiswell & Canfield, 2012). The role of Fe uptake (*versus* release of Fe) by ferruginous clay minerals, however, has been overlooked as a central factor in the marine iron cycle. In the following sections, the biogeochemistry and mineralogy of relevant Fe(II+III) mineral phases are reviewed, with special recognition of the currently underestimated role of clay mineral authigenesis in the low-temperature biogeochemical cycle of iron.

1.2 Biogeochemistry and mineralogy of native iron and Fe(II+III) minerals

The redox chemistry and bioavailability of dissolved and particulate Fe play an important role in most Earth`s surface processes, affecting a variety of biogeochemical processes and hence the rate of primary biomass production, with highly complex links between ocean chemistry and climate response. At the low temperature of Earth`s surface environments, Fe-minerals possess various oxidation states, from -2 to +6, but the most common forms are ferrous, Fe(II), and ferric, Fe(III), iron. A summary of the most relevant Fe(II+III) minerals in the past and present low-temperature cycle of iron, including their reactivity towards sulfide ions, is reported in Table 1.1. Importantly, metabolic cycling between reduced and oxidized chemical forms of Fe and other redox-sensitive elements, such as Mn, As, and Cr, ultimately affects the mineralogy and biogeochemistry of modern and ancient aquatic environments and associated sediments (Taylor & Konhauser, 2011).

Table 1.1: Common Fe(II+III)-bearing mineral phases present in Earth`s surface environments including their reactivity towards sulfide (modified from Taylor & Konhauser, 2011, and Raiswell & Canfield, 2012).

Mineral Class	Mineral Name	Structural Formula	Reactivity towards sulfide
Native or metal form	Native iron	Fe	-
Oxides/(Oxy)hydroxides	Ferrihydrite	$Fe^{3+}_{4\text{-}5}(OH,O)_{12}$	< 3 hours
	Goethite	$\alpha\text{-}Fe^{3+}O(OH)$	< 12 days
	Lepidocrocite	$\gamma\text{-}Fe^{3+}O(OH)$	< 3 days
	Hematite	$\alpha\text{-}Fe^{3+}_2O_3$	< 1 month
	Maghemite	$\gamma\text{-}Fe^{3+}_{2.67}O_4$	$< 10^2$ years
	Magnetite	$Fe^{2+}Fe^{3+}_2O_4$	$> 10^2$ years
	Green rust	$[Fe^{2+}_{(1\text{-}x)}Fe^{3+}_x(OH)_2]^{x+}\cdot[(x/n)A^{n-}\cdot(m/n)H_2O]^{x-}$,	$< 10^3$ years
		where x is the ratio of Fe^{3+}/Fe_{tot}	
Carbonates	Ankerite	$Ca(Fe^{2+},Mg,Mn)(CO_3)_2$	$< 10^3$ years
	Siderite	$Fe^{2+}CO_3$	$< 10^3$ years
Sulfides	Pyrrhotite	$Fe^{1+}_{1\text{-}x}S$, with x = 0 to 0.2	-
	Mackinawite	$(Fe^{1+},Ni)_{1+x}S$, with x = 0 to 0.1	-
	Pyrite	$Fe^{2+}S_2$	-
	Marcasite	$Fe^{2+}S_2$	-
	Greigite	$Fe^{2+}Fe^{3+}_2S_4$	-
Phosphates	Vivianite	$Fe^{2+}_3(PO_4)_2\cdot 8H_2O$	10^2-10^4 years
	Strengite	$Fe^{3+}PO_4\cdot 2H_2O$	10^2-10^4 years
Hydrous Sulphates	Melanterite	$Fe^{2+}SO_4\cdot 7H_2O$	$< 10^3$ years
	Jarosite	$KFe^{3+}_3(SO_4)_2(OH)_6$	$< 10^3$ years
Silicates	Berthierine	$(Fe^{2+},Fe^{3+},Al)_6[(Si,Al)_4O_{10}](OH)_8$	10^3-10^5 years
	Nontronite	$(Ca,Na)_{0.3}(Fe^{3+},Mg,Al)_2(Si,Al)_4O_{10}(OH)_2\cdot nH_2O$	10^3-10^5 years
	Saponite	$(Ca,Na)_{0.3}(Fe^{2+},Mg,Al)_3((Si,Al)_4O_{10})(OH)_2\cdot n(H_2O)$	10^3-10^5 years
	"Glauconite"	$(K,Na)_{0.6}(Fe^{3+},Fe^{2+}Mg,Al)_2[(Si,Al)_4O_{10}](OH)_2$	10^4-10^6 years
	Chamosite	$(Fe^{2+},Fe^{3+},Mg,Al)_6[(Si,Al)_4O_{10}](OH,O)_8$	10^5-10^6 years

Due to the oxidizing conditions of modern surface-near (aquatic and terrestrial) environments, native Fe, Fe(II)-minerals, and dissolved Fe^{2+} are rare, as these components or related short-range ordered transitional phases are rapidly oxidized to highly labile and often bioavailable Fe-(oxy)hydroxides. In mostly euxinic (deep-sea) and diagenetic settings, microbially-mediated reductive dissolution of unstable Fe-(oxy)hydroxides is an important process in sediments, which can promote the subsequent precipitation of phosphates, carbonates, Fe-silicates ("suboxic pathway" in Fig. 1.1), and, most importantly, Fe-sulfides ("anoxic pathway" in Fig. 1.1). The latter phases, *i.e.* pyrite (FeS_2) and iron monosulfide (FeS), typically form in the presence of sulfide-dominated pore waters. Quantitative removal of dissolved Fe^{2+} by pyrite precipitation causes Fe-limited pore water conditions and finally marks the end of Fe-mineral diagenesis (*e.g.* Berner, 1969; Canfield, 1989; Raiswell & Canfield, 1998; Poulton & Raiswell, 2002; Raiswell *et al.*, 2011). In many suboxic and initially sulfide-depleted systems, however, benthic transport of aqueous Fe^{2+} and subsequent enrichment of Fe^{2+} ions in pore waters can be significant. Such conditions usually result in the quantitative recycling of Fe and enhanced Fe bioavailability prior to the ultimate burial of Fe below the redoxcline (Severmann *et al.*, 2010; Homoky *et al.*, 2011; John *et al.*, 2012; Raiswell & Canfield, 2012; Homoky *et al.*, 2013). This environment is prone to the (neo)formation of ferruginous clay minerals (see Table 1.1), such as glauconite and berthierine minerals in low-temperature settings (< 25°C and < 500 m water depth) or nontronite, saponite, and chlorite minerals at elevated temperatures (> 50°C up to 250°C and > 2000 m water depth). In the modern oceans, Fe(II+III) bound to hydrous sulfates, phosphates, and carbonates is considered insignificant for the global Fe budget.

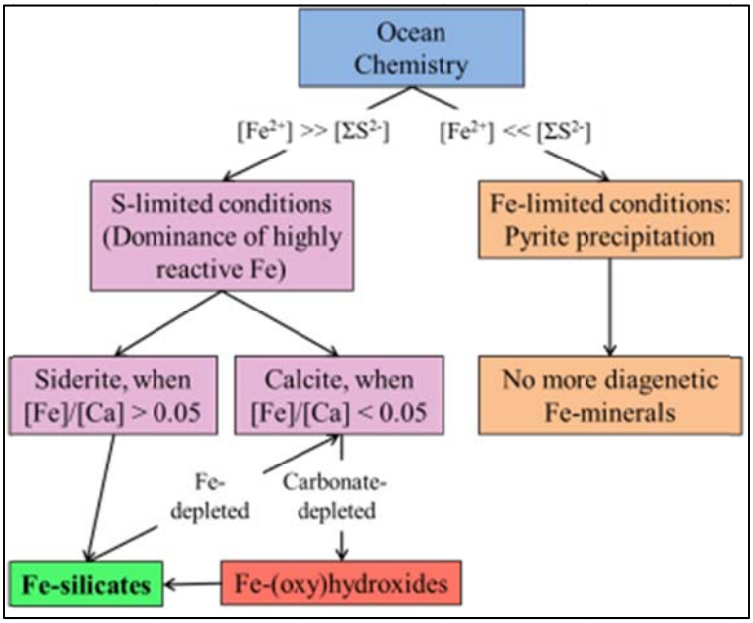

Fig. 1.1: Reaction pathways and chemical controls on Fe-mineral formation (adapted from Raiswell et al., 2011).

1.2.1 Biotic and abiotic controls on iron biogeochemistry

The occurrence of a variety of geologically, environmentally, and economically important Fe(II+III) minerals that form at ambient temperatures and under surface-near conditions is reflected by the complexity of multiple, partly microbially-catalyzed, Fe oxidation-reduction (redox) processes (Fig. 1.2). Iron valence state transformations, mainly from Fe(II) to Fe (III) and *vice versa*, provide an important energy source for biological activity and global element cycling in general, and thus they have been of major significance for the evolution of life forms and sediment deposition throughout the geological record.

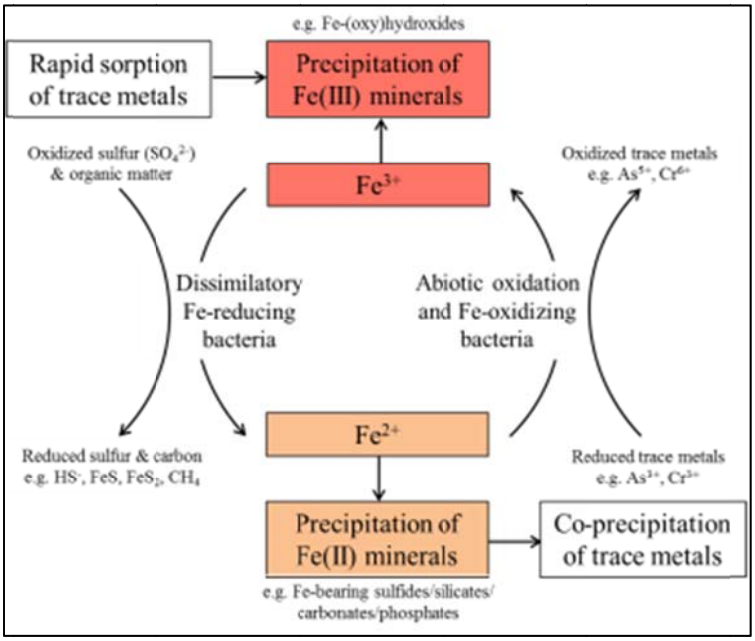

Fig. 1.2: Biotic and abiotic processes operating in the iron cycle (modified from Taylor & Konhauser, 2011).

Under the low temperatures of, for example, marine-diagenetic and deep-sea environments, and in the absence of dissolved sulfide (*e.g.* during the onset of the sulfate reduction zone), the reduction of Fe-(oxy)hydroxides to aqueous Fe^{2+} is driven mainly by dissimilatory Fe-reducing bacteria such as *Shewanella* sp. and *Geobacter* sp. (Taylor & Konhauser, 2011; Raiswell & Canfield, 2012; Köhler *et al.*, 2013; Posth *et al.*, 2014). These microbes gain energy during the Fe(III) to Fe^{2+} reduction, which is triggered by the coincident oxidation of biodegradable organic matter. The aqueous Fe^{2+} produced is typically released to the surrounding (pore) waters, where it reacts with sulfide ions and/or silica gels to form either Fe-sulfides or Fe-rich clay minerals (Schulz & Zabel, 2006). In contrast, the oxidation of Fe^{2+} to Fe(III) usually follows an abiotic reaction pathway because this process is rapid and microbes cannot compete with the abiotic reaction (Fig. 1.2). At the low pH of acid-mine drainage systems and

under the oxygen-limited conditions of *e.g.* Fe-rich hot springs, Fe^{2+} oxidation by acidophilic and neutrophilic bacteria can be significant (Templeton, 2011). In strong acid environments, however, both Fe^{3+} and Fe^{2+} ions occur and can be mobilized in aqueous media.

The interplay of (predominantly abiotic) Fe^{2+} oxidation and (mostly microbially-catalyzed) Fe(III) reduction is therefore considered to be one of the most important chemical controls in the low-temperature cycle of iron. Fe redox reactions operate on much shorter timescales than silicate and phosphate mineral formation processes (see Table 1.1 for mineral reactivity) and thus they provide the first-order controls for the Fe fluxes measured in the modern oceans and associated sediments (Raiswell & Canfield, 2012; Baldermann *et al.*, 2015; Dale *et al.*, 2015). Due to the close coupling of the marine iron cycle with the other (major and trace) elements, the redox state of Fe in aquatic environments largely controls the mineralogy (and reactivity) of co-precipitating Fe(II+III) minerals (Fig. 1.2), which can further act as long-term sources or sinks for contaminant metals incorporated *via* isomorphic substitution (Morse & Luther, 1999; Taylor *et al.*, 2008; Taylor & Konhauser, 2011). The latter feature is of great importance for many applications in environmental technology, *i.e.* removal of (potentially toxic and/or cancerogenic) trace elements such as As, Al, Cr, Ni, and U from waste water.

1.2.2 Bioavailability and reactivity of iron in aquatic environments

Due to prevailing oxidizing conditions and near-neutral pH in most aquatic Earth`s surface environments, aqueous Fe^{2+} occurs mainly in trace-level concentrations (~0.1-0.5 $nM \cdot L^{-1}$ Fe) in the modern ocean, while elevated concentrations of Fe^{2+}, from 1-10 $nM \cdot L^{-1}$, are recognizable only in the spatially restricted environments of hydrothermal vents (Turekian, 1968; Chester, 2000). The vast majority of the aqueous Fe (< 0.45 μm by definition) in the ocean is present as Fe(III) organic aquo-complexes, among minor amounts of uncomplexed ferric and ferrous Fe (Raiswell & Canfield, 2012). These Fe species are highly bioavailable and thus they can be directly taken up by eukaryotic phytoplankton and prokaryotes by photochemical reduction, reduction of colloidal Fe particles that are adsorbed to the cell surface, and production of siderophores (Hudson & Morel, 1990; Maldonado & Price, 2001; Sunda, 2001).

In accordance, about 99.9% of the so-called filterable Fe(II+III) fraction (< 0.45 μm) is primarily bound to organic ligands, Fe colloids, or comprises of inorganic, (nano)particulate Fe-(oxy)hydroxides, such as highly labile ferrihydrite (Fig. 1.3-A). The spatiotemporal variability of Fe in modern aquatic settings, *i.e.* the (surface) ocean, is therefore controlled mainly by (i) the equilibrium partitioning of Fe between soluble and colloidal ligands, (ii) Fe uptake in the photic zone by phytoplankton growth, and (ii) loss of colloidal and particulate Fe by scaven-

ging (Wu *et al.*, 2001; Cullen *et al.*, 2006; Bergquist *et al.*, 2007; Raiswell & Canfield, 2012). Complexation of Fe colloids and Fe-(nano)particles with organic matter, organic ligands, and/or adsorption onto clay mineral surface sites are key processes that control the reactivity and thus the distribution of dissolved *vs.* particulate Fe in aquatic systems. In particular, the physical, chemical, and surface properties (*i.e.* surface charge and surface area; amphoteric behavior) of Fe-(oxy)hydroxide-clay mineral-organic matter aggregates are modified, compared with that of "free" Fe ligands (Boye *et al.*, 2010), and this results in a decreasing reactivity of the aggregates with increasing ageing (Fig. 1.3-B). The latter feature is of great importance for primary biomass production, *i.e.* in high-nutrient, low-chlorophyll (HNLC) regions of the Southern Ocean (*e.g.* Martin, 1990; Martin *et al.*, 1994; Coale *et al.*, 1996; Blain *et al.*, 2007; Cessar *et al.*, 2007; Taylor & Konhauser, 2011), because the mineralogical transformation from labile ferrihydrite precursors into thermodynamically more stable goethite and hematite reduces the bioavailability of Fe in aquatic surface environments (Raiswell & Canfield, 2012). Some uncertainties still persist regarding the reaction pathways and mechanisms involved in the change from reactive to less reactive forms of Fe-(oxy)hydroxides, but temperature and pH are considered to be the most important variables that control the transformation rate and subsequently the reactivity of recrystallized Fe(II+III) minerals (see Table 1.1 and Fig. 1.3-B).

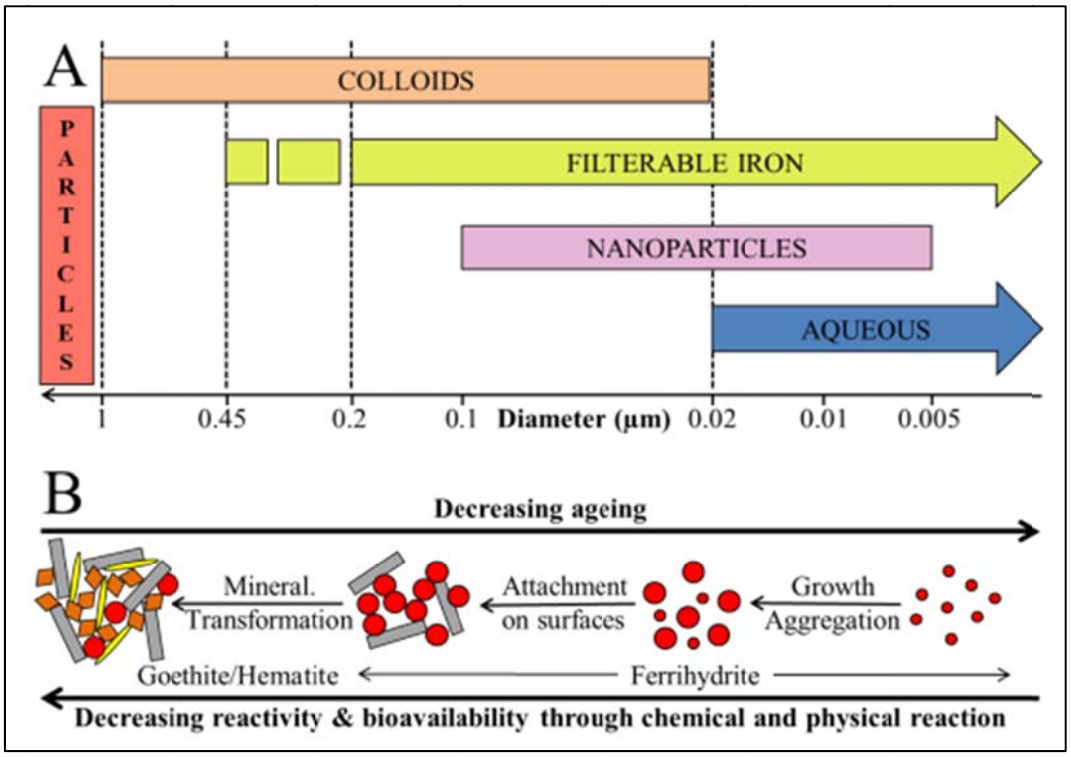

Fig. 1.3: A) Size ranges of Fe-(nano)particles, colloids, and aqueous Fe^{2+} in relation to the extractable (filterable) Fe fraction (modified from Raiswell & Canfield, 2012). B) Idealized ageing and reaction pathway from highly labile ferrihydrite to thermodynamically more stable goethite and hematite (modified from Raiswell, 2011).

The iron hypothesis. Because bioavailable Fe – that is supplied either in the particulate or dissolved form – is an important limiting micro-nutrient for marine biomass production (*e.g.* plankton) in the surface oceans, the biogeochemical cycle of iron is closely coupled with the marine carbon cycle. This observation has led to a reevaluation of the global carbon fluxes measured in the modern oceans; for example, large-scale Fe fertilization experiments have been carried out in HNLC areas of the Southern Ocean in order to re-estimate the effect of enhanced plankton growth on the net uptake of atmospheric CO_2 and its subsequent transport, in the form of primary biomass, to oceanic sediments (*e.g.* Martin, 1990; Martin *et al.*, 1994). It has been compellingly demonstrated that these Fe-fertilized and thus "geo-engineered" systems can foster the carbon sequestration rate on a local scale (*e.g.* Coale *et al.*, 1996; Blain *et al.*, 2007), but it is considered unlikely that Fe fertilization of biologically poor regions can create a quantitatively significant sink for carbon over the long-term (Lampitt *et al.*, 2008; Taylor & Konhauser, 2011).

1.2.3 Iron mineralogy and iron supply to the oceans

Advances in our knowledge of the biogeochemistry and mineralogy of Fe over the past three decades have significantly improved our understanding of the importance of Fe-mineral phase transformations on controlling the global fluxes in the marine iron cycle, with recognition of multiple Fe sources and sinks (Canfield, 1989; Raiswell & Canfield, 1998; Poulton & Raiswell, 2002; Elrod *et al.*, 2004; Jickells *et al.*, 2005; Raiswell *et al.*, 2006; Cassar *et al.*, 2007; Poulton & Canfield, 2011; Raiswell, 2011; Homoky *et al.*, 2013; Baldermann *et al.*, 2015). On the basis of previous work, five fundamental processes have been identified, which supply the majority of dissolved and particulate Fe to the oceans: (i) wet and dry deposition of atmospheric dust, (ii) riverine transport, (iii) deposition and recycling of ocean floor sediments (the so-called benthic shuttle), (iv) hydrothermal emissions, and (v) supply from glaciers and sea ice (*e.g.* Taylor & Konhauser, 2011; Raiswell & Canfield, 2012). In the following sections, the sources of dissolved Fe^{2+} and of relevant Fe(II+III) minerals as well as their qualitative contribution to the iron biogeochemical cycle are briefly explained. Quantitative information on global fluxes of Fe between continental Fe sources and (deep-sea) sediment sinks for Fe is provided in the section 1.3.2.

Dissolved Fe. Only emissions from spatially restricted (deep-sea) hydrothermal systems, such as black and white smokers, as well as riverine input provide Fe in the dissolved form to the modern oceans (Fig. 1.4). These sources of dissolved Fe^{2+}, however, are of minor importance, compared to the (nano)particulate input of Fe(III) from, for example, shelf and slope sedi-

ments (Dale *et al.*, 2015). Dissolved Fe^{2+} is almost instantaneously transformed – following either an abiotic or a biotic reaction pathway – into more stable (nano)particulate Fe-(oxy)-hydroxides under oxidizing conditions or Fe-sulfides under reducing conditions (see sections 1.2.1 and 1.2.2 for details).

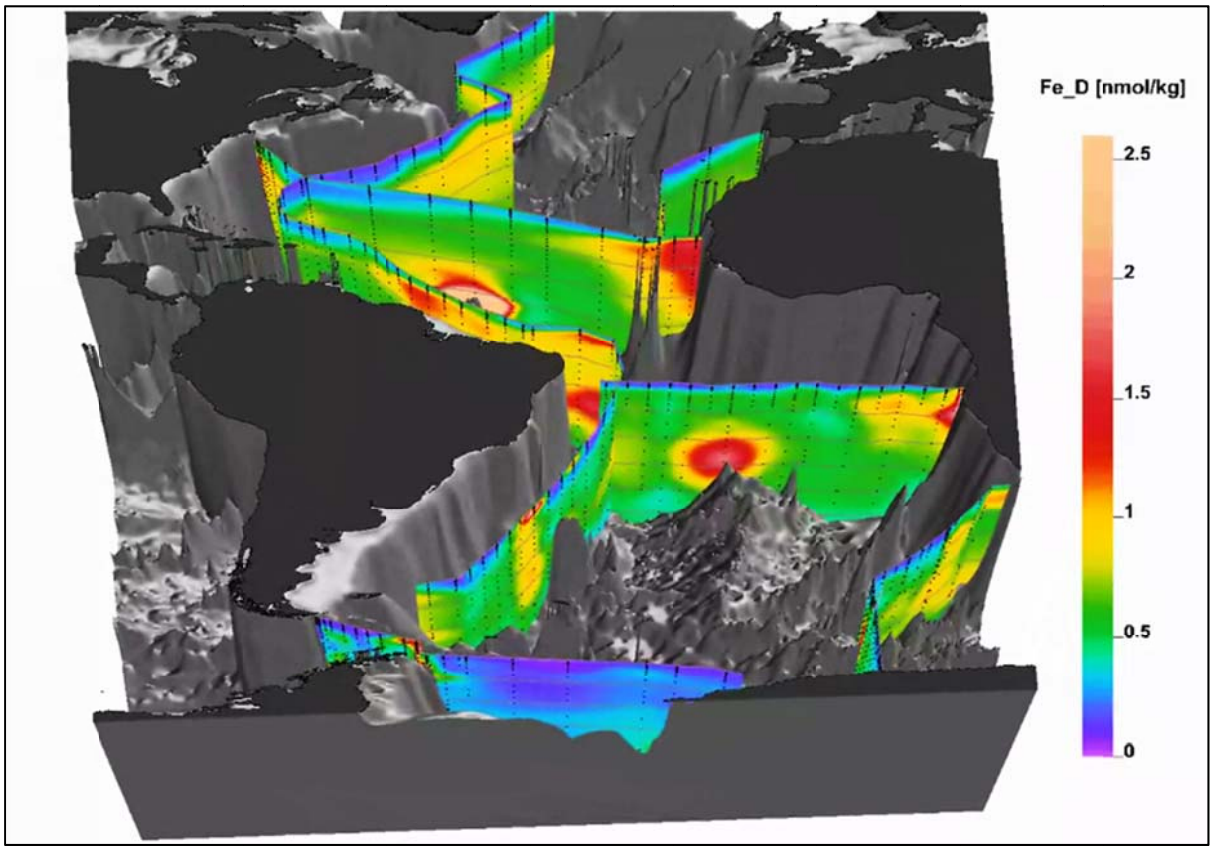

Fig. 1.4: Distribution of dissolved Fe^{2+} in the Atlantic Ocean measured along transects during the GEOTRACES program (http://www.egeotraces.org/scenes/Atlantic_Fe_D_CONC_BOTTLE.html; 15th September 2015).

Particulate Fe. The total load of (nano)particulate Fe(III) to the oceans that is delivered from rivers, glaciers, atmospheric dust (Fig. 1.5), and recycled sediments is about three orders of magnitude higher than the global dissolved Fe^{2+} load supplied from the rivers and hydrothermal vents (*e.g.* Taylor & Konhauser, 2011; Raiswell & Canfield, 2012; Dale *et al.*, 2015). The quantitatively most important continental Fe sources mentioned above supply the particulate Fe(III) mainly in the form of either labile and bioavailable Fe-(oxy)hydroxides or poorly reactive Fe bound to detrital clay minerals such as illite, smectite, and chlorite (Baldermann *et al.*, 2014). In contrast to the Fe^{2+} sources, the Fe(III) pool is almost insoluble in seawater. An overview of the biogeochemistry, mineralogy, and properties of the major Fe(II+III) minerals is provided in Cornell & Schwertmann (2003). Here, only a short summary of the relevant Fe sources bound in (oxy)hydroxides, carbonates, sulfides, and silicates is given (Fig. 1.6).

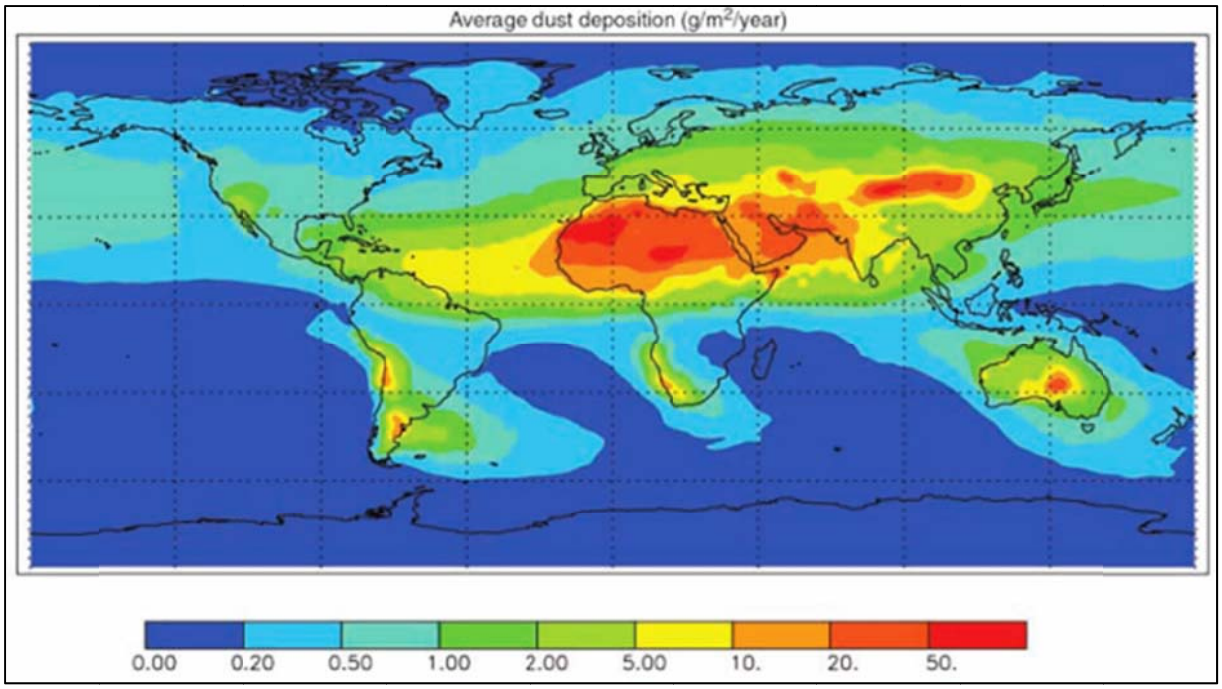

Fig. 1.5: Rates of atmospheric dust deposition worldwide (from Jickells *et al.*, 2005). The total dust input to the oceans is 450 Tg·year^{-1}, which is equivalent to a total Fe(III) input of 30 Tg·year^{-1} (Poulton & Raiswell, 2002). Percentage inputs of dust to ocean basins are as follows: North Atlantic, 43%; South Atlantic, 4%; North Pacific, 15%; South Pacific, 6%; Indian, 25%; and Southern Ocean, 6%.

Fe-(oxy)hydroxides. Particulate Fe(III) that is supplied in the form of Fe-(oxy)hydroxides, Fe_{Ox}, is the most important source of highly reactive Fe, Fe_{HR}, in the oceans, and it largely controls the productivity of plankton. This Fe pool includes bioavailable ferrihydrite, lepidocrocite, goethite, hematite, and subordinate magnetite, and is delivered by wind-blown dust as well as recycled river, shelf and slope, soil, and iceberg-hosted sediments (*e.g.* Jickells *et al.*, 2005; Raiswell *et al.*, 2006; Theng & Yuan, 2008; Raiswell, 2011). However, Fe-(oxy)hydroxides may also form in seawater through (i) diffusion of dissolved Fe^{2+} from reducing sediments into the overlying oxygenated waters, where Fe^{2+} reacts with dissolved O_2 to form (nano)particles of Fe-(oxy)hydroxides, (ii) oxidative weathering of Fe(II) minerals such as siderite, biotite, amphibole, and pyroxene, and (iii) mineralogical transformation of pre-existing Fe colloids and unstable ferrihydrite and lepidocrocite precursor phases (Raiswell, 2011).

Fe-carbonates. Since the great oxygenation of the world`s oceans in the late Neoproterozoic, dissolved Fe^{2+} occurs only in trace-level concentrations in aquatic environments, and particulate Fe is supplied to the oceanic sediments mainly in the form of Fe(III), *i.e.* Fe-(oxy)hydroxides (Canfield *et al.*, 2007; Baldermann *et al.*, 2015). Hence, in the modern biogeochemical cycle of iron, Fe(II)-hosting carbonates such as siderite, ankerite, and ferrous dolomite are of minor importance as Fe^{2+} sources, but they are still a significant sink for Fe during sediment

burial and late diagenesis (see section 1.3.2 for further explanations). Fe-carbonates, Fe_{Carb}, are therefore a minor part of the highly reactive Fe pool in near-subsurface sediments.

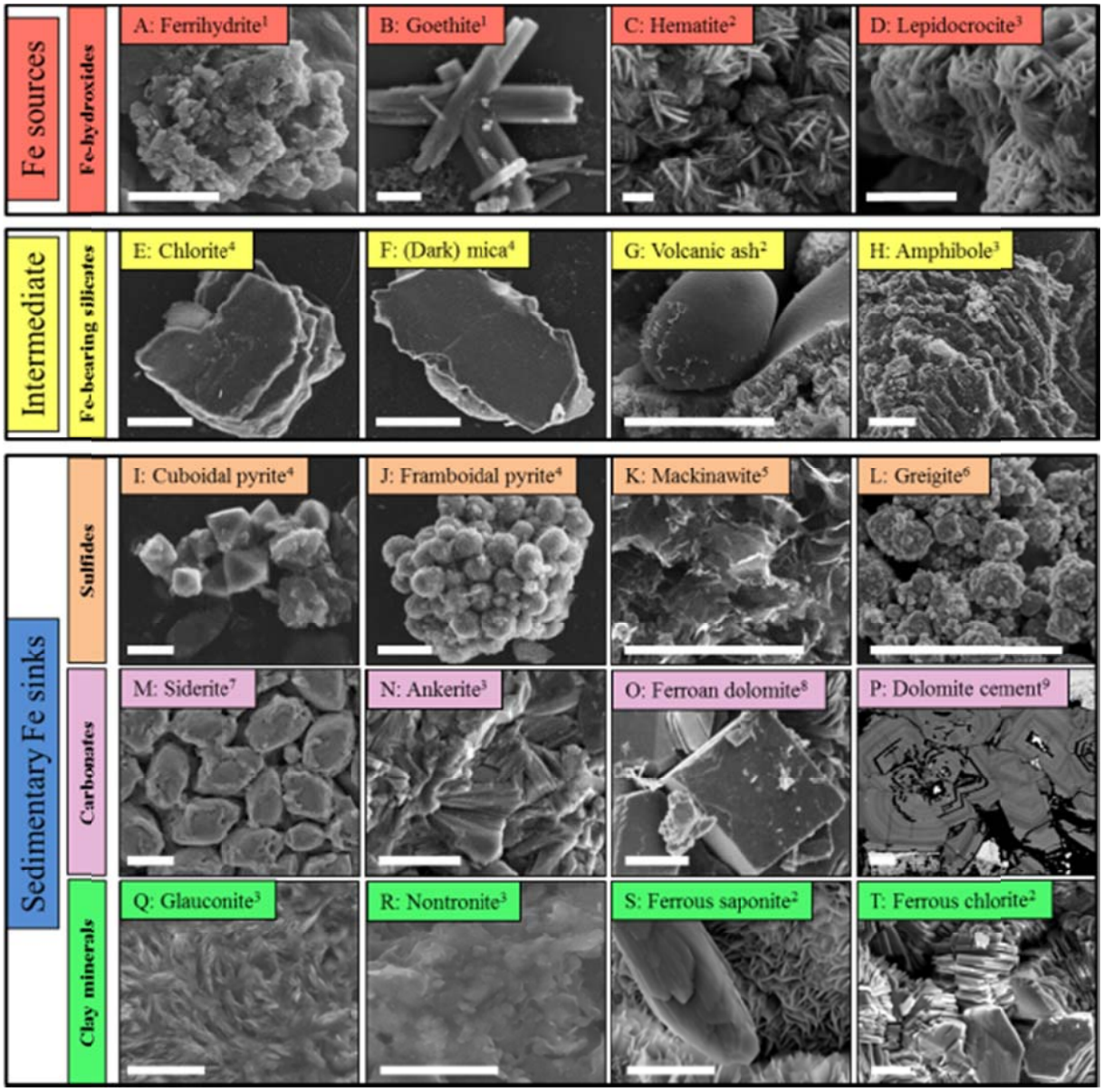

Fig. 1.6: Secondary electron (SE) images of Fe(II+III) mineral phases that act as important Fe sources (A-D, scale bar: 200 µm), intermediate (poorly reactive) phases (E-H, scale bar: 50 µm), or sedimentary Fe sinks (I-T, scale bar: 10 µm). Image sources: (1) Raiswell & Canfield (2012); (2) Image reproduced from the Images of Clay Archive of the Mineralogical Society of Great Britain & Ireland and The Clay Minerals Society; (3) Baldermann (unpublished); (4) Baldermann *et al.* (2013); (5) Zolla *et al.* (2009); (6) Hunger & Benning (2007); (7) Rohrssen (2007); (8) de Souza *et al.* (1995); (9) Baldermann *et al.* (2015b).

Fe-sulfides. After sediment deposition, partly microbially-catalyzed, reductive dissolution of unsulfidized Fe-(oxy)hydroxides occurs immediately, accompanying the oxidation of marine organic matter and bacterial sulfate reduction. These processes produce anaerobic conditions

and provide the Fe^{2+} and sulfide ions that are required for the early diagenetic precipitation of Fe-sulfides such as pyrite (Fe_{Py}), mackinawite, and greigite. Fe-sulfides are now considered to be the quantitatively most important sink for Fe and other heavy metals such as Co, Ni, Cd, Mo, Cu, Pb, and Zn in marine sediments and black shales (Canfield *et al.*, 1993; Passier *et al.*, 1997; Raiswell & Canfield, 1998; Raiswell & Canfield, 2012). However, this sedimentary Fe pool is almost completely decoupled from biogeochemical processes that take place in oxidizing aquatic environments and thus the oxidation of Fe-sulfides is negligible as a secondary Fe source to the surface oceans.

Silicates bearing Fe(II+III). In contrast to the above mentioned Fe-bearing mineral phases, Fe bound to silicates is almost unreactive and less bioavailable. The poorly reactive Fe(III) fraction, Fe_{PR}, is typically associated with detrital silicates, *e.g.* amphibole, pyroxene, and volcanic ash as well as clay minerals such as detrital (dark) mica, chlorite, and smectite, and is supplied to the oceans by deposition of atmospheric dust, riverine load, recycling of sediments, and, to a minor extent, iceberg-hosted sediments (Raiswell & Canfield, 2012). Due to to the low reactivity of Fe_{PR} (see Table 1.1) this detritally-derived Fe pool plays only a minor role as an oceanic Fe sink, and is largely decoupled from Fe redox (re)cycling processes. However, recent work on the early to late diagenetic formation of authigenic Fe(II+III)-bearing clays, *e.g.* glauconite minerals, nontronite, ferrous saponite, and Fe-chlorite, has demonstrated that green-clay authigenesis can sequester quantitatively important amounts of dissolved Fe^{2+} that could otherwise be supplied to the deep oceans (*e.g.* Baldermann *et al.*, 2012-2015).

1.3 Iron minerals in marine sediments

As a consequence of the redox chemistry and bioavailability of Fe in modern aquatic systems, oxidation of dissolved Fe^{2+} takes place rapidly, following aggregate formation, scavenging, and burial of the neo-formed (nano)particulate Fe-(oxy)hydroxides that are almost immediately transformed to pyrite in mostly anaerobic surface-near sediments. This Fe shuttle provides the first-order control for global Fe fluxes measured in the modern ocean. In suboxic sediments, however, Fe sequestration by green-clay authigenesis can be significant, while burial of Fe attributed to the formation of carbonate concretions (*i.e.* siderite and ankerite) or cement (*i.e.* ferrous dolomite) is usually associated with the later stages of (marine) diagenesis. The major Fe(II+III) minerals, which have an active role either as Fe sources or Fe sinks or both in the modern and past iron biogeochemical cycle, are shown in Fig. 1.6. In the following sections, the fate of Fe(II+III) minerals in the low-temperature cycle of iron is addressed by dis-

cussing implications for Fe sequestration and (re)cycling in ancient *versus* modern sediments. Special focus is given on assessing the global Fe fluxes between continental sources of solid-phase Fe(III) and multiple marine sediment sinks for Fe(II+III).

1.3.1 Iron diagenesis: Implications from ancient sediments

The Proterozoic to late Neoproterozoic period (~3.8 billion years to ~580 million years ago). The history of the ancient iron biogeochemical cycle is closely coupled to the evolution of the marine and atmospheric geochemical cycle of oxygen. Roughly 3.8 to 1.8 billion years ago and during the so-called Snowball Earth period, ~750 million years ago, the vast majority of Fe was deposited on the seafloor in the form of *banded iron formations* (BIF; see 1.7-A). These Fe(III)-rich sedimentary rocks were spatially and temporally linked to extensive eruptions of submarine volcanic rocks, and form massive and banded layers of hematite and magnetite that range from submillimeter to several meters thickness. BIFs typically comprise of ~20-40 wt.% of Fe, with some laminae being rich in silica (~40-50 wt.% of SiO_2). Interestingly, the world`s largest BIF deposits have been formed by precipitation from a dominantly anoxic water column (Taylor & Konhauser, 2011), in which the dissolved Fe^{2+} concentration exceeded by far that of the modern oceans.

The mechanisms proposed for the transformation of Fe^{2+}-rich oceanic waters to Fe(III)-rich sediments are (i) ultraviolet photooxidation at the ocean surface, (ii) oxidation of ferrous Fe by reaction with dissolved O_2 produced by primitive cyanobacteria, and (iii) anaerobic photosynthesis, in which bacteria convert CO_2 into biomass while using Fe^{2+} as electron donator (Bekker *et al.*, 2010; Konhauser *et al.*, 2011). Since the rise of the dissolved and atmospheric O_2 concentration in the late Neoproterozoic (~600-550 million years ago), BIFs disappeared from the sedimentary record, which was due to the reaction of Fe^{2+} ions with O_2, resulting in a quantitative removal of dissolved Fe^{2+} from aquatic Earth`s surface environments. The continuous increase in the atmospheric oxygenation likely enhanced the weathering of terrestrial sulfide minerals at that time, which triggered the delivery of sulfate ions to the oceans (Taylor & Konhauser, 2011). Ongoing with the development of new bacteria groups that were able to gain their energy demand through sulfate reduction, dissolved sulfide was generated in quantities sufficient to remove all of the remaining Fe^{2+} ions *via* precipitation as Fe-sulfide minerals. The growing impact of sulfate-reducing bacteria and the rise in the O_2 level finally resulted in (i) the fast and abrupt transition from anoxic to oxic conditions in the oceans during the Pre-Cambrian-Cambrian boundary and subsequently (ii) denoted the change from BIFs to pyrite being the new major sink for Fe (*e.g.* Canfield *et al.*, 2007; Raiswell & Canfield, 2012).

The Phanerozoic period (~545 million years ago to the present). The sedimentary rock record deposited throughout the Phanerozoic is dominated by Fe-bearing diagenetic mineral assemblages of (partly intercalated) pyrite (1.7-B), siderite (1.7-C), and green clays such as glauconite, berthierine (1.7-D), and chamosite (a Fe-rich chlorite), forming the so-called *sedimentary ironstone* deposits (Taylor & Macquaker, 2011). In contrast to the ancient marine iron cycle, where Fe was delivered mainly in its dissolved form by hydrothermal emissions, Fe-(oxy)hydroxide (nano)particles supplied from continental sources, *i.e.* recycling of shelf and slope sediments, riverine input, atmospheric dust deposition, and supply from iceberg-hosted sediments, are until now the main source of solid-phase Fe(III) to the oceans and surface oceanic sediments (see section 1.2.3). Due to the prevailing oxygenated conditions in the ocean and associated near-subsurface sediments, bacterially-mediated reductive dissolution of Fe(III) and accompanying oxidation of organic matter, and sulfate reduction, are required to produce conditions favorable for the precipitation of Fe-carbonates, Fe-sulfides, and/or Fe-clays during the early to late stages of marine diagenesis (Poulton & Canfield, 2011).

In localized oceanic basins, dissolved O_2 is consumed rapidely within the water column due to the oxidative decay of organic matter, allowing hydrogen sulfide (H_2S) to accumulate in deep and stagnating bottom waters. The Black Sea and the Landsort Deep, which is located in the eastern central Baltic Sea, are modern examples of euxinic basins (Passier *et al.*, 1997). In the Phanerozoic, several periods have been postulated, where regional and most probably global oceanic anoxia have been existed – during the so-called *oceanic anoxic events*; conditions that generally resulted in the greater formation of pyrite in deep-sea environments (*e.g.* Poulton & Canfield, 2011; Taylor & Konhauser, 2011; Raiswell & Canfield, 2012). In contrast to these deep-water settings, quantitatively important Fe sequestration through Fe(II+III) mineral deposition also took place, for example, during the Ordovician, in the Early Jurassic, and throughout the entire Cretaceous in extensive shallow-shelf regions, especially during periods of major sea-level lowstands and highstands (Taylor & Konhauser, 2011). The economically significant sedimentary iron ores were deposited mainly in the form of *oolitic ironstones*, which typically comprise of Fe-rich silicates with distinctive oolitic textures among variable proportions of siderite and ankerite. It is worth commenting that modern, natural analogues for the widespread oolitic ironstone deposits formed during the entire Phanerozoic are scarce, and restricted to mobile mudbelts found in tropical settings (Aller & Blair, 2006).

Overall, the spatiotemporal evolution of the marine biogeochemical cycle of iron is linked to the development of the oxygen and sulfur cycle, and bacterial activity, and is reflected by the nature of Fe(II+III) minerals preserved in the rock record.

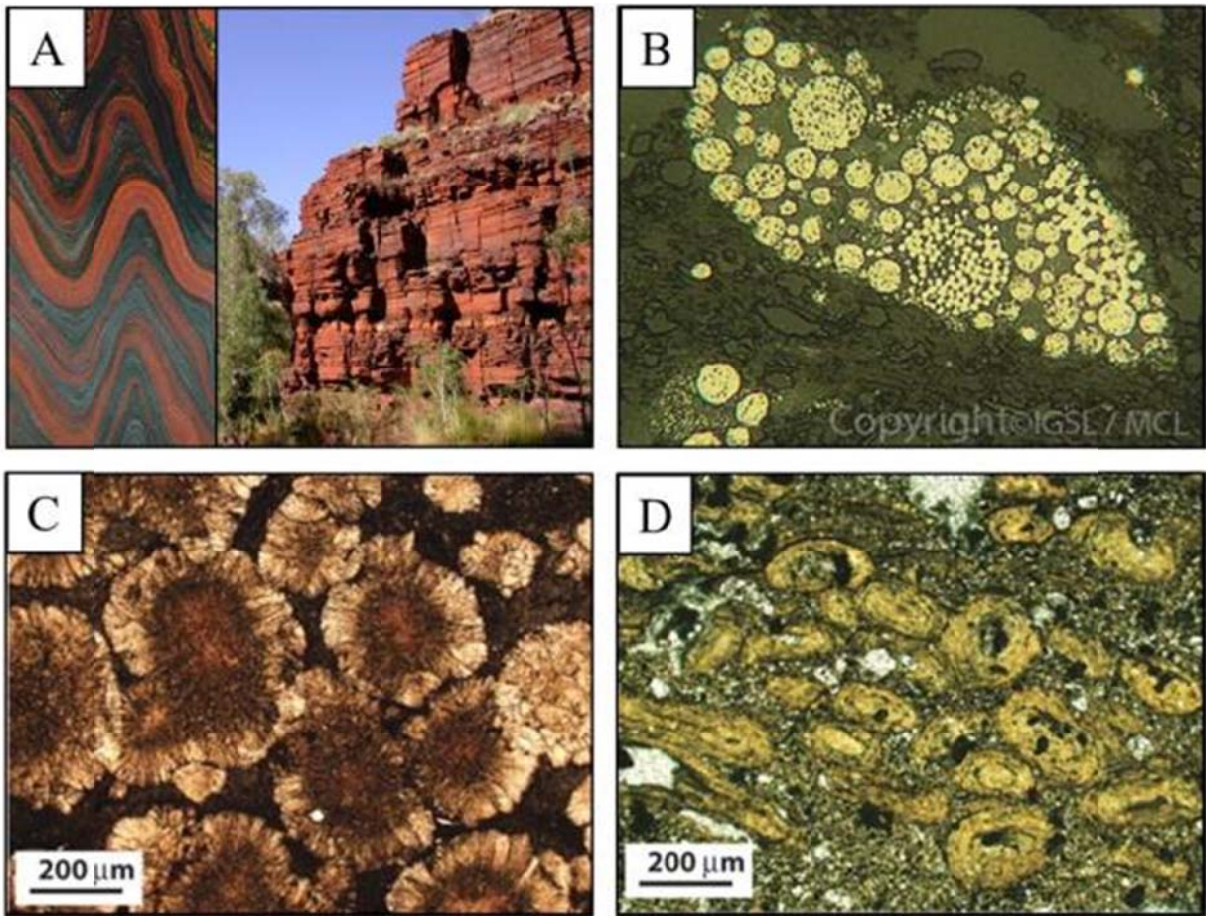

Fig. 1.7: Images of Fe(II+III) minerals forming economically important sedimentary ironstone deposits in the rock record. A) Banded iron formation (BIF) from the Paleoproterozoic Hamersley Group, Western Australia (image source: Poulton & Canfield, 2011). B) Framboidal pyrite (strata unknown). C) Spherulitic siderite from the Lower Cretaceous Walden strata, Southern England (image source: Taylor & Konhauser, 2011). D) Berthierine ooids from the Lower Jurassic Frodingham Ironstone, Eastern England (image source: Taylor & Konhauser, 2011).

1.3.2 Reservoir fluxes in the modern marine iron cycle

The vast majority of particulate Fe(III) and, to a minor extent, dissolved Fe^{2+} are delivered to the modern (surface) ocean through wet and dry deposition of atmospheric dust, riverine load, recycling of continental shelf and slope sediments, hydrothermal emissions, and supply from iceberg-hosted sediments (see section 1.2.3). The relative proportions of mostly particulate Fe input supplied from glaciers, dust, and rivers have been hard to quantify (*e.g.* Raiswell, 2011; Taylor & Konhauser, 2011), but riverine load is undoubtable the most important supplier of Fe(III) to coastal sediments, whereas dust- and glacially-derived particle input is considered to be the dominant supplier of particulate Fe(III) to the open ocean (for global estimates see the boxes in Fig. 1.8; Raiswell & Canfield, 2012). In the last decade, however, the ability to measure Fe isotopes (δ^{56}Fe in ‰) at a high precision has led to the identification of another major

process controlling global fluxes in the modern (and past) biogeochemical cycle of iron; the so-called "*benthic iron shuttle*". In this process dissolved Fe^{2+} (enriched in the light Fe isotopomer) from the reducing pore water inventory of shallow-shelf sediments is supplied back *via* diffusion and/or during sediment re-suspension events to the overlying oxidizing water masses, where the aqueous Fe^{2+} ions immediately precipitate in the form of bioavailable Fe-(oxy)hydroxides (Severmann *et al.*, 2008; Homoky *et al.*, 2009; Severmann *et al.*, 2010; Homoky *et al.*, 2013). These isotopically light (up to -3‰) and labile Fe-(oxy)hydroxide (nano)-particles are finally transported into the deeper waters by the benthic iron shuttle, and are to our current knowledge by far the most important source of solid-phase Fe(III) to the deep ocean (Boyd & Ellwood, 2010). Moreover, the results of the study of Dale *et al.* (2015) indicate that the benthic iron shuttle is a major variable for controlling the fluxes of unsulfidized, highly reactive Fe between deep-sea sediments and oceanic bottom waters prior to the ultimate burial of Fe below the redoxcline (global estimates are indicated in brackets in Fig. 1.8).

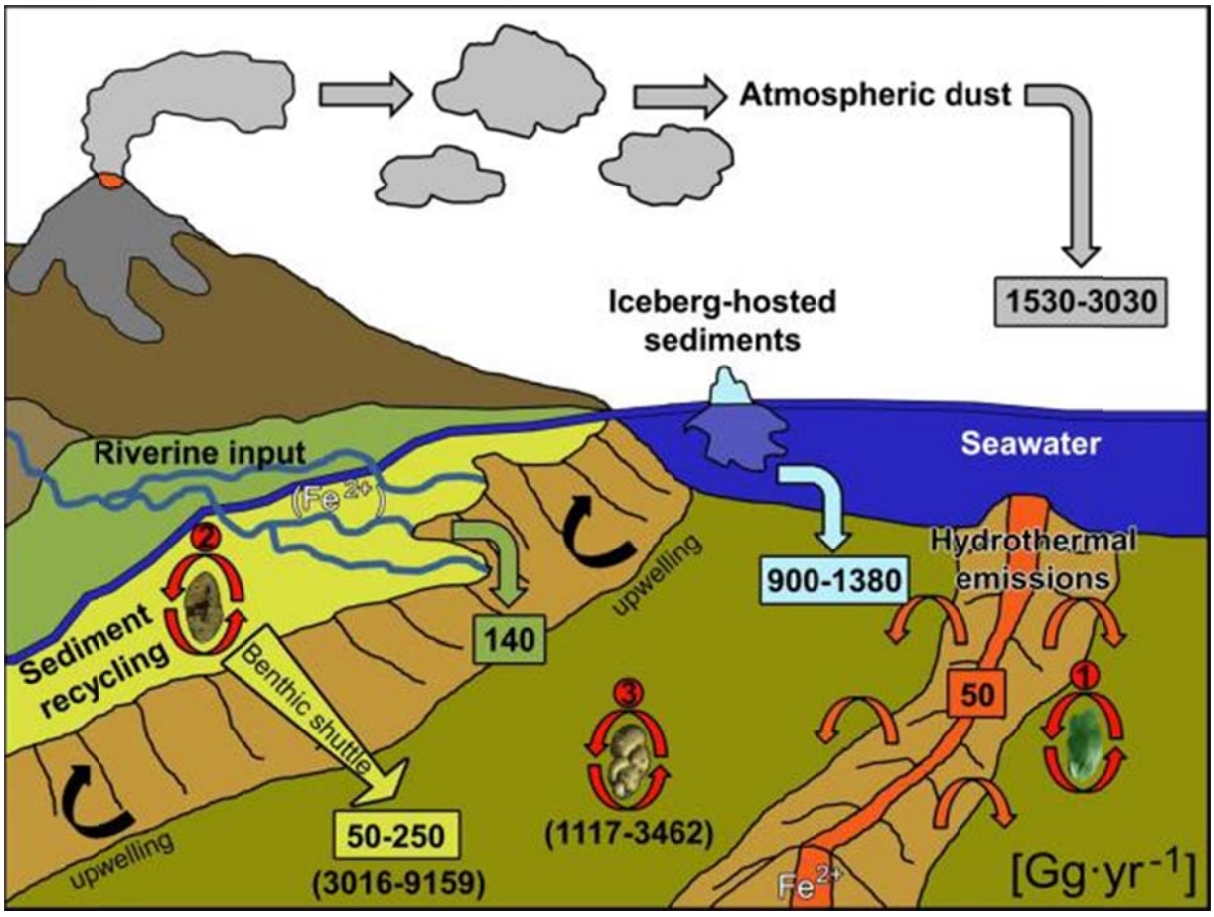

Fig. 1.8: Global fluxes in the modern biogeochemical cycle of iron. Estimates for fluxes of the filterable Fe fraction (< 0.45 µm) between continental Fe sources and deep-sea sediment sinks are indicated in boxes (Raiswell & Canfield, 2012). Numbers in brackets indicate fluxes of dissolved Fe^{2+} between shelf and deep-sea sediment sources and the overlying water masses *via* the benthic iron shuttle (Dale *et al.*, 2015).

Despite the high input of particulate Fe(III) from continental sources, the overall deposition rate of Fe on the modern ocean floor is considered low (< 100 µmol $Fe \cdot cm^{-2} \cdot yr^{-1}$), in particular in remote areas of the open ocean that are characterized by low clastic sedimentation rates of about 1-2 $cm \cdot kyr^{-1}$ (Chester, 2000; Raiswell, 2011). Here, sedimentary redox (re)cycling of unsulfidized Fe_{OX} and/or enrichment of dissolved Fe^{2+} in reducing pore water masses can be significant before this labile Fe pool is finally transformed into pyrite – the quantitatively most important authigenic sink for Fe in marine sediments – during sediment ageing and diagenesis (Canfield *et al.*, 1993; Raiswell & Canfield, 1998; Raiswell & Canfield, 2012). In contrast, significant Fe burial may occur in restricted (peri-marine and deep) oceanic basins, such as in the Black Sea and in the Orca basin, where dissolved Fe^{2+} is effectively removed beneath the euxinic water column by precipitation of pyrite (Passier *et al.*, 1997). The early diagenetic transformation of Fe-(oxy)hydroxides into pyrite in reducing marine sediments as well as the synsedimentary precipitation of pyrite from an euxinic water column are currently believed to denote the end of Fe-mineral diagenesis by ultimate burial of Fe (Fig. 1.1). Thus, present biogeochemically-coupled ocean circulation models that are used for estimating the global Fe fluxes typically assume a long-term steady-state between continental Fe sources and marine, mostly pyritic, sediment sinks (Raiswell & Canfield, 2012), although the dynamics in the marine (sedimentary) iron cycle are notably more complex. Besides pyrite formation (and ironstone mineralization, see section 1.3.1) during early diagenesis there is growing evidence for a significant transformation of Fe_{HR}, *i.e.* the sum of Fe_{OX}, Fe_{Py}, and Fe_{Carb}, to Fe_{PR}, which is attributed to the formation of ferruginous clay minerals in the "critical zones" – namely (1) mid-oceanic ridge sites, (2) reducing shelf sediments, and (3) deep-sea environments (areas marked in red in Fig. 1.8).

1.3.3 The role of iron sequestration by authigenic clay minerals in the critical zones

Although the ambient (paleo-)environmental controls and physicochemical conditions leading to the formation of *ferruginous green marine clays* in diagenetic environments are generally considered to be well understood, the links between the pore water geochemistry including Fe, and the timing, mineralogy, and geochemistry of the precipitating clay minerals bearing Fe(II+III) are not yet well constrained. Thus, the reaction mechanisms and chemical rates of Fe incorporation and burial related to green-clay authigenesis are still unknown, and hence the role of ferruginous clay mineral reactions is, at present, not included in both conceptual and numerical models of the iron biogeochemical cycle. Below, three environments are briefly summarized, in which green-clay authigenesis acts as an important authigenic sink for Fe.

(1) Ferrous saponite formation and its potential importance for Fe sequestration at mid-oceanic ridge sites (chapter 1). Fluxes in the dissolved Fe^{2+} concentrations associated with hydrothermal emission at mid-oceanic ridge sites are currently believed to be only of minor importance for the iron biogeochemical cycle (Fig. 1.8), although the rate of Fe sequestration related to the formation of ferruginous clay minerals, such as ferrous saponite, can locally exceed 1000 μmol $Fe \cdot cm^{-2} \cdot kyr^{-1}$ (*e.g.* Chester, 2000). In order to gain a better understanding of the underlying reaction mechanisms linked to the formation of saponite and the subsequent rate of Fe incorporation, ferrous saponite was precipitated in the temperature range from 60°C to 180°C from reducing and alkaline experimental solutions that contained variable molar Mg:Fe:Si ratios. The relations between the hydrogeochemistry of the reactive fluids and the mineralogy, stability, structure, and composition of the laboratory grown ferrous saponite is discussed in chapter 2. It is shown that a positive relationship exists between the proportion of Fe precipitated in ferrous saponite and the composition of the mineralizing fluids as well as the synthesis temperature (Baldermann *et al.*, 2014); relations that could be potentially used as an indicator for reconstructing fluid-solid compositions at mid-oceanic ridge sites, in soil environments, and in nuclear waste disposal sites.

(2) The role of Fe and K availability during micromilieu-controlled glauconite formation in shallow-shelf sediments (chapter 3). In organic carbon-bearing shelf sediments, partly microbially-catalyzed, reductive dissolution of highly labile Fe-(oxy)hydroxides results in the formation of a secondary pool of dissolved Fe^{2+} immediately after final sediment deposition, and accompanying sulfate reduction typically leads to the almost instantaneous precipitation of Fe^{2+} ions in the form of pyrite (Raiswell, 2011). In many shallow-shelf areas, however, the onset of the zone of sulfate reduction is suppressed (*e.g.* Taylor & Macquaker, 2011), which promotes the accumulation of high Fe^{2+} concentrations in reduced pore waters. Such environments have the potential to supply the dissolved Fe^{2+} back to the overlying oxygenated water masses (about 20 μg $Fe \cdot cm^{-2} \cdot yr^{-1}$; Elrod *et al.*, 2004) *via* the benthic iron shuttle (see section 1.3.2). In the presence of organic-rich semi-confined micro-environments, however, such as in fecal pellets and in foraminifera tests, and under sulfide-depleted conditions, Fe(III)-smectites, glauconite-smectite, and subsequently glauconite minerals may form, which can significantly reduce the pore water inventory of dissolved Fe^{2+}. The environmental conditions and reaction mechanisms involved in the glauconitization versus pyritization of fecal pellets in shallow-shelf sediments are discussed in chapter 3. The availability and concentration of Fe^{2+} and K^{+} ions in marine near-subsurface sediments are introduced as important parameters in the low-temperature Fe-smectite to glauconite reaction – in particular during periods of the

ancient Earth, where the seawater sulfate concentration was low – which explains both the spatiotemporal distribution and the variable abundance of green glauconitic grains in the rock record (*e.g.* Baldermann *et al.*, 2012).

(3) Fe sequestration during green-clay authigenesis in modern deep-sea environments (chapters 4 and 5). The bioavailability and (redox) chemistry of Fe significantly influences biogeochemical processes in Earth`s surface and deep-sea ecosystems, and has therefore been of major significance for the evolution of ocean geochemistry, life forms, and associated sediments throughout the geological record (*e.g.* Baldermann *et al.*, 2015). Historically, fluxes in the marine iron cycle have been calculated considering changes in the (nano)particulate Fe-(oxy)hydroxide inputs from continental sources, the dissolved (< 0.45 μm) Fe concentration in seawater, and multiple Fe(II+III) mineral sinks in marine sediments (*e.g.* Parekh *et al.*, 2004). Due to the prevailing oxygenated conditions in the global ocean since at least the late Neoproterozoic (Canfield *et al.*, 2007), current biogeochemically-coupled ocean circulation models are quantifying mass balance relationships in the marine iron cycle using *in-situ* measured rates of dissolved Fe^{2+} reflux from marine sediments (Boyd & Ellwood, 2010; Dale *et al.*, 2015). Although these models indirectly account for the bulk of all Fe mineral sources and sinks in the marine iron cycle, at present, only little is known about the individual rate of Fe sequestration attributed to green-clay formation versus pyrite precipitation. In the chapters 4 and 5, the relations between pore water geochemistry and the development of micromilieus in foraminifera tests that are suitable for glauconitization are highlighted, and a new model for glauconite mineral formation in a modern deep-sea environment is presented (Baldermann *et al.*, 2013). Using sequential extraction and subsequent quantification of multiple Fe-mineral reservoirs recorded in the near-subsurface sediments, Fe burial rates attributed to green-clay authigenesis versus pyrite precipitation are presented for the first time (Baldermann *et al.*, 2015). It is suggested that green-clay authigenesis limits the pore water inventory of dissolved Fe^{2+} in suboxic pelagic sediments, and hence needs to be considered in current (conceptual and numerical) models of the marine iron cycle.

Chapter 2

The Fe-Mg-saponite solid solution series – a hydrothermal synthesis study

2.1 Abstract

The boundary conditions of saponite formation are generally considered to be well known, but significant gaps in knowledge persist in respect to the influence of solution chemistry, temperature, and reaction time on the mineralogy, structure, stability, and chemical composition of laboratory grown ferrous saponite. In the present study, ferrous saponite and Mg-saponite were synthesized in Teflon-lined, stainless steel autoclaves at 60°C, 120°C, and 180°C, alkaline pH, reducing conditions, and initial solutions with molar Si:Fe:Mg ratios of 4:0:2, 4:1:1, 4:1.5:0.5, 4:1.75:0.25, and 4:1.82:0.18. The experimental solutions were prepared by dissolution of sodium orthosilicate (Na_4SiO_4), iron(II)sulphate ($FeSO_4 \cdot 6H_2O$) and magnesium chloride salts ($MgCl_2 \cdot 6H_2O$ with ≤ 0.005 mass% of K and Ca) in 50 mL ultrapure water that contained 0.05% sodium dithionite as the reducing agent. The precipitates obtained at 2, 5, and 7 days of reaction time were investigated by X-ray diffraction techniques, transmission electron microscopy analysis, infra-red spectroscopy, and thermo-analytical methods.

The precipitates were composed mainly of trioctahedral ferrous saponite, with small admixtures of co-precipitated brucite, opal-CT, and 2-line ferrihydrite, and nontronite as the probable alteration product of ferrous saponite. The compositions of the obtained ferrous saponites were highly variable, $(Na_{0.44\text{-}0.59}K_{0.00\text{-}0.05}Ca_{0.00\text{-}0.02})(Fe^{2+}_{0.37\text{-}2.41}Mg_{0.24\text{-}2.44}Fe^{3+}_{0.00\text{-}0.28})\Sigma_{2.65\text{-}2.85}$ $[(Fe^{3+}_{0.00\text{-}0.37}Si_{3.63\text{-}4.00})O_{10}](OH)_2$, but show similarities with natural occurring trioctahedral Fe and Mg end members, except for the Al content. This suggests that a complete solid solution may exist in the Fe-Mg-saponite series.

A conceptual reaction sequence for the formation of ferrous saponite is developed based on the experimental solution and solid compositions. Initially, at pH ≥ 10.4, brucite-type octahedral template sheets are formed, where dissolved Si-O tetrahedrons are condensed. Subsequent re-organization of the octahedra and tetrahedra via multiple dissolution-precipitation

processes finally results in the formation of saponite structures, together with brucite and partly amorphous silica. The extent of Fe^{2+} incorporation in the octahedral template sheets via isomorphic substitution is suggested to stabilize the saponite structure, explaining (i) the abundance of saponite enriched in $^{VI}Fe^{2+}$ at elevated Fe supply and (ii) the effect of structural Fe on controlling the net formation rates of ferrous saponite.

2.2 Introduction

The mineral type saponite, $M^{+}_{x}(Mg)_{3.0}[(Al_xSi_{4-x})O_{10}](OH)_2$, is a Mg-rich trioctahedral 2:1 clay mineral of the smectite group with ferro-saponite, $M^{+}_{x}(Fe^{2+}_{2.0}Mg_{1.0})[(Al_xSi_{4-x})O_{10}](OH)_2$, as Fe-rich member (Jasmund & Lagaly, 1993). In mostly oxidizing near-surface environments ferrous saponite is rarely found (e.g. Köster, 1993) and nontronite dominates as the most common ferric dioctahedral smectite (Decarreau & Bonnin, 1986), despite there are several environments that generate saponite. Under natural conditions the formation of saponite is typically attributed to hydrothermal alteration of (ultra)mafic igneous rocks, tuffs, and more rarely siliceous dolostone at temperatures usually below 150°C and under strictly reducing conditions (*e.g.* Post, 1984, Schiffman & Staudigel, 1995, Dill *et al*., 2011). Saponite can also be formed below 50°C such as within soil profiles by the weathering of Mg-rich silicates under climatic conditions (Wildman *et al.*, 1971). Trioctahedral saponite-type clay minerals have also been interpreted to form in both marine and lacustrine evaporitic lakes by precipitation from gel precursors under alkaline conditions (Sandler *et al.*, 2001, Akbulut & Kadir, 2003) or by transformation of dioctahedral clay minerals (Deocampo *et al.*, 2009).

The chemical composition of naturally occurring saponite is highly variable due to common Fe^{2+}, Fe^{3+}, and Al^{3+} substitutions for Mg^{2+} in the octahedral sheet (Decarreau & Bonnin, 1986), which are accompanied by partial Al^{3+} and Fe^{3+} substitutions for Si^{4+} in the tetrahedral sheet (e.g. Jasmund & Lagaly, 1993). It is well known from both natural and synthesized nontronites that the proportion of ferric ^{VI}Fe has a significant impact on the physicochemical properties of smectites such as their thermal stability (Wolters & Emmerich, 2007, Decarreau *et al.*, 2008). However, the influence of Fe^{2+} incorporation during saponite formation and related changes in mineralogical, geochemical, and the thermal properties of ferrous saponite are still poorly investigated (*e.g.* Velde, 1992). Several deposits of ferrous saponite have been reported (*e.g.* Badaut *et al.*, 1985, Brigatti *et al.*, 1999, Porter *et al.*, 2000, Dill *et al.*, 2011), but there is only one location worldwide, called the Lovoberezhye Iceland spar deposit in Siberia (Russia), where Fe ions are the major occupants of the octahedral sheet of saponite. This

mineral type, $(Ca_{0.31}Na_{0.04}K_{0.01})(Fe^{2+}_{1.56}Fe^{3+}_{0.52}Mg_{0.87})_{\sum 2.95}[(Fe^{3+}_{0.06}Al_{1.03}Si_{2.91}O_{10}](OH)_2$, is referred to as ferro-saponite (Chukanov *et al.*, 2003).

In order to investigate the boundary conditions of (ferrous) saponite formation, Caillère *et al.* (1953, 1955) performed synthesis experiments by aging diluted solutions containing aqueous silica and Mg^{2+}, Al^{3+}, and Fe^{2+} or Fe^{3+} ions (from dissolution of chlorides) at 100°C and pH from 8.5 to 9.5. Harder (1976, 1978) claimed to have synthesized ferrous saponites within only 15 days, under reducing conditions, and at low temperatures of 3°C and 20°C in a similar way by a sol-gel process. The formation mechanism proposed was that of precipitation of thin octahedral sheets with a brucite [$Mg(OH)_2$] (or a gibbsite [$Al(OH)_3$]) structure, which served as a template for subsequent condensation of dissolved silica. Unfortunately, neither X-ray diffraction patterns nor chemical data were presented in the experimental studies of Harder to validate the nature, composition, and crystallinity of the synthesized solids, as recommended by Kloprogge *et al.* (1999). Despite the apparent lack of constraints it is generally accepted that smectite formation is usually enhanced at neutral to alkaline pH, in the presence of Mg, at silica concentrations typically undersaturated with respect to amorphous silica, and as the geochemical composition of the initial solution is equal to ideal smectite stoichiometry (Harder, 1972, Kloprogge *et al.*, 1999). There remains, however, a significant gap in knowledge concerning the effect of Fe^{2+} incorporation on the properties and structure of trioctahedral ferrous saponite.

The aim of the present study was to determine the influence of solution chemistry, temperature, and reaction time of synthesis on the mineralogy, composition, and thermal and chemical stability of synthetic ferrous saponite. The recognized chemical variability of synthesized and natural occurring trioctahedral clay minerals in the Fe-Mg-saponite solid solution is discussed in relation to the boundary conditions of ferrous saponite formation.

2.3 Experimental design and methods

2.3.1 Experimental design and clay mineral synthesis

Ferrous saponite was synthesized in Teflon-lined, stainless steel autoclaves under hydrothermal conditions. Freshly prepared solutions with distinct Si:Fe:Mg ratios, which equaled ideal smectite compositions, were obtained by mixing appropriate volumes of sodium orthosilicate (Na_4SiO_4), iron(II)sulphate ($FeSO_4 \cdot 6H_2O$), and magnesium chloride ($MgCl_2 \cdot 6H_2O$ with $\leq$ 0.005 mass% of K and Ca) of analytical grade. In all experiments (Table 2.1), a total of two grams of the salts were diluted in 50 mL of ultrapure water, which contained 0.05 mass% of

sodium dithionite ($Na_2S_2O_4$) to establish reducing conditions. The pH of the initial solutions was adjusted to 8.5 ± 0.1 by stepwise addition of 1 M NaOH. In order to investigate the influence of the solution chemistry on the clay mineral composition the solutions containing initial molar Si:Fe:Mg ratios of 4:1.82:0.18 (N13-15), 4:1.75:0.25 (N1-3), 4:1.5:0.5 (N7-9), 4:1:1 (N4-6), and 4:0:2 (N16-18) were aged at 120°C ± 5°C. The effect of temperature on clay mineral for-mation was studied by aging solutions with a molar Si:Fe:Mg ratio of 4:1:1 at 60°C (N19-21), 120°C (N4-6), and 180°C (N10-12), each ± 5°C. After a reaction time of 2, 5, and 7 days the respective individual experiment was cooled down to about 40°C within 12 hours and precipitates separated by filtration using 0.45 µm acetate filters. Subsequent to drying at 40°C, adsorbed electrolytes were removed from precipitates by dialysis (24 hours, three times). The final experimental solutions were filtered and acidified with 6% nitric acid to prevent Fe oxidation and further precipitation.

Table 2.1: Experimental setup and chemical compositions of the initial experimental solutions. Reducing conditions were achieved in all experiments by addition of the reducing agent sodium dithionite.

Experimental design			Initial experimental solution chemistry				
	T	Reaction time	Si:Fe:Mg	Si	Fe	Mg	Initial
Sample	[°C]	of synthesis	[molar]	[mg·L^{-1}]	[mg·L^{-1}]	[mg·L^{-1}]	pH
N1	120	2 days	4:1.75:0.25	3537	3152	201	8.4
N2	120	5 days	4:1.75:0.25	3536	3155	201	8.4
N3	120	7 days	4:1.75:0.25	3539	3154	200	8.4
N4	120	2 days	4:1:1	3690	1885	824	8.4
N5	120	5 days	4:1:1	3692	1885	823	8.4
N6	120	7 days	4:1:1	3692	1885	823	8.4
N7	120	2 days	4:1.5:0.5	3581	2742	399	8.5
N8	120	5 days	4:1.5:0.5	3581	2742	399	8.5
N9	120	7 days	4:1.5:0.5	3581	2742	399	8.5
N10	180	2 days	4:1:1	3690	1885	825	8.5
N11	180	5 days	4:1:1	3691	1885	825	8.5
N12	180	7 days	4:1:1	3690	1885	824	8.5
N13	120	2 days	4:1.82:0.18	3514	3270	138	8.5
N14	120	5 days	4:1.82:0.18	3514	3270	138	8.5
N15	120	7 days	4:1.82:0.18	3514	3270	138	8.5
N16	120	2 days	4:0:2	3935	0	1753	8.5
N17	120	5 days	4:0:2	3935	0	1753	8.5
N18	120	7 days	4:0:2	3935	0	1753	8.5
N19	60	2 days	4:1:1	3693	1884	824	8.5
N20	60	5 days	4:1:1	3691	1887	825	8.5
N21	60	7 days	4:1:1	3691	1884	837	8.5

2.3.2 Analytical methods

The pH of the initial and final experimental solutions was measured with a WTW Multi 350i at 25°C. For the calibration of the Multi-parameter probe buffer solutions of pH 4, 7, and 10 were used. The Fe, Mg, and Si concentrations of the acidified final experimental solutions were analyzed by inductively coupled plasma optical emission spectroscopy (ICP-OES) using

a PerkinElmer Optima 4300 DV. A NIST 1640a standard was measured at the beginning and at the end of the analyses, with an analytical error of < 10% for the above elements.

X-ray diffraction (XRD) patterns of randomly oriented preparations were recorded to identify the mineralogy of the synthesized precipitates using a PANalytical X'Pert PRO diffractometer (Co-Kα radiation) operated at 40 kV and 40 mA. For the preparation of the specimens the top loading technique was used. The diffractometer is equipped with a Scientific X'Celerator detector, 0.5° antiscattering and divergence slits, spinner stage, primary and secondary soller, and automatic sample changer. The preparations were X-rayed from 4-85° 2θ with a step size of 0.008° $2\theta \cdot s^{-1}$ and a count time of 40 $s \cdot step^{-1}$. Oriented preparations were made for further XRD analysis of the clay minerals using a Phillips PW 1830 diffractometer (Cu-Kα radiation, 40 kV and 30 mA) outfitted with automatic slits, a graphite monochromator, and a scintillation counter. For the preparation of the samples 50 mg of the precipitate was mixed with 5 mL of deionized water and dispersed for 10 min in an ultrasonic bath. Oriented mounts were then prepared by suction of the clay-in-suspension through a ceramic tile of about 4 cm². These thin clay films were X-rayed from 3-30° 2θ with a step size of 0.02° $2\theta \cdot s^{-1}$ and a count time of 2 $s \cdot step^{-1}$, each at air dried conditions and subsequent to the solvation of the preparations with ethylene glycol (EG) and heating of the specimens to 550°C for one hour.

The composition of the synthesized clay matter was analyzed with a Phillips CM 20 transmission electron microscope (TEM) equipped with a Noran high purity Germanium (HPGe) detector for energy-dispersive X-ray spectroscopy (EDX) analysis. Twelve precipitates from experiments N4-15, the samples which contained ferrous saponite, were prepared on holey C grids, following standard TEM preparation procedures. An accelerating voltage of 200 kV and a count time of 30 s were applied to reduce element migration and element loss during the TEM-EDX measurements. In order to verify the accuracy of the EDX results two clay mineral standards, the Garfield nontronite and ferroan saponite (Dill *et al.*, 2011), were analyzed accordingly. The analytical reproducibility was 5-10% for Fe_2O_3, Al_2O_3, SiO_2, and MgO analysis and 10-30% for K_2O, CaO, and Na_2O analysis, which is equivalent to an analytical error of < 3 mass% for Fe_2O_3, Al_2O_3, SiO_2, and MgO, and < 1 mass% for K_2O, CaO, and Na_2O, respectively.

TEM images, selected area electron diffraction (SAED) patterns, and electron energy-loss spectroscopy (EELS) data were obtained using a FEI Tecnai F20 instrument fitted with a single-crystal LaB_6 Schottky Field Emitter, a Gatan imaging filter, and an UltraScan CCD camera. The EELS spectra were acquired in the TEM collection mode of the microscope using a convergence semi-angle of 6.06 mrad, a semi-angle of 11.9 mrad, 200 kV accelerating

voltage, and an acquisition time of 100 s. The energy resolution was ΔE_{FWHM} = 0.5 eV, expressed as the full width at half maximum (FWHM) of the zero-loss peak. Instrumental details and potential effects on the Fe oxidation state induced by electron beam irradiation as well as the evaluation of the EELS data are discussed in detail by van Aken *et al.* (1998) and Garvie *et al.* (1994). Background subtraction of the EELS spectra was realized using an inverse power-law function, which was extrapolated from the O K pre-edge region. The intensity ratio of the Fe^{3+} L_3 and Fe^{2+} L_2 lines, I_{L3}/I_{L2}, was calculated by integration over the 708.5–710.5 eV and 719.7–721.7 eV ranges (Lanson *et al.*, 2012). The $Fe^{3+}/\Sigma Fe$ ratio and the corresponding ferrous/ferric Fe ratio in minerals was determined using the integral Fe $L_{2,3}$-edge white-line intensity ratios, expressed as I_{L3}/I_{L2}, as a function of the ferric iron concentration, as reported in van Aken *et al.* (1998). Finally, structural formulae were calculated for the synthesized clay minerals, on the basis of 22 negative charges (Bailey *et al.*, 1980), using the Fe^{2+}/Fe^{3+} ratios determined by TEM-EELS and assuming (i) tetrahedral Si^{4+} + Al^{3+} + Fe^{3+} is equal to 4, (ii) $Fe^{3+}{}_{rest}$, $Al^{3+}{}_{rest}$, Fe^{2+}, and Mg^{2+} occupy the octahedral sheet, and (iii) K^+, Na^+, and Ca^{2+} are located in the interlayer sites (see discussion for further explanations).

The thermal evolution of synthesized precipitates was studied using combined thermo-gravimetry (TG), differential scanning calorimetry (DSC), and mass spectrometry (MS) performed on a Netzsch 409 PC thermobalance apparatus connected to a Pfeiffer Thermostar quadrupole mass spectrometer. 100 mg of precipitate was equilibrated at 53% relative humidity and then heated from 30°C to 1000°C at a constant heating rate of 10 K/min under air flow.

Mid-infrared spectra (MIR) were obtained for saponite identification. Standard KBr pellets were therefore prepared by mixing 1 mg of sample with 200 mg KBr. Subsequently, Fourier transform infrared spectroscopy (FTIR) was carried out on a Thermo Nicolet Nexus FTIR spectrometer fitted with a DTGS TEC detector. The spectra were recorded in the range from 4000 to 450 cm^{-1} with a resolution of 2 cm^{-1}.

2.4 Results

2.4.1 Evaluation of synthesized precipitates and final experimental solutions

The bulk mineralogy of the synthesized precipitates and the geochemical compositions of the final experimental solutions are reported in Table 2.2. The highest proportion of ferrous saponite was obtained in experiments N4-N15 (T ≥ 120°C). At the lower temperature of 60°C and in the absence of Fe^{2+} supply only trace amounts of ferrous saponite (N19-21) and minor Mg-saponite (N16-18) were detected, whereas possibly antigorite was formed in experiments N1-

3. In addition to the trioctahedral clay minerals, 2-line ferrihydrite, brucite, and opal-CT were identified by XRD study of the received precipitates. The proportion of individual reaction products depended mainly on the initial solution chemistry (Table 2.1). Due to abundant 2-line ferrihydrite most of precipitates had a yellowish orange to reddish brown color. Accordingly, the final experimental solutions were optically clear with only little yellow coloration attributed to the presence of small amounts of ferric Fe (0.1-2.3 $mg \cdot L^{-1}$). The solubility product of ferrihydrite is considerable low at strongly alkaline conditions such as that of the final experimental solutions, thus, ferric Fe concentrations should reflect occurrences of (nano)particulate ferrihydrite. The Mg concentrations were found to be always below the detection limit of the ICP-OES analyses (< 0.1 $mg \cdot L^{-1}$). The final Si concentrations remained at a low to moderate level, with concentrations ranging from 90 up to 2600 $mg \cdot L^{-1}$. In the following section, the mineralogy and composition as well as the spectroscopic and thermo-analytical results are presented, in particular of synthesized precipitates from experiments N4-15, the samples that contained ferrous saponite.

Table 2.2: Chemical compositions of the final experimental solutions. The final Mg concentrations were always below the detection limit (b.d.l.) of ICP-OES analyses. The mineralogy and color of synthesized precipitates are indicated on the right.

Experimental design			Final experimental solution chemistry			Characterization of the synthesized precipitates						
	T	Reaction time	Si	Fe	Final	Mineralogical composition						Color
Sample	[°C]	of synthesis	[mg·L⁻¹]	[mg·L⁻¹]	pH	Fe-Sap	Sap	Atg (?)	Fh	Brc	CT-Op	[Munsell Chart]
N1	120	2 days	119	0.2	12.6	-	-	+	+++	+	++	Dusky brown
N2	120	5 days	108	0.5	12.6	-	-	+	+++	+	++	Dusky brown
N3	120	7 days	89	0.5	12.6	-	-	+	+++	+	++	Moderate brown
N4	120	2 days	2498	1.4	12.3	++	-	-	++	++	+	Yellowish orange
N5	120	5 days	2395	1.0	12.4	++	-	-	++	++	+	Yellowish orange
N6	120	7 days	1968	1.8	12.5	+++	-	-	++	++	+	Yellowish orange
N7	120	2 days	2061	0.7	12.5	++	-	-	++	-	++	Reddish brown
N8	120	5 days	1584	1.3	12.7	+++	-	-	++	-	+	Reddish brown
N9	120	7 days	2555	0.5	12.7	+++	-	-	+	-	+	Yellowish orange
N10	180	2 days	1451	2.3	12.6	+++	-	-	+	*	-	Olive brown
N11	180	5 days	433	0.7	12.9	+++	-	-	+	*	-	Olive brown
N12	180	7 days	569	b.d.l.	12.7	+++	-	-	+	*	-	Olive brown
N13	120	2 days	1705	0.6	12.7	+++	-	-	++	*	+	Yellowish orange
N14	120	5 days	2222	0.1	12.6	+++	-	-	+	*	++	Yellowish orange
N15	120	7 days	1678	1.2	12.6	+++	-	-	+	*	+	Yellowish orange
N16	120	2 days	2365	b.d.l.	12.7	-	+	-	-	+++	++	white
N17	120	5 days	2578	b.d.l.	12.6	-	+	-	-	+++	++	white
N18	120	7 days	1877	b.d.l.	12.7	-	+	-	-	+++	++	white
N19	60	2 days	2562	0.6	12.7	*	-	-	++	+++	++	Reddish brown
N20	60	5 days	2184	0.9	12.6	*	-	-	++	+++	+++	Reddish brown
N21	60	7 days	2460	0.2	12.6	*	-	-	++	+++	++	Reddish brown

2.4.2 Mineralogical composition of synthesized clay minerals

The XRD patterns of randomly oriented precipitates from experiments N4-N15 (see Fig. 2.1) display broad d_{001}-reflections between 12.5 Å to 14.0 Å, indicative of smectite with one to two water layers in the interlayer. No *00l*-reflections were detected at lower diffraction angles, suggesting a lack of ordered interstratification. At higher diffraction angles broad, asymmetric peaks were recognized at 4.58-4.62 Å (d_{11-02}), 3.10-3.15 Å (d_{004}), 2.61-2.64 Å (d_{13-20}), and

1.70-1.72 Å ($d_{15\text{-}24\text{-}31}$). The diagnostic d_{060}-value was at 1.534-1.544 Å. At an elevated temperature of 180°C and with increasing molar Fe:Mg ratio of the initial solution, the d_{060}-value shifted to lower diffraction angles (Fig. 1), which documents the incorporation of ferrous Fe in the saponite structure. Decarreau *et al.* (2008) also reported a d_{060}-value at 1.54 Å for synthetic, strictly ferric nontronite. The existence of nontronite in our samples, as the most likely alteration product of ferrous saponite, can therefore not be ruled out. However, it is evident that trioctahedral structural units dominate in our precipitates, as evident by comparison with XRD pattern of natural Ballarat saponite (Post, 1984), because the position of all *hkl*-reflections mentioned are similar, except for the lower intensities and notably higher d_{060}-value for all types of synthesized clay minerals. The d_{060}-value for the Ballarat saponite was reported to be 1.53 Å (Post, 1984). These differences reflect variations in Fe content of the ferrous saponites synthesized in the present study compared with that of the Ballarat saponite.

The XRD patterns of the oriented, air dried clay preparations show d_{001}-values from 12.0 Å to 13.5 Å, indicating that Na^+ ions mainly occupy the interlayer sites of the synthesized clay matter. After EG-solvation of the clay preparations the basal spacing increased to 16.9-17.1 Å (Fig. 2.1), reflecting the smectitic nature of the clay mineral precipitates. Thus, no indication for ordered interstratification was evident in the XRD patterns. Subsequent to heating the clay films to 550°C the d_{001}-value decreased to ~10.0 Å, reflecting the collapse of the interlayer sites of the ferrous saponites. With increasing temperature of synthesis, from 120°C to 180°C, the d_{001}- as well as the *hkl*-reflections of the synthesized ferrous saponite became sharper, associated with an increase in diffraction intensity (Figs 2.1-A and 2.1-B). At an elevated molar Fe:Mg ratio of the initial solution, a similar trend was recognized (Figs 2.1-A and 2.1-D), suggestive of more ordered stacking sequences in ferrous saponite at an elevated structural Fe content. Only, the ferrous saponite obtained from a molar Fe:Mg ratio of 1.5:0.5 frequently yielded broader and less intense *hkl*-reflections (Fig. 2.1-C). However, all diffraction peaks became more well-defined and sharper with longer reaction time of synthesis. The latter feature is suggested to reflect changes in the crystallite size of the synthesized ferrous saponite, as discussed below.

2.4.3 Particle shape, mineralogy and composition of synthesized clay minerals

Representative TEM images of the precipitates (Fig. 2.2) obtained after five days of reaction time typically show micrometer-sized aggregates of clumped clay mineral particles. The individual particles are < 50 nm in size, have a platy shape with curled edges, and are mixed with fibrous particles ~50-200 nm in length, as seen in precipitate N5 (Fig. 2.2-A).

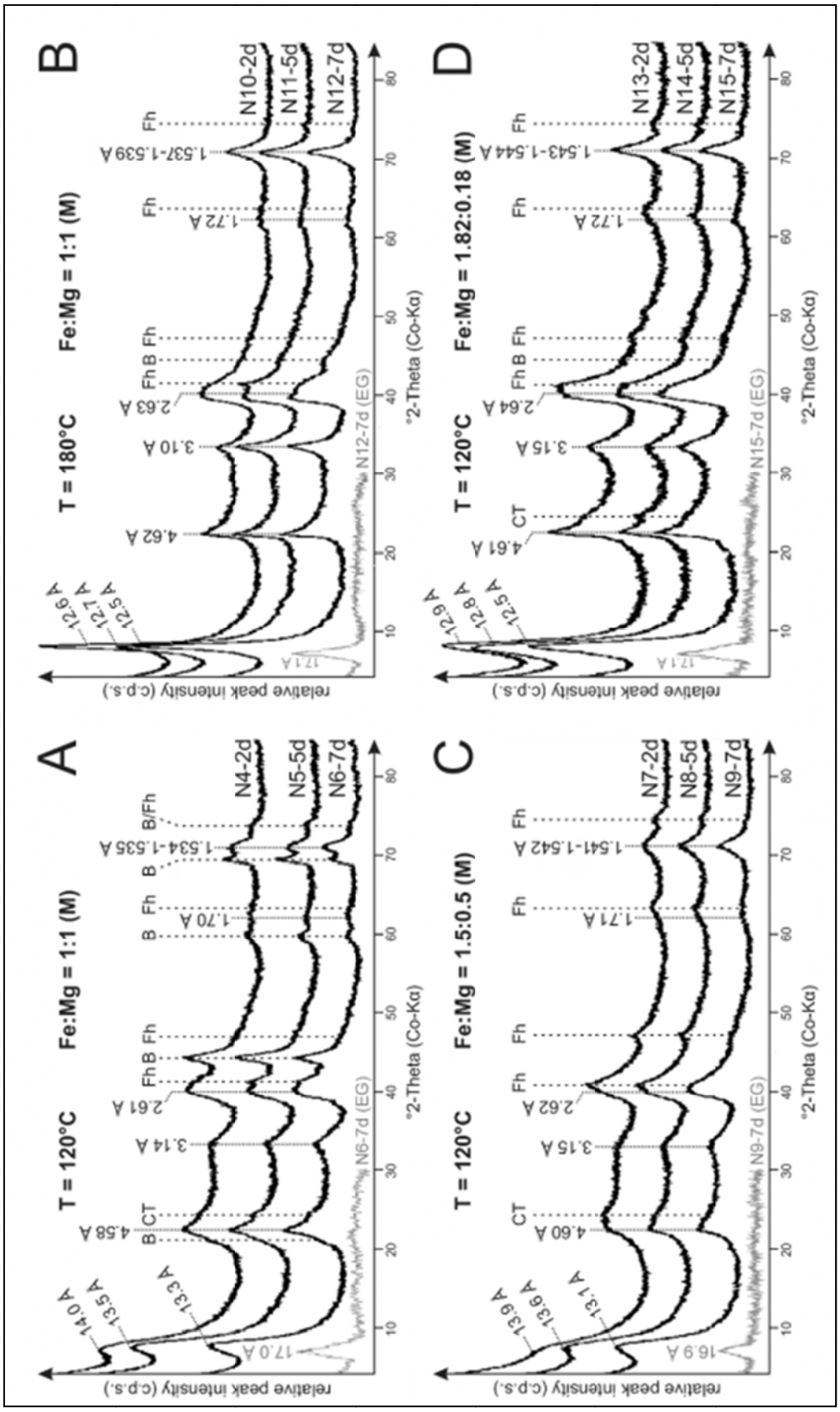

Fig. 2.1: XRD patterns of randomly oriented preparations (black curves) of precipitates from experiments N4-N15. XRD patterns of glycolated clay films (grey curves) show that the synthesized clay matter is purely smectitic. The unlabeled peaks correspond to trioctahedral ferrous saponite. Coding: B: brucite; CT: opal-CT; Fh: 2-line ferrihydrite; d: days reaction time.

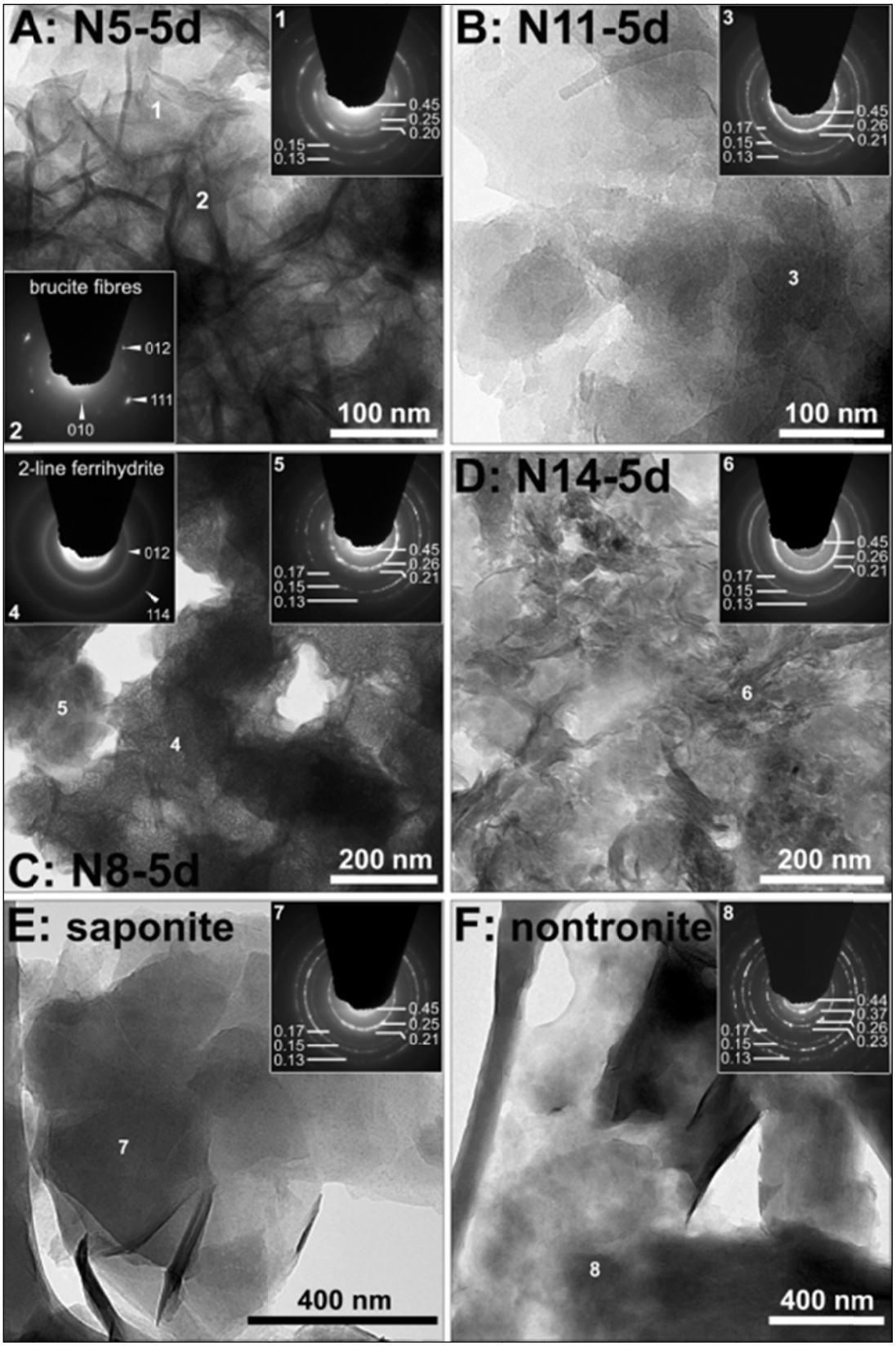

Fig. 2.2: Low-resolution TEM images and SAED patterns of precipitates obtained after 5 days of reaction time for (A) Fe:Mg = 1:1 (M), T = 120°C, (B) Fe:Mg = 1:1 (M), T = 180°C, (C) Fe:Mg = 1.5:0.5 (M), T = 120°C, and (D) Fe:Mg = 1.82:0.18 (M), T = 120°C. Natural occurring ferroan saponite (E) and Garfield nontronite (F) are shown for comparison. The SAED patterns of all types of synthesized ferrous saponites (insets 1, 3, 5-6) are similar to that of the natural trioctahedral analogue (distances in the SAED patterns are labeled in nm).

The SAED patterns of clay mineral particles show weak diffraction rings, indicative of turbostratically disordered smectite, whereas the SAED patterns of the fibrous particles display discrete Bragg spots, typical for brucite. In the precipitate N8, aggregated particles, ~20-50 nm in diameter with either a platy or a pseudo-hexagonal shape occurred (Fig. 2.2-C). Both of the particle types display weak, but diagnostic diffraction rings, indicative of smectite and 2-line ferrihydrite. The precipitate N14 was composed mainly of aggregated smectite particles that are commonly < 50 nm in size (Fig. 2.2-D). Larger smectite crystallites ~50-100 nm in their largest dimension were recognized only in precipitate N11 (Fig. 2.2-B), probably reflecting the higher synthesis temperature of 180°C. Small admixtures of 2-line ferrihydrite and brucite were also identified in this sample. The SAED patterns of all types of synthesized smectite are similar to that of the natural occurring ferroan saponite (Fig. 2.2-E), but differ from that of Garfield nontronite (Fig. 2.2-F), as seen by the absence of the 0.37 nm diffraction ring. This structural similarity suggests the nature of the synthesized clay minerals to be mostly trioctahedral, as confirmed by the XRD data.

In order to determine the composition and the oxidation state of Fe within the synthesized ferrous saponites 59 TEM-EDX and 42 TEM-EELS analyses were made on single clay mineral particles from experiments N4-N15. The areas of investigation were selected carefully by previous analysis of the SAED patterns to ensure the absence of brucite and 2-line ferrihydrite in the EDX spot analyses. The EELS data of ferrous saponite particles revealed $Fe^{3+}/\Sigma Fe$ ratios ranging from 0.16 to 0.20, which is equivalent to Fe^{2+}/Fe^{3+} ratios from 5.3 to 4.0, respectively (Fig. 2.3). The $Fe^{3+}/\Sigma Fe$ ratio of the natural occurring ferroan saponite was slightly higher (0.38), with a correspondingly lower Fe^{2+}/Fe^{3+} ratio of 1.6, compared to the synthesized saponites. In contrast, the Fe bound in the Garfield nontronite was mainly ferric, as expressed by the elevated $Fe^{3+}/\Sigma Fe$ ratio of 0.9. Due to the fact that the Fe^{2+}/Fe^{3+} ratios for wuestite and hematite as well as for the two clay mineral standards were in accordance with the literature, changes in the valence state of Fe due to electron beam irradiation during the TEM-EELS analysis are considered unlikely.

By combining the Fe^{2+}/Fe^{3+} ratios derived from the EELS data with the compositions based on TEM-EDX analysis, structural formulae were calculated for the ferrous saponites (Table 2.3). The octahedral occupancies of the ferrous saponites ranged from 2.65-2.85 and are close to the trioctahedral end member. It was recognized that the proportion of Fe^{2+} and Fe^{3+} in the octahedral sheet of the ferrous saponites increased notably with the increasing molar Fe:Mg ratio of the initial solutions. This was seen in the evolution of $^{VI}Fe^{2+} + {}^{VI}Fe^{3+}$ content (based on $O_{10}(OH)_2$) for the ferrous saponite synthesized at 120°C, with 0.37-0.61 atoms per formula

unit (a.p.f.u.) at Fe:Mg = 1:1, 1.03-1.52 a.p.f.u. at Fe:Mg = 1.5:0.5, and 2.18-2.69 a.p.f.u. at Fe:Mg = 1.82:0.18. A higher $^{VI}Fe^{2+}$+$^{VI}Fe^{3+}$ content of 0.58-1.01 a.p.f.u. was found in the ferrous saponites synthesized at 180°C and at the initial molar Fe:Mg ratio of 1:1. Abundant Fe^{3+} substitutions for Si^{4+} (0.00-0.37 a.p.f.u.) were evident in the tetrahedral sheets (Table 2.3) of all types of synthesized ferrous saponites, and Na^{+} (0.44-0.59 a.p.f.u.), among small proportions of K^{+} and Ca^{2+}, was found to be the dominant ion occupying the interlayer sites.

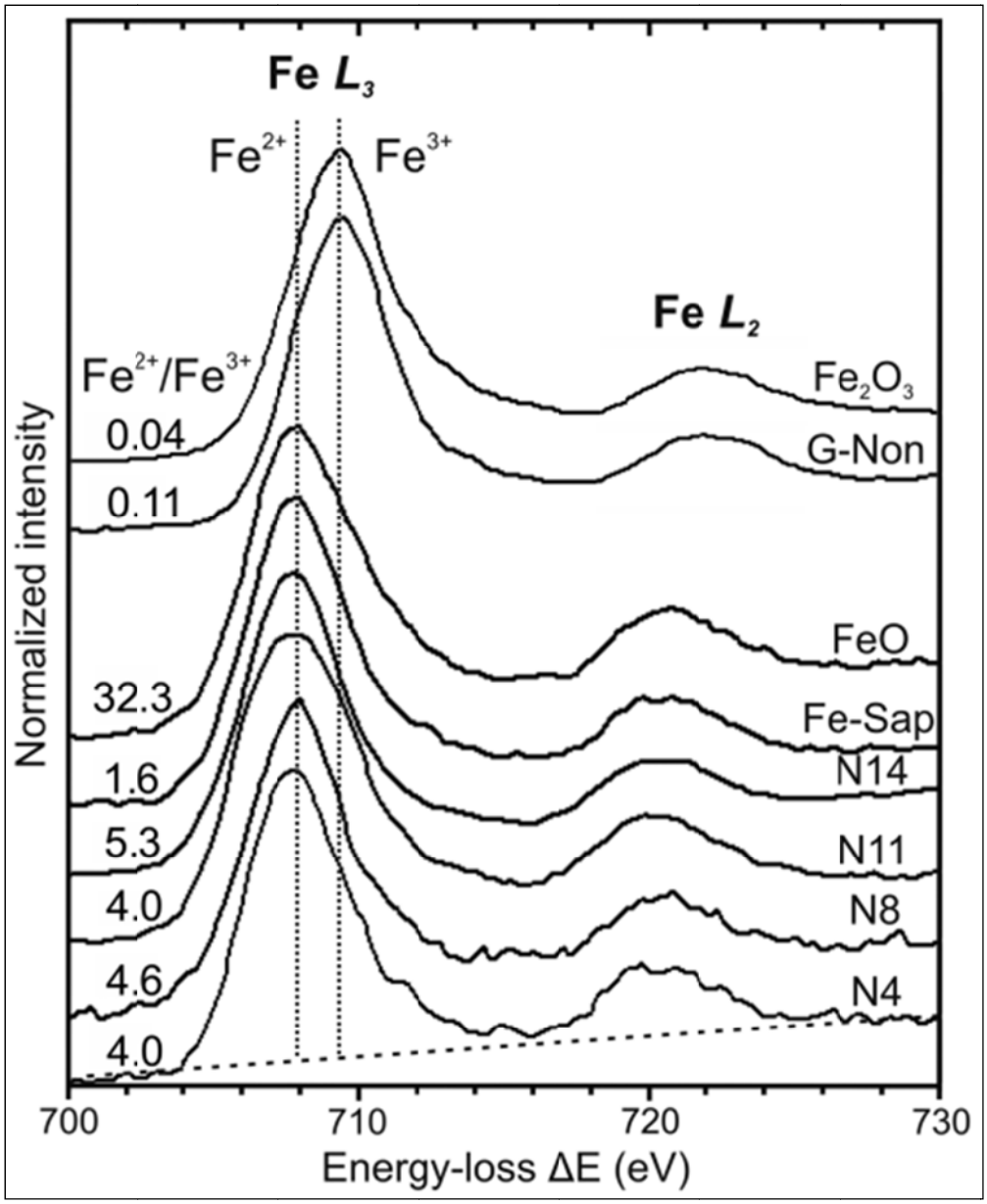

Fig. 2.3: Fe $L_{2,3}$-edge electron energy-loss near-edge structures of single ferrous saponite particles (N4, N8, N11, and N14) obtained after five days of reaction time. The EELS spectra of ferroan saponite (Fe-Sap), Garfield nontronite (G-Non), wuestite (FeO), and hematite (Fe_2O_3) are implemented for comparison. All data have been normalized to the integral $L_{2,3}$-edge intensity of spectra N4. The dashed line represents the background function used for determination of the $Fe^{3+}/\Sigma Fe$ ratio. The dotted lines indicate the Fe^{2+}- and Fe^{3+}-maxima at the L_3-edge, which are located at 707.8 and 709.5 eV, respectively.

Table 2.3: Individual and averaged (Ø) chemical compositions and calculated structural formulae of ferrous saponite particles from experiments N4-N15. The Fe^{2+}/Fe^{3+} ratios were derived from TEM-EELS analyses.

Elemental chemistry of synthetic clay mineral particles (in mass%) based on TEM-EDX;												initial Si:Fe:Mg (M) = 4:1:1;				T = 120°C	
	N4	N4	N4	N4	N4 (Ø)	N5	N5	N5	N5	N5	N5 (Ø)	N6	N6	N6	N6	N6	N6 (Ø)
SiO_2	62.01	64.09	61.22	59.54	61.71	61.80	64.27	61.67	61.38	57.71	61.36	59.66	63.18	63.48	60.40	60.84	61.51
FeO	7.84	7.03	7.95	8.85	7.92	8.64	7.08	7.95	6.88	9.38	7.98	9.57	8.33	7.47	6.91	8.10	8.08
Fe_2O_3	2.18	1.95	2.21	2.46	2.20	2.40	1.97	2.21	1.91	2.61	2.22	2.66	2.31	2.07	1.92	2.25	2.24
MgO	24.18	22.88	24.55	25.20	24.20	22.89	22.10	23.97	25.78	25.59	24.07	23.69	21.87	22.67	26.38	24.56	23.83
Na_2O	3.79	4.05	4.07	3.94	3.97	3.81	4.04	4.07	3.90	4.15	3.99	4.20	3.93	4.08	4.25	3.87	4.07
K_2O	b.d.l.	b.d.l.	b.d.l.	b.d.l.	b.d.l.	0.46	0.55	0.14	0.16	0.56	0.37	0.21	0.38	0.23	0.13	0.38	0.26
Sum	100.00	100.00	100.00	100.00	100.00	100.00	100.00	100.00	100.00	100.00	100.00	100.00	100.00	100.00	100.00	100.00	100.00
Atoms per formula unit (a.p.f.u.) based on $O_{10}(OH)_2$																	
	N4	N4	N4	N4	N4 (Ø)	N5	N5	N5	N5	N5	N5 (Ø)	N6	N6	N6	N6	N6	N6 (Ø)
Si^{4+}	3.95	3.99	3.91	3.84	3.94	3.96	4.00	3.94	3.90	3.80	3.93	3.86	4.00	3.99	3.86	3.90	3.93
$^{IV}Fe^{3+}$	0.05	0.01	0.09	0.16	0.06	0.04	0.00	0.06	0.10	0.20	0.07	0.14	0.00	0.01	0.14	0.10	0.07
T.C.	-0.05	-0.01	-0.09	-0.16	-0.06	-0.04	0.00	-0.06	-0.10	-0.20	-0.07	-0.14	0.00	-0.01	-0.14	-0.10	-0.07
$^{VI}Fe^{2+}$	0.42	0.37	0.43	0.48	0.42	0.46	0.41	0.42	0.37	0.41	0.43	0.52	0.44	0.40	0.37	0.43	0.43
$^{VI}Fe^{3+}$	0.05	0.06	0.02	0.00	0.04	0.08	0.09	0.04	0.00	0.00	0.03	0.00	0.08	0.09	0.00	0.01	0.04
$^{VI}Mg^{2+}$	2.30	2.28	2.34	2.36	2.30	2.19	2.20	2.28	2.44	2.40	2.30	2.29	2.18	2.22	2.42	2.35	2.27
Σ^{VI}	2.77	2.71	2.79	2.84	2.76	2.73	2.70	2.74	2.81	2.81	2.76	2.81	2.70	2.71	2.79	2.79	2.74
O.C.	-0.41	-0.52	-0.40	-0.32	-0.44	-0.46	-0.51	-0.48	-0.38	-0.38	-0.45	-0.38	-0.52	-0.49	-0.42	-0.41	-0.48
Na^+	0.47	0.50	0.50	0.49	0.49	0.47	0.50	0.50	0.48	0.52	0.50	0.53	0.49	0.50	0.53	0.48	0.50
K^+	0.00	0.00	0.00	0.00	0.00	0.04	0.04	0.01	0.01	0.05	0.03	0.02	0.03	0.02	0.01	0.03	0.02
I.C.	0.47	0.50	0.50	0.49	0.49	0.51	0.54	0.51	0.49	0.57	0.53	0.55	0.52	0.52	0.54	0.51	0.52

Elemental chemistry of synthetic clay mineral particles (in mass%) based on TEM-EDX;												initial Si:Fe:Mg (M) = 4:1.5:0.5;				T = 120°C	
	N7	N7	N7	N7	N7	N7 (Ø)	N8	N8	N8	N8	N8	N8 (Ø)	N9	N9	N9	N9	N9	N9 (Ø)
SiO_2	55.81	56.45	55.63	55.13	55.13	55.63	56.27	56.97	53.93	55.92	54.50	55.52	55.44	57.05	56.84	55.09	55.99	56.08
FeO	21.48	19.94	17.97	19.63	21.58	20.12	19.80	18.31	22.61	19.70	21.61	20.41	20.11	21.89	21.00	22.41	18.42	20.77
Fe_2O_3	5.24	4.86	4.38	4.79	5.26	4.91	4.83	4.47	5.51	4.80	5.27	4.98	4.91	5.34	5.12	5.47	4.49	5.06
MgO	13.16	14.36	17.70	16.12	13.65	15.00	15.23	16.08	13.74	15.32	14.52	14.98	15.09	11.54	13.48	12.81	17.15	14.01
Na_2O	4.32	3.97	4.20	3.97	4.09	4.11	3.54	3.97	4.03	4.23	3.89	3.93	4.21	3.81	3.56	4.20	3.51	3.86
K_2O	b.d.l.	0.34	b.d.l.	0.37	0.10	0.16	0.19	0.20	0.07	0.02	0.20	0.14	0.24	0.26	b.d.l.	0.01	0.25	0.15
CaO	b.d.l.	0.07	0.11	b.d.l.	0.19	0.07	0.14	b.d.l.	0.10	b.d.l.	0.01	0.05	b.d.l.	0.11	0.01	0.00	0.19	0.06
Sum	100.00	100.00	100.00	100.00	100.00	100.00	100.00	100.00	100.00	100.00	100.00	100.00	100.00	100.00	100.00	100.00	100.00	100.00
Atoms per formula unit (a.p.f.u.) based on $O_{10}(OH)_2$																		
	N7	N7	N7	N7	N7	N7 (Ø)	N8	N8	N8	N8	N8	N8 (Ø)	N9	N9	N9	N9	N9	N9 (Ø)
Si^{4+}	3.85	3.87	3.78	3.79	3.82	3.82	3.85	3.86	3.77	3.83	3.78	3.82	3.81	3.93	3.89	3.83	3.81	3.86
$^{IV}Fe^{3+}$	0.15	0.13	0.22	0.21	0.18	0.18	0.15	0.14	0.23	0.17	0.22	0.18	0.19	0.07	0.11	0.17	0.19	0.14
T.C.	-0.15	-0.13	-0.22	-0.21	-0.18	-0.18	-0.15	-0.14	-0.23	-0.17	-0.22	-0.18	-0.19	-0.07	-0.11	-0.17	-0.19	-0.14
$^{VI}Fe^{2+}$	1.24	1.14	1.02	1.13	1.25	1.16	1.13	1.04	1.32	1.13	1.25	1.17	1.16	1.26	1.20	1.30	1.15	1.19
$^{VI}Fe^{3+}$	0.12	0.12	0.01	0.03	0.09	0.07	0.09	0.09	0.05	0.08	0.06	0.07	0.07	0.20	0.16	0.11	0.04	0.12
$^{VI}Mg^{2+}$	1.35	1.47	1.79	1.65	1.41	1.54	1.55	1.63	1.43	1.56	1.50	1.54	1.55	1.19	1.38	1.33	1.64	1.44
Σ^{VI}	2.71	2.73	2.82	2.81	2.75	2.77	2.77	2.76	2.80	2.77	2.81	2.78	2.78	2.65	2.74	2.74	2.83	2.75
O.C.	-0.46	-0.42	-0.35	-0.35	-0.41	-0.39	-0.37	-0.39	-0.35	-0.38	-0.32	-0.37	-0.37	-0.50	-0.36	-0.41	-0.30	-0.38
Na^+	0.58	0.53	0.55	0.53	0.55	0.55	0.47	0.52	0.55	0.56	0.52	0.52	0.56	0.51	0.47	0.57	0.46	0.51
K^+	0.00	0.03	0.00	0.03	0.01	0.01	0.02	0.02	0.01	0.00	0.02	0.01	0.02	0.02	0.00	0.00	0.02	0.01
Ca^{2+}	0.00	0.01	0.01	0.00	0.01	0.01	0.01	0.00	0.01	0.00	0.00	0.00	0.00	0.01	0.00	0.00	0.01	0.00
I.C.	0.58	0.58	0.57	0.56	0.58	0.58	0.51	0.54	0.58	0.56	0.54	0.53	0.58	0.55	0.47	0.57	0.50	0.52

Elemental chemistry of synthetic clay mineral particles (in mass%) based on TEM-EDX;												initial Si:Fe:Mg (M) = 4:1:1;				T = 180°C	
	N10	N10	N10	N10	N10	N10 (Ø)	N11	N11	N11	N11	N11	N11 (Ø)	N12	N12	N12	N12	N12	N12 (Ø)
SiO_2	60.43	59.91	58.81	58.54	60.51	59.64	59.89	57.87	61.08	57.75	60.45	59.41	58.46	61.51	58.54	58.16	61.37	59.61
FeO	12.05	10.74	13.38	12.98	13.54	12.54	10.76	12.25	13.75	13.21	12.56	12.51	14.26	11.73	13.84	15.07	12.35	13.45
Fe_2O_3	3.35	2.62	3.26	3.17	3.30	3.14	2.99	2.99	3.35	3.22	3.06	3.12	3.96	2.86	3.38	3.68	3.01	3.38
MgO	20.06	23.05	20.91	21.54	18.75	20.86	22.81	22.94	18.01	21.63	20.19	21.12	19.41	20.05	20.29	18.72	19.63	19.62
Na_2O	4.11	3.69	3.63	3.78	3.90	3.82	3.55	3.95	3.81	4.19	3.74	3.85	3.92	3.69	3.45	4.37	3.47	3.78
K_2O	b.d.l.	b.d.l.	b.d.l.	b.d.l.	b.d.l.	b.d.l.	b.d.l.	b.d.l.	b.d.l.	b.d.l.	b.d.l.	b.d.l.	b.d.l.	0.17	0.50	b.d.l.	0.17	0.17
Sum	100.00	100.00	100.00	100.00	100.00	100.00	100.00	100.00	100.00	100.00	100.00	100.00	100.00	100.00	100.00	100.00	100.00	100.00
Atoms per formula unit (a.p.f.u.) based on $O_{10}(OH)_2$																		
	N10	N10	N10	N10	N10	N10 (Ø)	N11	N11	N11	N11	N11	N11 (Ø)	N12	N12	N12	N12	N12	N12 (Ø)
Si^{4+}	3.94	3.88	3.87	3.85	3.97	3.90	3.88	3.83	4.00	3.82	3.94	3.89	3.87	3.99	3.87	3.87	3.99	3.92
$^{IV}Fe^{3+}$	0.06	0.12	0.13	0.15	0.03	0.10	0.12	0.17	0.00	0.18	0.05	0.11	0.13	0.01	0.13	0.13	0.01	0.08
T.C.	-0.06	-0.12	-0.13	-0.15	-0.03	-0.10	-0.12	-0.17	0.00	-0.18	-0.09	-0.11	-0.13	-0.01	-0.13	-0.13	-0.01	-0.08
$^{VI}Fe^{2+}$	0.66	0.58	0.74	0.71	0.74	0.69	0.58	0.67	0.75	0.73	0.69	0.68	0.79	0.64	0.77	0.84	0.67	0.74
$^{VI}Fe^{3+}$	0.11	0.01	0.03	0.01	0.13	0.06	0.03	0.00	0.17	0.00	0.09	0.04	0.07	0.13	0.04	0.06	0.14	0.09
$^{VI}Mg^{2+}$	1.95	2.23	2.05	2.11	1.83	2.04	2.21	2.18	1.77	2.10	1.98	2.06	1.92	1.94	2.00	1.86	1.90	1.92
Σ^{VI}	2.72	2.82	2.82	2.83	2.70	2.79	2.82	2.85	2.69	2.83	2.76	2.78	2.78	2.71	2.81	2.76	2.71	2.75
O.C.	-0.45	-0.35	-0.33	-0.33	-0.47	-0.36	-0.33	-0.30	-0.45	-0.34	-0.39	-0.40	-0.37	-0.45	-0.34	-0.42	-0.44	-0.41
Na^+	0.52	0.46	0.46	0.48	0.50	0.48	0.45	0.50	0.48	0.54	0.47	0.49	0.50	0.46	0.44	0.56	0.44	0.48
K^+	0.00	0.00	0.00	0.00	0.00	0.00	0.00	0.00	0.00	0.00	0.00	0.00	0.00	0.01	0.04	0.00	0.01	0.01
I.C.	0.52	0.46	0.46	0.48	0.50	0.48	0.45	0.50	0.48	0.54	0.47	0.49	0.50	0.47	0.48	0.56	0.45	0.49

b.d.l.: below detection limit; T.C.: tetrahedral charge; O.C.: octahedral charge; I.C.: interlayer charge.

Table 2.3: Continued.

Elemental chemistry of synthetic clay mineral particles (in mass%) based on TEM-EDX;													initial Si:Fe:Mg (M) = 4:1.82:0.18;					T = 120°C
	N13	N13	N13	N13	N13	N13 (Ø)	N14	N14	N14	N14	N14	N14 (Ø)	N15	N15	N15	N15	N15	N15 (Ø)
SiO_2	49.72	49.37	51.88	49.65	50.53	50.23	51.49	48.84	50.93	47.45	49.68	49.68	47.62	51.37	52.40	52.51	50.15	50.81
FeO	36.37	36.69	34.17	36.88	35.56	35.93	34.23	36.73	35.12	37.47	36.14	35.94	37.65	34.97	34.13	33.82	35.54	35.22
Fe_2O_3	7.70	7.77	7.23	7.80	7.52	7.60	7.24	7.77	7.43	7.93	7.65	7.61	7.97	7.40	7.22	7.16	7.52	7.45
MgO	2.17	2.13	2.48	2.22	2.56	2.31	3.46	2.64	2.64	3.16	2.83	2.94	2.75	2.79	2.42	2.92	2.69	2.72
Na_2O	3.92	3.80	3.71	3.34	3.63	3.68	3.08	3.82	3.76	3.99	3.56	3.64	3.81	3.23	3.69	3.34	3.60	3.54
K_2O	0.13	0.25	0.54	0.10	0.21	0.24	0.27	0.19	0.11	b.d.l.	0.05	0.12	0.19	0.06	0.08	0.25	0.46	0.21
CaO	b.d.l.	b.d.l.	b.d.l.	b.d.l.	b.d.l.	b.d.l.	0.24	b.d.l.	b.d.l.	b.d.l.	0.09	0.06	b.d.l.	0.18	0.04	b.d.l.	0.03	0.05
Sum	100.00	100.00	100.00	100.00	100.00	100.00	100.00	100.00	100.00	100.00	100.00	100.00	100.00	100.00	100.00	100.00	100.00	100.00
Atoms per formula unit (a.p.f.u.) based on $O_{10}(OH)_2$																		
	N13	N13	N13	N13	N13	N13 (Ø)	N14	N14	N14	N14	N14	N14 (Ø)	N15	N15	N15	N15	N15	N15 (Ø)
Si^{4+}	3.75	3.74	3.85	3.75	3.79	3.78	3.82	3.71	3.80	3.63	3.74	3.74	3.65	3.82	3.87	3.87	3.77	3.80
$^{IV}Fe^{3+}$	0.25	0.26	0.15	0.25	0.21	0.22	0.18	0.29	0.20	0.37	0.26	0.26	0.35	0.18	0.13	0.13	0.23	0.20
T.C.	-0.25	-0.26	-0.15	-0.25	-0.21	-0.22	-0.18	-0.29	-0.20	-0.37	-0.26	-0.26	-0.35	-0.18	-0.13	-0.13	-0.23	-0.20
$^{VI}Fe^{2+}$	2.30	2.32	2.12	2.33	2.23	2.26	2.12	2.33	2.19	2.40	2.28	2.27	2.41	2.18	2.11	2.09	2.23	2.20
$^{VI}Fe^{3+}$	0.19	0.18	0.26	0.20	0.21	0.21	0.22	0.15	0.22	0.09	0.18	0.18	0.11	0.24	0.28	0.27	0.21	0.23
$^{VI}Mg^{2+}$	0.24	0.24	0.27	0.25	0.29	0.26	0.38	0.30	0.29	0.36	0.32	0.31	0.31	0.31	0.27	0.32	0.30	0.30
Σ^{VI}	2.73	2.74	2.65	2.78	2.73	2.73	2.72	2.78	2.70	2.85	2.78	2.76	2.83	2.73	2.66	2.68	2.74	2.73
O.C.	-0.35	-0.34	-0.44	-0.24	-0.33	-0.33	-0.34	-0.29	-0.38	-0.21	-0.26	-0.30	-0.23	-0.30	-0.40	-0.37	-0.31	-0.31
Na^+	0.57	0.56	0.53	0.49	0.53	0.54	0.44	0.56	0.54	0.59	0.52	0.53	0.57	0.47	0.53	0.48	0.53	0.51
K^+	0.01	0.02	0.05	0.01	0.02	0.02	0.03	0.02	0.01	0.00	0.00	0.01	0.02	0.01	0.01	0.02	0.04	0.02
Ca^{2+}	0.00	0.00	0.00	0.00	0.00	0.00	0.02	0.00	0.00	0.00	0.01	0.01	0.00	0.01	0.00	0.00	0.00	0.00
I.C.	0.58	0.58	0.58	0.50	0.55	0.56	0.51	0.58	0.55	0.59	0.54	0.56	0.59	0.50	0.54	0.50	0.57	0.53

b.d.l.: below detection limit; T.C.: tetrahedral charge; O.C.: octahedral charge; I.C.: interlayer charge.

2.4.4 Thermal analysis of synthesized precipitates

The TG curves of the synthesized ferrous saponites and experimental by-products (Fig. 2.4-A) obtained after seven days of reaction time exhibited a first strong weight loss of -12.4 to -15.0 mass% between 100°C and 200°C, a second moderate one between 350°C and 420°C (-1.1 to -2.9 mass%), and a third rather small weight loss between 760°C and 780°C. The latter weight loss (-0.3 mass%) was most obvious in precipitate N12, which according to the XRD results is considered to contain the highest proportion of ferrous saponite, together with traces of 2-line ferrihydrite and brucite. As evident in the MS (H_2O) curves (Fig. 2.4-C) all of these weight losses result from the stepwise removal of free water, surface water (~150°C) or structural water (760-780°C) from ferrous saponite, or reflect the dehydration of 2-line ferrihydrite (~125°C) or the dehydroxilation of brucite (350-420°C). One small MS (CO_2) peak was found near 300°C, which may reflect the oxidation of organic matter, although we do not have a proper explanation for the origin of organics in our precipitates.

The DSC curves (Fig. 2.4-B) displayed two well-defined endothermic peaks at 125°C and 150°C, which correspond to the dehydration of 2-line ferrihydrite (Eggleton & Fitzpatrick, 1988) and ferrous saponite, respectively. The strong endothermic peak near 380°C documents the dehydroxylation of brucite (Ramachandran *et al.*, 2002). No clear indication of oxidation of ferrous iron was found in the entire DSC curve. It may occur already during dehydration or could also be a continuous process of a broad temperature span. The constant but slow exo-

thermic reaction between 400-750°C may be attributed to partial dehydroxylation of nontronite-like domains within the ferrous saponite structure, but it can be also simply baseline drift.

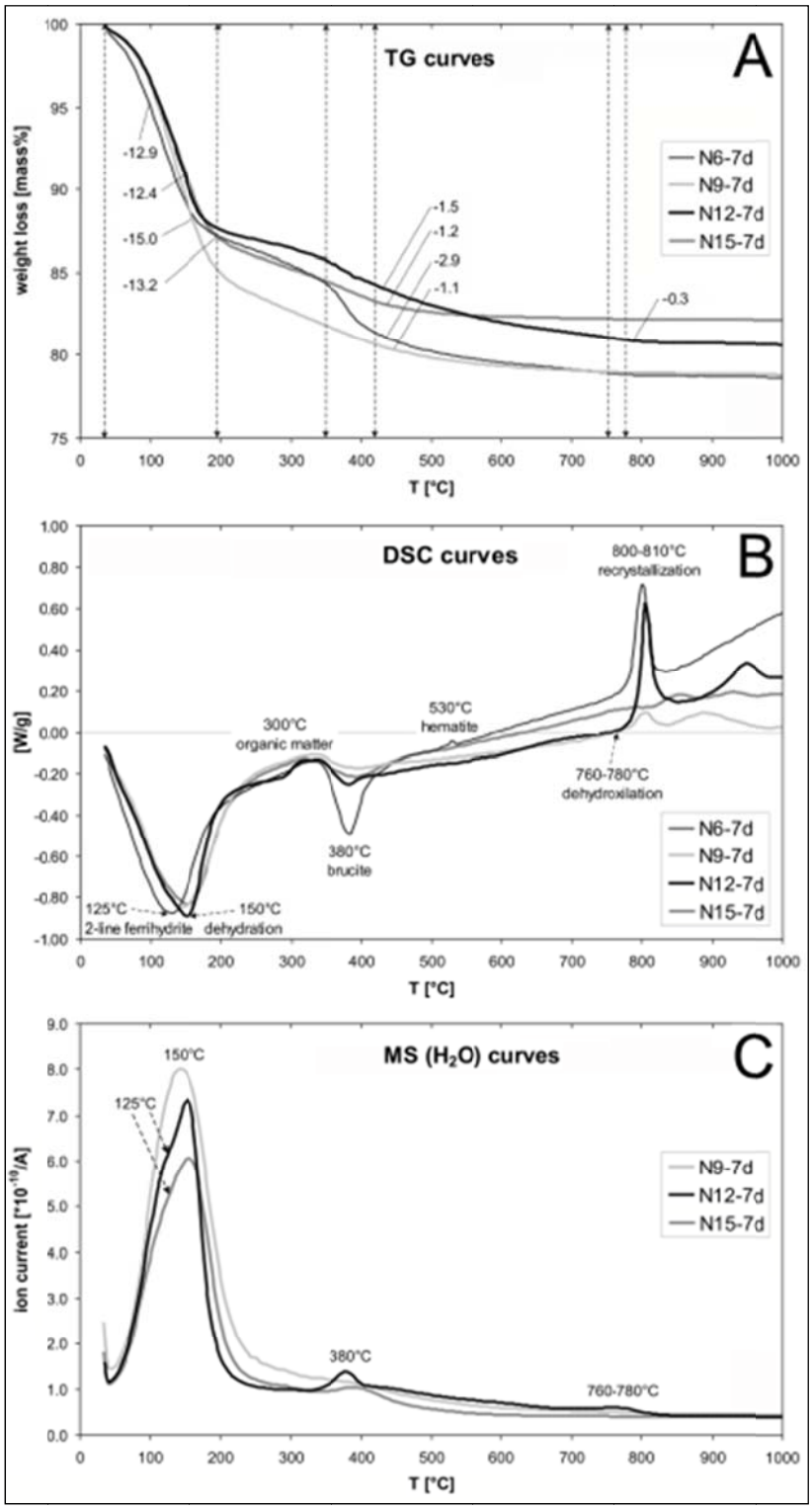

Fig. 2.4: Thermo-analytical results of mineral precipitates obtained after 7 days of reaction time. A) Thermogravimetric (TG) curves. B) Differential scanning calorimetry (DSC) curves. C) Mass spectrometry (MS-H_2O) curves. The DSC and MS-H_2O peaks at 150°C and between 760°C to 780°C reflect the dehydration and dehydroxylation temperature of synthesized ferrous saponite.

At 530°C another small exothermic peak was detected, which probably reflects the crystallization of hematite (*e.g.* Decarreau & Bonnin, 1986), *i.e.* from dehydrated ferrihydrite precursors. The 380°C and 530°C DSC peaks were most obvious in the precipitate of experiment N6, which based on XRD data, contains moderate proportions of ferrihydrite and brucite and major ferrous saponite. Precipitate N12 produced another small endothermic peak between 760°C and 780°C, followed by a strong exothermic peak at 800-810°C. These DSC peaks are suggested to reflect final dehydroxylation of Mg-rich trioctahedral compositions within the ferrous saponite structure and subsequent recrystallization into enstatite (Che et al., 2011).

2.4.5 Mid-infrared spectra of synthesized precipitates

The FTIR spectra of the synthesized precipitates obtained after 7 days of reaction time as well as of natural ferroan saponite are presented in Fig. 2.5. The IR spectrum of the < 2 µm grain size fraction of natural saponite yielded a well-defined IR band at 3680 cm^{-1} and another less intense IR band at 3630 cm^{-1} (Fig. 2.5-A). These IR bands are attributed to the Mg_3OH and AlMgOH stretching vibrations (Dill *et al.*, 2011) and are diagnostic for saponite. These IR bands are rather weak (3680 cm^{-1}) or absent (3630 cm^{-1}) with regard to the synthesized ferrous saponites. Iron substitution in Mg-rich clays moves the Mg_3OH stretching band towards a lower frequency (Cuadros *et al.*, 2008) and the synthetic clay minerals show some, but not totally resolved modulations below 3680 cm^{-1} that may correspond to such substitutions. In the precipitates a strong IR band was found around 3560 cm^{-1} (Fig. 2.5-A), which corresponds to FeFeOH and FeMgOH stretching vibrations (Dill *et al.*, 2011). This band is indicative of a dioctahedral structure. However, the Mg_3OH deformation band at 680 cm^{-1}, which was observed in all samples (Fig. 2.5-B), indicates the dominance of trioctahedral structural units. The low intensity of the stretching mode may be explained by the fact that the dioctahedral bands are generally more intense than trioctahedral ones, so that their relative intensities are not proportional to the abundance of these structures in the samples (Russell & Fraser, 1994). The presence of dioctahedral clay minerals such as nontronite and/or nontronitic domains is indicated by infrared spectroscopy, contradictory to the XRD results. The IR band at ~3560 cm^{-1} thus reflects Fe^{2+} and Fe^{3+} substitutions for Mg^{2+} in the octahedral sheet of the synthesized clay minerals, as seen by the progressively stronger 3560 cm^{-1} band at higher Fe:Mg ratios of the initial solutions. Further IR bands were detected at 816 cm^{-1} (FeOHFe and Si-O-Si bending), 720 cm^{-1} (Si-O bending), and 600 cm^{-1} (Fe-O-Si bending) (*e.g.,* Russell, 1979, Madejová *et al.*, 1996, Cuadros *et al.*, 2008). The IR bands below 500 cm^{-1} are not well resolved and hence cannot be interpreted further.

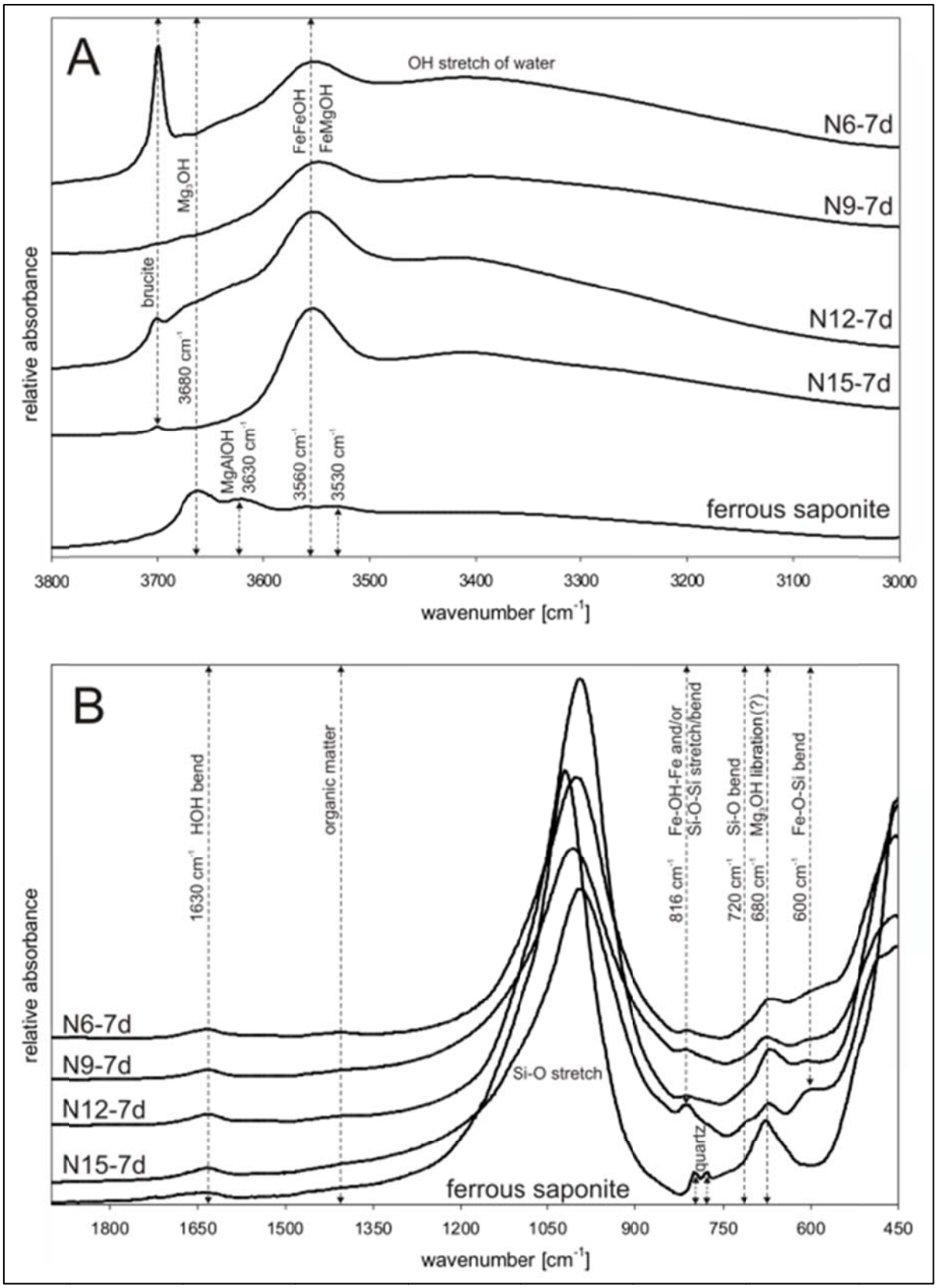

Fig. 2.5: FTIR spectra of precipitates obtained after 7 days of reaction time. A) OH stretching region. B) Si-O stretching and OH deformation region.

2.5 Discussion

Laboratory studies on the formation conditions, chemical variability, and structural modifycations of synthesized Mg-saponite are numerous (*e.g.* Breukelaar *et al.*, 1989, 1990, Farmer *et al.*, 1994, Grauby *et al.*, 1994), but only few experimental studies focused on characterizing the nature and properties of ferrous saponites. Decarreau & Bonnin (1986) reported on the nucleation of ferrous stevensite, synthesized at 75°C. In contact with air the obtained stevensite altered rapidly into nontronite-like smectite, suggesting that the primary precipitate was metastable. Caillère *et al.* (1953, 1955) and Harder (1976, 1978) proposed to have synthesized ferrous saponite in a similar way by a sol-gel process, but unfortunately insufficient data to clarify the nature and composition of their precipitate was provided. In the following section, the evolution of the solution chemistry and precipitates is discussed by addressing the effects of the molar Fe:Mg ratio of the initial experimental solution, temperature, and the reaction time of synthesis on the mineralogy, structure, stability, and composition of the synthesized ferrous saponites. The evolution of the crystallite size and a new approach to ferrous saponite formation is discussed, together with implications for understanding Fe-Mg-saponite solid solution.

2.5.1 Evolution of solution chemistry and synthesized precipitates

In the final experimental solutions the Mg (< 0.1 $mg \cdot L^{-1}$) and Si (90-2600 $mg \cdot L^{-1}$) concentrations were reduced by >99% and ~29-97%, respectively, compared with the initial solutions. Small amounts of remaining ferric Fe (0.1-2.3 $mg \cdot L^{-1}$) refer to minor ferrihydrite, indicating an almost complete removal of Fe^{2+} in the final solutions, whereas the Na concentrations remained constant at ~10,000 $mg \cdot L^{-1}$. Notably, the solution pH strongly increased from about 8.5 to between 12.3 and 12.9 (Table 2.2). This almost total removal of Mg and Fe ions from the solution, and the substantial removal of Si ions (Tables 2.1 and 2.2) resulted in 0.3 to 0.6 g of precipitates. Taking into account that the maximum amount of precipitate is 0.65±0.05 g, calculated on a water-free basis and assuming a 100% removal of Mg, Fe, and Si ions, an overall precipitation quota of 55-98% was achieved in the present experiments.

As evident from the XRD patterns (Fig. 2.1 and Table 2.2) and TEM-EDX data (Table 2.3) the precipitates from experiments N4-N15 are predominantly composed of trioctahedral ferrous saponite, with small admixtures of 2-line ferrihydrite, brucite, opal-CT, and nontronite. Modeling of the initial and final solution chemistry as well as of the saturation indexes (SI) of the relevant mineral phases with the computer code PHREEQC using the minteq.v4 database suggests that the salts containing Mg and Fe should be completely dissolved at pH 8.5 and

25°C. Due to rapid hydrolysis of the Na-orthosilicate and the resultant progressive increase in pH the solubility of amorphous silica changed from about 1200 $mg \cdot L^{-1}$ at pH 10.8 to 40,000 $mg \cdot L^{-1}$ at pH 11.3 (Greenberg & Price, 1957, Greenberg, 1958). This indicates that all experimenttal solutions were undersaturated in respect to amorphous silica at pH ≥ 11. At pH ≥ 10.4 the experimental solutions became oversaturated with respect to brucite (SI ≥ 0.5) and trioctahedral clay minerals such as chrysotile and antigorite (SI ≥ 10), and probably saponite. This explains the abundant brucite in experiments N16-N21, the existence of antigorite in precipitates N1-3, and the formation of ferrous saponite in experiments N4-15. The co-precipitation of Fe^{3+}-hydrates such as goethite, lepidocrocite and 2-line ferrihydrite was initially thermodynamically inhibited due to the high solubility of most ferrous Fe species under the experimental reducing and alkaline conditions (Cornell & Schwertmann, 2003). The dominant aqueous species in such reducing environments are reflected to $Fe(OH)_3^-$ and $Fe(OH)_2^0$. During quenching and subsequent filtration of the final experimental solutions at the end of the respective experiments the reducing agent Na-dithionite is considered to have been decomposed rapidly (*e.g.* Harder, 1976). This resulted in oxidizing conditions in the final solutions, allowing Fe oxidation to takes place and subsequently 2-line ferrihydrite and nontronite were formed. The competing formation of brucite and ferrous saponite is discussed later in the paper.

2.5.2 Chemical stability of ferrous saponite

Badaut *et al.* (1985) studied the authigenic nature of trioctahedral ferrous smectite that formed in recent superficial sediments of the Red Sea Atlantis II Deep and found these clay minerals to be highly metastable. In contact with air and oxygenized water the saponite altered rapidly into a dioctahedral nontronite-like smectite and Fe-hydroxides, whereby the alteration started at particle peripheries and progressed into particle centers. Decarreau & Bonnin (1986) observed similar alteration features associated with the oxidation of ferrous stevensite. In the present study, the IR data provide clear evidence for oxidative alteration of the synthesized clay matter into a dioctahedral nontronite-like clay mineral. However, neither a separation of the $d_{(060)}$-reflection was evident in the XRD and TEM-SAED data, as it had been reported by Badaut *et al.* (1985) for altered ferrous saponite, nor changes in the particle shape were found. This suggests that the compositions reported for the synthesized saponites represent unaltered signatures. The oxidation of Fe^{2+} in clay mineral structures is highly limited particularly in the absence of water and these conditions are ideal for preservation of Fe^{2+} in the synthetic saponites. The rate of such oxidation reactions is controlled mainly by the clay's surface properties such as surface area and particle thickness. The conversion rate of synthetic ferrous saponites

into stable nontronite is thus expected to be slow, suggesting that the reported compositions reflect original states (Table 2.3).

2.5.3 Crystallinity of synthesized ferrous saponite

Previous experimental studies on the formation of saponite-type clay minerals have demonstrated that the crystallinity (particle size and ordering) of initially poorly crystalline saponite particles increases (i) upon aging in aqueous solution (Decarreau, 1980, 1985), (ii) with increasing solution pH (Caillère *et al.*, 1954, Henin & Robichet, 1954), and (iii) at elevated temperatures of synthesis (Kuchta & Fajnor, 1988). The XRD patterns of our precipitates (Fig. 2.1) also indicate a progressively higher state of ordering in the stacking sequences of ferrous saponite particles with increasing reaction time, at higher temperatures from 120°C to 180°C (only traces of poorly crystalline saponite were detected at 60°C), and in particular with increasing molar Fe:Mg ratio of the initial solution. This is expressed by the successive decrease of the FWHM, measured on the basal reflections of the ferrous saponite, which changes from 1.91-1.77° 2θ (N4-6; T = 120°C; Fe:Mg = 1:1) and 1.73-1.51° 2θ (N13-15; T = 120°C; Fe:Mg = 1.82:0.18) to 1.02-0.92° 2θ (N4-6; T = 180°C; Fe:Mg = 1:1). Only the precipitates obtained from experiments N7-9 (T = 120°C; Fe:Mg = 1.5:0.5) revealed a slightly higher FWHM of 2.21-1.97° 2θ, indicative of less crystalline ferrous saponite.

High-resolution TEM (HRTEM) fringe images, taken parallel to the layer plane of the ferrous saponites, support the above changes in the crystallinity (Fig. 2.6). The lattice imaging of ferrous saponite particles from experiments N4-6 (Figs 2.6-A to C) show about 50-200 Å thick poorly-ordered stacking sequences with abundant layer terminations and layer deformations, i.e. lattice strain and folding. In contrast, straight, well-defined, and almost defect-free stacking sequences with thicknesses of ~100-300 Å were found in the clay mineral precipitates of experiments N10-12 (Figs 2.6-D to F) and N13-15 (Figs 2.6-G to I). Fast Fourier Transform (FFT) measurements of the noise-filtered HRTEM fringe images frequently yielded discrete (001) planes with an interplanar distance of ~1.3 nm (the upper inset in Fig. 2.6-H) as well as discrete (*hk0*) planes (the lower inset in Fig. 2.6-H) depending on the orientation of the clay mineral particles, which are indicative of well-crystalline ferrous saponite. FFT patterns of clay mineral particles from precipitate N4 show less abundant (001) planes with a crystallite thickness of ~50 Å (the lower inset in Fig. 2.6-A), suggestive of poorly-crystalline ferrous saponite. In addition, areas lacking any short-range order were found in close contact to the clay minerals (the upper inset in Fig. 2.6-A), which likely reflects the existence of unreacted gel precursors from which the ferrous saponites precipitated (Decarreau & Bonnin, 1986).

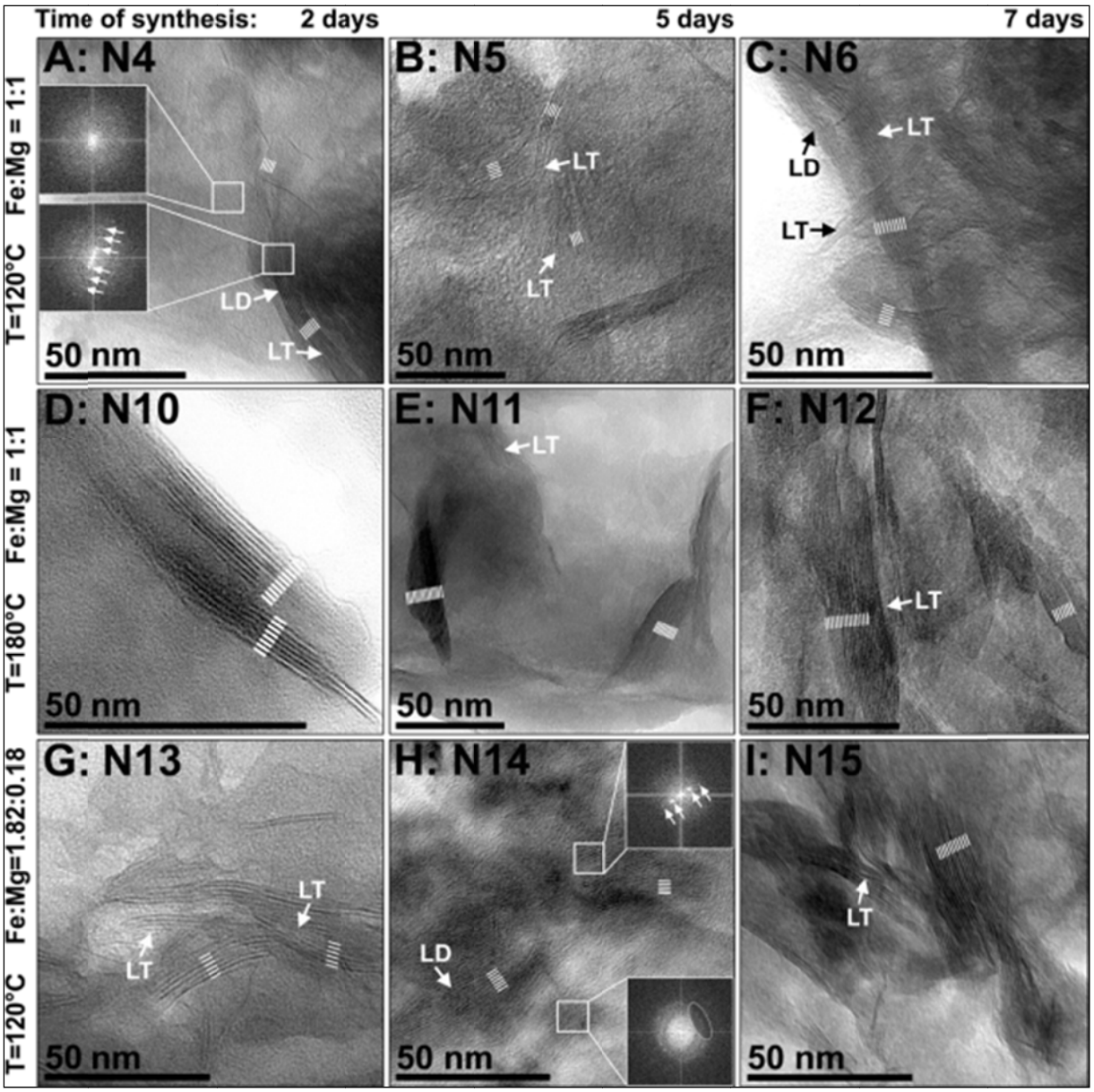

Fig. 2.6: High-resolution TEM lattice fringe images and Fast Fourier Transform (FFT) patterns of TEM images of synthesized ferrous saponite showing the evolution of initially poorly crystalline saponite particles into well crystalline ferrous saponite particles as a function of the molar Fe:Mg ratio of the initial solution, temperature, and reaction time of synthesis. The white arrows in the inserted FFT patterns mark the interplanar distance of the (001) planes of ~1.3 nm. Abbreviations: LT = layer termination, LD = layer deformation.

2.5.4 Thermal stability of ferrous saponite

It is generally accepted that the thermal stability of di- and trioctahedral 2:1 clay minerals is affected mainly by their nature, composition, structure, and crystallinity (Drits et *al.*, 1995). In particular, the location and charge of the interlayer cations, c*is*/*trans* occupancies in the octahedral sheet, vacancies, and the structural Fe content among other factors have a large impact on controlling the dehydration and dehydroxylation temperatures of dioctahedral structures

(Drits *et al.*, 1984; Tsipursky & Drits, 1984; Wolters & Emmerich, 2007). Elevated structural $^{VI}Fe^{2+}$ + $^{VI}Fe^{3+}$ contents in dioctahedral clay minerals, for example, are considered to reduce the dehydroxylation temperatures significantly, as reported for both kaolinites (Iriarte *et al.*, 2005) and smectites (Brigatti, 1983). The dehydroxylation reaction of trioctahedral structures, however, has not yet received particular attention, and thus the key factors that control the thermal stability of trioctahedral clay minerals remain unclear.

The DSC and MS(H_2O) curves of precipitates from experiment N12 (Fig. 2.4), which is composed mainly of ferrous saponite that contains on average 0.83 a.p.f.u. of $^{VI}Fe^{2+}$ + $^{VI}Fe^{3+}$ exhibited a weak, endothermic dehydroxylation peak between 760°C and 780°C. Dill *et al.* (2011) and Parthasarathy *et al.* (2003) reported dehydroxylation temperatures of 840°C and between 800-860°C for two types of natural ferroan saponite that contained, on average, 0.44 a.p.f.u. and 1.98 a.p.f.u. of $^{VI}Fe^{2+}$ + $^{VI}Fe^{3+}$. Post (1984) found the dehydroxylation temperature of the Ballarat saponite with 0.05 a.p.f.u. of $^{VI}Fe^{2+}$ + $^{VI}Fe^{3+}$ occurs at 810°C. Therefore, the extent of $^{VI}Fe^{2+}$ and $^{VI}Fe^{3+}$ substitution for Mg^{2+} may only has a minor effect on reducing the dehydroxylation temperature of trioctahedral saponites. The proportion and distribution of di- and trioctahedral compositions in trioctahedral structural units seems to have substantially more impact on thermal stability, as currently demonstrated by Cuadros *et al.* (2013). Additional factors that affect the thermal stability of both natural and synthesized saponites seem to be the formation temperature and related variations in the crystallinity such as particle size and disorder/order (see Figs 2.1 and 2.6), and the location of bi- and trivalent cations (octahedral vacancies) in the saponites octahedral sheet. Estimations of the effect of composition, crystallinity, crystal size, and surface area on the dehydration and dehydroxylation temperatures of trioctahedral ferrous saponite-type clay minerals do, however, require further investigations.

2.5.5 Chemical composition of synthesized ferrous saponite

The XRD data (Fig. 2.1) clearly demonstrate that the synthesized clay minerals from experiments N4-15 are mainly composed of trioctahedral ferrous saponite, as seen by the diagnostic d_{060}-value at 1.534-1.543 Å. No evidence for ordered interstratification was found, as evident by the strong rational *00l*-reflections of the oriented, EG-solvated clay preparations. XRD analyses of the oriented air-dried clay films yielded d_{001}-values at 12.5-13.5 Å, suggestive of ferrous saponite with Na^+ ions as the main interlayer cation, a feature confirmed by the high Na concentration (10,000 mg·L^{-1}) in the final experimental solutions (Table 2.2). The dominance of monovalent cations within the interlayer sites of synthesized ferrous saponite is also responsible for the well-defined, endothermic dehydration peak, centered at 150°C (Fig. 2.4).

If larger proportions of bivalent cations such as Mg^{2+} or Ca^{2+} would be present in the interlayer sites then the dehydration peak is considered to shift to temperatures of about 200°C, according to Kawano & Tomita (1991). However, the existence of some Mg^{2+} in the interlayer sites (~10-20%) of the ferrous saponites is possible, because Mg^{2+} ions preferentially substitute for Na^{+} and this can affect the structural formulae. Abundant Mg^{2+} substitutions for Na^{+} in the interlayer sites of the ferrous saponites synthesized in the present study are suggested to be unlikely, as seen in the XRD patterns and DSC curves, and in the final experimental solution data. Thus, the ferrous saponites reported in the present study are characterized by a high interlayer charge of 0.45-0.59 a.p.f.u., which is close to the upper limit for smectites at about 0.60 a.p.f.u..

In addition to the XRD data, the trioctahedral nature of most of the synthesized clay matter is evident from the TEM-SAED analysis and the high Fe^{2+}/Fe^{3+} ratios of 4.0 to 5.3, calculated from TEM-EELS data. However, the visible IR band at around 3560 cm^{-1} clearly shows the presence of some dioctahedral domains or nontronite in the synthesized clay matter (Fig. 2.5), a feature, which should affect the chemical composition data. An elevated octahedral Fe content in the synthesized, almost pure, ferrous saponites was recognized with increasing reaction temperature and in particular with increasing molar Fe:Mg ratio of the initial solutions (Table 2.3). This structural $^{VI}Fe^{2+}$ + $^{VI}Fe^{3+}$ content correlates well with shifts in the position of the $d_{(060)}$-reflection (Fig. 2.7). This trend to progressively higher d-values can be explained by the positive linear correlation between the total amount of structural Fe in clay mineral structures and resultant changes in the cell edge length *b*, as proposed by Heuser *et al.* (2013) for a range of dioctahedral smectites. The consistency of the chemical and XRD data suggests the synthetic ferrous saponites to be chemically variable, with compositions ranging from $(Na_{0.44\text{-}0.59}K_{0.00\text{-}0.05}Ca_{0.00\text{-}0.02})(Fe^{2+}_{0.37\text{-}2.41}Mg_{0.24\text{-}2.44}Fe^{3+}_{0.00\text{-}0.28})\Sigma_{2.65\text{-}2.85}[(Fe^{3+}_{0.00\text{-}0.37}Si_{3.63\text{-}4.00})O_{10}](OH)_2$.

2.5.6 Ferrous saponite formation – implications for a solid solution

In natural environments ferrous saponite is typically formed during hydrothermal alteration of andesitic volcanic rocks at temperatures usually below 150°C and near-neutral pH (*e.g.* Dill *et al.*, 2011). Ferrous saponite authigenesis also takes place in reducing near-surface regimes and is frequently associated with weathering of basaltic oceanic crust at temperatures between 15-64°C (Porter *et al.*, 2000). In most of these environments the weathering of pyroxene-, amphibole-, plagioclase-, and biotite-rich host rocks is caused by intense interactions with the surrounding high to moderate temperate meteoric or hydrothermal solutions (Dill *et al.*, 2011). Progressive decomposition of the less weathering resistant (ultra)mafic minerals is suggested

to mobilize Mg^{2+}, Al^{3+}, Fe^{2+}, Ca^{2+}, and Na^{+} ions as well as silica, and all these ions are required for the formation of trioctahedral saponite.

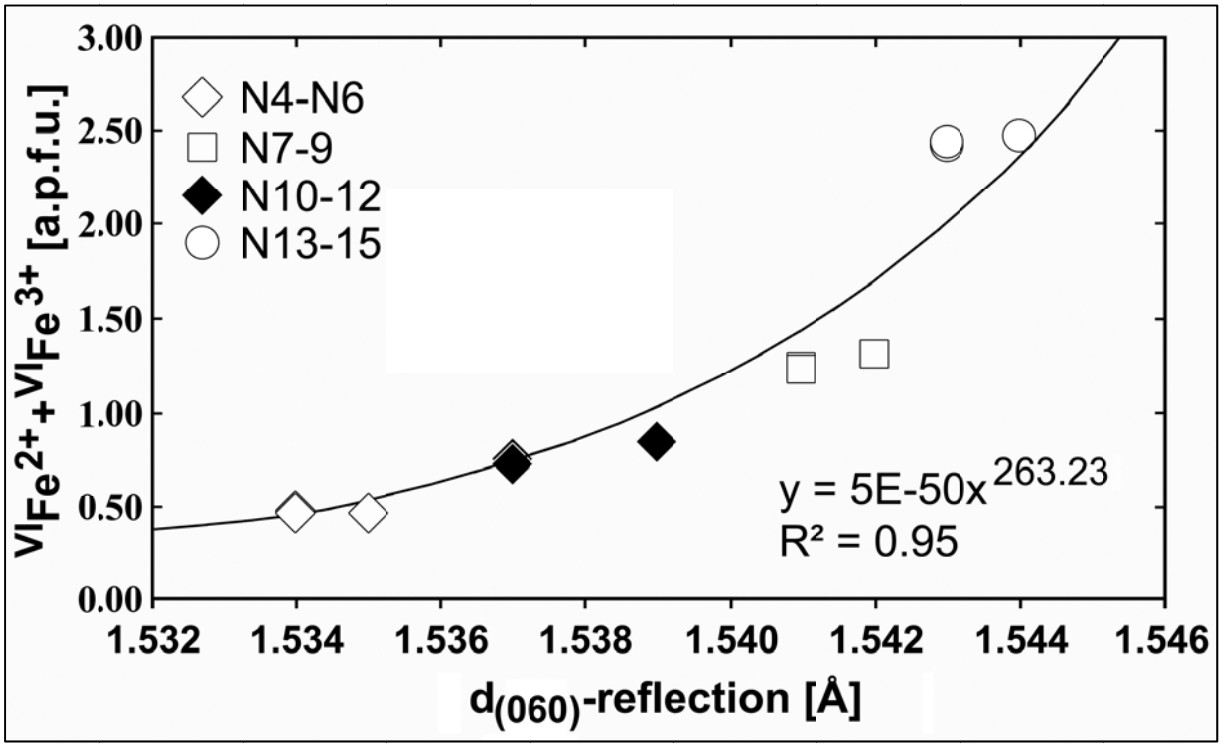

Fig. 2.7: Cross plot of octahedral Fe^{2+} and Fe^{3+} content of synthesized ferrous saponite, based on TEM-EDX, plotted against the position of the $d_{(060)}$-reflection.

In the present experimental study, ferrous saponite was synthesized under initially reducing and alkaline conditions, at variable temperatures, and in the presence of solutions containing Mg^{2+}, Fe^{2+}, Na^{+}, and silica in variable quantities. These boundary conditions may resemble that of the Atlantis II Deep (Red Sea) conditions where ferrous saponites are formed in superficial sediments (Badaut *et al.*, 1985). As the compositions (Table 2.3) of our saponites were highly variable and depended on the molar Fe:Mg ratio of the initial experimental solution, temperature, and the reaction time of synthesis, it is notable that these compositions have similarities with numerous naturally occurring ferroan saponites, except for their Al content. The compositions of the synthesized ferrous saponites plot well in the SiO_2 – MgO – FeO + Fe_2O_3 field of trioctahedral smectites (Fig. 2.8-A) and are similar to those of the natural Fe (*e.g.* Lovoberezhye *ferro*-saponite, Siberia, Russia) and Mg (*e.g.* Ballarat saponite, California, USA) members. The $\sum {}^{VI}Fe^{2+} + {}^{VI}Fe^{3+}$ versus ${}^{VI}Mg^{2+}$ cross plot (Fig. 2.8-B) therefore suggests that a complete solid solution series may exist between the Fe-Mg-saponite end members, without a miscibility gap. Thus, the Fe-Mg-saponite series may display a similar behavior as the well-known annite – phlogopite solid solution series (*e.g.* Tischendorf *et al.*, 2007).

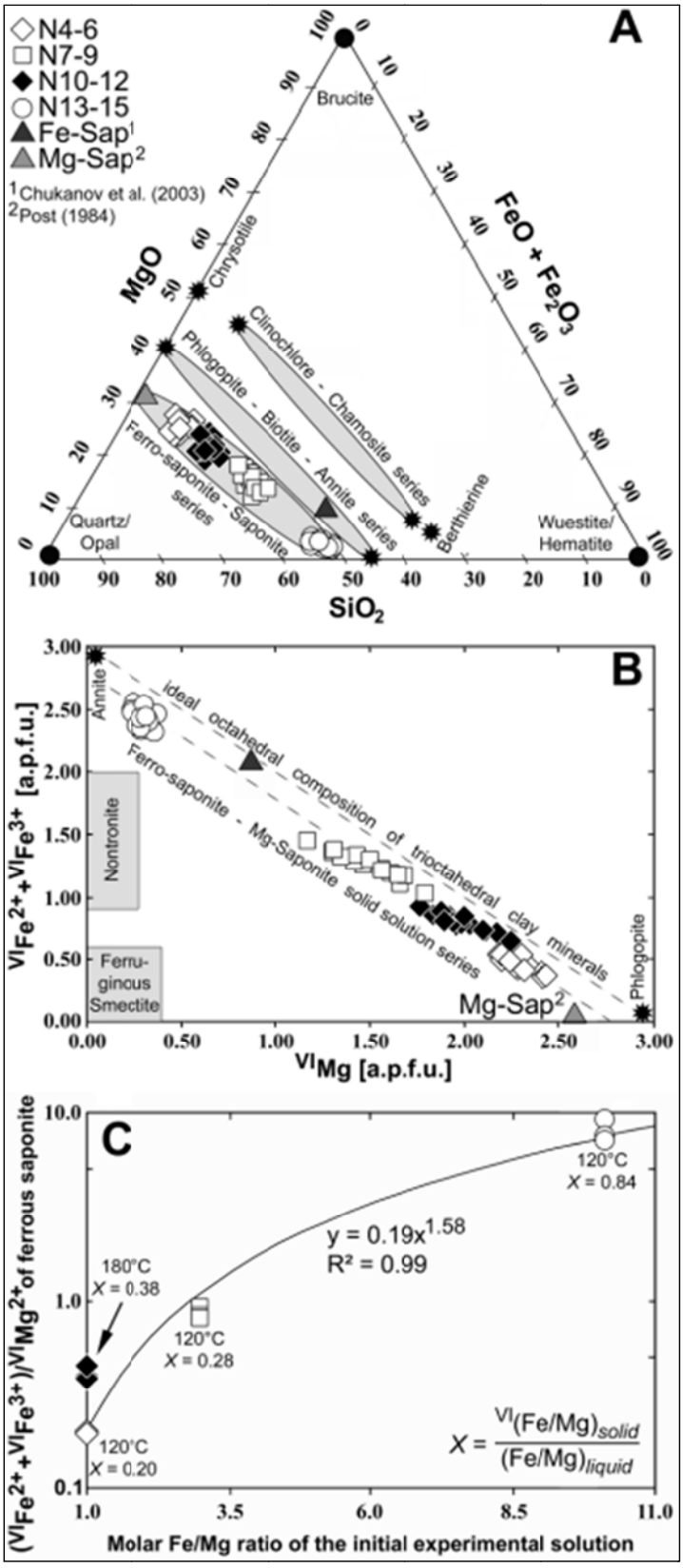

Fig. 2.8: **A**) SiO_2 – MgO – $FeO+Fe_2O_3$ triplot of trioctahedral clay minerals illustrating **t**he compositional similarity of synthesized ferrous saponite to their natural occurring trioctahedral Fe and Mg **e**nd members. **B**) Octahedral substitutions. **C**) Semi-logarithmic plot of $^{VI}Fe_{total}/^{VI}Mg^{2+}$ in the ferrous saponite structure plotted against the molar Fe:Mg ratio of the initial experimental solution. The molar fraction partitioning coefficient $X_{Fe^{2+}\text{-}Mg}$ shows the importance of Fe during ferrous saponite formation.

In order to explain the evolution of the crystallinity as well as the variable chemical composition of the synthesized ferrous saponites, the following reaction path of ferrous saponite formation is proposed. Experimental data from the literature and hydrochemical modeling of the experimental solutions indicate that Fe^{2+} and Si were completely dissolved at pH ≥ 11 (25°C-180°C) and at the given reducing conditions, whereby brucite precipitation could take place as soon as pH values ≥ 10.4 were reached. In the case of Si, the solubility of amorphous silica is well-known to strongly increase with temperature and pH (*e.g.* Iler, 1979). At pH ≥ 12 and in the presence of aqueous Na the dissolved silica mainly consists of negatively charged deprotonized monosilicic acid, sodium silicate aquo complexes, and a variety of negatively charged polysilicic acids (*e.g.* Dietzel & Letovsky-Papst, 2002). The predominance of these Si species results in the experimentally obtained solubility of amorphous silica of ~40,000 $mg \cdot L^{-1}$ at pH 11.3 (Greenberg & Price, 1957, Greenberg, 1958). Thus, with increasing temperature and pH of the experimental solutions the solubility of silica increased simultaneously, with abundant negatively charged dissolved species and partly Si-O-Si cross linked silica molecules.

In a simplified reaction sequence for ferrous saponite formation the precipitation of octahedral brucite-like template sheets subsequently induce condensation of dissolved Si-O tetrahedrons. Ongoing re-organization via dissolution and recrystallization of the octahedra and tetrahedra finally result in saponite structures, besides brucite and partly amorphous silica. Fe^{2+} is by far more soluble than brucite especially at pH ≥ 10.4, as indicated by PHREEQC modeling, but Fe^{2+} can substitute for Mg^{2+} in the octahedral position of the metastable template sheets. Thus, the structural Fe content in the final ferrous saponite precipitates may largely depend on the extent of incorporation of Fe^{2+} via isomorphic substitution in early octahedral template sheets, where elevated Fe supply should yield in saponite enriched in $^{VI}Fe^{2+}$. Subsequent to the nucleation and condensation reactions, the poorly-crystalline ferrous saponite particles evolve into well-crystalline ferrous saponite, as seen in the evolution of crystallinity with increasing reaction time of synthesis. It is suggested that the observed systematic changes in particle size and order result from multiple dissolution-recrystallization reactions, as indicated by the increase in the main crystallite thickness with increasing aging time for all types of the synthesized ferrous saponites (see Figs 2.1 and 2.6).

A further approach for characterization of the conditions of crystal growth during the formation of ferrous saponite is based on foreign metal ion versus $^{VI}Mg^{2+}$ distribution of both the neo-formed clay mineral and the either natural or experimental solutions from which the clay mineral has been precipitated. The incorporation of foreign metals in clay mineral structures was used by *e.g.* Corliss *et al.* (1987) and Dymond *et al.* (1973) to distinguish sedimentary

environments such as oceanic hydrothermal and metalliferous deposits, by using kind of crystal/liquid molar fraction coefficient, $X_{(M^{2+}\text{-}Mg)}$, according to the expression 2.1:

$$X_{(M^{2+}-Mg)} = \frac{(M^{2+})/(Mg)_{solid}}{(M^{2+})/(Mg)_{liquid}} \quad (2.1).$$

In the present study, the liquid ratio is referred to the molar Fe and Mg concentrations in the initial experimental solution, whereas the solid ratio is based on the $\sum {}^{VI}Fe^{2+} + {}^{VI}Fe^{3+}$ versus ${}^{VI}Mg^{2+}$ ratio, per $O_{10}(OH)_2$, of ferrous saponite obtained at a given reaction time. In this approach the existence of a solid solution between the foreign metal ion M^{2+} and Mg^{2+} in the octahedral sheet of a clay mineral is assumed, but is validated from Figs 2.7 and 2.8 for Fe^{2+} incorporation in saponite (in accordance with Decarreau, 1985). The $X_{Fe^{2+}\text{-}Mg}$ values calculated range from 0.20 to 0.94, with averages of 0.20, 0.28, 0.38, and 0.84 for the respective experiments N4-6, N7-9, N10-12, and N13-15 and depend mainly on the temperature and on the molar Fe:Mg ratio of the initial solution (Fig. 2.8-C). Decarreau (1985) did not recognize any systematic changes in the $X_{Me^{2+}\text{-}Mg}$ values in the temperature range from 25°C to 75°C and suggested that variations in the crystallite size of clay minerals have more impact on controlling element partitioning during clay mineral formation than the temperature and the solution chemistry. However, the relative structural and compositional heterogeneity of the ferrous saponites (Table 2.3) in the individual experiments may indicate that equilibrium conditions are not easily reached during the formation of ferrous saponite. This is despite that Fe^{2+} substitutions for Mg^{2+} in the octahedral sheet of the neo-formed ferrous saponite are suggested to be thermodynamically favorable, as suggested by Decarreau (1985). Thus, the extent of ferric and ferrous Fe incorporation can play an important role on controlling the formation of di- and trioctahedral clay minerals by affecting the chemical composition, structure, crystallite size and structural order, and in particular the bulk rates of chemical reaction. The importance of Fe as the probable overall rate-determining element in the Fe-smectite-to-glauconite reaction, as suggested by Baldermann *et al.* (2013), is indicated in the present study to also apply to the Fe-saponite – Mg-saponite solid solution series.

2.6 Summary and conclusions

Ferrous saponite was synthesized successfully in Teflon-lined stainless steel autoclaves within only 2 to 7 days at temperatures of 60°C, 120°C and 180°C, reducing conditions, and at variable molar Fe:Mg ratios of 1.82:0.18, 1.5:0.5, and 1:1 of the initial solution. XRD, TEM-EELS

as well as thermal and spectroscopic analysis preformed on the synthesized precipitates confirm the nature of the clay minerals to be trioctahedral ferrous saponite, with minor proportions of brucite, opal-CT, 2-line ferryhydrite and nontronite. The compositions of the synthesized ferrous saponites, determined by TEM-EDX, were highly variable and depended mainly on the molar Fe:Mg ratio of the initial experimental solution and on the formation temperature and to some degree on the reaction time of synthesis. The mineralogy, composition, and structure of the synthesized ferrous saponites were in accordance to that of natural occurring trioctahedral Fe and Mg end members, suggesting a complete solid solution to be valid in the Fe-Mg-saponite series, without a miscibility gap. HRTEM analysis of the synthesized ferrous saponites revealed an increase in crystallinity and crystallite thickness with increasing temperature and molar Fe:Mg ratio of the initial solution. It is suggested that the extent of $^{VI}Fe^{2+}$ substitutions for $^{VI}Mg^{2+}$ during the first nucleation of brucite-like octahedral template sheets has a stabilizing effect on the subsequently formed ferrous saponite nuclei, as indicated by the molar fraction coefficients $X_{Fe^{2+}\text{-}Mg}$ of 0.20 up to 0.94, from low to high $(Fe/Mg)_{(aq),i}$ ratios. This general behavior reflects the positive effect of structural Fe on the bulk formation reaction rate of ferrous saponite.

Chapter 3

Micromilieu-controlled glauconitization in fecal pellets at Oker (Central Germany)

3.1 Abstract

Although numerous models for the formation of glauconite have been presented, the precise process and micro-environment of glauconitization are still poorly constrained. We characterize the special micromilieu of glauconitization developed during early diagenesis and present a model for glauconite formation in fecal pellets.

Glauconitization at Oker (Central Germany) occurred predominantly in fecal pellets deposited in a shallow marine-lagoonal environment during the Kimmeridgian. Within the fecal pellets, rapid oxidation of organic matter provides the post-depositional, physicochemical conditions favorable for glauconitization. Replacements of matrix calcite, dissolution of detrital quartz, K-feldspar, and clay minerals, and Fe redox reactions were observed within the early micro-environment, followed by the precipitation of euhedral pyrite, matrix-replacive dolomite, and megaquartz accompanied by IS formation as thin section analyses and SEM observations show. Carbonate geochemical compositions based on ICP-OES and stable oxygen and carbon isotope signatures demonstrate that glauconite formation started in a suboxic environment at a pH of 7-8 and a temperature of 22±3ºC to 37±2ºC at maximum.

TEM-EDX-SAED and XRD analyses on separated glauconite fecal pellets and on the < 2 µm clay mineral fraction reveal the predominance of authigenic $1M_d$-glauconite, $1M_d$-glauconite-smectite, and $1M_d$ cis-vacant I-S, besides accessory, detrital $2M_1$-illite and montmorillonite. Kinetic modelling of the glauconite (93-94% Fe-illite layers and 6-7% Fe-smectite layers, R3) and of I-S (66-68% Al-illite layers and 32-34% Al-smectite layers, R1) leads us to conclude that the I-S formed solely by slow burial diagenesis, whereas the glauconite formed close to the seafloor, suggesting significantly faster kinetics of the glauconitization reaction compared with smectite illitization related to burial diagenesis. Thermodynamically, the substitution of octahedral Al^{3+} for Fe^{3+} and Mg^{2+} during the Fe-Mg-smectite to glauconite reaction via the

formation of glauconite-smectite mixed-layered clay minerals may have resulted in a higher reaction rate for this low-temperature glauconitization process.

3.2 Introduction

Mineralogically, glauconite is a dioctahedral, Fe-rich illite that is interlayered with < 5-10% Fe-smectite layers. Based on the definition of the AIPEA Nomenclature Committee (Bailey *et al.*, 1980), the mineral glauconite is composed of (i) tetrahedral $Al^{3+} > 0.2$ atoms per formula unit (a.p.f.u.) based on $O_{10}(OH)_2$, (ii) the sum of trivalent cations occupying the octahedral sheet is > 1.2 a.p.f.u. with $Fe^{3+} > Al^{3+}$ and $Mg^{2+} > Fe^{2+}$, (iii) the d_{060} reflection is > 1.51 Å, and (iv) K^+ dominants the interlayer sites (> 0.6 a.p.f.u.). The term "glauconitic" (nomenclature of Odin, 1988) is used for minerals of the "glaucony facies", which cover a complete genetically related mineral series from Fe-rich smectite to Fe-rich illite (glauconitic mica) that are the end-member types of the glaucony group. In this paper, we use the term "glauconitic" synonymous with the precursor phases of glauconite such as Fe-rich smectite and glauconite-smectite, not including the mineral glauconite *sensu stricto*.

Although numerous models for the formation of glauconite have been presented, the precise process and timing of glauconite genesis is still under debate. Suggestions range from (i) the alteration of biotite (Galliher, 1935) or (ii) alteration of volcanic mineral residues (Ojakangas & Keller, 1964), (iii) precipitation of glauconite from hydroxides and amorphous silicate gels (*e.g.* Kohler & Köster, 1976; Harder, 1980), (iv) transformation of degraded, detrital Al-rich smectites into glauconite, known as the "lattice layer" or "transformation theory" developed by Burst (1958a,b) and Hower (1961), and (v) precipitation of Fe-rich smectites directly from seawater, followed by a recrystallization into glauconite during early diagenesis. The latter formation mechanism was proposed by Odin & Matter (1981) and is referred to as the "neoformation and recrystallization theory". Recent studies on authigenic, green, glauconitic clay minerals (*e.g.* Charpentier *et al.*, 2011; Gaudin *et al.*, 2005) suggests that neo-formed Fe-rich, smectitic clays are the most probable precursor phases of glauconite, which is consistent with Odin's (1988) model of glauconite formation. The Fe-smectite-to-glauconite reaction is described to be either a dissolution-recrystallization process (*e.g.* Buatier *et al.*, 1989) or a solid solution (transformation) mechanism (*e.g.* Meunier & El Albani, 2007).

However, a glauconitization model needs to explain why glauconite commonly forms in restricted to shallow-marine shelf environments at water depths < 200 m and temperatures below 15ºC (Odin, 1988), but also on the continental slope (*e.g.* Rao *et al.*, 1995), in deep-sea low-

temperature (> 2000 m, 3-6ºC) environments (Giresse & Wiewióra, 2001; Charpentier *et al.*, 2011; Cuadros *et al.*, 2011), at mid-oceanic ridges (Buatier *et al.*, 1989), in onshore lacrustrine-pedogenic (Huggett & Cuadros, 2010) and in brackish-lagoonal deposits (El Albani *et al.*, 2005). What most of these depositional environments have in common are low sedimentation rates, an Eh about 0, pH 7-8, granular (siliciclastic or carbonaceous) habitats with a high porosity and permeability, a long residence time (10^3-10^6 years) close to the sediment-seawater interface and, most importantly, organic-rich micro-environments within *e.g.* fecal pellets that provide the post-depositional, physicochemical conditions favorable for glauconitization (summarized in Odin, 1988).

Recent fecal pellets are commonly produced by suspension-feeding crustacean zooplankton (Pilskaln & Honjo, 1987) and contain large amounts of undigested organic matter (5-50 wt.%) and clay minerals (10-90 wt.%) with trace contents of carbonate, opaline silica, and detrital, siliciclastic grains such as quartz and feldspar (Pryor, 1975; Pilskaln & Honjo, 1987). During early diagenesis, the organic matter oxidizes rapidly, reducing the Eh and pH within the fecal pellets. Whole or partial decomposition of incorporated detrital clay minerals such as mica, chlorite, kaolinite, and mixed-layered clay minerals takes place under these conditions (Pryor, 1975) releasing the cations needed for the glauconitization process. However, mineral dissolution and Fe redox reactions that occur within the specific micro-environment in fecal pellets and related changes in the physicochemical conditions are still poorly characterized, hence, the precise process and micromilieu of glauconitization remains enigmatic so far.

In this paper, we focus on the mineralogical and chemical characterization of the fecal pellet's micro-environment and present a model for glauconite formation that is adequate to explain the mineralogical, geochemical and structural changes associated with the glauconitization of fecal pellets. We discuss the precursor phases of glauconite, the temperature range, kinetics and thermodynamics of the glauconitization reaction as well, and compare the estimated formation conditions with that of smectite-illitization related to burial diagenesis. To this end, we analyzed glauconitized fecal pellets formed in a shallow-marine to lagoonal environment of Upper Jurassic age (Kimmeridgian from Oker, Central Germany) and illite-smectite mixed-layered clay minerals (I-S) formed during burial diagenesis, because of the special mineralogy of these sedimentary units (see below) and the well-known burial history.

3.3 Geological setting

The Langenberg quarry at Oker is located 5 km east of Goslar near the Harz Mountains, northern Germany, and exposes a complete lithological profile of the marine Upper Jurassic (Ox-

fordian to Kimmeridgian) about 150 m thick (Fig. 3.1). Well-bedded micritic limestones intercalated with thin greenish, marly layers and some dolomite beds are the dominant sedimentary units at this locality. The basal part of the Langenberg section comprises brownish, fully marine, ferrous oolites of Oxfordian age (‘‘Korallenoolith’’) that were deposited in a shallow epeiric sea, particularly connected with the Jurassic Tethys Ocean. During the Lower Kimmeridgian, the depositional environment changed to lagoonal conditions caused by increased freshwater influx and global sea level changes. This led to intense facies changes of greyish argillite-marlstone-limestone alternations dominated by carbonates (~70-90%) with sections containing high input from the Pompecki block of detrital illite, chlorite, feldspar, quartz and pebbles (~10-20%; Fischer, 1991). Authigenic minerals (~10%) such as glauconite, pyrite, bioapatite, and I-S occur as well. Both the mineral assemblage and facies indicate that the depositional environment was either a seasonal anoxic, shallow water basin or a lagoonal to estuarine environment with moderate terrestrial input. At the top of this unit, limestones and dolomite beds of Middle to Upper Kimmeridgian age are exposed, showing the shift back to shallow marine conditions.

A precise biostratigraphic correlation of the Langenberg units with the subboreal standard zonation based on ammonoids is problematic because index fossils are rare at Oker (van der Lubbe *et al.*, 2009). Based on Rb/Sr modulations on bioapatite, Mudroch (2001) calculated a depositional age of 170 Ma for the bulk sediment. Including the biostratigraphic classification of Fischer (1991), 154 Ma was reconstructed for the authigenic minerals such as glauconite and bioapatite (I-S was not identified, yet) and 260 Ma for the detrital components.

The Langenberg section was buried to a depth of 1500-2000 m (at most 2500 m) during the Upper Jurassic to the Lower Cretaceous due to subsidence. Based on a geothermal gradient of 2.7ºC/100 m, the maximum temperature of burial is about 60-70ºC for the Jurassic sediments from Oker (Mazur & Scheck-Wenderoth, 2005; Nollet *et al.*, 2005). Due to strong uplift of about 1 mm/a related the development of the Harz Thrust Fault during the Upper Cretaceous and a second uplift period in the Tertiary, the Langenberg section was inverted and now dips at an angle of 50-70º to the south. Alterations within the Langenberg sequence caused by uplift or weathering are negligible (Mudroch, 2001).

3.4 Material and methods

Glauconite containing marly mudstones (GGÖ3 and GGÖ5), packstones (GGÖ6), and clayey mudstones without glauconite (GGÖ8 and GGÖ1) were sampled from a sequence of Lower to

Middle Kimmeridgian age from Oker (Fig. 3.1). Thin sections of GGÖ5 and GGÖ6 were prepared for petrographic investigations. For the mineralogical and geochemical analyses on the clay minerals, the carbonate matrix was first dissolved using 10% HCl following the procedure in Moore & Reynolds (1997). Afterwards, the glauconite pellets were separated by hand using a binocular microscope (GGÖ5GL and GGÖ6GL) and the glauconite-free < 2 µm size fraction of the washed acid insoluble residuals (GGÖ3X2, GGÖ6X2, and GGÖ8X2) was collected in order to characterize the authigenic and the detrital clay minerals.

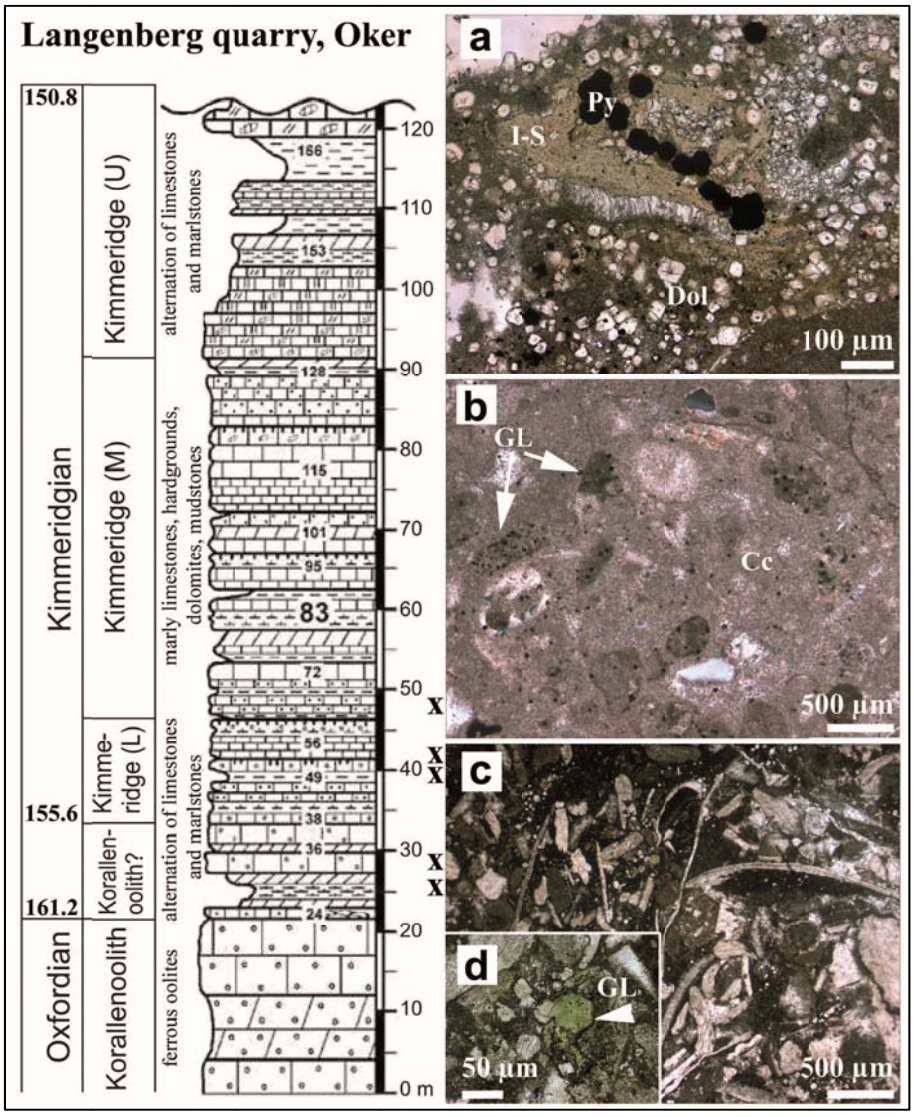

Fig. 3.1: Lithostratigraphic profile of the Langenberg quarry at Oker (Central Germany) with sampled layers (from the bottom to the top: GGÖ8, GGÖ6, GGÖ5, GGÖ3, and GGÖ1). Numbers within the profile mark stratigraphic head beds. Thin sections on the right: sample GGÖ5 (a and b) is a moderately bioturbated mudstone with subparallel arranged, greenish I-S, framboidal pyrite (Py), matrix-replacive, rhombohedral dolomite (Dol) (a), and authigenic, light green, pelloidal glauconite (GL) together with euhedral pyrite in a non-bioturbated, calcite (Cc) matrix (b). The thin section of GGÖ6 (c and d) displays a glauconite-bearing packstone. d is an enlarged view of C showing a light green, highly porous, glauconitized (GL) fecal pellet.

3.4.1 X-ray diffraction (XRD)

Random powder analyses of bulk rock samples were made for mineral identifications using a Siemens D5000 diffractometer equipped with a Cu-Kα tube (40 kV, 30 mA), Ni-filter, and 1º antiscattering and divergence slits. Illite polytypes were determined on isolated, finely ground glauconite pellets and on separated < 2 μm grain size fractions. The powdered material was step-scanned from 3 to 63º 2θ using a step size of 0.02º $2\theta \cdot s^{-1}$ and a count time of 25 $s \cdot step^{-1}$. The proportion of illite (%illite) in mixed-layered clay minerals such as glauconite, I-S, and detrital illite was estimated on oriented, glycolated preparations scanned from 3 to 35º 2θ with 0.02º $2\theta \cdot s^{-1}$ and 2 $s \cdot step^{-1}$ using the program Sybilla© developed at ChevronTexaco. Calculations were run only for the mixed-layered clays, thus, the R_{WP} is not indicated, here. The error of the %illite calculations was determined to be ±10% for the I-S and ±5% for the glauconite and detrital illite.

3.4.2 Electron microscopy (SEM and TEM)

Scanning electron microscopy (SEM) was used to study the microstructures of separated, C-coated glauconite pellets and I-S aggregates using a Jeol JXA-840A Micro Probe Analyzer. The mineralogy and composition of the glauconitized fecal pellets was analyzed with a FEI Quanta 400 equipped with an Ametek Edax Jenesis 4000 detector at the Baltic Sea Research Institute, Warnemünde (Germany) using polished thin sections of GGÖ5 and GGÖ6 and combined backscattered electron images and energy-dispersive X-ray spectroscopy (EDX).

Transmission electron microscopy (TEM) was carried out on a JEM 1210 Electron Microscope with a Pentafel Link/Model 6635 Oxford Instruments detector for combined high-resolution imaging, geochemical analyses (EDX) and electron diffraction (SAED). Three samples (GGÖ5GL, GGÖ6GL, and GGÖ6X2) treated with 10% HCl to remove free Al and Fe oxides, were first dispersed ultrasonically in deionized water; then the < 2 μm size fraction was dropped on a carbon film stretched over a TEM copper grid. Individual clay particles were analyzed using an accelerating voltage of 200 kV and a count time of 8 s to reduce K^+ migration. The analytical error of each EDX measurement varies with clay composition and thickness, but is generally < 1-2 wt.%. According to Bailey *et al.* (1980), the structural formulae were calculated on the basis of $O_{10}(OH)_2$ assuming (i) tetrahedral $Si^{4+} + Al^{3+} = 4$, (ii) Fe^{3+}, Fe^{2+}, Mg^{2+}, and Al^{3+}_{rest} occupy any of the octahedral sheet sites, and (iii) $K^+ + Ca^{2+}$ within the interlayer sites. The proportion of ferrous Fe was calculated assuming a Fe^{2+}/Fe^{3+} ratio of 0.15 (in agreement with the Fe^{2+}/Fe^{3+} ratios in Odom, 1976; Longuépée & Cousineau, 2006; and Hug-

gett & Cuadros, 2010; in addition it agrees with the GL-O glauconite standard defined in Odin, 1982).

3.4.3 Geochemical analyses (XRF, ICP-OES and stable isotope measurements)

The < 2 µm size fraction of GGÖ6X2 was analyzed using a Philips PW2404 wavelength dispersive X-ray fluorescence spectrometer (XRF). Sample preparation followed that described in Brown *et al.* (1973). A range of USGS standards were run to verify that the accuracy of the measurement is 0.5-1 wt.% for the major elements.

Major and minor element compositions of the 0.5 M HCl soluble phases of GGÖ3-1, GGÖ3-2, GGÖ5-1, GGÖ5-2, GGÖ6, and GGÖ8 were analyzed with a Thermo Fisher ICap 6300 inductively coupled plasma optical emission spectrometer (ICP-OES) at the Baltic Sea Research Institute, Warnemünde. The diluted extractions were run together with in-house standards. The analytical error is < 3% for the major elements and < 6% for the minor elements.

Stable isotope measurements of $\delta^{13}C$ and $\delta^{18}O$ were carried out to estimate the carbon source and the formation temperatures of the carbonate. Measurements of the six samples (see ICP-OES) were carried out on a ThermoFisher Electron Finnigan MAT 253 gas mass spectrometer (IRMS) connected to a Thermo Finnigan Flash elemental analyzer at the Baltic Sea Research Institute, Warnemünde. Stable isotope values are given in the conventional d-notation via the V-PDB (Vienna Pee Dee Belemnite) standard with a 2σ standard deviation of 0.1‰.

3.5 Results

In this section, the petrographic (thin sections and SEM), mineralogical (XRD), and geochemical (TEM-EDX, XRF, ICP-OES, and stable isotopes) results are presented for the authigenic glauconite and I-S compared with the detrital illite as well as the carbonates in order to characterize the glauconitization process in fecal pellets at Oker.

3.5.1 Petrographic observations

Medium to dark green glauconitized fecal pellets (~95% of the total green grain fraction) and subordinate incomplete, light green glauconitic infillings (~5% of the total green grain fraction) of foraminifera, echinoids and shells are minor constituents (< 1 wt.%) within the partly dolomitized mudstones and packstones. Thin section images (see Fig. 3.1b and 3.1c) illustrate that the glauconite pellets are highly porous, commonly around 100-700 µm in size, and often have a diffuse contact with the micritic (calcitic) matrix, indicative of calcite replacements.

No signs of reworking or re-deposition were observed, also implying that the glauconite is authigenic and *in situ*. Bioclast fragments, detrital quartz grains and remnants of K-feldspar frequently occur in the exterior of the fecal pellets. In the interior of the organic-rich fecal pellets, both framboidal and euhedral pyrite is present, suggesting suboxic to anoxic formation conditions.

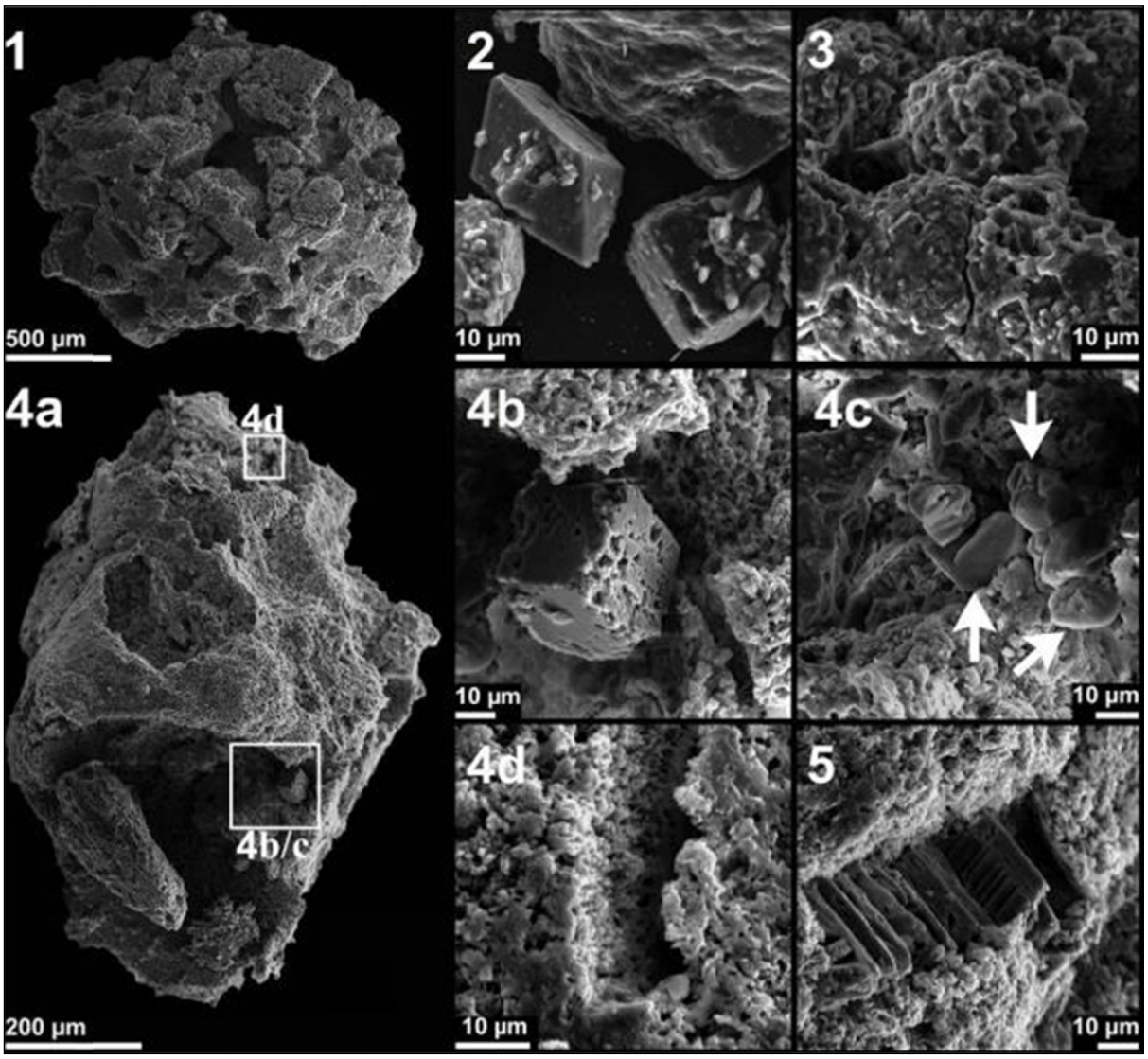

Fig. 3.2: SEM images of highly porous, glauconitized fecal pellets (1 and 4a). Dissolution of K-feldspar (4b), growth of megaquartz (4c), and aragonite/bioclast replacements (4d and 5) occur within the micro-environment. Honeycomb-like glauconite overgrowths on framboidal pyrite (3) indicate formation in a suboxic environment. I-S associated with rhomboidal dolomite (2).

Brown to greenish, sub-parallel oriented aggregates of I-S particles (for identification see XRD results) are mainly present in the moderately bioturbated, clayey mudstones (Fig. 3.2-1a), but cover the whole Upper Jurassic profile including horizons where glauconite pellets

can be found. I-S is always associated with euhedral (rhombohedral), matrix calcite-replacive dolomite that typically forms in sabkha environments among framboidal and euhedral pyrites. In contrast, the glauconite pellets only occur in distinct, calcite-dominated layers where I-S and dolomite are practically absent.

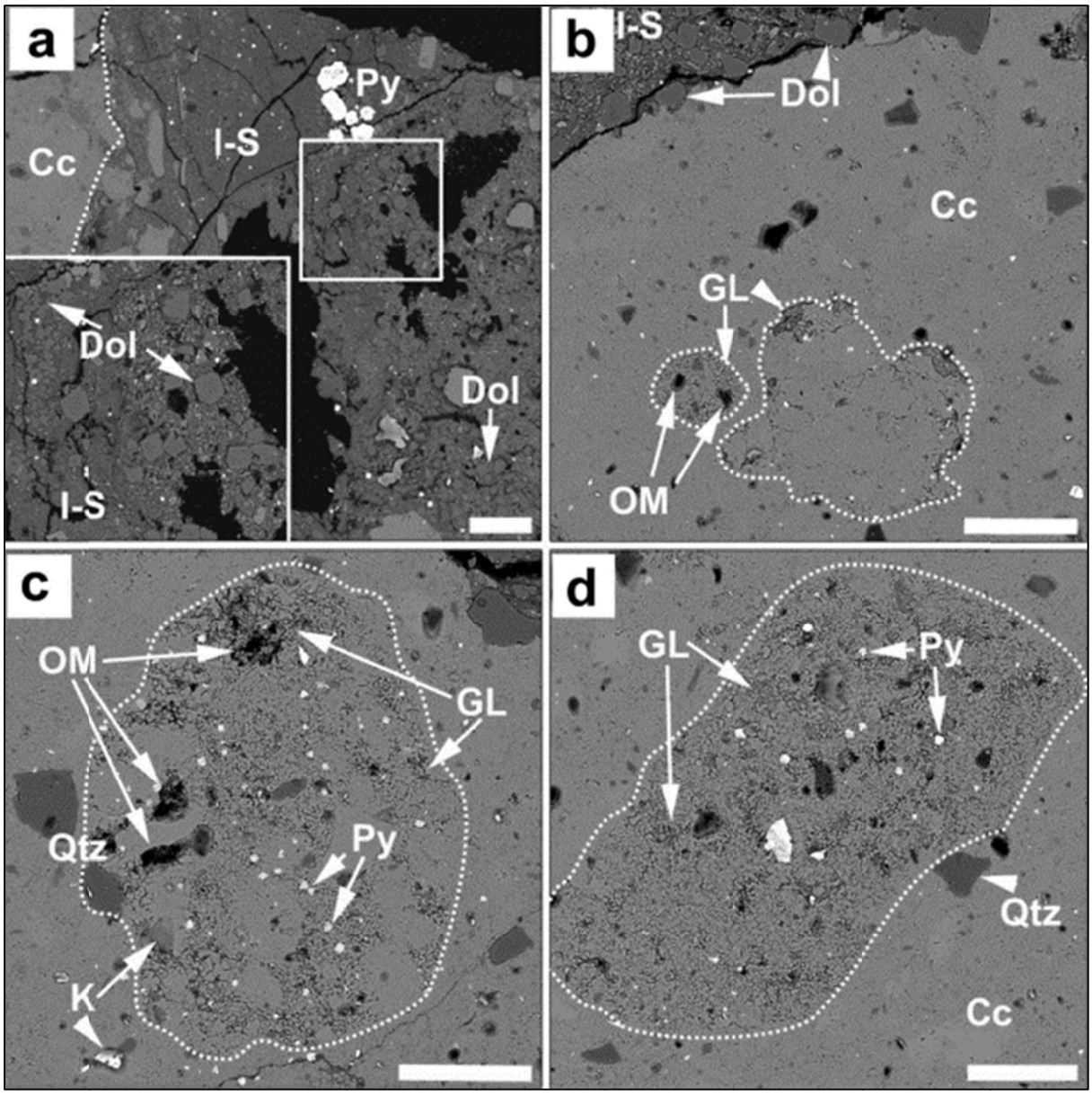

Fig. 3.3: Backscattered electron images of polished thin sections of GGÖ5 (a-c) and of GGÖ6 (d). I-S (a) associated with matrix-replacive dolomite (Dol) and framboidal pyrite (Py). The enlarged view of a shows subparallel growth structures of I-S and dolomite suggesting simultaneous formation. Highly porous, partly glauconitized (GL) fecal pellets rich in organic matter (OM) embedded in a calcite matrix (Cc) are shown in b. On top, dolomite replaces the micritic calcite. Porous, glauconitized fecal pellet (c) including framboidal pyrite in the interior and remnants of detrital quartz (Qtz) and K-feldspar (K) in the exterior. Highly glauconitized fecal pellet (d) with a higher packing density of the microstructures. Note that siliciclastic components are absent at this stage of glauconitization. Scale bar: 100 µm.

SEM images (Figs 3.2 and 3.3) of the partly glauconitized fecal pellets predominantly show 1-2 µm large, diffuse arranged crystallites with a low packing density of the microstructures (Fig. 3.2-1 to 3.2-5). Generally, the fecal pellets (Fig. 3.3-b to 3.3-d) are composed of glauconite (20-50%), matrix calcite mixed with bioclast debris (40-70%), preserved organic matter (5-10%), detrital siliciclastics such as quartz grains, clay minerals and K-feldspar (5-10%) and pyrite (< 5%). Both the green-clay microstructures and the composition of the fecal pellets imply that the glauconitization process is incomplete. Dissolution of K-feldspar (Fig. 3.2-4b and 3.3-c), quartz grains (Fig. 3.3-c and 3.3-d) and bioclasts (Fig. 3.2-4d and 3.2-5) was observed mainly within the fecal pellets exterior, while framboidal pyrite is present in the interior of the glauconitized pellets (Fig. 3.3-c and 3.3-d), showing the diversity of mineral dissolutions, Fe redox reactions and replacement reactions within the micro-environment related to glauconitization. One instance of honeycomb-like overgrowths of glauconite on framboidal pyrite was also found (Fig. 3.2-3).

Within larger cavities of the glauconitized fecal pellets, 10-30 µm large, euhedral quartz crystals can be found, but are scarce (Fig. 3.2-4c). Euhedral quartz (megaquartz) forms during the slow burial diagenesis, where smectite-illitization occurs (***e.g.*** Hower ***et al.***, 1976; Veizer & McKenzie, 2005). I-S generally forms aggregates with embedded rhomboidal dolomite crystals that are about 5-30 µm in size (Figs 3.2-2 and 3.2-3a). The growth structures of I-S and dolomite indicate that both phases were formed simultaneously. Sparse octahedral and framboidal pyrite was also observed.

Based on these petrographic observations, the following sequence of mineral growth can be recognized: matrix calcite – glauconite – framboidal and euhedral pyrite – dolomite and I-S. The estimated formation conditions and depositional environment of glauconite and I-S are discussed later.

3.5.2 Mineralogy of the glauconite fecal pellets and I-S

The XRD patterns of textured and randomly oriented preparations of the separated glauconite fecal pellets (GGÖ5GL and GGÖ6GL) and I-S samples (GGÖ3X2 and GGÖ8X2) are shown in Figs 3.4 and 3.5.

Oriented, glycolated preparations of the glauconite pellets show a broad d001 reflection at 9.96 Å, a weak d_{002} reflection at 5.03-5.04 Å, and a strong d_{003} reflection at 3.33 Å with an IR ratio of 1.4-1.5 (Środoń & Eberl, 1984). Based on Sybilla© modeling (Fig. 3.4-b and 3.4-c), the glauconite pellets contain a mixed-layered I-S, referred to as glauconite-smectite (nomenclature of Odin & Matter, 1981), with 93-94% Fe-illite layers and 6-7% Fe-smectite layers

(R3 ordered) and about 1.0-1.2 Fe and 0.55-0.6 K a.p.f.u. A weak d_{020} peak at 4.53 Å is present due to limited perfect particle orientation during sample preparation caused by small impurities of calcite, gypsum, and K-feldspar within the glauconitized fecal pellets. Random powder XRD patterns of the separated green pellets show a broad 10.1 Å peak (d_{001}), a weak d_{002} at 5.02 Å, and the diagnostic d_{060} reflection at 1.52 Å (Moore & Reynolds, 1997), typical for glauconite or glauconite-smectite. Polytype diagnostic reflections reveal a $1M_d$ polytype, because the 1M polytype diagnostic reflections of glauconite are absent (see Fig. 3.5). Traces of the $2M_1$ polytype are also present (< 10%), but do not belong to the glauconites.

The glycolated I-S samples show broader d_{00l} reflections at 17.2 Å (d_{001}), 9.57 Å (d_{002}), and 5.28 Å (d_{003}). Sybilla© modeling (Fig. 3.4-a and 3.4-d) reveals that the I-S consists of about 66-68% Al-illite layers and 32-34% Al-smectite layers (R1 ordered) containing approximately 0.3-0.5 K and 0.25 Fe a.p.f.u.. A well ordered illite, which contains about 0.25 Fe and 0.75 K a.p.f.u. was also identified based on the sharp d_{00l} reflections at 9.98 Å (d_{001}), the high d_{002} at 4.96 Å, and d_{003} at 3.34 Å with an IR ratio of 1.1-1.2 (Środoń & Eberl, 1984), indicative of an Fe-poor illite (R3 ordered) that consist of 95-99% Al-illite layers and 1-5% expandable layers. The Fe-poor illite and I-S have a d_{060} reflection at 1.50 Å, showing the dioctahedral nature of both clay minerals (Moore & Reynolds, 1997). Polytype determinations (Fig. 3.5) of the Fe-poor illite reveal a $2M_1$-polytype, which is common for detrital clays in marine sediments (Grathoff et al., 2000) and for I-S a $1M_d$ cis-vacant structure implying an authigenic origin.

3.5.3 TEM of the authigenic and detrital clay minerals

TEM-EDX analyses were realized on 53 single clay particles GGÖ5GL and GGÖ6GL) from the glauconite pellets and on the < 2 µm size fraction of GGÖ6X2. The geochemical compositions and calculated structural formulae of the individual particles are reported in Table 3.1, average compositions and structural formulas are presented in Table 3.2. Representative TEM images and SAED patterns of the authigenic $1M_d$ glauconite-smectite, 1M glauconite, and I-S compared with the detrital, Fe-poor illite and montmorillonite are shown in Fig. 3.6.

The first two types of particle ($1M_d$ glauconite-smectite and 1M glauconite) have a lath-like morphology and are between 600-900 nm in length (Fig. 3.6-a to 3.6-c). Semi-quantitative EDX analyses of the lath-like particles from GGÖ5GL range from 56.6-62.2 wt.% SiO_2, 5.4-15.8 wt.% Al_2O_3, 3.5-5.5 wt.% MgO, 4.6-7.5 wt.% K_2O, 14.7-26.8 wt.% Fe_2O_3, and 0.2-0.5 wt.% CaO; GGÖ6GL ranges from 53.1-58.7 wt.% SiO_2, 4.2-18.9 wt.% Al_2O_3, 3.0-5.5 wt.% MgO, 4.9-8.3 wt.% K_2O, 11.8-30.2 wt.% Fe_2O_3, and 0.1-1.2 wt.% CaO, indicating overall glauconite-smectite composition and glauconite compositions respectively.

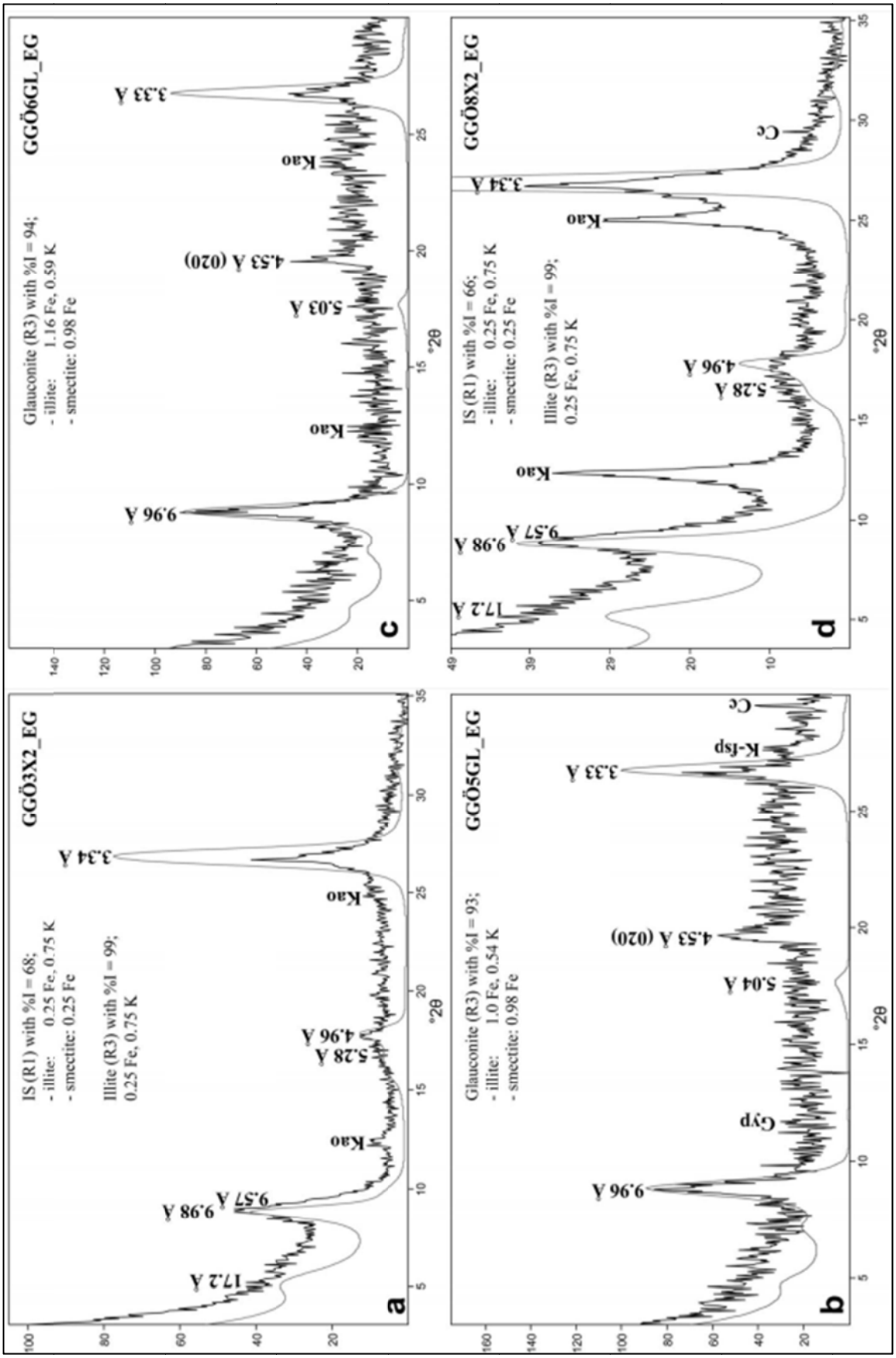

Fig. 3.4: Oriented, glycolated XRD patterns of mixed I-S and Fe-poor illite (a and d), and glauconite (b and c). Input parameters for Sybilla© modeling (smoothed curves) are indicated in the figure.

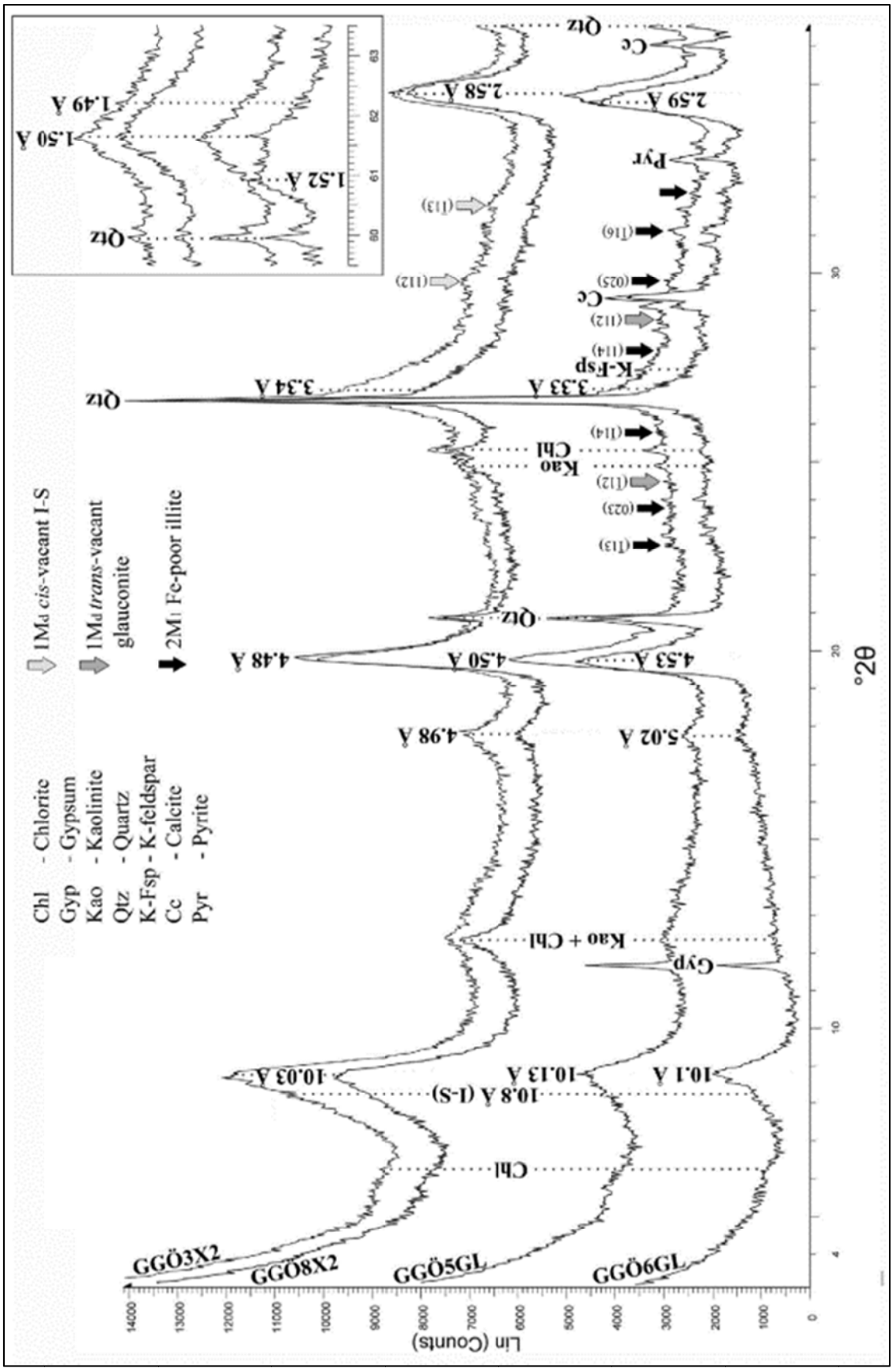

Fig. 3.5: Random XRD powder patterns of the separated glauconite fecal pellets (GGÖ5GL and GGÖ6GL) displaying their $1M_d$ polytype. GGÖ3X2 and GGÖ8X2 dominantly contain authigenic $1M_d$ cis-vacant I-S and trace amounts of Fe-poor $2M_1$-illite. The enlarged d_{060} reflection displays the dioctahedral nature of all clay phases.

P_2O_5, SO_3, TiO_2, and MnO only occur in negligible amounts. Generally, these impurities are associated with small amounts of Ti/Mn oxides, sulphates, and phosphates, rather than belonging to the glauconite structure (Kohler & Köster, 1976). SAED patterns of the lath-like clays show either particles with discrete Bragg patterns that have two diagnostic non-basal reflections corresponding to an ordered 1M structure (Fig. 3.6-a, seldom) or smeared Bragg patterns with weak diffraction rings indicative of a highly disordered 1Md-structure (Fig. 3.6-b, often). Hence, the glauconitized fecal pellets consist mostly of $1M_d$ and minor 1M polytypes, suggesting an authigenic origin (*e.g.* Pevear, 1999). Rarely, contacts between disordered glauconite-smectite particles and bacteria were observed (Fig. 3.6-c), but only within GGÖ5GL. The bacteria are commonly surrounded by a diffuse biofilm and contain large amounts of P and S up to 4 at.%, suggesting a marine origin.

The third type of particle (I-S) is typically < 100 nm in size and shows irregular or flake morphology (Fig. 3.6-d). Traces of these particles were found in both glauconite samples, but are abundant in GGÖ6X2. Geochemically, these particles vary from 58.5-64.2 wt.% SiO_2, 19.2-28.0 wt.% Al_2O_3, 1.6-4.6 wt. % MgO, 3.6-6.9 wt.% K_2O, 4.2-6.9 wt.% Fe_2O_3, and 0.1-0.6 wt.% CaO with traces of P_2O_5, SO_3, TiO_2 and MnO. SAED patterns of this clay mineral show weak diffraction rings and subordinate discrete Bragg patterns, indicating a moderately disordered $1M_d$ structure and the presence of turbostratic layers corresponding to smectitic clays or I-S of authigenic origin.

The fourth particle type (Fe-poor illite) occurs mainly in GGÖ6X2. Individual particles are ca. 1 µm in largest dimension, plate-like, and often show partially curled edges (Fig. 3.6-e) with a chemical composition varying slightly between 53.3-54.6 wt.% SiO_2, 34.0-35.2 wt.% Al_2O_3, 0.4-0.8 wt.% MgO, 8.3-8.8 wt.% K_2O, and 2.1-2.5 wt.% Fe_2O_3. SAED patterns display four diagnostic non-basal reflections, implying a $2M_1$ polytype structure. Hence, this phase was identified as a dioctahedral, Fe-poor, $2M_1$-illite and detrital in origin.

Finally, a fifth phase with a platy morphology and SAED patterns similar to I-S (Fig. 3.6-f) was found, but with a different geochemical composition of 65.1-66.2 wt.% SiO_2, 25.3-26.6 wt.% Al_2O_3, 1.8-2.0 wt.% MgO, 0.6-0.7 wt.% K_2O, 2.9-3.1 wt.% Fe_2O_3, and 2.3-2.8 wt.% CaO, typical for detrital montmorillonite.

Calculated octahedral, tetrahedral and interlayer charges as well as octahedral substitution based on structural formulae are plotted on a standard charge distribution diagram shown in Fig. 3.7. The fields of glauconite and montmorillonite (modified from Kohler & Köster, 1976) are included for comparison.

Table 3.1: Geochemical compositions (wt.%) and calculated structural formulae of individual clay particles from the glauconite pellets (GGÖ6GL and GG´Ö5GL) and of the < 2 µm size fraction of GGÖ6X2 based on 53 TEM-EDX analyses. The Fe^{2+}/Fe^{3+} ratio was assumed to be 0.15.

GGÖ5GL	**1**	**2**	**3**	**4**	**5**	**6**	**7**	**8**	**9**	**10**	**11**	**12**	**13**	**14**
SiO_2	57.50	59.06	58.77	58.87	56.63	58.72	59.14	59.90	59.26	60.64	62.19	61.48	61.36	61.36
Al_2O_3	11.50	8.71	10.21	5.48	5.44	5.74	8.81	9.09	12.82	15.84	14.02	20.68	19.16	22.32
MgO	4.52	3.52	3.55	4.85	3.61	3.93	4.92	5.48	4.41	3.71	4.11	3.75	4.60	2.85
K_2O	6.44	5.83	6.01	5.97	7.42	7.50	5.91	4.76	5.34	4.58	4.61	6.43	4.51	4.04
Fe_2O_3	18.03	22.23	21.17	24.49	26.77	23.91	18.79	18.96	18.00	15.10	14.74	7.66	9.86	8.86
P_2O_5	0.56	n.d.	n.d.	n.d.	n.d.	n.d.	1.45	n.d.	n.d.	n.d.	n.d.	n.d.	n.d.	n.d.
SO_3	0.91	0.23	n.d.	n.d.	n.d.	n.d.	0.78	1.80	n.d.	n.d.	n.d.	n.d.	0.40	n.d.
CaO	0.54	0.39	0.28	0.34	n.d.	n.d.	0.19	n.d.	0.17	n.d.	0.15	n.d.	0.12	0.51
TiO_2	n.d.	0.02	n.d.	n.d.	0.14	n.d.	n.d.	n.d.	n.d.	0.14	n.d.	n.d.	n.d.	0.06
MnO	n.d.	n.d.	n.d.	n.d.	n.d.	0.20	n.d.	n.d.	n.d.	n.d.	0.18	n.d.	n.d.	n.d.
Sum	100.00	99.99	99.99	100.00	100.01	100.00	99.99	99.99	100.00	100.01	100.00	100.00	100.01	100.00
Morph.	hairy	hairy	hairy	hairy	hairy	hairy	hairy	hairy	hairy	hairy	hairy	flaky	flaky	flaky
GGÖ5GL	**1**	**2**	**3**	**4**	**5**	**6**	**7**	**8**	**9**	**10**	**11**	**12**	**13**	**14**
Si^{4+}	3.80	3.89	3.84	3.91	3.84	3.93	3.93	3.93	3.81	3.83	3.92	3.81	3.81	3.77
Al^{3+}	0.20	0.11	0.16	0.09	0.16	0.07	0.07	0.07	0.19	0.17	0.08	0.19	0.19	0.23
T.C.	-0.20	-0.11	-0.16	-0.09	-0.16	-0.07	-0.07	-0.07	-0.19	-0.17	-0.08	-0.19	-0.19	-0.23
Al^{3+}	0.69	0.56	0.63	0.34	0.27	0.38	0.62	0.63	0.78	1.01	0.96	1.32	1.21	1.38
Fe^{3+}	0.79	0.97	0.92	1.08	1.20	1.06	0.83	0.82	0.77	0.63	0.62	0.31	0.41	0.36
Fe^{2+}	0.12	0.15	0.14	0.16	0.18	0.16	0.13	0.12	0.12	0.10	0.09	0.05	0.06	0.05
Mg^{2+}	0.45	0.35	0.35	0.48	0.36	0.39	0.49	0.54	0.42	0.35	0.39	0.35	0.43	0.26
Σ_{OL}	2.05	2.03	2.04	2.06	2.01	1.99	2.07	2.11	2.09	2.09	2.06	2.03	2.11	2.05
O.C.	-0.42	-0.41	-0.37	-0.46	-0.51	-0.58	-0.41	-0.33	-0.27	-0.18	-0.30	-0.31	-0.16	-0.16
Ca^{2+}	0.04	0.03	0.02	0.02	0.00	0.00	0.01	0.00	0.01	0.00	0.01	0.00	0.01	0.03
K^+	0.54	0.49	0.50	0.51	0.64	0.64	0.50	0.4	0.44	0.37	0.37	0.51	0.36	0.32
I.C.	0.62	0.55	0.54	0.55	0.64	0.64	0.52	0.40	0.46	0.37	0.39	0.51	0.38	0.38
Interpret.	GL	GL-S	GL-S	GL-S	GL-S	GL-S	GL-S	GL-S	GL-S	GL-S	GL-S	I-S	I-S	I-S

GGÖ6GL	**1**	**2**	**3**	**4**	**5**	**6**	**7**	**8**	**9**	**10**	**11**	**12**	**13**	**14**	**15**	**16**	**17**	**18**	**19**
SiO_2	53.08	53.96	54.66	55.11	55.49	53.70	56.19	53.81	54.86	57.38	56.71	55.94	58.23	58.45	55.77	58.71	57.13	58.52	62.22
Al_2O_3	5.05	5.97	6.52	9.58	8.50	5.31	9.08	4.16	7.16	10.50	12.19	12.02	12.96	7.60	9.41	14.26	6.05	18.88	22.99
MgO	3.75	3.01	4.35	5.00	4.62	3.13	4.75	5.53	4.07	3.76	4.44	3.80	4.71	4.59	4.25	3.64	3.21	3.78	3.20
K_2O	7.40	6.84	7.64	8.26	7.52	7.48	6.70	7.50	7.28	7.30	7.68	6.56	5.45	6.07	5.82	4.88	5.50	5.08	3.71
Fe_2O_3	30.19	29.95	24.77	20.94	23.36	29.60	22.90	28.35	25.44	21.00	17.92	18.70	15.09	23.12	24.36	17.78	27.72	11.82	7.30
P_2O_5	n.d.	n.d.	0.47	0.79	n.d.	n.d.	n.d.	0.26	n.d.	n.d.	n.d.	0.31	2.38	n.d.	n.d.	0.18	n.d.	0.74	n.d.
SO_3	n.d.	n.d.	0.72	n.d.	n.d.	n.d.	n.d.	n.d.	n.d.	n.d.	n.d.	1.89	n.d.	n.d.	0.03	0.08	n.d.	n.d.	n.d.
CaO	n.d.	0.08	0.44	0.08	0.51	0.52	0.38	0.26	0.26	n.d.	0.24	0.78	1.18	0.08	0.16	0.41	n.d.	0.63	0.58
TiO_2	0.30	n.d.	0.35	0.06	n.d.	n.d.	n.d.	0.14	0.63	0.05	0.47	n.d.	n.d.	0.09	0.20	0.06	0.39	0.39	n.d.
MnO	0.23	0.20	0.07	0.19	n.d.	0.25	n.d.	n.d.	0.31	n.d.	0.34	n.d.	n.d.	n.d.	n.d.	n.d.	n.d.	0.16	n.d.
Sum	100.00	100.01	99.99	100.01	100.00	99.99	100.00	100.01	100.01	99.99	99.99	100.00	100.00	100.00	100.00	100.00	100.00	100.00	100.00
Morph.	hairy	hairy	hairy	hairy	hairy	hairy	hairy	hairy	hairy	hairy	hairy	flaky	hairy	hairy	hairy	hairy	hairy	hairy	flaky
GGÖ6GL	**1**	**2**	**3**	**4**	**5**	**6**	**7**	**8**	**9**	**10**	**11**	**12**	**13**	**14**	**15**	**16**	**17**	**18**	**19**
Si^{4+}	3.69	3.71	3.76	3.72	3.73	3.71	3.74	3.72	3.74	3.79	3.75	3.75	3.82	3.86	3.72	3.78	3.84	3.72	3.78
Al^{3+}	0.31	0.29	0.24	0.28	0.27	0.29	0.26	0.28	0.26	0.21	0.25	0.25	0.18	0.14	0.28	0.22	0.16	0.28	0.22
T.C.	-0.31	-0.29	-0.24	-0.28	-0.27	-0.29	-0.26	-0.28	-0.26	-0.21	-0.25	-0.25	-0.18	-0.14	-0.28	-0.22	-0.16	-0.28	-0.22
Al^{3+}	0.10	0.19	0.29	0.49	0.40	0.14	0.45	0.05	0.32	0.61	0.70	0.70	0.82	0.46	0.46	0.86	0.32	1.14	1.43
Fe^{3+}	1.39	1.36	1.13	0.94	1.04	1.35	1.01	1.30	1.15	0.92	0.78	0.83	0.66	1.01	1.08	0.76	1.23	0.50	0.29
Fe^{2+}	0.21	0.21	0.17	0.14	0.16	0.21	0.15	0.20	0.17	0.14	0.12	0.13	0.10	0.15	0.16	0.11	0.19	0.08	0.04
Mg^{2+}	0.39	0.31	0.45	0.50	0.46	0.32	0.47	0.57	0.41	0.37	0.44	0.38	0.46	0.45	0.42	0.35	0.32	0.36	0.29
Σ_{OL}	2.09	2.07	2.04	2.07	2.06	2.02	2.08	2.12	2.05	2.04	2.04	2.04	2.04	2.07	2.12	2.08	2.06	2.08	2.05
O.C.	-0.33	-0.31	-0.50	-0.43	-0.44	-0.47	-0.38	-0.41	-0.43	-0.39	-0.44	-0.39	-0.44	-0.39	-0.22	-0.22	-0.33	-0.20	-0.18
Ca^{2+}	0.00	0.01	0.03	0.01	0.04	0.04	0.03	0.02	0.02	0.00	0.02	0.04	0.08	0.01	0.01	0.03	0.00	0.04	0.04
K^+	0.66	0.60	0.67	0.71	0.64	0.66	0.57	0.66	0.63	0.62	0.65	0.56	0.46	0.51	0.49	0.40	0.47	0.41	0.32
I.C.	0.66	0.62	0.73	0.73	0.72	0.74	0.63	0.70	0.67	0.62	0.69	0.64	0.62	0.53	0.51	0.46	0.47	0.49	0.40
Interpret.	GL	GL	GL	GL	GL	GL	GL	GL	GL	GL	GL	GL	GL-S	GL-S	GL-S	GL-S	GL-S	GL-S	I-S

Abbreviations: GL = glauconite, GL-S = glauconite-smectite, I-S = illite-smectite, Mnt = montmorillonite, TC = tetrahedral charge, OC = octahedral charge, IC = interlayer charge.

Table 3.1: Continued.

GGÖ6X2	1	2	3	4	5	6	7	8	9	10	11	12	13	14	15	16	17	18	19	20
SiO_2	59.95	60.90	63.59	61.77	62.52	63.04	61.27	60.48	59.63	64.18	61.19	59.54	61.03	63.44	58.54	65.11	66.20	53.27	54.55	53.37
Al_2O_3	23.12	27.95	21.25	25.19	22.75	24.37	23.94	24.82	24.84	24.27	24.12	25.96	23.53	21.61	23.55	26.62	25.25	35.21	33.96	34.19
MgO	2.79	2.15	3.48	2.73	3.70	2.31	1.56	3.46	2.31	1.86	2.13	4.27	3.00	3.29	3.09	1.84	2.02	0.64	0.42	0.79
K_2O	5.00	4.31	3.55	3.90	4.66	5.17	5.66	4.43	5.75	3.84	6.68	4.96	6.74	4.35	6.87	0.73	0.58	8.69	8.28	8.78
Fe_2O_3	7.88	4.21	7.78	5.47	6.36	4.97	7.26	6.21	7.03	5.60	5.75	5.04	4.97	7.08	7.09	3.12	2.87	2.06	2.53	2.38
P_2O_5	0.65	n.d.	n.d.	0.61	n.d.	n.d.	n.d.	n.d.	n.d.	n.d.	n.d.	n.d.	0.18	n.d.	n.d.	0.23	n.d.	n.d.	0.25	0.18
SO_3	0.07	n.d.	n.d.	n.d.	n.d.	n.d.	n.d.	0.20	0.32	n.d.	n.d.	n.d.	0.56	0.11	n.d.	0.05	n.d.	n.d.	n.d.	0.20
CaO	n.d.	0.27	n.d.	0.23	n.d.	0.14	0.32	n.d.	n.d.	0.25	0.12	n.d.	n.d.	n.d.	0.19	2.31	2.84	n.d.	n.d.	n.d.
TiO_2	0.34	n.d.	0.34	0.10	n.d.	n.d.	n.d.	0.41	n.d.	n.d.	n.d.	0.24	n.d.	0.12	0.43	n.d.	0.23	0.13	n.d.	0.11
MnO	0.19	0.21	n.d.	n.d.	n.d.	n.d.	n.d.	n.d.	0.12	n.d.	n.d.	n.d.	n.d.	n.d.	0.24	n.d.	n.d.	n.d.	n.d.	n.d.
Sum	99.99	100.00	99.99	100.00	99.99	100.00	100.01	100.01	100.00	100.00	99.99	100.01	100.01	100.00	100.00	100.01	99.99	100.00	99.99	100.00
Morph.	flaky	flaky	flaky	flaky	flaky	flaky	flaky	flaky	flaky	flaky	flaky	flaky	flaky	flaky	flaky	platy	platy	platy	platy	platy
GGÖ6X2	**1**	**2**	**3**	**4**	**5**	**6**	**7**	**8**	**9**	**10**	**11**	**12**	**13**	**14**	**15**	**16**	**17**	**18**	**19**	**20**
Si^{4+}	3.73	3.68	3.87	3.74	3.81	3.82	3.76	3.70	3.69	3.86	3.76	3.64	3.77	3.87	3.67	3.84	3.90	3.30	3.38	3.33
Al^{3+}	0.27	0.32	0.13	0.26	0.19	0.18	0.24	0.30	0.31	0.14	0.24	0.36	0.23	0.13	0.33	0.16	0.10	0.70	0.62	0.67
T.C.	-0.27	-0.32	-0.13	-0.26	-0.19	-0.18	-0.24	-0.30	-0.31	-0.14	-0.24	-0.36	-0.23	-0.13	-0.33	-0.16	-0.10	-0.70	-0.62	-0.67
Al^{3+}	1.43	1.67	1.40	1.54	1.44	1.56	1.50	1.49	1.49	1.58	1.51	1.51	1.49	1.42	1.40	1.69	1.66	1.87	1.85	1.84
Fe^{3+}	0.32	0.17	0.31	0.25	0.26	0.20	0.30	0.25	0.29	0.22	0.23	0.20	0.20	0.29	0.29	0.12	0.11	0.08	0.10	0.10
Fe^{2+}	0.05	0.03	0.05	0.03	0.04	0.03	0.04	0.04	0.04	0.03	0.04	0.03	0.03	0.04	0.04	0.02	0.02	0.01	0.02	0.01
Mg^{2+}	0.26	0.19	0.32	0.25	0.34	0.21	0.14	0.32	0.21	0.17	0.20	0.39	0.28	0.30	0.29	0.16	0.18	0.06	0.04	0.07
Σ_{OL}	2.06	2.06	2.08	2.07	2.08	2.00	1.98	2.10	2.03	2.00	1.98	2.13	2.00	2.05	2.02	1.99	1.97	2.02	2.01	2.02
O.C.	-0.13	-0.04	-0.13	-0.07	-0.14	-0.24	-0.24	-0.06	-0.16	-0.20	-0.30	-0.03	-0.31	-0.19	-0.27	-0.21	-0.29	-0.01	-0.03	-0.02
Ca^{2+}	0.00	0.02	0.00	0.01	0.00	0.01	0.02	0.00	0.00	0.02	0.01	0.00	0.00	0.00	0.01	0.16	0.18	0.00	0.00	0.00
K^+	0.40	0.32	0.28	0.30	0.36	0.40	0.44	0.35	0.45	0.29	0.52	0.39	0.53	0.34	0.55	0.05	0.04	0.69	0.65	0.70
I.C.	0.40	0.36	0.28	0.32	0.36	0.42	0.48	0.35	0.45	0.33	0.54	0.39	0.53	0.34	0.57	0.37	0.40	0.69	0.65	0.70
Interpret.	I-S	I-S	I-S	I-S	I-S	I-S	I-S	I-S	I-S	I-S	I-S	I-S	I-S	I-S	I-S	Mnt	Mnt	Illite	Illite	Illite

Abbreviations: GL = glauconite, GL-S = glauconite-smectite, I-S = illite-smectite, Mnt = montmorillonite, TC = tetrahedral charge, OC = octahedral charge, IC = interlayer charge.

Table 3.2: Averaged geochemical compositions (wt.%) and structural formulae for glauconite-smectite (GL-S) glauconite (GL), illite-smectite (I-S), Fe-poor illite, and montmorillonite (Mnt) based on TEM-EDX (*m* = number of EDX analyses). The Fe^{2+}/Fe^{3+} ratio was assumed to be 0.15.

Sample	**GGÖ5GL**	**GGÖ5GL**	**GGÖ6GL**	**GGÖ6GL**	**GGÖ6X2**	**GGÖ6X2**	**GGÖ6X2**
SiO_2	58.14	61.14	55.29	62.22	60.82	65.48	53.60
Al_2O_3	9.62	20.63	9.06	22.99	23.86	25.87	34.37
MgO	4.16	3.72	4.08	3.20	2.78	1.92	0.62
K_2O	5.75	4.97	6.64	3.71	5.01	0.65	8.56
Fe_2O_3	19.85	8.76	22.66	7.30	6.12	2.99	2.32
P_2O_5	0.99	0.00	0.72	0.00	0.48	0.23	0.21
SO_3	0.91	0.40	0.67	0.00	0.25	0.05	0.20
CaO	0.29	0.31	0.40	0.58	0.22	2.57	0.00
TiO_2	0.10	0.06	0.26	0.00	0.28	0.23	0.12
MnO	0.19	0.00	0.22	0.00	0.19	0.00	0.00
Sum	100.00	100.00	100.00	100.00	100.00	100.00	100.00
m	11	3	18	1	15	2	3
Si^{4+}	3.87	3.79	3.75	3.78	3.76	3.87	3.33
Al^{3+}	0.13	0.21	0.25	0.22	0.24	0.13	0.67
T.C.	-0.13	-0.21	-0.25	-0.22	-0.24	-0.13	-0.67
Al^{3+}	0.63	1.30	0.48	1.43	1.49	1.68	1.85
Fe^{3+}	0.88	0.36	1.02	0.29	0.25	0.12	0.1
Fe^{2+}	0.13	0.05	0.15	0.04	0.04	0.02	0.01
Mg^{2+}	0.41	0.34	0.41	0.29	0.26	0.17	0.06
Σ_{OL}	2.05	2.05	2.06	2.05	2.04	1.99	2.02
O.C.	-0.39	-0.24	-0.38	-0.18	-0.18	-0.22	-0.01
Ca^{2+}	0.02	0.02	0.03	0.04	0.01	0.16	0
K^+	0.49	0.39	0.57	0.29	0.39	0.05	0.68
I.C.	0.53	0.43	0.63	0.37	0.41	0.37	0.68
Interpret.	**GL-S**	**I-S**	**GL**	**I-S**	**I-S**	**Mnt**	**Illite**

Abbreviations: TC = tetrahedral charge, OC = octahedral charge, IC = interlayer charge.

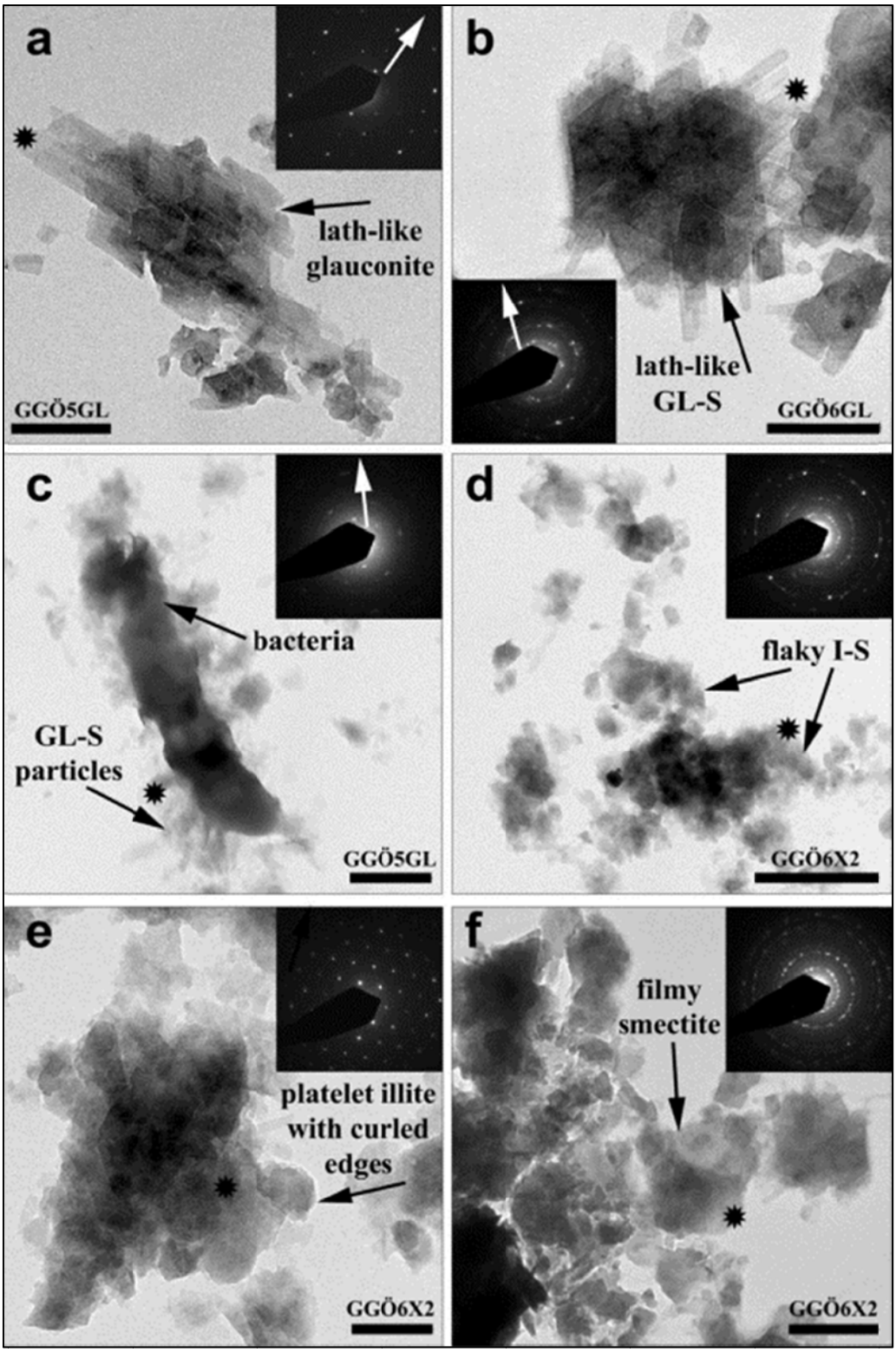

Fig. 3.6: TEM micrographs and SAED patterns of individual clay particles from GGÖ5GL (a, c), GGÖ6GL (b), and GGÖ6X2 (d, f). Authigenic, lath-like glauconite with 1M polytype (a, seldom). Lath-like glauconite-smectite (GL-S) with $1M_d$ polytype (b, often). Contact between bacteria and disordered glauconite-smectite particles (c). Flake-shaped I-S with $1M_d$ polytype indicative of an authigenic origin (d). Platelet, Fe-poor illite with curled edges and $2M_1$ polytype related to the detrital nature (e). Filmy, detrital montmorillonite with $1M_d$ polytype (f). The black stars show the location of the SAED spots; the white arrows within the SAED patterns mark the direction of the clay`s b axis. Scale bar: 200 nm.

All clay mineral phases plot well in the domain of dioctahedral clays (after Weaver & Pollard, 1973), but the Fe-poor $2M_1$-illites have the highest interlayer (0.65-0.70) and tetrahedral charges (-0.62 to -0.70). I-S has either moderate tetrahedral (-0.13 to -0.36) and octahedral charges (-0.03 to -0.31), but significantly lower interlayer charges (0.28-0.57) with K^+ predominantly occupying the interlayer sites. Montmorillonite charge distributions are close to that of I-S but have a slightly lower interlayer charge (0.37-0.40) with Ca^{2+} in the interlayer sites among less K^+. The glauconite-smectite of GGÖ5GL shows low tetrahedral (-0.07 to -0.20), high octahedral (-0.18 to -0.58) and moderate interlayer charges (0.37-0.64), whereas the pure glauconites from GGÖ6GL have moderate tetrahedral (-0.14 to -0.31), high octahedral (-0.20 to -0.50) and higher interlayer charges (0.40-0.71), related to an increased stage of glauconitization.
The geochemical and mineralogical characteristics of the glauconitized fecal pellets, I-S, and detrital, Fe-poor illite agree well with the XRD polytype analyses and Sybilla© modeling.

3.5.4 Geochemistry and stable isotope signatures of calcite and dolomite

The major and trace element compositions, the $d^{18}O$ and $d^{13}C$ stable isotope signatures and the calcite-dolomite ratios of six samples are presented in Table 3.3. Atomic Ca:Mg ratios range from 1:1 for stoichiometric dolomite (97±3 wt.% dolomite in GGÖ5-2) to 41:1 for the almost pure calcite (94±3 wt.% calcite in GGÖ5-1) with some calcite-dolomite mixtures that have been quantified using the linear equation of Weber & Smith (1961).
The calcite-dominated samples contain 200-300 ppm of Na, 300-500 ppm of Sr, 3500-3700 ppm of Mg, and minor amounts of Fe (200-400 ppm) and Mn (100-300 ppm). Isotope signatures for calcite range from -2 to -3‰ $\delta^{18}O$ and -1 to +1.5‰ $\delta^{13}C$, respectively. Both observations suggest direct precipitation of calcite from Jurassic seawater under oxygenated conditions (Price & Sellwood, 1994). In contrast, the dolomites contain only traces of Na (100-200 ppm) and Sr (20-80 ppm), but moderate Fe (4500-11000 ppm) and low Mn (100-150 ppm) contents, indicating that dolomite formation has occurred in a suboxic environment. Isotopic compositions range from +1.5 to +2‰ $\delta^{18}O$ and 0 to +0.5‰ $\delta^{13}C$, similar to recent sabkha dolomites (0 to +4‰ $\delta^{18}O$; +1.5 to +4‰ $\delta^{13}C$; McKenzie, 1981; Warren, 2000) or Jurassic tidal flat dolomites formed in semi-arid, lagoonal conditions (Rameil, 2008; Husenic & Read; 2010), hence suggesting an early diagenetic origin.
Assuming an equilibrium fraction coefficient between calcite and dolomite of 3‰, a value that is widely accepted, the $\Delta\ \delta^{18}O_{Dol\text{-}Cal}$ signature of 4-5‰ (> 3‰) implies that the dolomite precipitated from an evaporitic brine (Rameil, 2008). The lower $\delta^{13}C$ values of the Jurassic dolomites might be caused by precipitation from (i) mixed fresh water-seawater masses, (ii)

slightly modified seawater composition due to primary calcite precipitation, or (iii) oxidation of isotopically light organic matter related to early diagenesis (*e.g.* Reitsema, 1980).

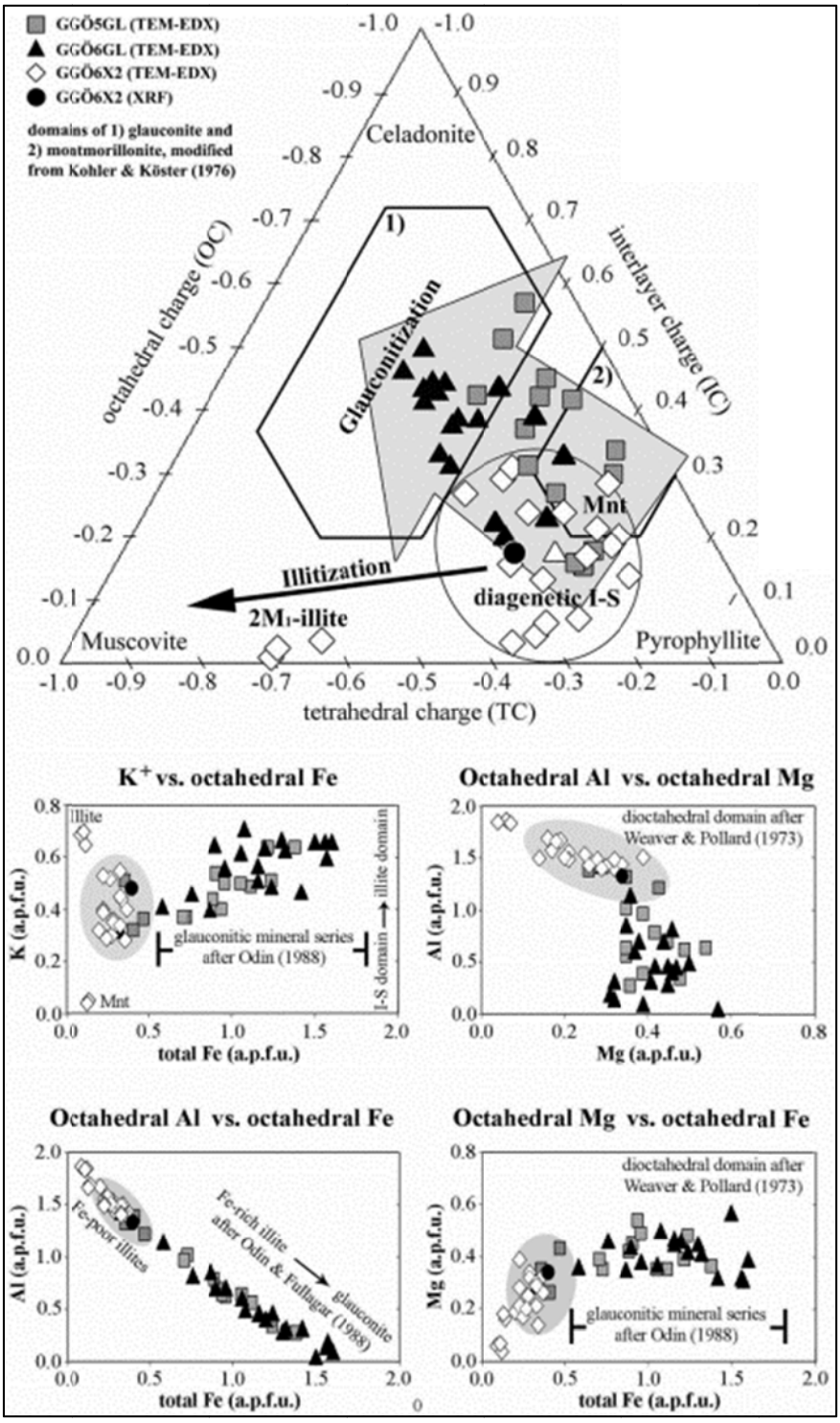

Fig. 3.7: On the top: Charge distribution diagram with the domains of glauconite and montmorillonite. The grey arrow shows the glauconite-smectite to glauconite reaction related to increased glauconitization. I-S plot in the field of authigenic I-S formed during burial diagenesis. Fe-poor, $2M_1$-illite and montmorillonite (Mnt) are detrital clays. Below: interlayer and octahedral substitutions for the authigenic and detrital clays. Symbols are larger than the analytical error.

Table 3.3: Major and trace element compositions, stable isotopes, and calcite-dolomite ratios quantified using the linear equation of Weber & Smith (1961). The Fe content (Fe_{Carb}) of the carbonates was recalculated by subtraction of Fe bound in pyrite. Isotope values and element compositions of calcite-dolomite mixtures were interpreted after proportional division assuming that GGÖ5-2 consists of almost pure dolomite. The unusually low Mg and Fe values of GGÖ8 are due to contamination during sample preparation. Therefore, data from GGÖ8 are not discussed, here.

Sample	Method	Ca	Mg	Ca/Mg	Fe	S	Fe_{Carb}	Mn	Na	Sr	Al	$\delta^{18}O$	$\delta^{13}C$	Dol	Cc
		%	%	atomic	%	%	ppm	ppm	ppm	ppm	ppm	‰PDB	‰PDB	%	%
GGÖ3-1	ICP-OES	22.83	6.24	2	1.08	0.71	4225	328	345	205	887	-0.8	-0.3	75±3	25±3
GGÖ3-2	ICP-OES	4.65	1.85	2	2.56	1.50	11578	123	170	51	2668	1.7	0.2	92±3	8±3
GGÖ5-1	ICP-OES	35.97	0.53	41	0.27	0.23	547	225	278	381	413	-2.3	-0.9	6±3	6±3
GGÖ5-2	ICP-OES	6.69	3.05	1	2.21	1.94	4523	136	190	83	1740	1.9	0.4	97±3	3±3
GGÖ6	ICP-OES	39.00	0.67	36	0.18	0.10	772	200	288	442	363	-2.9	1.4	10±3	90±3
GGÖ8	ICP-OES	7.08	0.34	13	2.77	3.47	-3530	150	213	300	2709	-3.4	-2.5	18±3	82±3
Sample	Method	CaO	MgO	Ca/Mg	Fe_2O_3	TiO_2	MnO	Na_2O	Sr	Al_2O_3	SiO_2	K_2O	P_2O_5	LOI	Sum
		wt.%	wt.%	atomic	wt.%	wt.%	wt.%	wt.%	wt.%	wt.%	wt.%	wt.%	wt.%	wt.%	wt.%
GGÖ6X2	XRF	1.68	3.05	0.3	6.95	0.69	0.01	0.13	0.12	18.48	48.93	4.97	0.36	13.55	98.80

3.6 Discussion

Recent studies have significantly improved the understanding of formation conditions, growth rates and mineralogy of glauconite. The role of mineral dissolution reactions linked to early diagenesis and related changes in physicochemical conditions in the micromilieu where glauconitization occurs, however, are still poorly constrained. In this section, we focus on the process of glauconite formation in fecal pellets and discuss the specific micro-environment, precursor phases, thermodynamics, temperature range and kinetics of the glauconitization reaction resulting in a model for glauconitization in fecal pellets.

3.6.1 Micromilieu of glauconitization

Glauconitization at Oker has occurred predominantly in fecal pellets. This special micro-environment provides the post-depositional conditions favorable for glauconite formation. Physicochemical reactions within this micromilieu are controlled by the oxidation of organic matter, silicate dissolutions, the recrystallization of high magnesium calcite (HMC) and aragonite, Fe redox reactions and interactions with seawater-pore water fluids.

Organic matter rapidly oxidizes after deposition of the fecal pellets resulting in local reducing and slightly acidic (pH about 5-6; MacKenzie, 2005) conditions. Both conditions enhance the dissolution of minerals incorporated in the fecal pellets and the surrounding sediment, such as

biogenic and matrix calcite, K-feldspar, quartz, detrital clay minerals and iron oxides, as our petrographic observations show (see Figs 3.2 and 3.3). Pyrite precipitation also occurs in this environment. However, silicate mineral dissolution releases Al^{3+}, Si^{4+}, Mg^{2+}, K^{+}, Fe^{2+}, ion complexes and amorphous gels (*e.g.* Hower, 1961) in the micromilieu, providing the essential cations for the precipitation of glauconite precursor phases (see below). Seawater and interstitial water masses provide additional cations such as K^{+}, Mg^{2+}, Ca^{2+} and Na^{+} as well as the sulfur anions needed for pyrite formation (Schulz & Zabel, 2006). Recrystallization of diagenetic unstable HMC into low magnesium calcite (LMC) also provides Mg^{2+} ions to the micromilieu, besides buffering the pH to about 7-8 (close to seawater pH) such as through aragonite dissolution (Tucker & Wright, 1990). Slightly alkaline pH conditions were found to be favorable for the precipitation of Fe-Mg-smectites and glauconite-smectite as demonstrated by the low-temperature synthesis experiments of *e.g.* Harder (1980) and thermodynamic modeling of *e.g.* Charpentier *et al.* (2011) and Chermak & Rimstidt (1989).

The concentration and activity of seawater K^{+} also has strong influence on the formation of glauconite on a global scale. Hardie (1996) predicted significant variations in the seawater K^{+} concentration, proposing that the seawater composition changed with both varying rates in seawater cycling through mid-ocean ridges and the magnitude of evaporate deposits. From the Cambrian to Silurian and Cretaceous to Miocene, for example, the estimated seawater K^{+} concentration was about 3-4 times higher compared with current seawater, whereas the proposed seawater K^{+} concentration was significantly lower (~400 ppm) from the Devonian to Triassic time period. Interestingly, the formation of most of the world's largest glauconite deposits occurred in intervals with elevated seawater K^{+} concentration, for example, in the Early Cambrian and Cretaceous (*e.g.* greensand deposits of New Jersey and Western Australia), whereas glauconite formation was inhibited in intervals with moderate to low seawater K^{+} concentration and restricted to more local environments. Certainly, Hardie's (1996) model greatly simplifies the effects on global seawater K^{+} cycling because the effect of spreading rates on seawater composition is more modest (Holland *et al.*, 1996; Horita *et al.*, 2002), but it is likely that there is a correlation between K^{+} in the oceans and global glauconitization events.

Iron plays another key role in the formation of glauconite and its precursor phases, but most of the Fe species in aquatic systems are primarily bound in Fe-(oxy)hydrates (Raiswell, 2011). Giresse & Wiewióra (2001) have shown that detrital amorphous Fe-oxides are by far the most effective Fe supplier at the Ivory Basin-Ghana Marginal Ridge, where glauconitic clays forms recently. On the contrary, Gaudin *et al.* (2005) and Charpentier *et al.* (2011) suggest that oxidation of pyrite provides the Fe needed for the glauconitization process. Our data support the

concept of Giresse & Wiewióra (2001), because glauconite formation occurred under suboxic conditions where framboidal pyrite is stable, but not the Fe-oxides. As soon as the Eh conditions within the fecal pellets micromilieu shift to low Eh values and thus anoxic conditions, the glauconitization process stops and euhedral pyrite forms, as our petrographic observations show (Figs 3.1 to 3.3). In addition, we found no evidence of sulfate minerals in the samples that are byproducts of pyrite oxidation. Hence, sulfide mineral precipitation generally competes with glauconite formation by removal of available pore water Fe^{2+} released during the reduction of Fe-(oxy)hydrates (Schulz & Zabel, 2006; Raiswell, 2011).

3.6.2 Precursor phases of glauconite and glauconitization process

As reported in the literature, precursor phases of glauconite range from detrital clays such as degraded mica, I-S, chlorite, or vermiculite to authigenic clays such as berthierine (a Fe-rich kaolinite), nontronite, and Fe-Mg-smectite depending on the depositional environment and the age of glauconitization (*e.g.* Odin, 1988; Buatier *et al.*, 1989). Recent studies on authigenic green clay minerals formed in a deep-sea environment of the Costa Rica Margin (*e.g.* Gaudin *et al.*, 2005) and of partly glauconitized fecal pellets deposited at the Mediterranean shallow shelf (*e.g.* Giresse *et al.*, 2004) suggest the predominance of neo-formed Fe-Mg-smectites and glauconite-smectite (~20% Fe-illite layers and ~80% Fe-smectite layers) in less glauconitized fecal pellets of Pleistocene to Holocene age. With increased stage of early diagenesis, most of the initial light green fecal pellets become dark green in color, while changing from Fe-Mg-smectite into glauconite composition via the formation of glauconite-smectite mixed-layered clays (*e.g.* Giresse et al., 2001). At Oker, Fe-smectite precursors were not observed. The presence of plenty, highly disordered glauconite-smectite particles (Fig. 3.6) in the fecal pellets (4.6-7.5 wt.% K_2O and 0.4-0.6 K^+ a.p.f.u., respectively), however, implies that glauconite formation by alteration of Fe-Mg-smectites or Fe-smectite-rich precursors might have occurred during the maturing of the fecal pellets related to increased glauconitization. The high proportion of Fe-illite layers in the separated, glauconitized pellets (~90-95% Fe-illite layers and ~5-10% Fe-smectite layers; see Fig. 3.4) suggest that the glauconitization process is almost complete and most of the precursor phases are already replaced by glauconite.

A further approach for characterization of the glauconitization process is the thermodynamic one. Using the Chermak & Rimstidt (1989) method of polyhedral substitutions to estimate thermodynamic properties of the Al-smectite to Al-illite reaction (*e.g.* illitization related to burial diagenesis) and the Fe-Mg-smectite to glauconite reaction (glauconitization reaction related to early diagenesis), the substitution of dioctahedral Al^{3+} for Fe^{3+} and Mg^{2+} moves the

stability field of glauconite and Fe-Mg smectite to much lower silica activities, from 10^{-2} to 10^{-3}. Fe-Mg-smectites, therefore, typically form in marine sediments when the silica activity is lower than 10^{-3} close to the saturation of opal-A. In addition, this model postulates that the geochemical composition of the Fe-Mg-smectite octahedral sheet, more precisely the extent of Fe^{2+}/Mg^{2+} substitution for Al^{3+}, is also very important for glauconitization. A higher proportion of Mg^{2+} and Fe^{2+} in the smectite octahedral sheet is associated with a higher octahedral charge, which is balanced by increased K^{+} fixation into the interlayer sites as our TEM-EDX data show (see Fig. 3.7). In this context, the glauconitization process of fecal pellets of marine origin is likely to be supported by bacterial activity present in the micro-environment (Fig. 3.6-c). Bacterial-induced Fe^{3+} reduction in nontronite, for example, greatly modifies the chemical composition of the octahedral sheet besides leading to significant changes in layer charge, which perhaps favors the formation of discrete illite layers (*e.g.* Jaisi *et al.*, 2001).

The neo-formation of Fe-Mg-smectites or glauconite-smectite, hence, is likely to have been the first step of an overall glauconitization process of fecal pellets at Oker. During early diagenesis, these smectite-rich clays grow into the open pore space within the highly porous fecal pellets, while (i) successively replacing the matrix calcite in a suboxic environment (see Fig. 3.1-3) and (ii) continuously changing into flaky glauconite-smectite and finally into lath-like, highly evolved (ordered) glauconite as our TEM observation indicate (Fig. 3.6). During this mineral conversion reaction, both octahedral (Mg^{2+}/Fe^{2+} for Al^{3+} substitutions) and tetrahedral (Al^{3+} for Si^{4+} substitutions) charges increase steadily leading to increasing charge deficiencies. This negative charge is balanced by the progressive fixation of K^{+} in the interlayer sites. Thus, the proportion of Fe-smectite layers decreases, while Fe-illite layers form, as our TEM-EDX data suggests (see Fig. 3.7 and Tables 3.1 and 3.2).

In summary, glauconitization at Oker is a two-step process (Fig. 3.8). First, Fe-Mg-smectites or glauconite-smectite precursors precipitate in the exterior of the fecal pellets followed by an early diagenetic alteration into glauconite as was shown by comparison of immature fecal pellets from GGÖ5GL and moderately mature ones from GGÖ6GL. With increasing stages of glauconitization, a continuous evolution from initially diffuse or honeycomb-arranged, light green clay microstructures to highly ordered, dark green rosette structures occurs resulting in (i) an increased packing density of the glauconite microstructures and (ii) a variety of mineral dissolutions and replacement reactions related to early diagenesis (see above). The key factors in the low-temperature Fe-Mg-smectite to Fe-illite process of glauconitization seem to be time ($> 10^4$ years), cation availability, and the preservation of the specific, semi-confined micro-environment during early diagenesis.

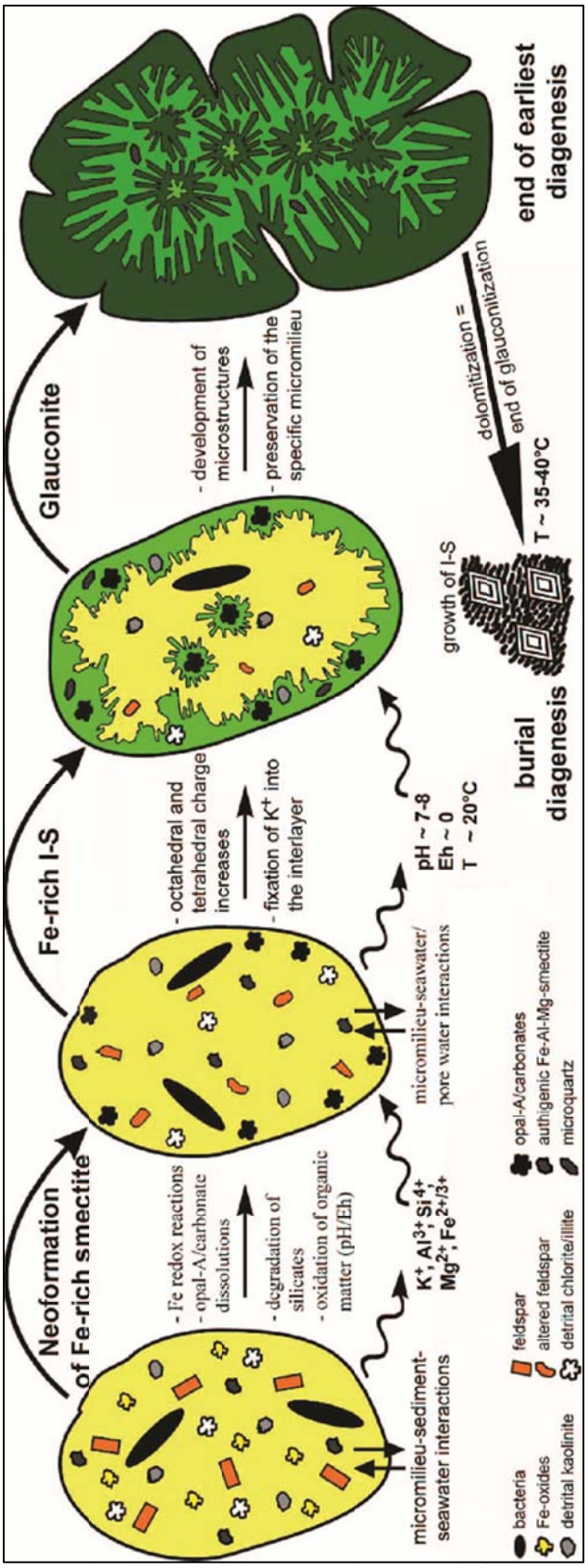

Fig. 3.8: Model for glauconitization in fecal pellets. Neo-formed, flaky Fe-Mg-smectites alter continuously into lath-like glauconite via the formation of glauconite-smectite mixed-layered clay minerals within an organic-rich, semi-confined micromilieu generated during early diagenesis. Cations, needed for the glauconitization process, are provided by silicate and carbonate dissolutions, Fe redox reactions, and seawater/pore water interactions.

3.6.3 Development of glauconite polytypes

Mineralogically, nascent glauconite-smectite with ~20-80% Fe-illite layers and ~20-80% Fe-smectite layers (R0 to R1 ordered) is predominantly of the $1M_d$ polytype, while glauconite with ~90-95% Fe-illite layers and 5-10% Fe-smectite layers (R3 ordered) consist mostly of the 1M with minor proportions of the $1M_d$ polytype (*e.g.* Odom, 1976; Odin & Matter, 1981). Interestingly, the glauconites from Oker mainly have a $1M_d$ structure as our polytype determinations reveal (see Fig. 3.5), but > 90% Fe-illite layers (R3).

A rapid transformation of the smectitic precursor phases into glauconite via the formation of disordered glauconite-smectite (Fig. 3.6-b and 3.6-c) in an unstable micro-environment might explain this behavior, for example, changes in cation availability or facies changes. Both the heterogeneity and the highly disordered structure of the glauconites, however, are indicative of the authigenic origin of glauconites formed under low-temperature conditions (*e.g.* Giresse *et al.*, 2004).

3.6.4 Temperature of glauconitization

Both the depositional environment and the formation temperature of the glauconite from Oker were estimated using carbonate signatures (Table 3.3). Petrographic observations (Figs 3.1 to 3.3) indicate that the glauconitization process started soon after precipitation of the micritic calcite and ended with the formation of matrix-replacive dolomite and I-S. According to these observations, the following sequence of early diagenetic mineral growth has been recognized: calcite – glauconite – dolomite.

However, carbonates often do not preserve their original isotope and geochemical signatures of formation due to (i) exposure to meteoric water masses and/or hydrothermal fluids (Price & Sellwood, 1994), (ii) fractionation effects caused by co-precipitation of $CaCO_3$-$CaMg(CO_3)_2$ (Rameil, 2008), and (iii) burial (*e.g.* Colombié *et al.*, 2011). Paleo-environmental reconstructtions and temperatures based on carbonates, thus, have to be interpreted carefully. A cross-plot of $\delta^{18}O$ and $\delta^{13}C$ (Fig. 3.9) shows that all samples plot well within the domains of unaltered Upper Jurassic platform calcites and unaltered Upper Jurassic dolomites, respectively, indicating preservation of the original isotope and chemical signatures. Furthermore, calcite isotope signatures are similar to those of unaltered Croatian and Swiss Jura platform carbonates (-4 to 0‰ $\delta^{18}O$; -2 to +3‰ $\delta^{13}C$, Husinec & Read, 2010; Colombié *et al.*, 2011), but strongly differ from Fe- and Mn-rich, but Na- and Sr-depleted calcite (-5 to -12‰ $\delta^{18}O$; -3 to +3‰ $\delta^{13}C$) formed at the elevated temperature during burial diagenesis *(e.g.* Reinhold, 1998; Nollet *et al.*, 2005). Deeply buried dolomites of late diagenetic origin formed at high tempera-

ture commonly have $\delta^{18}O$ values between -2 to -7‰ and $\delta^{13}C$ values between +1 to +4‰ (*e.g.* Reinhold, 1998), whereas matrix-replacive, tidal-flat and/or sabkha dolomites are isotopically heavier (+1 to +4‰ $\delta^{18}O$; Reinhold, 1998; Husinec & Read, 2010). Temperature estimations on calcite and dolomite samples from Oker, hence, should reflect the formation temperatures soon after deposition.

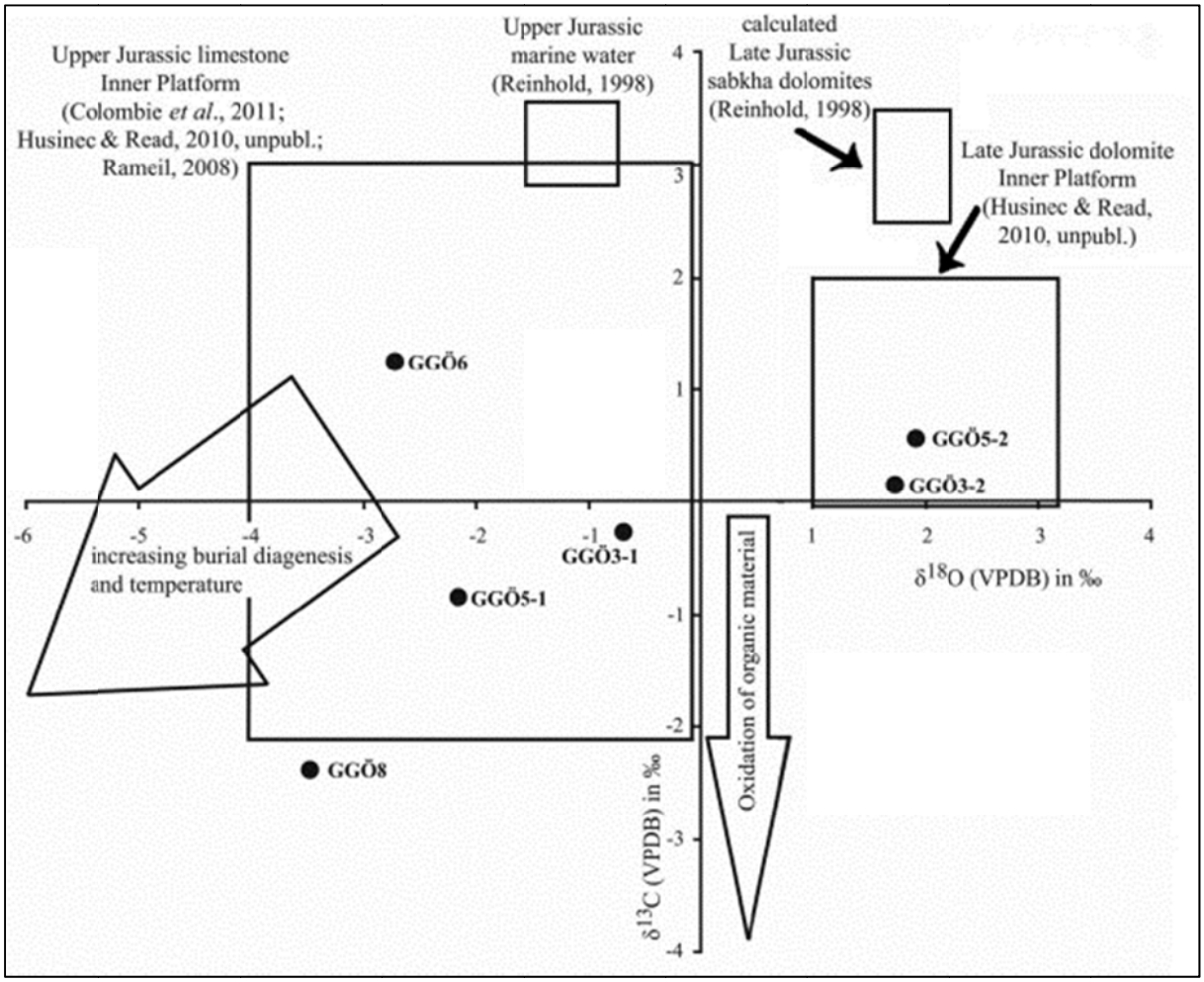

Fig. 3.9: $\delta^{18}O/\delta^{13}C$ cross-plot. Calcite sub-samples (GGÖ3-1, GGÖ5-1, and GGÖ6) plot within the domain of unaltered Upper Jurassic platform carbonates (matrix calcite). Dolomite sub-samples (GGÖ3-2 and GGÖ5-2) fall within the field of unaltered Upper Jurassic platform dolomites and sabkha dolomites.

Calcite temperatures were calculated based on the equation of Epstein *et al.* (1953) and Craig (1965) modified by Anderson & Arthur (1983). Equation 3.1 expresses the oxygen isotopic composition of the water (δ_W) from which the calcite has been precipitated relative to the international SMOW (Standard Mean Ocean Water) standard:

$$T\,(°C) = 16.0 - 4.14 \cdot (\delta_C - \delta_W) + 0.13 \cdot (\delta_C - \delta_W)^2 \qquad (3.1),$$

where δ_C equals the calcite oxygen isotope composition, relative to PDB. According to *e.g.* Price & Sellwood (1994), it has been assumed that the Upper Jurassic seawater was free from ice caps and would have been isotopically lighter (-1‰ $\delta^{18}O$, SMOW) then the recent ocean. Using this approach and a δ_C of -2 to -3‰ $\delta^{18}O$, PDB, (see Table 3.3), the micritic calcite was formed at 19.4±23.9ºC. Formation temperatures of calcite from the Kimmeridgian-Tithonian of Mallorca, for example, range between 21.1±22.5ºC (Price & Sellwood, 1994). Paleo-temperatures for dolomite were calculated using -1‰ $\delta^{18}O$ (SMOW) seawater composition and the equation 3.2 of Friedman & O'Neil (1977):

$$\delta_{Dol} - \delta_W = 3.20 \cdot (10^6 \cdot T^{-2}) - 1.50 \quad (3.2),$$

where δ_{Dol} equals the dolomite oxygen isotope signature against the PDB standard (Reinhold, 1998). Using a δ_{Dol} from +1.5‰ to 2.0‰ $\delta^{18}O$, PDB (Table 3.3), the dolomite formation temperatures range from 35.2±38.6ºC, similar to the matrix-replacive tidal flat dolomites formed in sabkha environments (Reinhold, 1998). Based on the above calcite – glauconite – dolomite growth sequence, glauconite formation at Oker occurred soon after matrix calcite precipitation in a suboxic, marine-lagoonal environment at 22±3ºC, but ended at 37±2ºC with the beginning of dolomite and I-S formation.

3.6.5 Kinetics of glauconitization and burial diagenesis smectite illitization

The diagenetic conditions and timing of both glauconite and I-S formation can be calculated using kinetic modeling. Based on our XRD data (Figs 3.4 and 3.5), I-S has ~65% Al-illite layers and ~35% Al-smectite layers (R1), whereas the glauconites have ~95% Fe-illite layers and ~5% Fe-smectite layers (R3). Both of these authigenic clay minerals have seen the same burial history that started with 2 km of burial (geothermal gradient: 27ºC/km, T_{max} = 75ºC) at 154-86 Ma, followed by quick uplift to ~500 m between 86-82 Ma (30ºC), isothermal at 82-55 Ma (30ºC) with the final uplift and erosion between 55-0 Ma (20ºC; *e.g.* Voigt *et al.*, 2004; Mazur & Scheck-Wenderoth, 2005). For the kinetic calculations using the Pytte & Reynolds (1988) model, we determined the maximum amount of illitization by simplifying the thermal history to a two-stage kinetic model: (1) burial between 154-86 Ma (T_{max} = 75ºC) and (2) isothermal conditions between 86-0 Ma (T = 30ºC). Kinetic modeling was preformed using (i) the kinetic parameters summarized in Elliott & Matisoff (1996), (ii) equilibrium conditions between K-feldspar and albite at the given temperature (Pytte & Reynolds, 1988), and (iii) initial K/Na ratios ranging from ~0.03 (seawater composition; Turekian, 1968) to ~0.1 (pore water fluids; *e.g.* Hanor, 1994).

The calculations resulted in 47-73% Al-illite layers and 27-53% Al-smectite layers for the I-S with an average of 60% Al-illite layers and 40% Al-smectite, respectively. Hence, the I-S can have formed solely by slow burial diagenesis, in contrast to the glauconites that formed during earliest diagenesis close to the seafloor. This suggests significant faster reaction kinetics for the glauconitization reaction, compared with smectite illitization related to burial diagenesis. The thermodynamic instability of the glauconite precursor phases during the earliest states of diagenesis might explain the higher reaction rates of the glauconitization process. Thermodynamic modeling of Charpentier *et al.* (2011) suggests that glauconite precursors form in equilibrium with the physicochemical conditions provided by the micromilieu such as in fecal pellets. Local changes within the micro-environment, for example, microbial activity, Fe redox reactions, silicate and carbonate dissolutions, or cation exchange reactions with the surrounding pore water fluids, would lead to dis-equilibrium conditions where Fe-smectite precursors become unstable and alter quickly into glauconite via the formation of glauconite-smectite mixed-layered clay minerals (Meunieu & El Albani, 2007; Gaudin *et al.*, 2004). In contrast, it seems that glauconite or glauconite-smectite is relatively stable through burial diagenesis, because the question arises as to why the glauconites are not altered into I-S or Al-illite. The reason for the resistance of the glauconites to alteration during burial may be due to (i) its high thermal stability (*e.g.* Strickler & Ferrell, 1990; Guimaraes *et al.*, 2000), (ii) the persistence of an impermeable corona composed of undigested organic matter or diagenetic apatite (*e.g.* Odom, 1976; Strickler & Ferrell, 1990; Baldermann, 2010), and/or (iii) the evolution of dense and impermeable microstructures formed during glauconite maturation (Stille & Clauer, 1994). The latter theories imply a dramatic loss of microporosity and permeability in the glauconite granules, thereby reducing the contact with surrounding diagenetic pore fluids.

3.7 Summary and conclusions

Glauconitized fecal pellets from carbonaceous rocks of Upper Jurassic age (Kimmeridgian) from Oker (Central Germany) were investigated mineralogically and chemically to determine the micro-environment, process, temperature, thermodynamics, and kinetics of the glauconitization reaction in a shallow marine-lagoonal environment. We conclude that:

(1) Glauconitization in fecal pellets is controlled by the presence of a semi-confined micro-environment, which provides the post-depositional, physicochemical conditions ideal for the formation of glauconite. Within this micromilieu, rapid oxidation of (marine) organic matter occurs soon after sediment deposition providing the Eh and pH conditions for silicate dissolu-

tions such as K-feldspar, quartz, and detrital clay minerals, Fe redox reactions, recrystallization of HMC, aragonite dissolutions, and pyrite formation as observed by XRD and SEM analyses. These conditions promote cation exchange reactions with the surrounding seawater and pore water fluids, which provide additional ions needed for the glauconitization process.

(2) An early diagenetic sequence of mineral growth of matrix calcite – glauconite – pyrite – matrix-replacive dolomite and I-S was recognized from our petrographic observations. The temperature range for the glauconitization reaction, based on carbonate stable isotope data, is 22±3ºC to 37±2ºC at maximum.

(3) The glauconite fecal pellets consist mostly of the $1M_d$ with minor proportions of the 1M polytype (93-94% Fe-illite layers and 6-7% Fe-smectite layers, R3), whereas the I-S formed during slow burial diagenesis has a $1M_d$ cis-vacant structure (66-68% Al-illite and 32-34% Al-smectite layers, R1). Detrital clays are Fe-poor, $2M_1$-illite and montmorillonite identified by XRD and TEM-EDX-SAED analyses on the < 2 μm size fractions.

(4) Kinetic modeling, using the Pytte & Reynolds (1988) model, results in 60-15% Al-illite layers and 40-15% Al-smectite layers in I-S, largely depending on the initial K^+ concentration and burial history, implying that the I-S was formed solely by slow burial diagenesis, in contrast to the glauconites formed during early diagenesis close to the seafloor.

(5) Using the thermodynamic approach of Charpentier *et al.* (2001), glauconitization in fecal pellets can be described as a two-step process: neo-formed, diagenetically unstable Fe-Mg-smectites alter rapidly into glauconite via the formation of glauconite-smectite mixed-layered clay minerals as observed by TEM study.

Chapter 4

The rate and mechanism of deep-sea glauconite formation at the Ivory Coast - Ghana Marginal Ridge

4.1 Abstract

The environmental conditions and reaction paths of shallow-water glauconitization (< 500 m water depth, ~15ºC) close to the sediment-seawater interface are generally considered to be well understood. In contrast, the key factors controlling deep-sea glauconite formation are still poorly constrained. In the present study, green grains formed in the recent deep-sea environment of the ODP Site 959, Ivory Coast – Ghana Marginal Ridge, (~2100 m water depth, 3-6ºC) were investigated by X-ray diffraction and electron microscopic methods in order to determine the rate and mechanism of glauconitization.

Green-clay authigenesis at Hole 959C occurred mainly in the tests of calcareous foraminifera which provided post-depositional conditions ideal for glauconitization. Within this organic-rich micro-environment, Fe-smectite developed < 10 ky after deposition of the sediments by precipitation from precursor gels containing Fe, Mg, Al, and silica. This gel formation was supported by microbial activity and cation supply from the interstitial solution by diffusion. At a later stage of early marine diagenesis (900 ky), the Fe-smectites reacted to form mixed-layered glauconite-smectite. Further down (~2500 ky), almost pure glauconite with no compositional gaps between the Fe-smectite and glauconite end members formed. This burial-related Fe-smectite-to-glauconite reaction indicates that the glauconitization process was controlled mainly by the chemistry of the interstitial solutions. The composition of the interstitial solution depends heavily on micro-environmental changes related to early diagenetic oxidation of biodegradable (marine) organic matter, microbial sulfate reduction, silicate alteration, carbonate dissolution, and Fe redox reactions. The availability of Fe is suggested as the proba-

ble limiting factor for glauconitization, explaining the various states of green-grain maturity within the samples, and this cation may be the most important rate-determining element.
The rate of glauconite formation at ODP Site 959 is given by equation 4.0:

$$\%Gl_{Sed} = 22.6 \cdot \log(age_{Sed}) + 1.6 \ (R^2 = 0.97) \quad (4.0),$$

where $\%Gl_{Sed}$ is the state of glauconitization in the sediment and age_{Sed} is the sediment age (in ky). This glauconitization rate depends mainly on continuous cation supply (in particular Fe) and is about five times less than that in shallow-shelf regions, suggesting significantly slower reaction at the lower temperature of deep-sea environments.

4.2 Introduction

The formation of glauconite, a dioctahedral, green, Fe-rich 2:1 illite mineral and mixed-layer glauconite-smectite (Gl-S) generally takes place in low-latitude, shallow-marine shelf regions at Eh ~0 mV, seawater pH (8.2), and low sedimentation rates (*e.g.* Odin & Fullagar, 1988). The presence of organic-rich, semiconfined micro-environments such as in foraminifera and in fecal pellets is considered to be a key factor for glauconitization, providing suitable post-depositional conditions (*e.g.* Odin & Matter, 1981; Baldermann *et al.*, 2012). In this respect, the occurrence of shallow-water glauconites formed in < 500 m water depth, at temperatures below 15ºC (Odin & Fullagar, 1988), and close to the sediment-seawater interface (Wiewióra *et al.*, 2001) represents the typical environment of glauconite formation.
In contrast, exotic occurrences of green-clay authigenesis and glauconite formation have been described in some low-temperature (< 6ºC), deep-sea (> 1000 m water depth) settings (*e.g.* Buatier *et al.*, 1989; Giresse & Wiewióra, 2001; Gaudin *et al.*, 2005; Cuadros *et al.*, 2011). Such cold-water environments differ significantly from that of the shallow shelf, with reduced hydrodynamic energy, limited supply and reflux of particular (silicate) mineral phases, low reaction rates, and less microbial activity (*e.g.* Schulz & Zabel, 2006). The effects of these parameters on the glauconitization reaction are still poorly known and only a few constraints are placed on the rates and mechanism of green-clay genesis in such recent deep-sea environments. Gaudin *et al.* (2005) proposed that early formed Fe-montmorillonite alters rapidly towards the glauconite member during marine diagenesis in which the availability of Al and K and low temperature are the most important rate-controlling factors for glauconitization.
Sediments from the ODP Site 959, Ivory Coast – Ghana Marginal Ridge, provide a condensed and undisturbed sedimentary record without long periods of sediment erosion. Since at least the Miocene, foraminifera and nanofossil oozes have been accumulated which are mixed with

green grains and minor amounts of detrital silicates (*e.g.* Mascle *et al.*, 1996). Based on petrographic, mineralogical, and geochemical analyses on separated bulk green-grain fractions, Giresse & Wiewióra (2001) and Wiewióra *et al.* (2001) established the authigenic nature of the green clay minerals in these sediments and determined their overall composition to be di-octahedral Fe^{3+}-montmorillonite, with minor proportions of interstratified Gl-S (~20% glauconite layers and ~80% Fe-smectite layers) in the more mature, dark green grains. Based on the association of green clay and occasional periods of sediment erosion, those authors proposed that the authigenic clay formed primarily at the water-sediment interface during phases of intense ion exchange with the seawater. The formation of glauconitic minerals was, therefore, expected to occur immediately after deposition of the sediments and not related to any burial or diagenetic reactions within the sediment pile. The glauconitization mechanism proposed was that of Fe-smectite-to-glauconite alteration via the formation of Gl-S.

In the present study, the mineralogical, chemical, and structural changes that occurred during deep-water glauconitization at the ODP Site 959 were documented in detail and burial-related changes in the development of glauconite are highlighted which have not been described to date in a deep-sea environment. Based on the depth-related changes in the maturity of the green clay minerals and interstitial solution chemistry, the rate and mechanism of glauconite formation are assessed and a reaction model is presented.

4.3 Geological setting

The Ivory Coast – Ghana continental margin is located in the eastern equatorial Atlantic Ocean (western Africa) and consists of two major segments. The northern segment is known as the Deep Ivorian Basin (synonymous with the Ivory Basin), an extensional margin that includes the eastern Ivorian continental slope and the southwestern Ghanaian upper slope (Fig. 4.1). The southern segment bounds the Ivory Basin toward the south in a NE-SW direction and is referred to as the Ivory Coast – Ghana Marginal Ridge: a feature that is 130 km long and 25 km wide (Mascle *et al.*, 1996). Owing to its moderate distance from the surrounding coastlines (~120 km), only a minor proportion of the terrigenous sediment input (suspension load) has reached Site 959C (Giresse & Wiewióra, 2001).

Sediment cores from the Ivory Coast – Ghana Marginal Ridge were recovered during Ocean Drilling Program (ODP) Leg 159, Site 959, in ~2100 m water depth and at 3-6ºC seawater temperature. The sediments are of particular interest because of their slow (~1-2 $cm \cdot ky^{-1}$) and continuous sedimentation rate from at least the Miocene to the Holocene (Wagner, 1998). Due

to the elevated position of this site (Latitude: 3º37.669‘N, Longitude: 2º44.116‘W), large hiatuses caused by deep-sea bottom currents or gravity-flow activity are absent (Fig. 4.1).

The upper 25 m of ODP Site 959, Hole C, consists of thin dark gray to greenish sedimentary layers of interbedded foraminifera and nanofossil oozes mixed with detrital quartz, feldspar, clay minerals, and radiolarians (bio-opal) forming darker horizons (Giresse *et al.*, 1998, Wagner, 1998, Wiewióra *et al.*, 2001). The brighter intervals rich in foraminifera tests frequently contain authigenic green clay and also pyrite infillings. Generally, the beds show a lack of sedimentary structures except for two scour contacts and small bioturbation features.

Stratigraphic classification of Hole 959C was derived from stable oxygen isotope records established on the basis of the epibenthic foraminifer *Cibicides wuellerstorfi* (Wagner, 1998). The $\delta^{18}O$ signal provides a nearly complete record over the last 25 oxygen isotope stages corresponding to the last ~1 My, with one notable stratigraphic gap of ~80 ky near 1.5 meters below the seafloor (mbsf). A longer hiatus of ~530 ky occurs at 11.9 mbsf which is slightly below oxygen isotope stage 25 (Wagner, 1998).

Sediments from the Hole 959C are, therefore, suitable for high-resolution study of the recent, green-clay authigenesis and for establishing the roles of deep-water chemistry, provenance, and composition of original sediment, and early marine carbonate diagenesis (*e.g.* Giresse *et al.*, 1998; Norris, 1998; Wagner, 1998).

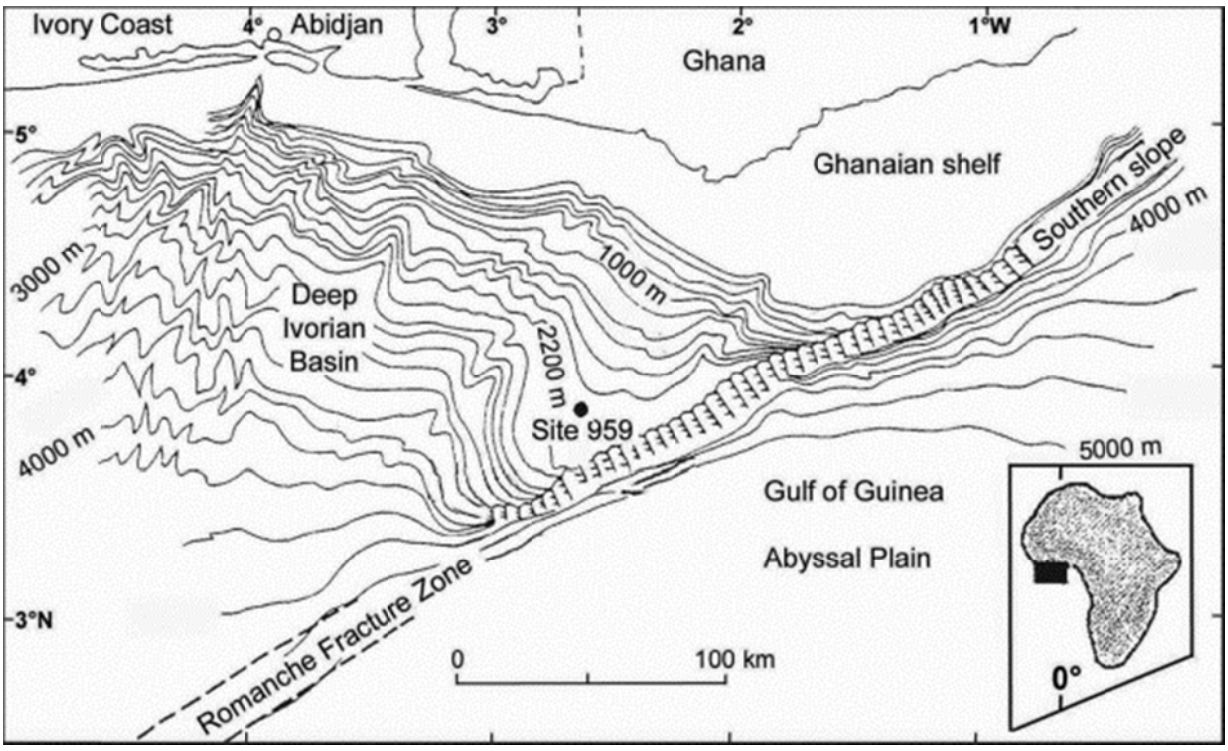

Fig. 4.1: Location map of the ODP Site 959 situated on a small plateau on the Ivory Coast – Ghana Marginal Ridge (western equatorial Africa) (modified after Wiewióra *et al.*, 2001).

4.4 Material and methods

4.4.1 Sampling and preparation

Bulk-sediment samples (21 in total), ~30 cm^3 in size, were taken from the upper 25 m of Hole 959C, the core of which is stored at the Bremen Core Repository (MARUM), Germany. This sampled section comprises a sedimentary sequence ranging from Early Holocene (0.16 mbsf, ~0.01 My) to Late Pliocene age (24.91 mbsf, ~2.5 My). Four sub-samples from 1.32, 10.23, 11.49, and 24.91 mbsf were impregnated with epoxy resin to study the microstructure of the green clay infillings in foraminifers' tests by optical microscopy of thin sections. For further mineralogical and chemical analyses of the bulk sediment and green-grain fraction, air-dried sediments were treated with 10% acetic acid for 1 h to dissolve carbonates. The proportion of the green-grain fraction was calculated by weighing the carbonate-free > 32 µm size fraction which contained < 5 wt.% quartz, radiolarians, and pyrite. In order to investigate the glauconitization process, ~50 mg of green grains were separated by hand picking under a binocular microscope from the pale to light green, the medium green, and the dark green-grain sub-fractions of samples taken at 0.16, 11.69, and 24.91 mbsf.

4.4.2 X-ray diffraction

X-ray diffraction (XRD) analyses were carried out for mineral identification and quantification using a Bruker D8 Advance instrument equipped with a Cu-target tube (40 kV, 30 mA), Ni-filter, 0.5º divergence slit, and a scintillation detector. Finely ground bulk samples were prepared (side-loaded) for random powder analyses and run over the range 4-65º 2θ using a step size of 0.02º $2\theta \cdot s^{-1}$ with a count time of 1 $s \cdot step^{-1}$. Rietveld-based phase quantification was carried out using the PANalytical X'Pert HighScore Plus software. The accuracy of these results was verified by comparison with mass-balance calculations based on X-ray fluorescence (XRF) data of the bulk sediment. Idealized compositions for orthoclase, albite, clinochlore (chlorite), Na-montmorillonite (smectite), and muscovite were assumed for the calculations (Baldermann, 2012). The deviation of the XRD and XRF calculations, expressed as error bars, were < 5 wt.% for kaolinite, calcite, and quartz, and < 3 wt.% for feldspar, smectite, chlorite, and illite/muscovite. The percentage of glauconite layers (%Gl) in Gl-S was determined on separated green-grain sub-fractions using oriented preparations. Oriented mounts were made by dispersion of 40 mg of green clay matter in 5 mL of ethanol and ultrasonic treatment for 10 min and then pipetting the clay-in-suspension onto 2 x 2 cm glass slides, which were subsequently left to air dry overnight. Preparations were run over the range 3-30º 2 θ using a step

size of 0.02º $2\theta \cdot s^{-1}$ and a count time of 0.5 $s \cdot step^{-1}$. The %Gl was calculated based on XRD patterns of ethylene glycol (EG)-solvated preparations, according to the equation 4.1:

$$\%Gl = 60.8 \cdot d_{EG}002 - 504.5 \quad (4.1),$$

which was obtained from NEWMOD-calculated %illite in illite-smectite vs. $d_{EG}002$ peak position relationships reported by Moore & Reynolds (1997). The peak reproducibility of the $d_{EG}002$-reflection was 0.01 Å, equivalent to an analytical precision of ±2%Gl in Gl-S. Results were compared with Sybilla© calculations to verify the accuracy of the %Gl estimations. For Sybilla© modeling, an illite-smectite structure with a large Fe content of 1.2 atoms per formula unit (a.p.f.u.) was assumed, based on $O_{10}(OH)_2$, in the octahedral sites.

4.4.3 Scanning and transmission electron microscopy

In order to study mineral alterations and dissolution features related to diagenesis, ~40 hand-picked, C-coated grains from 0.16 (least altered state) vs. 24.91 mbsf (most altered state) were analyzed by scanning electron microscopy (SEM) using a Jeol JXA-840A. For material disaggregation, the bulk sample was treated with 0.5 M HCl (for 1 h) to remove carbonates.

Transmission electron microscopy (TEM) was performed to determine the composition, form, and structure of clay mineral particles in the separated green-grain sub-fractions from 0.16, 11.69, and 24.91 mbsf using a Jeol JEM 1210 instrument equipped with an Oxford Instruments Pentafel Link-Model 6635 detector. The sample preparation was the same as described by Baldermann *et al.* (2012). Imaging, energy-dispersive X-ray spectroscopy (EDX), and selected area electron diffraction (SAED) analyses were performed on single clay mineral particles using a 200 kV accelerating voltage and 10 s count time to reduce K^+ migration. The analytical error of elemental analysis depends mainly on particle thickness and size. The standard deviations were < 30% for Na, K, and Ca, < 10-15% for Al and Mg, and < 5% for Si and Fe analyses, equivalent to an analytical error of < 2 wt.% for most of the major elements. Structural formulae were calculated on the basis of 22 negative charges, according to Bailey *et al.* (1980), assuming (1) the iron present is ferric Fe, (2) the tetrahedral Si^{4+} + Al^{3+} is equal to 4, (3) Fe^{3+}, Mg^{2+}, and Al^{3+}_{rest} occupying the octahedral sheet, and (4) K^+, Na^+, and Ca^{2+} are located within the interlayer sites.

4.4.4 Focused-ion beam and scanning electron microscope (FIB-SEM) study

The microfabrics of light and dark green clay infillings of the benthic foraminifer *Fursenkoina mexicana* were studied using a Zeiss Auriga CrossBeam FIB-SEM. A Pt-coated surface

area of ~20 x ~30 µm was tilted normal to the ion beam. Ion milling was applied to create a cross-sectional surface of ~15 x ~15 µm that was imaged by the electron beam with a 5 kV accelerating voltage. 3-D information was obtained using a serial sectioning procedure with alternating milling and imaging to acquire a 2-D image sequence across the selected volume (Warr & Grathoff, 2012). The acquired number of secondary electron images ranged between 100 and 300 with a 25 nm slice thickness. 3-D visualization was obtained from the sequence of SEM images using the ImageJ© software based on the gray-level contrasts. The distribution of clay matter, pore space, and skeletal calcite was reconstructed using the threshold method slightly modified from that described by Keller *et al.* (2011).

4.5 Results

In this section, the results of petrographic, mineralogical, geochemical, and structural studies of the bulk sediment and the green grains are compared in order to investigate the glauconitization process in the recent deep-sea environment of the ODP Site 959C.

4.5.1 Petrographic observations

The uppermost 25 m of sediment consists of slightly bioturbated, olive brown to olive-grayish green horizons of interbedded foraminifera and nanofossil oozes. The laminae which are rich in foraminifera tests are about 1 mm to 1 cm thick and show two scour contacts at ~3.8 and 10.4 mbsf. Giresse *et al.* (1998) interpreted these features as resulting from winnowing action or longer breaks in sedimentation. Darker intervals are rich in organic matter (0.7-1.6 wt.%) with a C/N ratio of 8-48 (14 on average), as reported by Baldermann (2012), which indicates the predominance of marine organic matter (Wagner, 1998). These thinner layers also contain large proportions of coccoliths which are mixed with a brownish clay matrix. Sparse occurrences of large detrital quartz and feldspar grains as well as plant debris were recognized over the whole sedimentary sequence whereas the proportions of pyrite and green clay infillings related to glauconitization increase slightly with increasing depth (Baldermann, 2012). No signs of gravity-flow or turbidity deposits are evident, indicating that the green grains were formed *in situ* rather than transported by reworking and re-deposition from the surrounding Ghanaian shelf and slope.

Examples of microfacies and microstructures from 1.32, 10.23, 11.49, and 24.91 mbsf (see Fig. 4.2) reveal that the sediment from 1.32 mbsf consists mainly of nanofossil ooze which is rich in the tests of globigerine and orbuline foraminifera that show a few incomplete, pale to

light green clay infillings in addition to some radiolarians (Fig. 4.2-a). No pyrite was found, suggesting that the uppermost sediments are the least altered in terms of diagenetic overprinting. At 10.23 mbsf, foraminifera tests mixed with partly dissolved radiolarians dominate in the sediment and some of these tests show immature, light to medium green clay infillings (Fig. 4.2-b). Many medium green internal moulds and subordinate pyrite infillings were found within foraminifera tests at 11.49 mbsf (Fig. 4.2-c). Radiolarians are absent at ≥ 11.49 mbsf, and skeletal calcite (*i.e.* foraminifera tests) has been partly dissolved. Abundant more-mature, medium to dark green grains with a fractured and broken morphology, and many pyrite infillings, were found at 24.91 mbsf (Fig. 4.2-d). The section ≥ 24.91 mbsf is, thus, considered to reflect the most altered sediment with respect to early diagenesis. An increased state of glauconitization is recognizable in the more deeply buried sediments, together with precipitation of pyrite and dissolution of both carbonate and bio-opal.

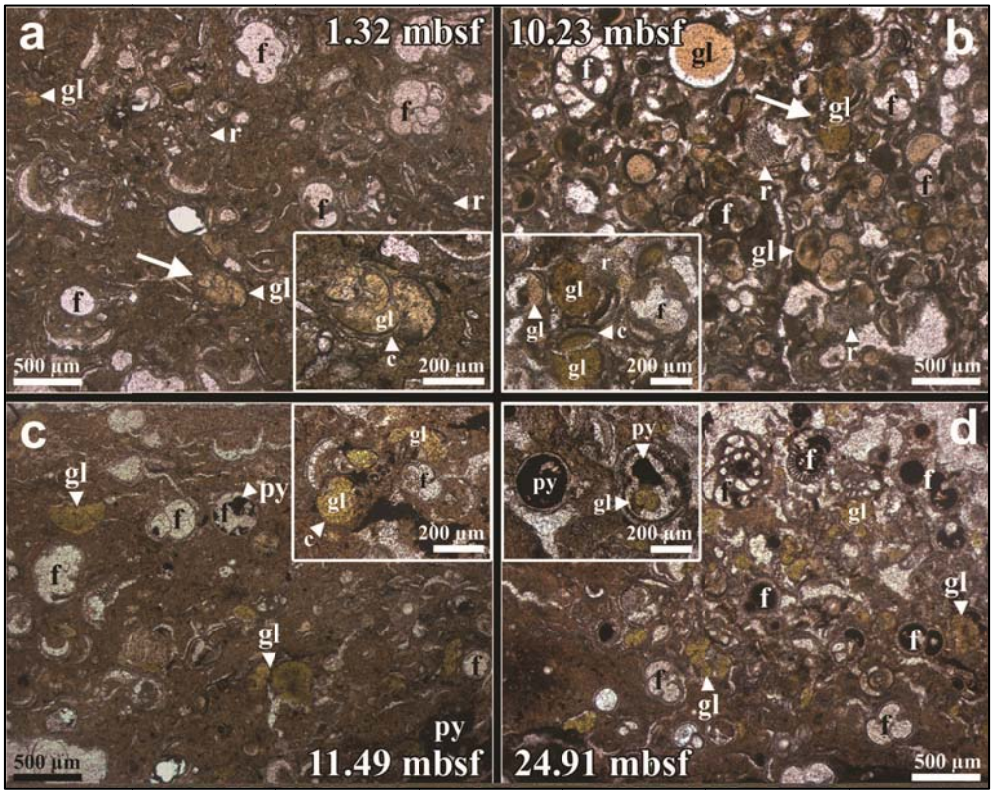

Fig. 4.2: Photomicrographs showing the development of microfacies and microstructure within the top 25 m of Hole 959C. (a) Clayey nanofossil ooze enriched in foraminifera (f) and radiolarians (r) from 1.32 mbsf. Incomplete, light green clay infillings (gl) are scarce. (b) Immature, light to medium green clay infillings in foraminafera ooze mixed with partly dissolved radiolarians from 10.23 mbsf. (c) Nanofossil ooze containing interbedded laminae of foraminifera tests rich in medium green clay and subordinate pyrite infillings (py). Radiolarians are absent at 11.49 mbsf and skeletal calcite (c) is partly dissolved. (d) Foraminifera-rich nanofossil ooze with large proportions of more mature dark green grains showing a modified (broken or cracked) morphology accompanying plentiful pyrite infillings from 24.91 mbsf.

4.5.2 Bulk mineralogy of Hole 959C

Quantitative XRD analyses of 21 bulk samples from Hole 959C (Fig. 4.3) revealed a constant background of siliciclastic input during the last 2.5 My, consisting of poorly crystalline kaolinite (21-34 wt.%), quartz (11-19 wt.%), and feldspar (3-8 wt.% of K-feldspar and albite), and minor amounts of detrital smectite (2-5 wt.%), illite/muscovite (1-5 wt.%), chlorite (1-3 wt.%) and anatase (0.3-0.6 wt.%). In addition to the detrital input, authigenic calcite (27-51 wt.%), Gl-S (1-6 wt.%, 2-3 wt.% on average), and pyrite (< 3 wt.%) were formed. Traces (< 1 wt.%) of aragonite, bio-opal, and Fe-(oxy)hydroxides as well as secondary halite, gypsum, and hexahydrite were also identified by SEM, most of which probably formed as alteration products during storage. No general variation with depth in the basic mineral assemblage was detected except an increase in the amount of pyrite (and Gl-S) and a decrease in the proportion of feldspar with increasing depth which can be attributed to diagenetic alterations (Fig. 4.3).

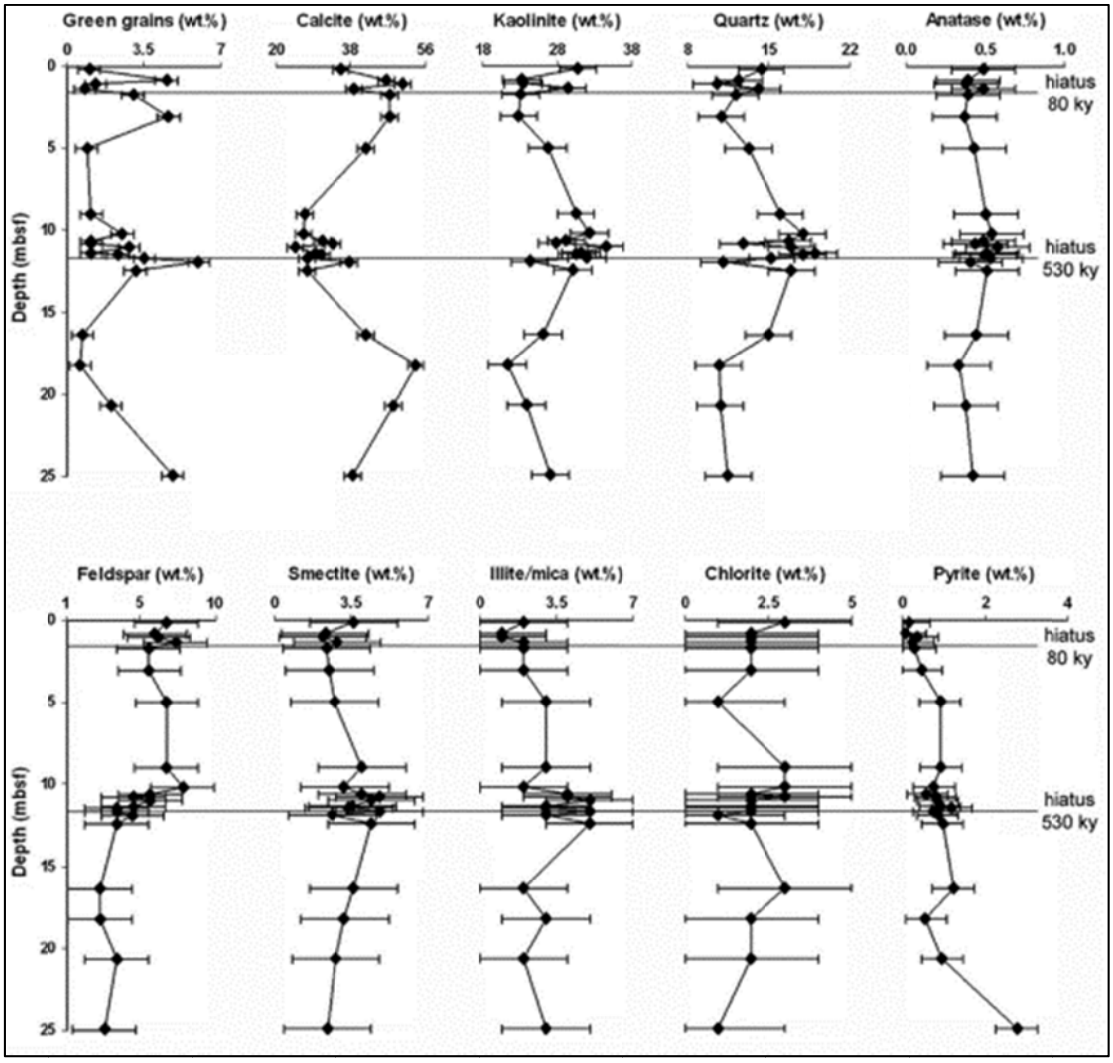

Fig. 4.3: Bulk mineralogy of the upper 25 m of Hole 959C based on XRD. The proportion of the green-grain fractions was determined by weighing.

Observations by SEM of carbonate-free sediment from 0.16 mbsf showed it to have slightly rounded quartz grains, in addition to detrital K-feldspar, albite, chlorite, and illite/muscovite particles that show clear cleavage directions and distinct crystal edges with no signs of diagenetic modification (Fig. 4.4). Modified habits, abundant dissolution pits, and decomposition features are evident at 24.91 mbsf, indicating silicate alterations related to progressing marine diagenesis. Fe-(oxy)hydroxides and unstable bio-opal (fragments of radiolarians, diatoms, and sponge needles) have been almost completely dissolved or have been partly glauconitized at 24.91 mbsf, whereas detrital smectite and kaolinite remained unaltered (Fig. 4.4). Neocrystallized pyrite with both framboidal and euhedral (octahedral) morphology is most abundant at 24.91 mbsf, together with authigenic Gl-S.

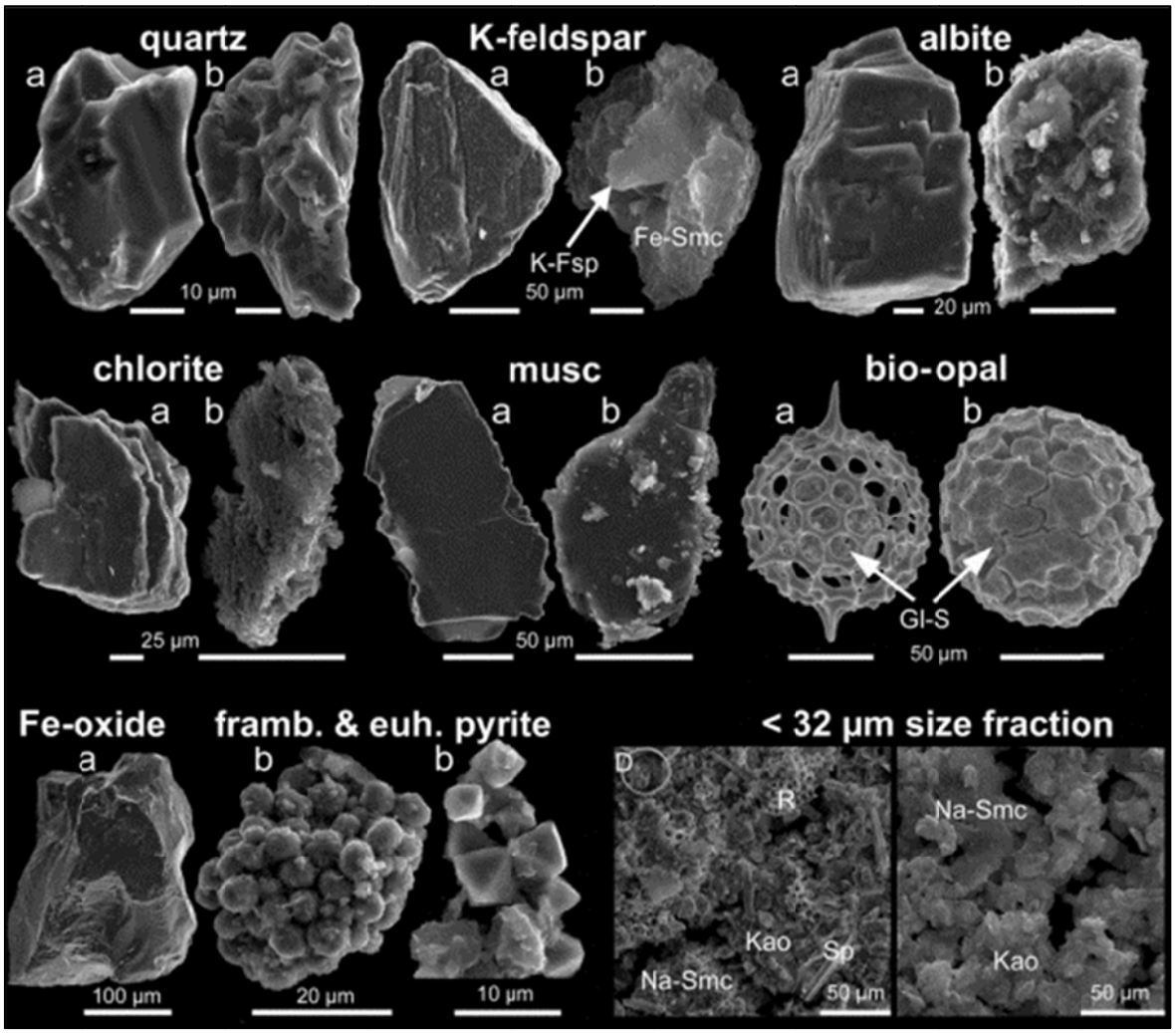

Fig. 4.4. SEM images of less altered grains from 0.16 mbsf (a) compared with the more altered grains from 24.91 mbsf (b). Quartz, K-feldspar, albite, chlorite, muscovite (musc), bio-opal (Sp = sponge needles, D = diatoms, R = radiolarians), and Fe-(oxy)hydroxide show abundant alteration and dissolution features, while detrital Na-smectite (Na-Smc) and kaolinite (Kao) remain unaltered. Glauconite-smectite (Gl-S) and framboidal and euhedral pyrite (framb. and euh. pyrite) were formed in situ during early marine diagenesis.

4.5.3 Mineralogy of the green-grain sub-fractions

The material inside the foraminifers' shells, namely the green clay infillings, was studied by XRD after removal of the skeletal carbonate and surrounding mud matrix. In order to investigate the state of glauconitization in the more deeply buried sediments, clay matter from the pale to light green, medium green, and dark green-grain sub-fractions from 0.16, 11.69, and 24.91 mbsf was analyzed using oriented clay preparations (Fig. 4.5). Air-dried clay from the light green grains from 0.16 mbsf displayed a d_{001} reflection at 13.3 Å which shifted to 16.5 Å after EG-solvation with the weak d_{002} reflection at 8.8 Å, typical for immature Fe-smectite-rich Gl-S. In contrast, air-dried clay matter from the buried dark green grains from 24.91 mbsf showed a d_{001} value at 11.4 Å which increased to 14.8 Å after EG solvation. The d_{002} value was 9.7 Å, indicative of a more mature glauconite-rich Gl-S. After heating to 550ºC for 1 h the basal spacing decreased to 10.0 Å.

Quantitative changes in both the composition of Gl-S and the percentage of each green-grain sub-fraction suggest a sequence of increased glauconitization with the increasing burial depth (Fig. 4.5). Using the linear relationship between the %Gl in Gl-S and related shifts in their basal spacings (adapted from Moore & Reynolds, 1997), the d_{002} reflections from EG-solvated clay matter were used to determine the %Gl in each green-grain sub-fraction (Fig. 4.5). Sybilla© modeling (see also Fig. 4.5) of the XRD patterns reveals that the most immature Gl-S from 0.16 mbsf contains ~32% Gl and ~68% Fe-smectite layers (R0 ordered), whereas the most mature Gl-S from 24.91 mbsf contains ~84% Gl and ~16% Fe-smectite layers (R3 ordered). These values are consistent with the %Gl values obtained by using the Moore & Reynolds method. The %Gl increased, together with greening of the grain color, from 32-51% (light green) and 39-74% (medium green) to 61-84% (dark green).

The mass fraction (determined by weighing) of the light green grains in the total green-grain fraction decreases with increasing depth, from 70 wt.% at 0.16 mbsf to 20 wt.% at 11.69 mbsf and to 5 wt.% at 24.91 mbsf. Correspondingly, the mass fractions of the medium green grains (30 wt.%, 50 wt.%, and 55 wt.%) and dark green grains (<5 wt.%, 30 wt.%, and 40 wt.%) increased at the three depths (see Fig. 4.5). In each grain color class the %Gl increased at elevated burial depths, from 32-39% at 0.16 mbsf and 36-61% at 11.69 mbsf to finally 51-84% at 24.91 mbsf, attributed to ongoing glauconitization related to progressive diagenesis. All %Gl values were notably greater than the value reported by Wiewióra *et al.* (2001) who estimated only ~20% Gl layers for the green-grain assemblages without separation of the light, medium, and dark sub-fractions.

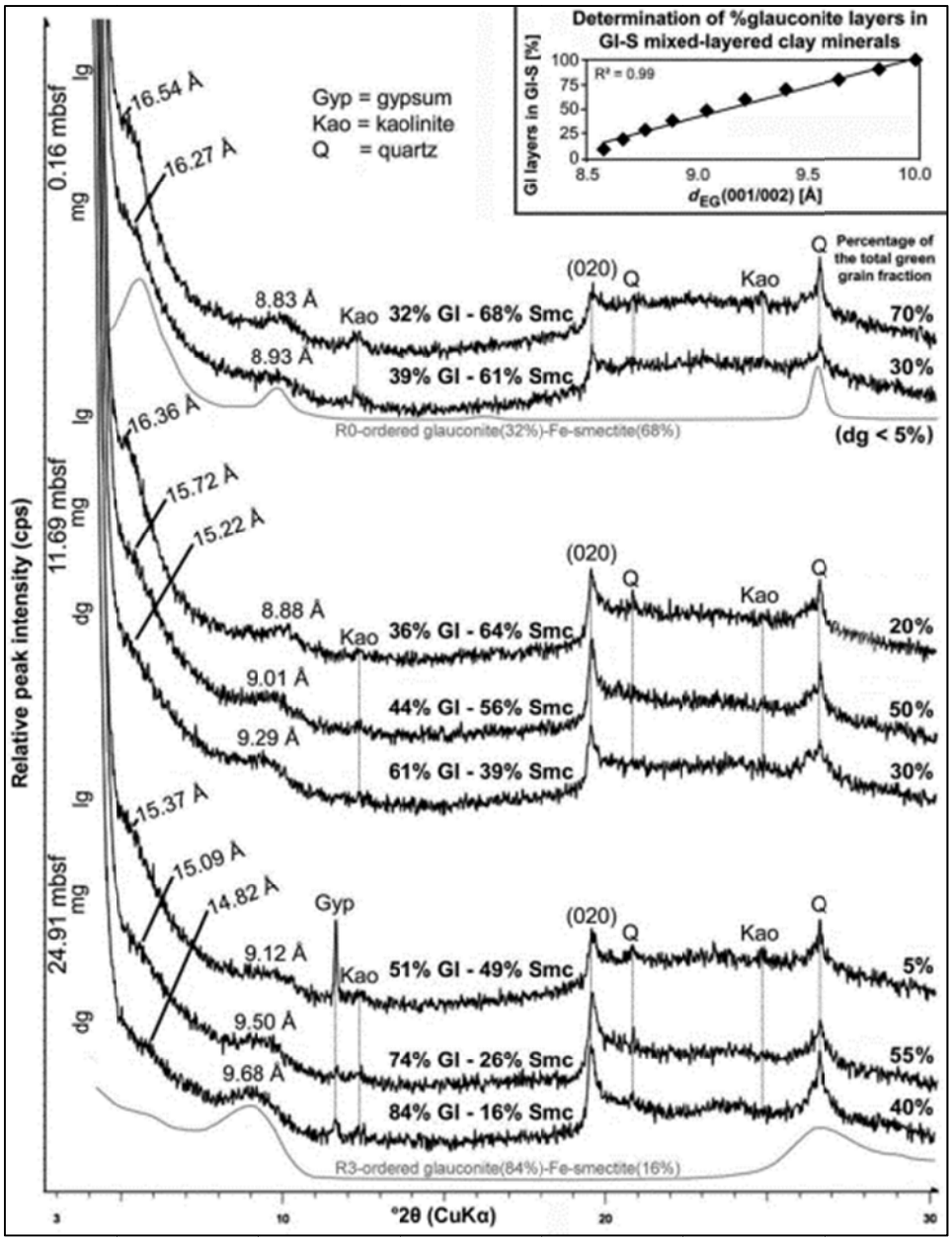

Fig. 4.5. XRD patterns of oriented, glycolated preparations of the separated light (lg), medium (mg), and dark green (dg) grains, collected from 0.16, 11.69, and 24.91 mbsf of Hole 959C. The %Gl in Gl-S was calculated using the linear equation (4.1) $\%Gl = 60.8 \cdot d_{EG}002 - 504.5$ derived from NEWMOD-calculated %illite in illite-smectite vs. $d_{EG}002$ peak-position relations reported by Moore & Reynolds (1997). The accuracy of the %Gl estimations was verified by comparison with Sybilla© calculations (gray curves). On the right, the percentage of each green-grain sub-fraction is given in wt.% of the total green-grain fraction (determined by weighing).

4.5.4 Composition, form and structure of clay minerals in the green-grain fractions

The composition, form, and structure of the clay mineral particles from the separated light, medium, and dark green-grain sub-fractions from 0.16, 11.69, and 24.91 mbsf of Hole 959C were studied by TEM-EDX and TEM-SAED in order to identify differences attributed to variations in these properties related to burial depth and color of the green clays (see Fig. 4.6

and Table 4.1). In total, 332 TEM-EDX analyses were carried out on single clay mineral particles and structural formulae were calculated, based on average compositions. Nine TEM-EDX analyses were also carried out on biofilm (see below).

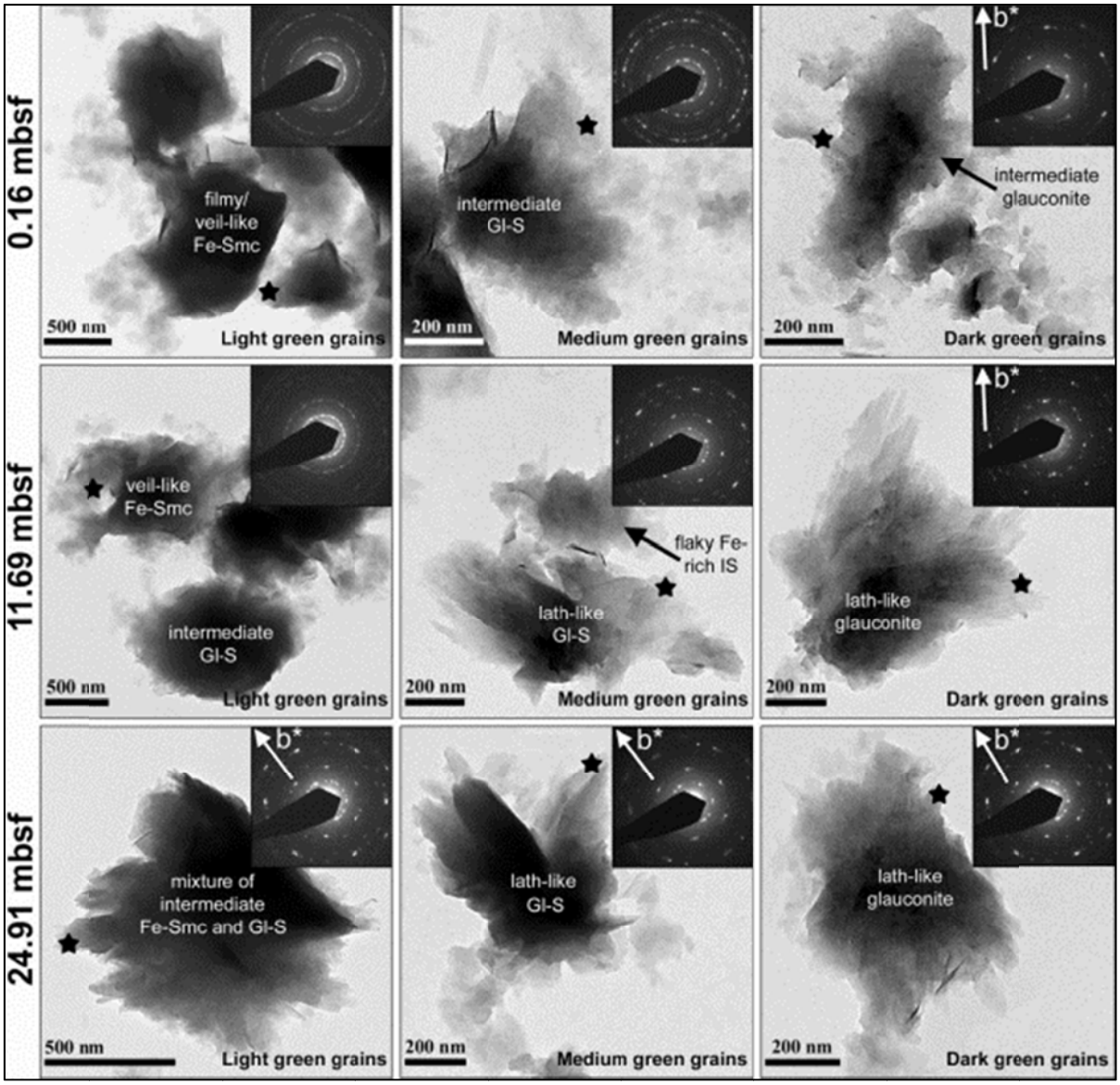

Fig. 4.6: TEM images and TEM-SAED patterns of representative clay mineral particles from the light, medium, and dark green-grain sub-fractions from 0.16 (a-c), 11.69 (d-f), and 24.91 mbsf (g-i) showing the development of particle form and composition at Hole 959C. Initial filmy or veil-like Fe-smectite (Fe-Smc) (a-d) with weak diffraction rings changes into intermediate, flaky or lath-like Gl-S (b, e, g, h) with weak or smeared Bragg spots and finally into lath-like glauconite (c, f, i). The two diagnostic, non-basal Bragg reflections (b* marks the direction of the b axis) indicate a transition from the poorly ordered $1M_d$ polytype to the ordered 1M polytype.

Particles of the light green sub-fractions generally have a veil-like or film morphology according to the nomenclature of Buatier *et al.* (1989). These particles consist mainly of Fe-smec-

tites and smectite-rich Gl-S that predominantly display weak diffraction rings reflecting their turbostratic nature (Figs 4.6-a, 4.6-d, 4.6-g). Bacteria are frequently present within the light green sub-fractions but they are less abundant in the darker, more mature grains. In close proximity to bacteria, biofilm is often mixed with thin Fe-smectite particles, suggestive of bacteria-clay mineral interactions. Intermediate Gl-S particles with both flaky and lath-like morphology occur rarely at 0.16 mbsf but their abundance increases with increasing depth along with greening of the grain color (Figs 4.6-b, 4.6-e, 4.6-g, 4.6-h). Accordingly, minor proportions of Fe-smectite-rich Gl-S with either smeared Bragg spots or weak diffraction rings still occur at 11.69 and 24.91 mbsf, but lath-like, glauconite-rich Gl-S with discrete Bragg spots predominate. Within the dark green sub-fractions, intermediate and lath-like glauconite particles as well as flake-shaped, glauconite-rich Gl-S are more frequent. The elongated form of these particle types (Figs 4.6-c, 4.6-f, 4.6-h, and in the lower right of panel 4.6-i) is evident from the high aspect ratio of 4:1 to 5:1. Such more evolved, lath-like particles commonly display discrete Bragg spots, documenting a more ordered mineral structure (*e.g.* Baldermann *et al.*, 2012) compared to that of Fe-smectite.

According to the chemical composition (based on TEM-EDX analysis), the clay mineral particles mainly consist of Si, Fe, Al, Mg, K, Ca, and O with small traces of P, S, Ti, and Mn (see Table 4.1). With increasing maturity of the grains, the following changes in elemental chemistry were recognized. Average compositions of light green clay mineral particles were rather poor in K_2O (1.8-2.9 wt.%), MgO (3.8-4.4 wt.%), and Fe_2O_3 (24.7-25.2 wt.%), whereas SiO_2 (60.0-61.1 wt.%), Al_2O_3 (7.1-7.6 wt.%), and CaO (0.4-0.8 wt.%) proportions were high. The medium green clay mineral particle s have moderate amounts of K_2O (2.6-4.3 wt.%), MgO (3.7-4.4 wt.%), CaO (0.4-0.8 wt.%), and Fe_2O_3 (25.0-26.0 wt.%), but less SiO_2 (58.8-61.1 wt.%) and Al_2O_3 (6.5-7.1 wt.%). Finally, the dark green clay mineral particles have the largest amounts of K_2O (4.3-5.4 wt.%) and Fe_2O_3 (24.0-27.3 wt.%), moderate MgO (4.2 wt.%) and CaO (0.4-0.8 wt.%), but the smallest amounts of SiO_2 (58.2-59.1 wt.%) and Al_2O_3 (5.2-7.3 wt.%). Based on the calculated, average structural formulae (Table 4.1), the light green clay mineral particles have an Fe-smectite composition of $(K_{0.18}Ca_{0.03})(Fe^{3+}_{1.19}Al_{0.50}Mg_{0.38})_{\Sigma 2.07}[Al_{0.08}Si_{3.92}O_{10}](OH)_2$ at 0.16 mbsf. Gl-S compositions in the range $(K_{0.26}Ca_{0.06})(Fe^{3+}_{1.26}Al_{0.39}Mg_{0.39})_{\Sigma 2.04}[Al_{0.11}Si_{3.89}O_{10}](OH)_2$ dominate in the medium green grains from 11.69 mbsf, and the most mature, dark green glauconite-rich Gl-S have compositions of $(K_{0.46}Ca_{0.03})(Fe^{3+}_{1.33}Al_{0.26}Mg_{0.42})_{\Sigma 2.01}[Al_{0.14}Si_{3.86}O_{10}](OH)_2$ at 24.91 mbsf. Due to the high Fe-smectite content, especially in the less evolved Gl-S, some of the Mg^{2+} may be located in the interlayer sites of the Fe-smectite which could increase the interlayer charge of Gl-S by a progressively higher

octahedral charge deficiency. The greener color of the more mature grains may also reflect the existence of some structural Fe^{2+} which could affect the structural formulae by decreasing the tetrahedral Si content. However, the Fe^{2+}/Fe^{3+} ratio in glauconite is commonly low, typically ranging from 0.05 to 0.5 at most (~0.15 is the average, inferred from the data reported by *e.g.* Meunier and El Albani, 2007), and the calculated structural formulae are balanced assuming the Fe is ferric (Table 4.1). The overall compositional changes mentioned above, thus, support a sequence of increased glauconitization with increasing burial depth, where initial Fe-smectites changed continuously into glauconite via the formation of Gl-S, as also indicated by the XRD data (see Fig. 4.5).

Table 4.1: Averaged compositions, excluding water of Gl-S, based on 332 TEM-EDX analyses, with calculated structural formulae of the separated light, medium, and dark green-grain sub-fractions from samples taken at 0.16, 11.69, and 24.91 mbsf.

Depth		**0.16 mbsf**			**11.69 mbsf**			**24.91 mbsf**	
Green grain sub-fraction	light	medium	dark	light	medium	dark	light	medium	dark
Particles analysed (n)	32	36	30	36	34	38	39	43	44
Averaged elemental chemistry in wt% based on TEM-EDX									
MgO	4.0	3.7	4.2	3.8	4.1	4.2	4.4	4.4	4.2
Al_2O_3	7.6	7.1	7.3	7.5	6.5	5.2	7.1	6.1	5.2
SiO_2	61.1	61.1	59.1	61.2	59.8	58.5	60.0	58.8	58.2
K_2O	2.2	2.6	4.6	1.8	3.1	4.3	2.9	4.3	5.4
Fe_2O_3	24.7	25.0	24.0	24.8	25.7	27.3	25.2	26.0	26.7
CaO	0.4	0.5	0.8	0.8	0.8	0.4	0.5	0.4	0.4
Total	100.0	100.0	100.0	100.0	100.0	100.0	100.0	100.0	100.0
Atoms per formula unit (a.p.f.u.) based on $O_{10}(OH)_2$									
^{IV}Al	0.08	0.06	0.14	0.07	0.11	0.14	0.12	0.14	0.14
Si	3.92	3.94	3.86	3.93	3.89	3.86	3.88	3.86	3.86
TC	-0.08	-0.06	-0.14	-0.07	-0.11	-0.14	-0.12	-0.14	-0.14
^{VI}Al	0.50	0.48	0.43	0.49	0.39	0.27	0.43	0.33	0.26
Fe(III)	1.19	1.21	1.18	1.20	1.26	1.36	1.23	1.28	1.33
Mg	0.38	0.36	0.41	0.37	0.39	0.42	0.42	0.43	0.42
$\Sigma(^{VI}Al + Fe(III) + Mg)$	2.07	2.05	2.02	2.06	2.04	2.05	2.08	2.04	2.01
OC	-0.17	-0.21	-0.35	-0.19	-0.27	-0.27	-0.18	-0.31	-0.39
K	0.18	0.21	0.38	0.15	0.26	0.36	0.24	0.36	0.46
Ca	0.03	0.03	0.05	0.06	0.06	0.03	0.03	0.04	0.03
IC	0.24	0.27	0.48	0.27	0.38	0.42	0.30	0.44	0.52

TC = tetrahedral charge, OC = octahedral charge, IC = interlayer charge.

4.5.5 3-D microstructure of light vs. dark green clay infillings

Differences of microstructure, microporosity, and mineralogy between the light vs. dark green clays were studied by comparison of 3-D reconstructions of infillings in the benthic foraminafer *Fursenkoina mexicana* (Fig. 4.7). At 0.16 mbsf, most of these shells are filled with light green clay matter but at 24.91 mbsf most are filled with dark green clay matter. One shell filled with light green clay matter and one filled with dark green clay matter were selected for the study. The following observations were made on the two varieties:

(1) The light green clay matter from 0.16 mbsf (Fig. 4.7-a to 4.7-c) consisted mainly of sets of Fe-smectite-rich Gl-S ~0.5-1.0 µm across and subordinate Fe-smectite particles. These poorly evolved clay minerals (nomenclature of Odin & Matter, 1981) typically form boxwork-like networks (Fig. 4.7-b) with a significant, well connected porosity of about 15-20% (Fig. 4.7-c). Fragments of partly dissolved calcite (Fig. 4.7-a) which are probably remnants of the foraminifera walls are well preserved between the clayey frameworks.

(2) The dark green clay matter from 24.91 mbsf (Fig. 4.7-d to 4.7-f) consisted mainly of glauconite-rich Gl-S and showed notably more complex microstructures than those of the light green clays. Sets of these clay mineral particles are ~0.5-2.0 µm in size and typically form flame- or rosette-like structures with a high packing density (Fig. 4.7d and 4.7-e), characteristics associated with the evolved state of glauconitization (Odin & Matter, 1981). At this state, the porosity (5-10%) is reduced and the skeletal calcite has largely been dissolved (Fig. 4.7-f). Such (micro)-textures indicate changes in the physicochemical conditions in the foraminifera tests during progressive glauconitization.

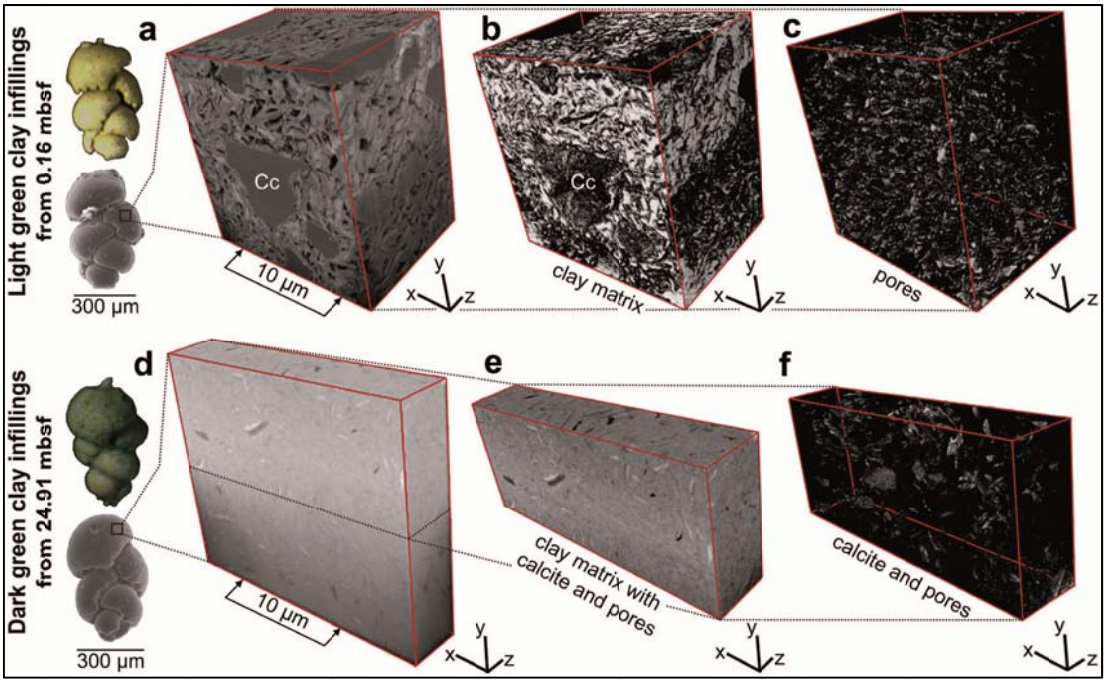

Fig. 4.7: 3-D reconstructions of green clay infillings of the benthic foraminifera *Fursenkoina mexicana* based on FIB-SEM images. Optical photomicrographs and SE images of the specimens, filled with either light green clay at 0.16 mbsf (a) or dark green clay at 24.91 mbsf (d), show the locations of the investigated areas. The light green clay matter (a to c) is composed mainly of 0.5-1 µm long Fe-smectite-rich Gl-S (white areas in part b) which forms boxwork-like networks with a high porosity (white areas in part c). Skeletal calcite (dark gray areas in part a marked with Cc) is largely preserved. The dark green clay matter (d-e) is composed of sets of 0.5-2 µm long glauconite-rich Gl-S (gray areas in part e) and forms rosette-like structures with a greater packing density. Pore space and skeletal calcite (white areas in part f) are largely reduced at this state of glauconitization.

4.6 Discussion

Previous studies demonstrated that in the deep-water environment of the Ivory Coast – Ghana Marginal Ridge (ODP Hole 959C), authigenic green clay minerals formed at the water-sediment interface during phases of enhanced ion exchange with the seawater (Giresse & Wiewióra, 2001; Wiewióra *et al.*, 2001). The reaction mechanism proposed was that of Fe-smectite-to-glauconite alteration by the formation of Gl-S, a feature confirmed in this study. However, detailed XRD and electron microscope analyses of representative green grains from different depths revealed a number of new features which were not characterized by previous authors: **(1)** the association of bacterial biofilm, gels, and precipitated Fe-smectite in less altered green grains; **(2)** the decrease in connected porosity with increasing depth; **(3)** a greater abundance of glauconite in Gl-S in all samples; and **(4)** a notable depth-dependent increase in the degree of glauconitization which was observed for all three types of green grains – light, medium, and dark – together with increasing proportions of the dark green grains with increasing burial depth. In this section, the key factors for glauconitization are discussed and a new interpretation of glauconite formation presented. The availability of Fe is suggested to be the most important rate-limiting factor for glauconitization in this low-temperature, deep-water setting.

4.6.1 The initial step to glauconitization – formation of Fe-smectite

Comparison of petrographic (Fig. 4.2), mineralogical (Fig. 4.5), and chemical (Table 4.1) data across the entire range of green clays from the immature light green grains from 0.16 mbsf to the most mature dark green grains from 24.91 mbsf suggests that a complete mineral series from Fe-smectite to glauconite exists via progressively more glauconitic Gl-S. Thus, the early diagenetic formation of Fe-smectite subsequent to sediment deposition seems to be a key factor for glauconitization of foraminifers' tests, as proposed by Giresse & Wiewióra (2001).

Authigenic veil-like Fe-smectite particles ~20-50 μm long are always associated with bacteria-produced biofilm (Fig. 4.8-a and 4.8-b). The biofilm contains on average high proportions of volatiles (89.1 wt.% CO_2 and 1.9 wt.% SO_3) and SiO_2 (4.6 wt.%), CaO (1.8 wt.%), P_2O_5 (1.6 wt.%), Fe_2O_3 (0.4 wt.%), MgO (0.4 wt.%), and K_2O (0.1 wt.%) based on nine TEM-EDX analyses (Fig. 4.8). Such a composition is indicative of bacterial biofilm of marine origin with incorporated amorphous gels, rather than that resulting from later contamination, with similarities to biofilm compositions produced in experimental studies of seawater, clay mineral, biofilm, and bacteria interactions (*e.g.* Chaerun & Tazaki, 2005; Warr *et al.*, 2009). According to Konhauser & Urrutia (1999), a Si-rich precursor gel is suggested to promote clay-mineral

authigenesis. Smectite precipitation from amorphous gels was proposed previously by Harder (1980), Jiménez-Millán *et al.* (1998), Kloprogge *et al.* (1999), and Gaudin *et al.* (2005). The biofilm can provide an early micro-environment where suitable conditions for the formation of amorphous Fe^{3+}/Mg^{2+}-rich hydrogel with co-precipitated Al^{3+} develop as soon as super-saturation is reached (Konhauser & Urrutia, 1999). Rapid chemisorption of dissolved silica onto this initial precipitate (Martín-Algarra & Sánchez-Navas, 1995) can finally lead to the development of poorly crystalline Fe-smectite-like phases, as found in the surface sediments of ODP Site 959 (Figs 4.8-b and 4.9). These largely unaltered Fe-smectite particles contain ~8% Gl and ~92% Fe-smectite layers and can be classified as the nascent state of glauconitization (nomenclature of Odin & Fullagar, 1988). The early micro-environment developed in the bacterial biofilm is, therefore, suitable for Fe-smectite formation which is likely to be the first step of the glauconitization process within the Ivory Coast sediments (Fig. 4.9).

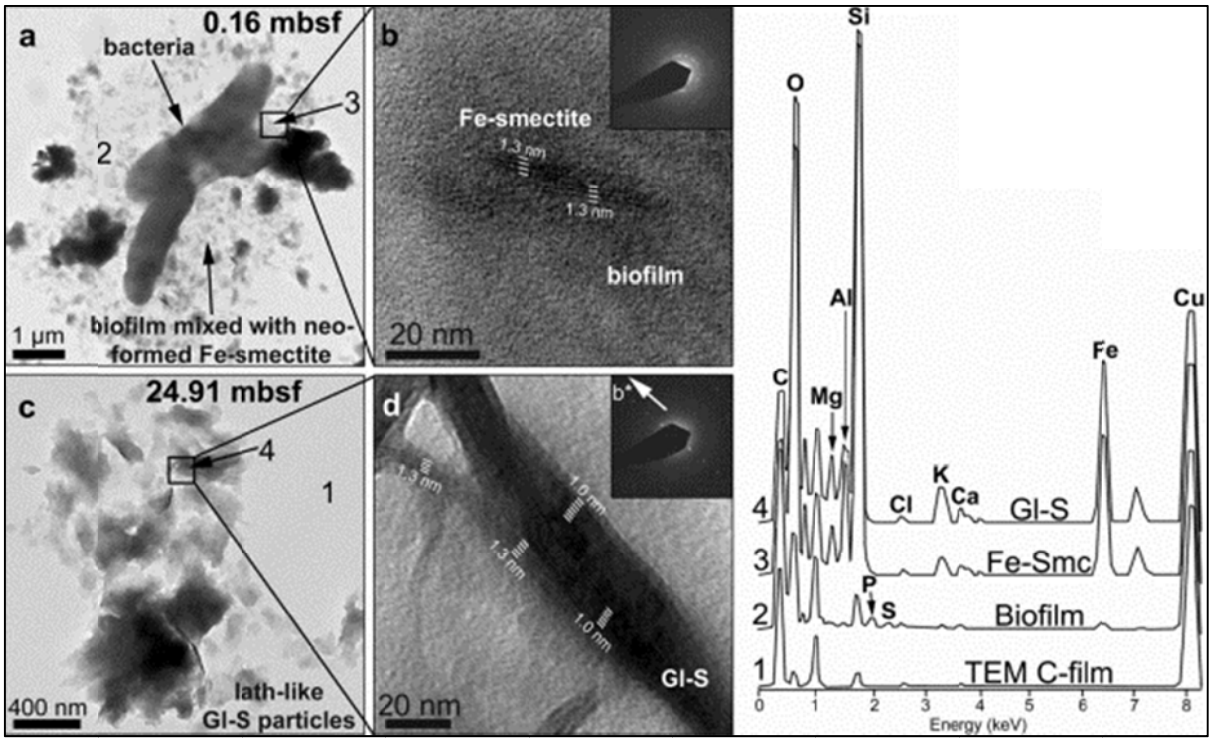

Fig. 4.8: TEM images illustrating the evolution of the green clay minerals at ODP Site 959. (a) Interactions of authigenic Fe-smectites and bacterial biofilm from 0.16 mbsf. (b) An enlarged view of (a) which shows the association of neo-formed Fe-smectite-like phases and biofilm. (c-d) Lath-like Gl-S particles without bacteria from 24.91 mbsf indicative of an ongoing glauconitization process. On the right, TEM-EDX spectra of TEM C-film (1), biofilm mixed with neo-formed Fe-smectite (2), pure Fe-smectite (3), and Gl-S (4) are shown.

With the increased state of glauconitization found in the more deeply buried sediments, the proportion of bacteria present within the internal moulds of the calcareous (pelagic) foramina-

fera decreased notably, probably reflecting the intense changes in pH and Eh conditions within the micro-environment. As the microbial activity decreases, the interstitial solution of the bulk sediment and its chemistry are expected to become more important and control the ongoing glauconitization process. This interstitial solution-driven Fe-smectite-to-glauconite reaction is evident from the greater degree of glauconitization observed at 24.91 mbsf (see Fig. 4.8-c and 4.8-d).

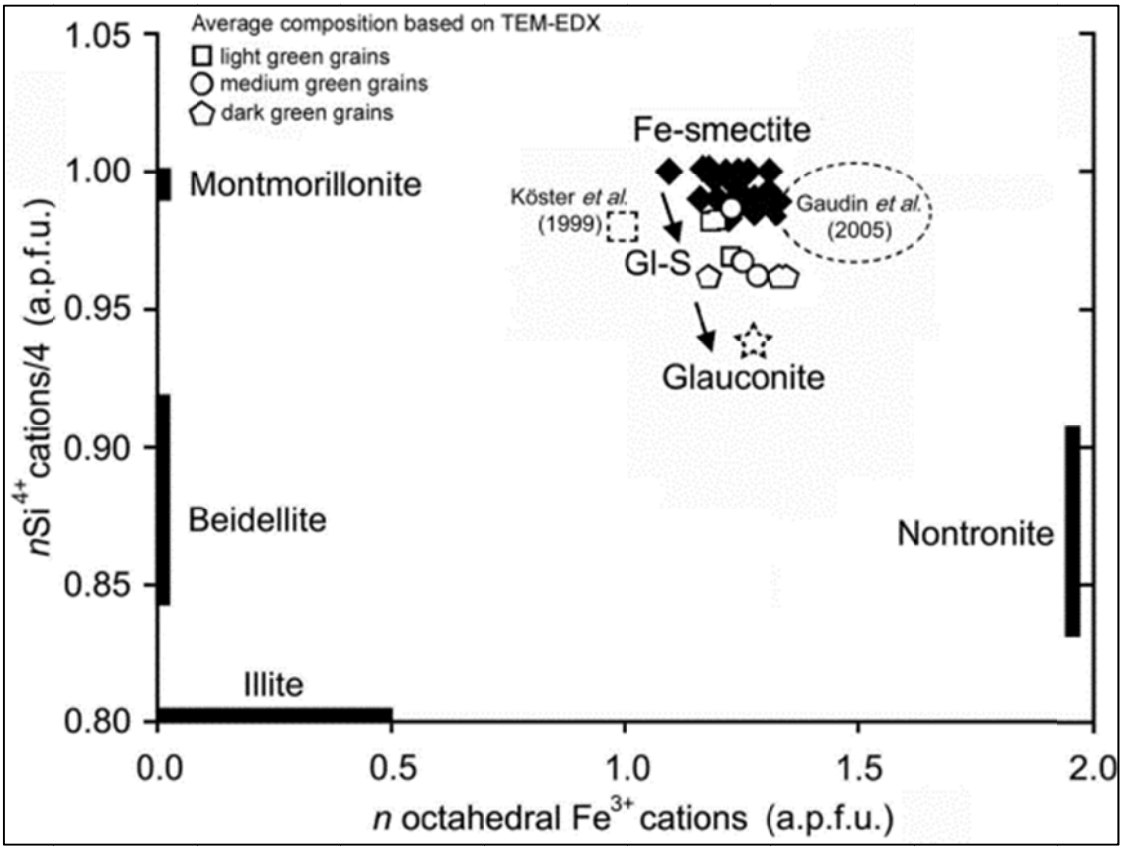

Fig. 4.9: TEM-EDX analyses of unaltered Fe-smectite particles from 0.16 mbsf of Hole 959C (black rhombs) plotted in the 4Si-Σ^{VI}Fe diagram of Gaudin *et al.* (2005). Average compositions of the separated green-grain sub-fractions (Table 4.1) are included to illustrate the ongoing glauconitization process. Reference data of Fe-smectite (dashed circle and square) and of the international GLO (glauconite) standard (dashed star) are included for comparison.

4.6.2 The driving force for glauconitization – interstitial solution chemistry

Recent green-clay authigenesis is commonly restricted to granular siliciclastic and calcareous habitats. The original composition of the sediment and the residence time close to the sediment-seawater interface (Giresse & Wiewióra, 2001) are thought to be the key factors controlling the glauconitization reaction. Such conditions imply continuous cation supply solely from seawater during the whole glauconitization process.

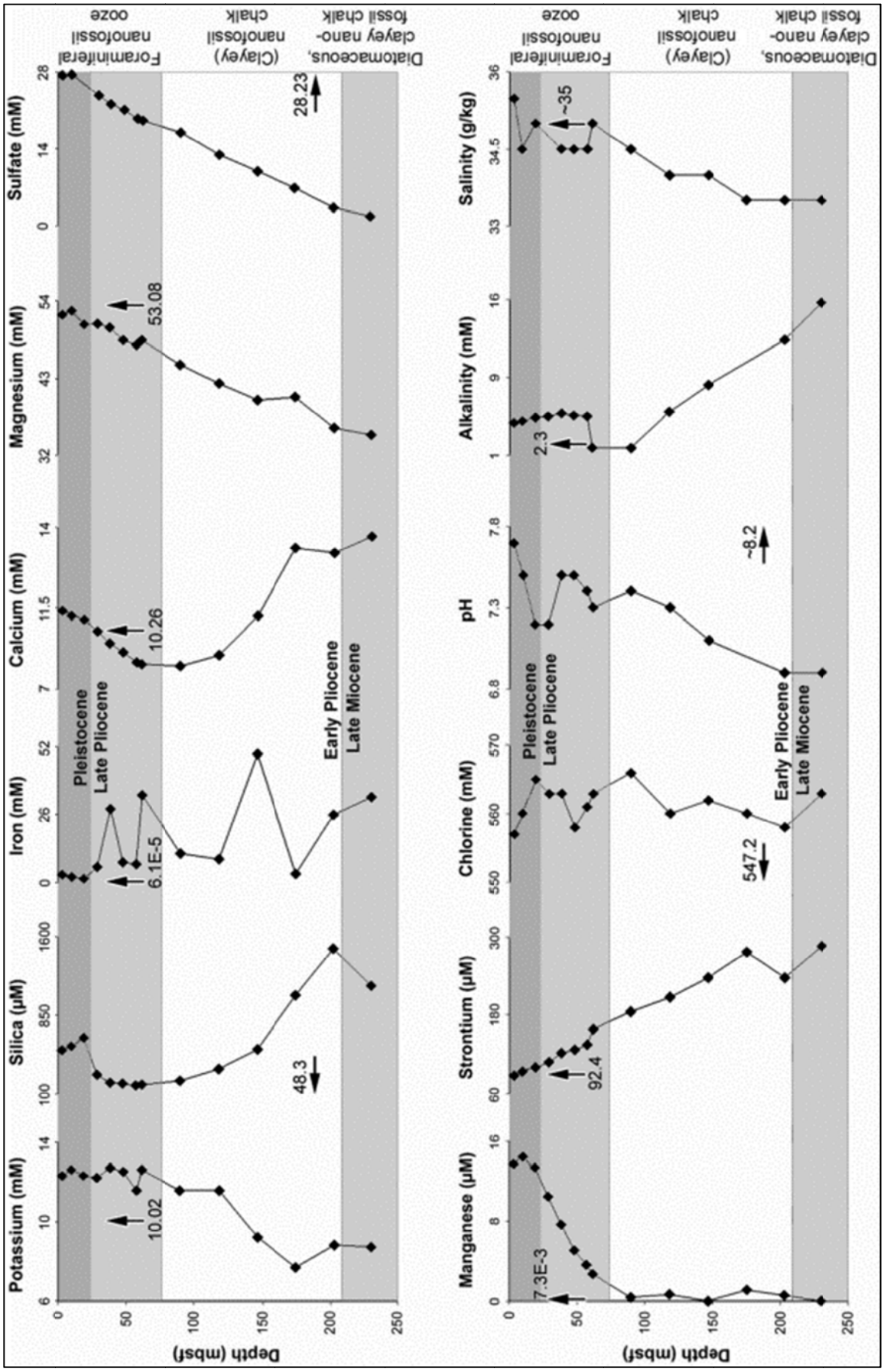

Fig. 4.10: Interstitial solution profiles for ODP Site 959 (data from Mascle *et al.*, 1996). Average seawater composition (black arrows) based on Turekian (1968) and the lithology of Hole 959C are labeled for comparison.

Effective cation exchange can only take place in the first centimeters of clayey substrates and in the first meters of granular substrates, depending on the properties of the sediment such as permeability, porosity, tortuosity, and mainly on the sedimentation rate (Meunier & El Albani, 2007). At Hole 959C, the sediment's properties (Mascle *et al.*, 1996) and sedimentation rates (Wagner, 1998) have not changed noticeably over the last 2.5 My, whereas XRD, TEM-EDX, and FIB-SEM data from the present study clearly reveal an increasing state of glauconitization with increasing depth (Figs 4.6 to 4.9), thus indicating that the glauconitization reaction is not restricted to the seafloor-sediment interface and proceeds further during progressive burial. Furthermore, if the Fe-smectite pre-cursors were precipitated from seawater, then an explanation is required for why the mineralogy (Fig. 4.5) and the chemistry of the green grains differ (Table 4.1), despite a similar residence time close to the sediment-seawater interface at this site (~1 $cm \cdot ky^{-1}$) characterized by constant cation supply. These relationships may be explained by the interstitial solution geochemistry being modified by microbially-catalyzed oxidation of biodegradable (marine) organic matter, causing Fe redox reactions and silicate alterations (Figs 4.2 to 4.4) that promoted the ongoing glauconitization process within the sediment pile.

Microbial oxidation of marine organic matter was suggested by Mascle *et al.* (1996) to have had a major impact on the diagenetic reactions observed at Site 959, namely glauconitization and pyritization. Within the first few meters of sediments, the SO_4^{2-} concentration of the interstitial solution drops below the level of the seawater, owing to microbial sulfate reduction. Thus, dissolved oxygen has been consumed quantitatively (Schulz & Zabel, 2006), followed by Mn^{4+} and Fe^{3+} reduction (Fig. 4.10), *e.g.* from (oxy)hydroxides. Accompanying ongoing SO_4^{2-} reduction with increasing depth, H_2S accumulated successively in the interstitial solution, providing the anions for framboidal and euhedral pyrite formation (Fig. 4.3 and 4.4). Fe-sulfide precipitation is, hence, a limiting factor for glauconitization because it competes with the primary formation of Fe-smectites by removal of ferrous Fe. As a consequence. the Fe interstitial solution profile displays large variation in Fe content without any systematic depth trend which was interpreted by Mascle *et al.* (1996) as a dynamic redistribution of Fe within the sediment column.

The oxidation of marine organic matter and also sulfate reduction are likely to play a key role in regulating the pH of the interstitial solution, as indicated by the drop in pH from 7.7 to 7.2 in the first 20 mbsf (Fig. 4.10) which reflects the formation of *e.g.* carboxylic acids and H_2S (Mascle *et al.*, 1996). At this site, the interstitial solution pH is buffered by $CaCO_3$ dissolution, as documented by the increase in total alkalinity and Sr^{2+} content. Hence, the pH within

organic-rich micro-environments such as in the biofilm within foraminifera tests is probably much lower (pH < 5) than that of the interstitial solution. Such locally occurring acidic conditions can promote dissolution of detrital silicates such as feldspar, as documented by the present XRD and SEM data (Fig. 4.3 and 4.4). As a consequence, the concentration of silicic acid in the interstitial solution increases with burial depth (Fig. 4.10), reaching a first maximum at 20 mbsf (~650 mM). Alterations of bio-opal and clay minerals (Fig. 4.4) provide additional ions such as Al^{3+}, Fe^{2+}, Na^{+} , Ca^{2+}, and Mg^{2+} (*e.g.* MacKenzie, 2005) that are required for ongoing glauconitization.

Due to intense silicate weathering, the K^{+} concentration of the interstitial solution (Fig. 4.10) in the first 50 mbsf (12.2-12.7 mM) is ~20-25% greater than that of seawater (10.02 mM) but it decreases continuously below 120 mbsf. An elevated K^{+} concentration of the interstitial solution probably favors the glauconitization reaction by irreversible K^{+} fixation, as indicated by the TEM-EDX data and by previous studies on the illitization of smectite (Hower *et al.*, 1976; Kaufhold & Dohrmann, 2010).

In summary, the interstitial solution chemistry at ODP Site 959 was modified by early diagenetic silicate mineral alteration, microbial sulfate reduction, Fe redox reactions, carbonate dissolution, and oxidation of organic matter, and is probably the driving force for glauconitization within the sedimentary pile.

4.6.3 Rate of deep-water glauconitization

At the ODP Site 959, Fe-smectite formation is considered to be the initial step to glauconitization which occurred in semi-confined, organic-rich micro-environments, as provided within the tests of foraminifera. According to chemical modeling of Fe-smectite formation in deep-sea sediments from the Costa Rica margin (*e.g.* Charpentier *et al.*, 2011), several thousands of years are required to precipitate Fe-smectite in large quantities. Gaudin *et al.* (2005) suggested that these neo-formed Fe-smectites are thermodynamically unstable during early marine diagenesis and alter rapidly into glauconite via Gl-S formation. Evidence for such a progressive Fe-smectite into glauconite alteration is given by the positive correlation ($R^2 = 0.89$) between the increasing percentage of %Gl in Gl-S and the associated higher K^{+} content per a.p.f.u. (Fig. 4.11) with grain maturity, according to the expression 4.2:

$$\%Gl = 108.4 \cdot \log(K^{+}) + 116.1 \text{ for } K+ < 0.7 \text{ a.p.f.u.} \quad (4.2).$$

The proportion of %Gl in Gl-S of the total green grains at a given depth, namely, the state of overall glauconitization in the sediment ($\%Gl_{Sed}$), was calculated with equation 4.2 using the

average K content (±0.05 K a.p.f.u.) of each green-grain sub-fraction (Table 4.1) multiplied by its percentage (±5%) in the total green-grain fraction from each depth (Fig. 4.5). These calculations revealed 30, 60, and 75% Gl_{Sed}, each ±10%, at 0.16, 11.69, and 24.91 mbsf which correspond to sediment ages of ~10, 900, and 2500 ky, respectively, given by Giresse & Wiewióra (2001). Assuming that the formation of Fe-smectite with initially little if any %Gl requires ~1 ky (Charpentier *et al.*, 2011), an average glauconitization rate for the ODP Site 959 can be obtained by plotting ($R^2 = 0.97$) the $\%Gl_{Sed}$ against the age of the sediment (age_{Sed} in ky), according to the equation 4.3:

$$\%Gl_{Sed} = 22.6 \cdot \log(age_{Sed}) + 1.6 \text{ for } age^{Sed} < 10 \text{ My} \quad (4.3).$$

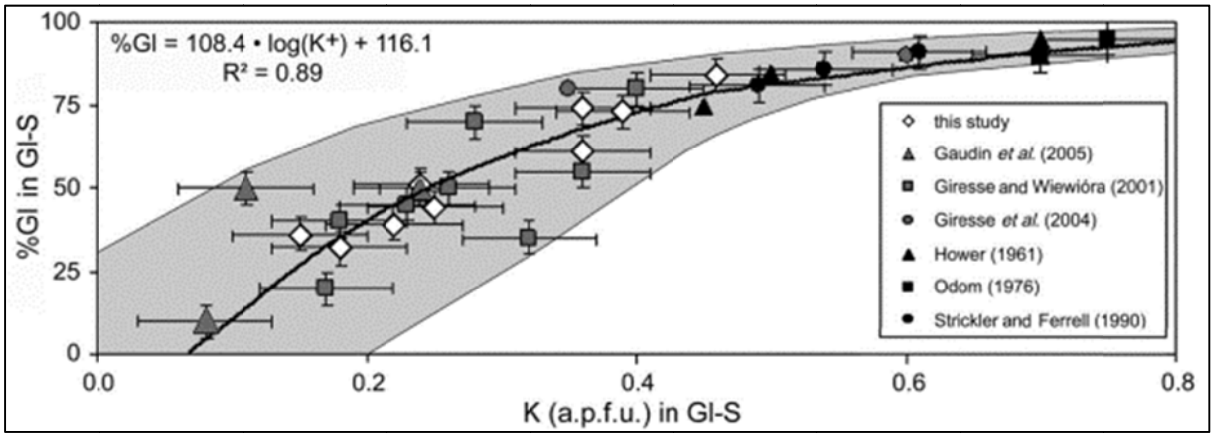

Fig. 4.11: Relationship between %Gl and interlayer K^+ content in Gl-S. Glauconite formation is accompanied by a continuous K^+ uptake.

The glauconitization rate in this modern deep-sea environment (ODP Site 959) is about five times less than that in the shallow shelf (*e.g.* Odin & Fullagar, 1988) which probably reflects the lower temperatures (~3-6ºC) and the limited supply and reflux of essential cations which are required for glauconitization such as Fe^{2+}, K^+, Mg^{2+}, and silica. However, the rate of deep-sea glauconite formation is notably faster than that of smectite illitization that occurs during burial diagenesis (*e.g.* Hower *et al.*, 1976), which may reflect the role of Fe, as shown by the positive linear correlation ($R^2 = 0.98$) between the increasing Fe_2O_3 content and the associated higher percentages of %Gl in Gl-S (Fig. 4.12).

As previously suggested by Baldermann *et al.* (2012), the availability of Fe and subsequently the extent of $Fe^{3+/2+}/Mg^{2+}$ for Al^{3+} substitutions in the octahedral sheet of the neo-formed Fe-smectite and related Gl-S is expected to have a major impact on the rate of glauconitization. With increasing proportion of bivalent octahedral cations such as Fe^{2+} and Mg^{2+} the octahedral charge increases and K^+ is progressively fixed into the interlayer sites to balance charge,

as documented by the TEM-EDX compositions of the Ivory Coast glauconites and Gl-S (Table 1). The proportion of Fe^{2+} in the green grains could not be determined in the present study due to the small amount of green grains available. However, the greening of the grain color with increasing burial depth indicates that some Fe^{2+} in the structural formulae of Gl-S is probable. Thus, the progressive fixation of Fe as well as Fe reduction during glauconitiza.-tion is considered to be a likely rate-controlling factor, as expressed in the linear relationship of increasing Fe_2O_3 contents and the state of glauconitization (Fig. 4.12).

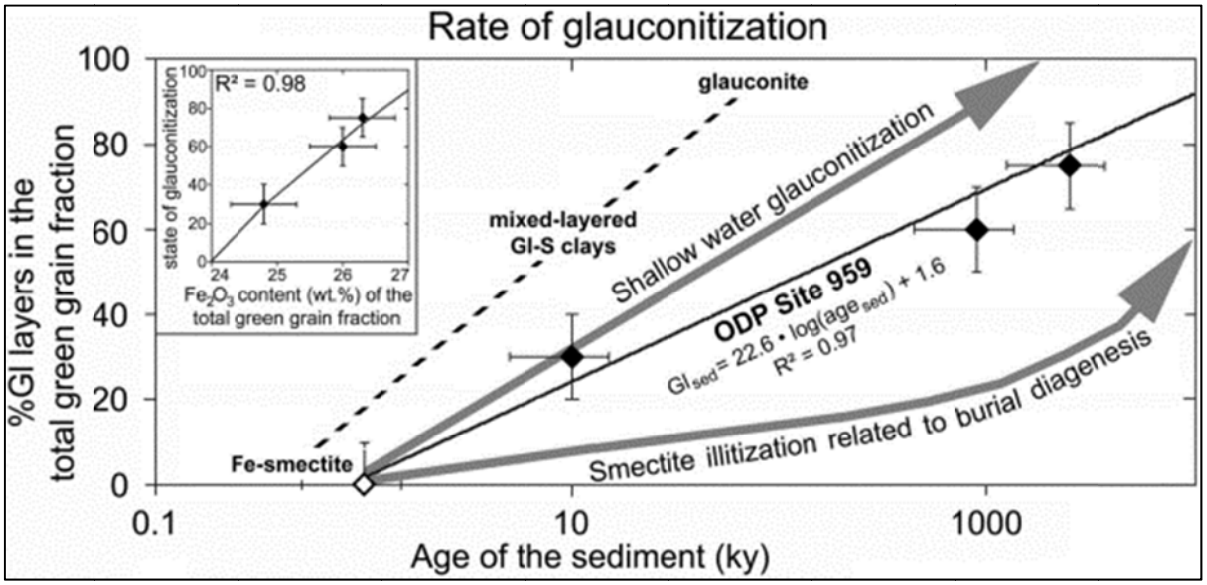

Fig. 4.12: Glauconitization rate for the ODP Site 959. The positive, linear correlation between increasing Fe_2O_3 content and the state of glauconitization implies that Fe could be the overall rate-limiting element (inserted box). The rate of shallow-water glauconitization, as suggested by Odin & Fullagar (1988) and the rate of illitization of smectite, as proposed by Hower *et al.* (1976) for the Gulf Coast sediments, are included for comparison.

4.6.4 Model for deep-water glauconite formation

As a result of the petrographic, mineralogical, and chemical observations in the present study, the glauconitization process of foraminifers' tests at ODP Site 959 is proposed to occur in three dominant steps (Fig. 4.13).

(1) After sedimentation (~0.01-1 ky), most of the marine organic matter was oxidized. This resulted in locally reducing and slightly acidic conditions ($pH_\mu < pH_{Sed} < pH_{SW}$) in the micro-environment of glauconitization (pH_μ) and the surrounding sediment (pH_{Sed}) compared to the seawater pH (pH_{SW}), as documented by the interstitial solution data (Fig. 4.10). Such conditions favored the dissolution of carbonate, biogenic opal, and silicate minerals (*e.g.* Raiswell & Canfield, 2012), making dissolved K^+, Mg^{2+}, and silica readily available at the ODP Site 959.

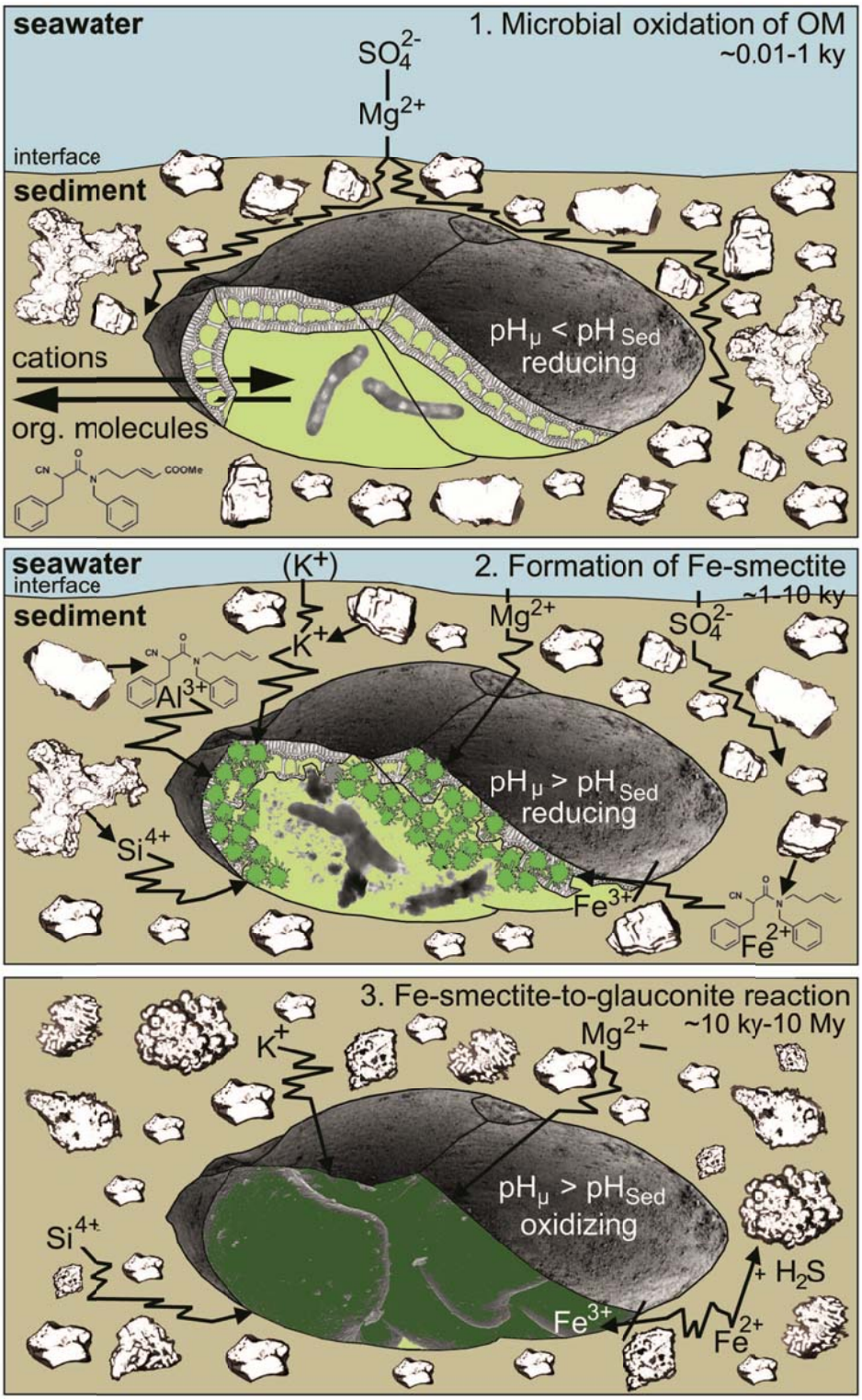

Fig. 4.13: Glauconitization model for ODP Site 959. (1) Microbial oxidation of organic matter (OM) generates locally occurring reducing and acidic conditions in the micro-environment of glauconitization such as in foraminifera tests and the surrounding sediment. These conditions enhance (silicate) mineral dissolution and the formation of cation-organic aquo-complexes. (2) As soon as the OM is consumed, oxidation of the organic complexes and of Fe^{2+} occurs. Subsequently, Fe-smectite formation takes place which is promoted by microbial activity and cation supply from the interstitial solution, while dissolution of skeletal calcite buffers the pH. (3) The Fe-smectite-to-glauconite reaction is controlled by the composition of the bulk interstitial solution and requires ~10 My to complete.

The mobilization and transport of Al and (in particular) Fe were probable limiting factors for the advance of glauconitization (Fig. 4.12). Iron and Al are virtually absent from aquatic systems at seawater pH and at the analyzed pH of the interstitial solutions (Turekian, 1968). One key mechanism for the mobilization of Fe and Al is the microbial oxidation of biodegradable (marine) organic matter within the foraminifera tests which is expected to reduce the pH by the supply of *e.g.* carboxylic acids (MacKenzie, 2005). At pH < 5 the solubility of FeO-OH and Al-O-OH notably increases through the dominance of aqueous $Fe(OH)^{2+}$ and $Al(H_2O)_6^{3+}$ species in the Fe_2O_3–Al_2O_3–H_2O system. The occurrence of Fe- and Al-containing organic aquo-complexes is enhanced under such conditions (*e.g.* McBride, 1994; Tipping, 2002).

(2) Immediately after the biodegradable marine organic matter was oxidized, the bacterial activity decreased, as indicated by the TEM observations (Fig. 4.8), and an oxidation front developed in the tests of foraminifera (Gaudin *et al.*, 2005). This initiates a local micro-environment suitable for glauconitization. In the presence of an expanding oxidation front, rapid degradation of Fe- and Al-organic aquo-complexes could take place and Fe^{2+} and Al^{3+} cations were released temporarily. Accompanied by a constant re-oxidation of Fe^{2+} to Fe^{3+} and rapid Al^{3+} supply, the formation of gel occurred contemporaneously with direct precipitation from bacterial biofilm. Subsequently, Fe-smectite formed within the amorphous precursor gels (see Fig. 4.8), initiated by the continuous cation supply from the surrounding sediment by chemical diffusion at moderate pH (pH_μ & $pH_{SW} > pH_{Sed}$) (see Martín-Algarra & Sánchez-Navas, 1995). Charpentier *et al.* (2011) suggested that ~1-10 ky are required for the quantitative precipitation of Fe-smectite in deep-sea, low-temperature environments.

(3) The Fe-smectite-to-glauconite reaction was then promoted by diffusion-controlled cation exchange between the micromilieu and the interstitial solutions ($pH_\mu < pH_{Sed}$; Eh ~ 0 mV), whereby both the initial sediment and the micro-environment of glauconitization became modified by several early diagenetic dissolution and replacement reactions, as described above. As dissolved K^+, Mg^{2+}, and silica are considered to have always been present in the interstitial solutions (Fig. 4.10), the availability of Fe is suggested to be the most important rate-limiting factor for glauconitization of the Ivory Coast sediments. As soon as the Fe supply stopped, *e.g.* by changes in the pH and Eh conditions within the micro-environment of glauconitization the Fe-smectite-to-glauconite reaction stopped as well. Such unsuitable conditions for the formation of glauconite could occur locally within the same micromilieu such as within one single foraminifera test, a feature which explains why green grains with varying color, reflecting a divergent state of maturity, are present within the same horizon.

The physical properties of the sediment such as porosity, permeability, and tortuosity appear to have been additional key factors for glauconitization, by influencing the interstitial solution chemistry and its exchange with the micro-environment via diffusion. Changes in the diffusion rate in the micro-environment, especially that of Fe and K, due to the loss of porosity and connectivity of pore space (Fig. 4.7-c and 4.7-f), may explain why the glauconitization rate slows down with increasing burial depth and aging of the sediment (Fig. 4.12). A reduced diffusion rate may also imply that as glauconization progresses the rate of K^+ fixation in Gl-S is relatively enhanced compared to the rate of formation of new Fe-smectite layers which can explain the logarithmic relationship between increasing %Gl in Gl-S and K content (see Fig. 4.11). This feature is probably attributed to the low thermodynamic stability of the Fe-smectite precursors (Gaudin *et al.*, 2005). Thus, the rate of glauconitization does decrease with increasing burial depth and subsequent ageing of the original sediments, and at these low temperatures the process requires ~10 My to complete in the deep-water environment of the ODP Site 959, compared to < 2 My in a shallow-water setting (Odin & Fullagar, 1988).

4.7 Summary and conclusions

Authigenic, green glauconitic grains, formed in the recent deep-sea environment (~2100 m) of the ODP Site 959, Ivory Coast – Ghana Marginal Ridge, were studied in order to characterize the key factors controlling the rate and mechanism of deep-sea glauconite formation at low temperatures (~3-6ºC). The following conclusions were reached:

(1) Glauconitization occurred mainly in calcareous, planktonic, and benthic foraminifera tests. These semi-confined, organic-rich micro-environments provided the post-depositional conditions suitable for glauconitization.

(2) XRD, TEM, and FIB-SEM results of the unaltered light green grains from 0.16 mbsf revealed Fe-smectites as the precursor phases for glauconite formation. The Fe-smectites were formed by direct precipitation from amorphous gels containing Fe, Mg, Al, and silica generated from microbial biofilm with cations supplied by diffusion from interstitial solutions.

(3) During the later stages of early marine diagenesis, the neo-formed Fe-smectites changed into Gl-S and finally into glauconite with no recognizable compositional gaps between the Fe-smectite and glauconite end members, as identified by combined Sybilla© modeling, XRD, TEM-EDX, and TEM-SAED analysis.

(4) The composition of the interstitial solution was influenced heavily by microbial oxidation of marine organic matter, Fe-redox reactions, and silicate and carbonate mineral weathering, as indicated by the SEM and hydrochemical results, and all of these early diagenetic alteration processes were important for maintaining glauconitization within the sediment pile.

(5) The rate of deep-water glauconite formation depended mainly on continuous Fe supply but due to the low-temperature conditions the rate of reaction was about five times less than that in shallow-shelf regions.

Chapter 5

Substantial iron sequestration during green-clay authigenesis in modern deep-sea sediments

3.1 Abstract

In much of the global ocean, Fe is a limiting nutrient for marine productivity. The formation of pyrite has been considered the most important sink of reactive Fe in modern, organic-rich sediments. However, clay mineral transformations can also lead to long-term sequestration of Fe during late diagenesis and in hydrothermal settings. Here we present evidence for substantial F sequestration during the early diagenetic formation of ferruginous clay minerals, also called green-clay authigenesis, in the deep-sea environment of the Ivory Coast–Ghana Marginal Ridge. Using high-resolution electron microscopic methods and sequential sediment extraction techniques, we demonstrate that Fe uptake by green-clay authigenesis can amount to 76±127 μmol $Fe \cdot cm^{-2} \cdot kyr^{-1}$, which is on average six times higher than that of pyrite in suboxic subsurface sediments 5 m below the seafloor or shallower. Even at depths of 15 m below the seafloor or greater, rates of Fe burial by green clay and pyrite are almost equal at ~80 μmol $Fe \cdot cm^{-2} \cdot kyr^{-1}$. We conclude that green-clay formation significantly reduces the pore water inventory of dissolved Fe in modern and ancient pelagic sediments, which challenges the long-standing conceptual view that clay mineral diagenesis is of little importance in current biogeochemical models of the marine iron cycle.

5.2 Introduction

The redox chemistry and bioavailability of iron plays an important role in many Earth surface processes (Martin, 1990; Martin *et al.*, 1994; Coale *et al.*, 1996; Blain *et al.*, 2007; Taylor & Konhauser, 2011; Posth *et al.*, 2014), and has been of major importance in the evolution of

ocean geochemistry and life forms throughout the geologic record (Poulton *et al.*, 2010; Taylor & Macquaker, 2011; Raiswell & Canfield, 2012; Köhler *et al.*, 2013). Advances in the study of iron biogeochemistry over the past three decades have greatly improved our understanding of fluxes in the marine iron cycle, with the recognition of multiple Fe sources and sinks (Berner, 1969; Canfield, 1989; Raiswell & Canfield, 1998; Poulton & Raiswell, 2002; Elrod *et al.*, 2004; Jickells *et al.*, 2005; Raiswell *et al.*, 2006; Cassar *et al.*, 2007; Homoky *et al.*, 2013). Such studies reveal highly complex linkages between modern ocean geochemistry, biological response, and the mineralogy and composition of marine sediments (Raiswell & Canfield, 2012; Johnson *et al.*, 2003; Boyd & Ellwood, 2010; Cumming *et al.*, 2013).

A number of numerical reservoir-flux and ocean circulation models have attempted to quantify the mass balance relationships in the global iron cycle on the basis of fluxes in the continental solid-phase Fe input, its concentration in seawater, and in oceanic sediments (Poulton & Raiswell, 2002; Johnson *et al.*, 2003; Parekh *et al.*, 2004). Since the oxygenation of the deep ocean in the late Neoproterozoic, ocean basins generally contain dissolved Fe in trace level concentrations (*e.g.* Canfield *et al.*, 2007). Fluxes in the ancient marine iron cycle have therefore been reconstructed on the basis of the sequential extraction and subsequent quantification of multiple Fe mineral reservoirs recorded in sedimentary archives, assuming steady state between continental Fe sources and marine sediment sinks (*e.g.* Canfield *et al.*, 1993; Poulton & Raiswell, 2005; Raiswell *et al.*, 2006; Raiswell & Canfield, 2012). In present biogeochemically coupled ocean circulation models, the fluxes in the modern marine iron cycle are routinely estimated using *in situ* measured rates of dissolved Fe release from the seafloor, which indirectly account for the bulk of all Fe mineral sources and sinks (Elrod *et al.*, 2004; Boyd & Ellwood, 2010; Severmann *et al.*, 2010; Homoky *et al.*, 2011; John *et al.*, 2012; Homoky *et al.*, 2013; Dale *et al.*, 2015). Today, the main fraction of continental Fe input into the oceans is attributed to (nano)particulate Fe-(oxy)hydroxides (Raiswell, 2011). In anoxic pore waters, such as in the Black Sea and the Orca Basin, Fe-sulfide formation occurs following reductive dissolution of highly labile Fe-(oxy)hydroxides, and is considered to be the most important sink of reactive Fe in modern, organic-rich sediments (Canfield *et al.*, 1993; Passier *et al.*, 1997; Raiswell & Canfield, 1998; Raiswell & Canfield, 2012).

Clay mineral transformations are now also being considered as key sources and sinks within the marine iron cycle. For example, the early diagenetic release of smectite nano-particles bearing Fe(III) can provide an intermediary source of dissolved Fe to some deep-ocean waters (*e.g.* Homoky *et al.*, 2011). There is also growing evidence for significant transformation of highly reactive (unsulfidized) Fe to clay mineral sinks during late diagenesis (Poulton *et al.*,

2010) and in hydrothermal settings (Chester, 2000). The rate of Fe sequestration by green-clay authigenesis, however, has been overlooked as a central factor controlling the burial of Fe in pelagic sediments of modern and ancient oceans.

At ODP Site 959 (Fig. 5.1-A), on the Ivory Coast – Ghana Marginal Ridge (eastern equatorial Atlantic Ocean), the majority of the highly reactive solid-phase Fe input is directly utilized during green-clay authigenesis to form Fe(III)-smectite, mixed-layered glauconite-smectite (Gl-S), and finally glauconite minerals (Baldermann *et al.*, 2013). The availability of reactive Fe in suboxic near-subsurface sediments is therefore suggested to be the most important rate-determining factor for the also-called glauconitization reaction (Baldermann *et al.*, 2013), albeit no attempt has been made so far to quantify the rate of Fe burial attributed to this authigenic green-clay sink (Dale *et al.*, 2015). For the first time, we present rates of Fe sequestration related to early diagenetic green-clay formation versus pyrite precipitation. Our results suggest that Fe uptake during green-clay authigenesis significantly lowers the efficiency of benthic Fe redox (re)cycling in modern and ancient sediments.

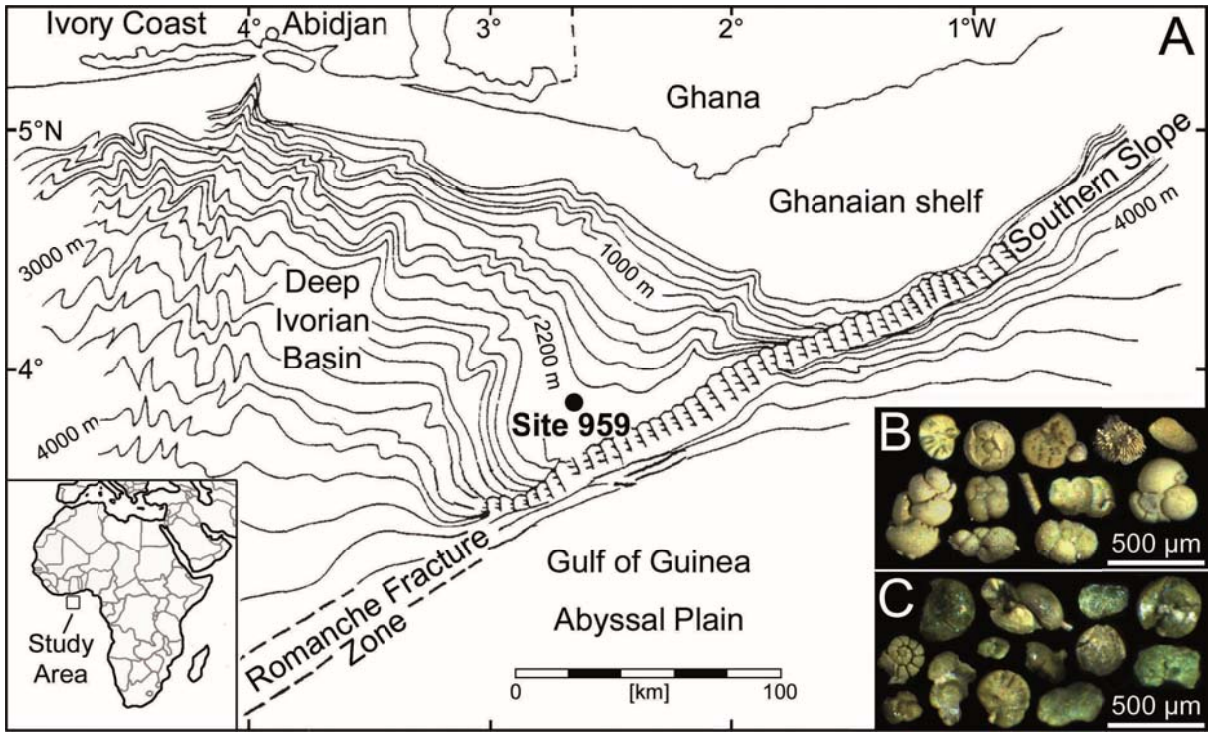

Fig. 5.1: Appearance and evolution of Fe-bearing, authigenic green-clay minerals in the Ivory Coast deep-sea sediments (ODP Site 959). A) Location map of ODP Hole 959C on the Ivory Coast – Ghana Marginal Ridge. B-C) Light microscopy images of immature (smectite-rich), light green grains from 0.16 mbsf (B) and of evolved (glauconite-rich), medium to dark green grains from 24.91 mbsf (C). The changes in the color and in the maturity of the green grains downwards in the sedimentary pile are due to a significant uptake of dissolved Fe from pore waters.

5.3 Methods

5.3.1 Materials and sampling strategy

During ODP Leg 159 in 1996, Hole 959C (latitude: 3°37.6690 N, longitude: 2°44.1160 W) was drilled on a small plateau on the northern flank of the Ivory Coast–Ghana Marginal Ridge in a water depth of 2100 m and 3°C seawater temperature. Cores from this site are of particular interest, because of their slow and continuous sedimentation rates (1-2 $cm \cdot kyr^{-1}$) from at least the Miocene to the Holocene. Sediments from Hole 959C are thus ideal for high-resolution and long-scale reconstruction of the fluxes in the marine iron cycle. Sediment volumes of ~30 cm^3 (21 samples in total) were taken from the top 25 m of ODP Hole 959C, from the core which is stored at the Bremen Core Repository (BCR), using sediment sample slices (4 cm long, 3 cm wide and 4 cm thick). The sampled section covers a sedimentary sequence from the Early Holocene (0.16 mbsf, ~0.01 Myr ago) to the Late Pliocene (24.91 mbsf, ~2.5 Myr ago). Rietveld-based mineral quantification of powder XRD patterns obtained from bulk sediment samples, as well as from the separated < 32 µm and < 5 µm size fractions, reveals that secondary gypsum, if present, occurs only in trace amounts (< 0.1 wt.% from 0.16-20.71 mbsf and ~0.2 wt.% at 24.91 mbsf), suggesting insignificant pyrite of oxidation occurred during storage at the BCR. The bulk mineralogy of samples is reported in SI Table 5.1.

5.3.2 Separation and characterization of the authigenic green clay mineral fraction

The authigenic green grain fraction was determined on an aliquot of air-dried sediment after collection using a 32 µm sieve and following dissolution of carbonate content with 10% acetic acid for 1 h. The amount of green grains was then calculated by weighing the carbonate-free size fraction coarser than 32 µm after subtraction of the radiolarian, pyrite and quartz content of < 5 wt.%. The dominance of glauconite minerals in the > 32 µm size fraction (> 95 wt.%) and their absence in the < 32 µm size fraction (detection limit < 3 wt.%) was controlled by quantitative X-ray diffraction analysis. However, owing to the poor crystalline nature and the geochemical and mineralogical heterogeneity of mixed-layered Gl-S phases, the accuracy of the estimated green-clay mineral content is ±5%.

To study the burial diagenetic uptake of Fe by glauconitization ($Fe_{Gl\text{-}S}$), ~50 mg of the green grains were separated by hand-picking under a binocular microscope from the pale to light green, the medium green and the dark green grain sub-fractions of samples taken at 0.16 mbsf (10 kyr), 11.69 mbsf (900 kyr) and 24.91 mbsf (2500 kyr). The chemical composition of clay mineral particles in the separated green grain sub-fractions was determined by energy-disper-

sive X-ray spectroscopy (EDX) using a Jeol JEM 1210 transmission electron microscope equipped with an Oxford Instruments Pentafel Link-Model 6635 detector at Greifswald University. TEM-EDX analyses were performed on single clay mineral particles using an accelerating voltage of 200 kV and 10 s count time to reduce element migration and loss. The standard deviations were < 30% for Na, K and Ca, < 10-15% for Al and Mg, and < 5% for Si and Fe analysis, which is equivalent to an analytical error of < 2 wt.% for the above elements. The chemical compositions and calculated structural formulae of clay mineral particles in the collected green grain sub-fractions are reported in Baldermann *et al.* (2013).

High-resolution TEM lattice fringe images were collected parallel to the (001)-plane of the clay minerals using a FEI Tecnai F20 instrument operated at 200 kV accelerating voltage and fitted with a Schottky field emitter, a Gatan imaging filter, and an UltraScan CCD camera (Graz University of Technology). For further calculation of the Fe(II)/Fe(III) ratios in the green-clay sub-fractions, electron energy-loss spectroscopy (EELS) data were recorded in the TEM mode of the microscope using a convergence semi-angle of 6.06 mrad, a semi-angle of 11.9 mrad, 200 kV accelerating voltage, and an acquisition time of 100 s. The energy resolution was determined to be 0.5 eV at the full-width at half-maximum of the zero-loss peak. Background subtraction of the EELS spectra was realized using an inverse power-law function, which was extrapolated from the O K pre-edge region. The intensity ratio of the Fe L_3 and L_2 lines was then calculated by integration over the 708.5-710.5 eV and 719.7-721.7 eV ranges, and the Fe(II)/Fe(III) ratio calculated using the integral Fe $L_{2,3}$-edge white-line intensity ratio as a function of the $Fe^{3+}/\Sigma Fe$, as reported in van Aken *et al.* (1998) and Baldermann *et al.* (2014). Based on the combination of EDX and EELS data, the chemical compositions and structural formulae of the authigenic clay mineral particles, reported in Baldermann *et al.* (2013), have been corrected for the Fe(II)/Fe(III) ratios and are shown in SI Table 5.2.

5.3.3 Bulk and sequential sediment extraction techniques

The fraction of Fe originally present as pyrite (Fe_{Py}) was estimated on the basis of the total sulfur (S_{tot}) contents of bulk sediment samples, which were obtained by elemental analysis after combustion in a CE Instruments EA 110 CHN elemental analyzer (Leibniz Institute for Baltic Sea Research, Warnemünde). A range of in-house standards was run at the beginning and at the end of the sulfur measurements and the analytical error was determined to be < 5% for S_{tot} analyses.

Air-dried bulk sediment samples were subjected to a two-stage extraction procedure to determine the proportion of Fe attributed to highly reactive Fe-(oxy)hydroxides and poorly reac-

tive silicate phases, using the sequential sediment extraction procedure of Poulton & Raiswell (2005). The fraction of Fe present in amorphous and crystalline Fe-(oxy)hydroxides (Fe_D), such as goethite, ferrihydrite, lepidocrocite and hematite (with the exception of magnetite), is highly reactive towards dissolved sulfide and was solubilized in a citrate-buffered sodium dithionite solution (pH=4.8) for 2 h. The boiling 12 N HCl extraction technique was then used to remove Fe, which reacts only slowly with dissolved sulfide (Fe_H). This technique additionnally extracts the dithionite-extractable minerals, magnetite, and partly attacks sheet silicates. Thus, Fe_H-Fe_D-$Fe_{Gl\text{-}S}$ represents a poorly reactive Fe fraction that is attributed to detrital clay minerals bearing Fe(III) (Fe_{DC}) – that is illite, smectite, and chlorite. The extracted Fe concentrations were analyzed with a PerkinElmer Optima 4300 DV ICP-OES at Graz University of Technology. Fe measurements of replicate extractions (n=4) of the Toronto Harbour sediment standard TH-2 were within ±3% of the certified value. Finally, the total Fe_2O_3 content of bulk sediment samples (Fe_T) was measured by wavelength-dispersive X-ray fluorescence (XRF) spectroscopy using a Philips PW2404 X-ray spectrometer (Graz University of Technology). Tablets were run together with a range of USGS standards, and the analytical error was determined to be < 4% for the major elements, including Fe.

Fe_T can be used to estimate the remaining fraction of Fe that is bound in silicates, and this Fe fraction is considered to be unreactive towards dissolved sulfide (Fe_U). Here, the difference between Fe_T and $Fe_{HR} + Fe_{Py} + Fe_{Gl\text{-}S} + Fe_{DC}$ yielded ΔFe values from -0.1 to +0.2 wt.%, which is equivalent to a total Fe mass balance error of ±2%, on average. This observation indicates that the analytical approach used in this study is suitable to determine the proportions of Fe present in multiple-mineral sources and sinks to a high degree of accuracy. Hence, variations in the abundances of Fe_{HR}, Fe_{Py}, $Fe_{Gl\text{-}S}$ and Fe_{DC}, relative to Fe_T, should reflect early diagenetic mass transfer of Fe within the sedimentary column. The solid-phase speciation data of detrital (Fe_D and Fe_{DC}) versus authigenic ($Fe_{Gl\text{-}S}$ and Fe_{Py}) ferruginous mineral phases for ODP Hole 959C are reported in SI Table 5.3, and calculated Fe supply and Fe sequestration rates are provided in SI Table 5.4.

5.4 Results

5.4.1 The glauconitization process

The near-surface sediments (≤ 3 mbsf) of the Ivory Coast – Ghana Marginal Ridge that are rich in foraminifera tests show mostly light green-clay infillings (0.9-6.0 wt.% with an average of 2.5 wt.%) related to glauconitization (Fig. 5.1-B). Medium to dark green grains domi-

nate in the more deeply buried sediments below 5 mbsf (Fig. 5.1-C), and occur together with late diagenetic pyrite overgrowths (see SI Table 5.1 for bulk mineralogy). High-resolution TEM lattice fringe images of light green clay matter from 0.16 mbsf show the predominance of immature Fe(III)-smectite and smectite-rich Gl-S phases, with an average smectite lattice thickness of 1.3 nm (Fig. 5.2-A). Abundant glauconite layers each 1.0 nm thick occur within more mature Gl-S phases and pure glauconite grains (Fig. 5.2-B) that dominate between 11.69 mbsf and 24.91 mbsf depth.

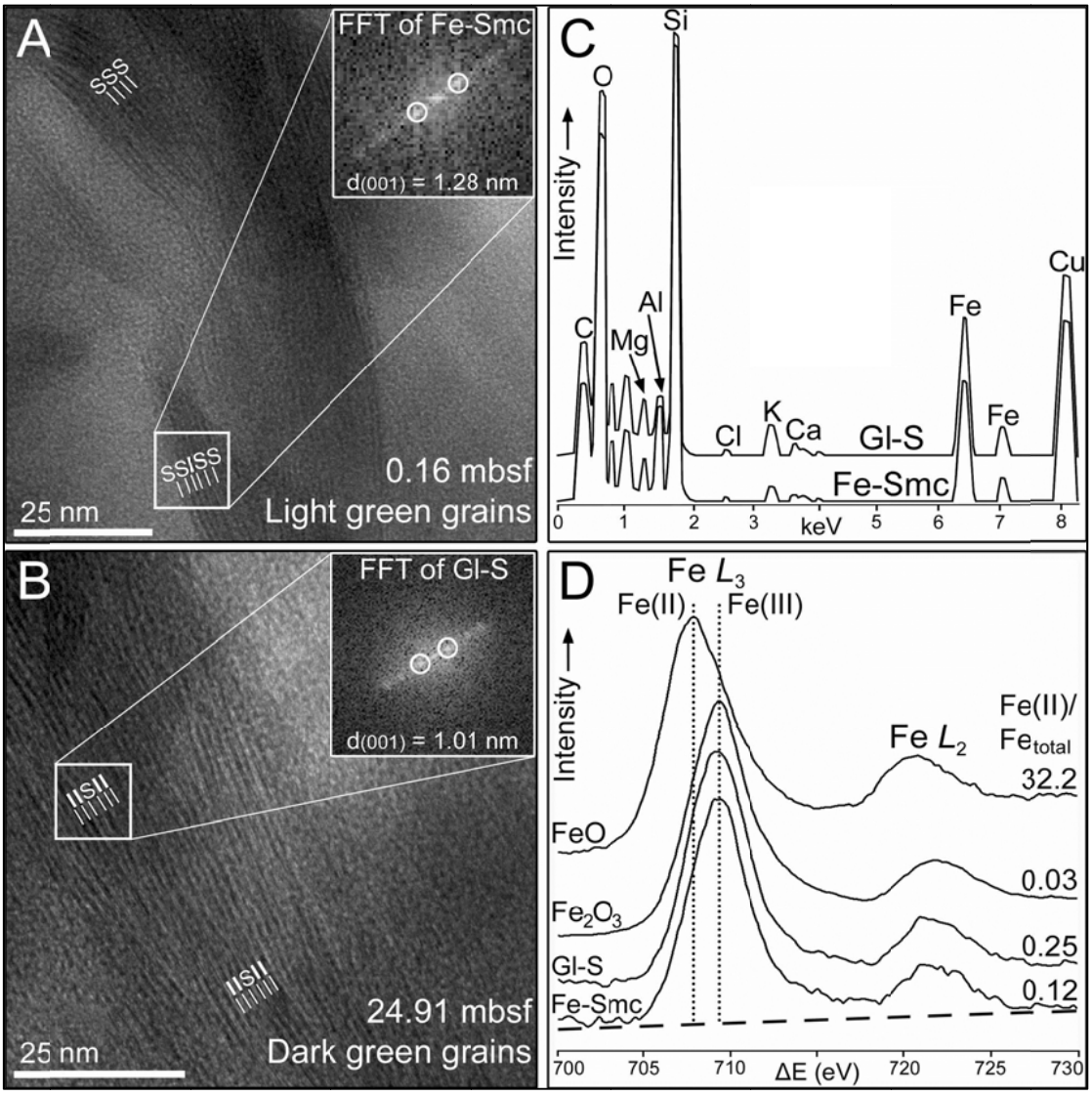

Fig. 5.2: Reaction mechanism and Fe uptake during green-clay authigenesis. A-B) High-resolution TEM lattice fringe images and fast Fourier transform (FFT) patterns of original Fe-smectite (Fe-Smc) particles (A) that are subsequently transformed into glauconite-smectite (Gl-S) particles (B) with the increasing state of burial diagenesis. I = glauconite layers; S = smectite layers. C) Chemical composition of authigenic Fe-Smc and Gl-S, with notably more Fe and K in Gl-S. D) Electron energy-loss spectroscopy data and calculated Fe(II)/Fe_{total} ratios of Fe-Smc and Gl-S, exhibiting a significant increase in the Fe(II) content by ~133% as glauconitization progresses. Hematite (Fe_2O_3) and wüstite (FeO) are standards.

Recent work on deep-water glauconitization of foraminifera tests suggests that Fe(III)-smectite forms close to the sediment-seawater interface within less than 10 kyr by crystallization from Fe-Mg-Al-silica-rich precursor gels present in bacteria-produced biofilms (*e.g.* Charpentier *et al.*, 2011; Baldermann *et al.*, 2013). The burial diagenetic Fe(III)-smectite to glauconite reaction is driven by continuous cation supply from surrounding slightly alkaline and reducing pore waters, with the essential Fe^{2+} (and K^{+}) ions being delivered by microbial-mediated reductive dissolution of highly labile Fe-(oxy)hydroxides and progressive alteration of K-rich, detrital silicates and carbonate minerals (Baldermann *et al.*, 2013).

Accordingly, quantitative geochemical analysis of the green-clay fraction collected at various depths beneath the sediment-seawater interface show compositions ranging from pure Fe(III)-smectite to Gl-S, with notably more K and Fe but less Al in glauconitic Gl-S (Figs 5.2-C and 5.2-D). A strong Fe(II) increase of ~133% and a moderate total Fe(II+III) gain of ~8% is evident with the advancing states of green-clay maturity (see SI Table 5.2 for chemical composition data). The availability and the concentration of Fe^{2+} ions in the interstitial solutions, and hence the extent of Fe(II) incorporation through the entire Fe(III)-smectite to glauconite reaction, is therefore expected to be a key factor that controls the rate of Fe sequestration during deep-water glauconitization. These observations explain both the occurrence of more glauconite layers in Gl-S phases with ageing of the sediment and the depth-dependent greening of the grain color with elevated Fe(II) contents. Moreover, these findings are suggestive of an authigenic origin for the green-clay infillings (Baldermann *et al.*, 2013).

5.4.2 Distribution of solid-phase iron present in detrital vs. authigenic sources

The detrital Fe(III)-bearing clay mineral fraction (Fe_{DC}) of illite, chlorite, and smectite show no significant vertical changes, relative to the bulk sediment Fe content, Fe_T ($Fe_{DC}/Fe_T = 0.11 \pm 0.08$), indicating a constant background sedimentation at ODP Site 959 and a poorly reactive nature of Fe_{DC} during diagenesis. Indeed, a significant decrease of ~58% of the labile Fe-(oxy)hydroxide fraction, Fe_D, was observed downwards in the sedimentary column (Fig. 5.3-A and SI Table 5.3), which is equivalent to a reduction of the Fe_D/Fe_T ratio from 0.80 to 0.34 (Fig. 5.3-B). Reductive dissolution of Fe_D is facilitated under the suboxic conditions at this site (Mascle *et al.*, 1996), and this reaction supplied the majority of Fe^{2+} ions to the pore water that are required for the early diagenetic glauconitization and late diagenetic pyritization (Fig. 5.3-D). Accordingly, a slight depth-dependent increase in the proportion the green-clay infillings (2.5 wt.% on average), $Fe_{Gl\text{-}S}$, and, more noticeably, of pyrite (0.2 to 2.5 wt.%), Fe_{Py}, was recognized to occur with burial (Fig. 5.3-A). These variations reflect vertical changes in

the $Fe_{Gl\text{-}S}/Fe_T$ ratio from 0.06 to 0.47 (0.16 on average) and from 0.01 to 0.25 for Fe_{Py}/Fe_T (Figs 5.3-A and 5.3-B). In the sediment top layers (≤ 5mbsf), Fe uptake related to green-clay authigenesis is thus three to seven times (in one case up to 37 times) higher than that of pyrite formation. At greater depths (≥ 15 mbsf), pyritization becomes more important, but ~50% of net Fe sequestration is still attributed to glauconitization (Fig. 5.3-C).

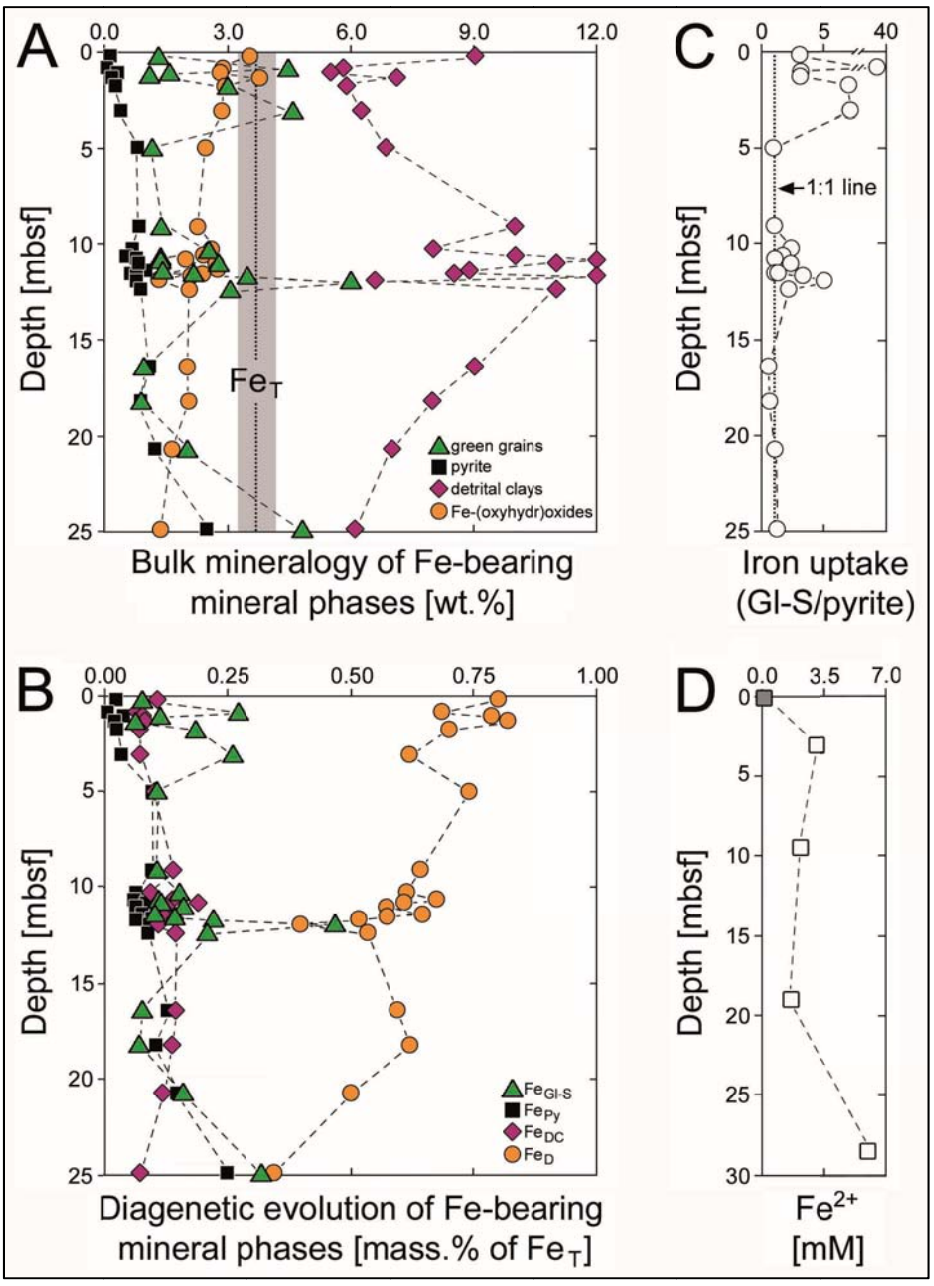

Fig. 5.3: Composition, distribution and spatial evolution of solid-phase Fe at ODP Site 959. A) Depth profiles for Fe-(oxy)hydroxides (Fe_D), detrital clays (Fe_{DC}), authigenic green grains ($Fe_{Gl\text{-}S}$), and pyrite (Fe_{Py}). The $Fe_{Gl\text{-}S}$ and Fe_{Py} data are from Baldermann *et al.* (2013). The range of the bulk sediment Fe_2O_3 contents, Fe_T, is indicated by the grey box. B) Spatial variations in the solid-phase Fe speciation within the sedimentary column. C) Ratio of Fe sequestration related to glauconitization versus pyritization. D) Dissolved Fe concentration in seawater (grey square) and local pore waters (white squares, data from Mascle *et al.*, 1996).

5.5 Discussion

5.5.1 Rate of iron supply and iron sequestration at ODP Site 959

Our solid-phase Fe speciation data indicates that the continental Fe input is attributed to Fe_D and subordinate Fe_{DC} sources (Figs 5.3-A and 5.3-B), which have been delivered by wet and dry deposition of Saharan dust and recycling of coastal sediments (Giresse *et al.*, 1998). Considering no significant changes in the source and mineralogy of solid-phase Fe input occurred during the past 2.5 Myr (Giresse *et al.*, 1998) and low but linear sedimentation rates (Wagner, 1998), the bulk accumulation rate of solid-phase Fe (AR_{Fe}) at this site (Fig. 5.4) ranged from 287 to 783 µmol $Fe \cdot cm^{-2} \cdot kyr^{-1}$ (459 µmol $Fe \cdot cm^{-2} \cdot kyr^{-1}$ on average), calculated on the basis of Fe_T (SI Table 5.4). The estimated AR_{Fe} is~2.6 to 4.3 times higher than that of open-ocean North Pacific sediments, but is in the range of AR_{Fe} observed in modern, circum-equatorial Pacific sediments (200-900 µmol $Fe \cdot cm^{-2} \cdot kyr^{-1}$) and in Atlantic Ocean deep-sea sediments (Chester, 2000). As a first approximation, aeolian Fe inputs ranged from ~90 to 197 µmol $Fe \cdot cm^{-2} \cdot kyr^{-1}$, which is equivalent to ~25 to 31% of AR_{Fe}, using deposition rates of atmospheric dust for western equatorial Africa (Jickells *et al.*, 2005) from 5 to 10 $g \cdot m^{-2} \cdot yr^{-1}$ and a Fe_D content of Saharan dust of 1.08 ± 0.15 wt.% (Poulton & Raiswell, 2005). About 75 to 69% of AR_{Fe} is therefore expected to be supplied from resuspended shelf sediments and by coastal upwelling. These rate estimates may be biased towards changes in the deposition rates of Saharan dust and any other sources of particulate iron – for example, surface runoff. The accumulation rate estimates also ignore minor fractional uptake of Fe by phytoplankton in the photic zone (*e.g.* Johnson *et al.*, 1994; Jickells *et al.*, 2005; Cassar *et al.*, 2007; Boyd & Ellwood, 2010). How-ever, owing to the low organic carbon accumulation rates of ~10 µg $C \cdot cm^{-2} \cdot kyr^{-1}$ and the oxi-dizing pore water conditions in the near-subsurface layers of the Ivory Coast sediments, AR_{Fe} should reflect mainly initial Fe_D and Fe_{DC} deposition (*e.g.* Giresse *et al.*, 1998; Jickells *et al.*, 2005).

At ≤ 5 mbsf (Fig. 5.4), Fe_D ranged from 225 to 485 µmol $Fe \cdot cm^{-2} \cdot kyr^{-1}$, but it decreased with burial down to 179 µmol $Fe \cdot cm^{-2} \cdot kyr^{-1}$ at 24.91 mbsf owing to ongoing reductive dissolution of Fe_D under the given redox conditions. In contrast, Fe_{DC} delivery remained constant at 51 ± 30 µmol $Fe \cdot cm^{-2} \cdot kyr^{-1}$ within the top 25 m of sediments. Microbial reduction of highly labile Fe_D during early diagenesis provides a secondary pool of dissolved Fe that is required for glauconitization, as reflected by the syngenetic formation of Fe(III)-smectite and smectite-rich Gl-S phases (Figs 5.2-A and 5.3-D). Under the initial sulfide-depleted conditions in the Ivory Coast pore waters, pyrite precipitation is ineffective and accounted only for 2 to 29 µmol

$Fe \cdot cm^{-2} \cdot kyr^{-1}$, which is in the narrow range of the global burial rate of Fe associated with pyrite in near-surface, organic-poor deep-sea sediments (~30 µmol $Fe \cdot cm^{-2} \cdot kyr^{-1}$; Berner, 1982). Hence, in the top 5 m of sediment, Fe sequestration during green-clay authigenesis (23 to 204 µmol $Fe \cdot cm^{-2} \cdot kyr^{-1}$ with an average rate of 76 µmol $Fe \cdot cm^{-2} \cdot kyr^{-1}$) is on average six times faster than pyritization. During advanced stages of diagenesis, microbial heterotrophic and abiotic sulfate reduction results in elevated pore water sulfide concentrations, as recorded by late diagenetic pyrite overgrowths that occur together with evolved Gl-S phases and pure glauconite minerals (Figs 5.2-B and 5.3-A). Thus, between 5 and 15 mbsf, pyritization progresssively becomes more important (36 µmol $Fe \cdot cm^{-2} \cdot kyr^{-1}$), but even at depth (≥ 15 mbsf) there is almost a 50% distribution between Fe uptake by green-clay (80 µmol $Fe \cdot cm^{-2} \cdot kyr^{-1}$) versus pyrite (81 µmol $Fe \cdot cm^{-2} \cdot kyr^{-1}$).

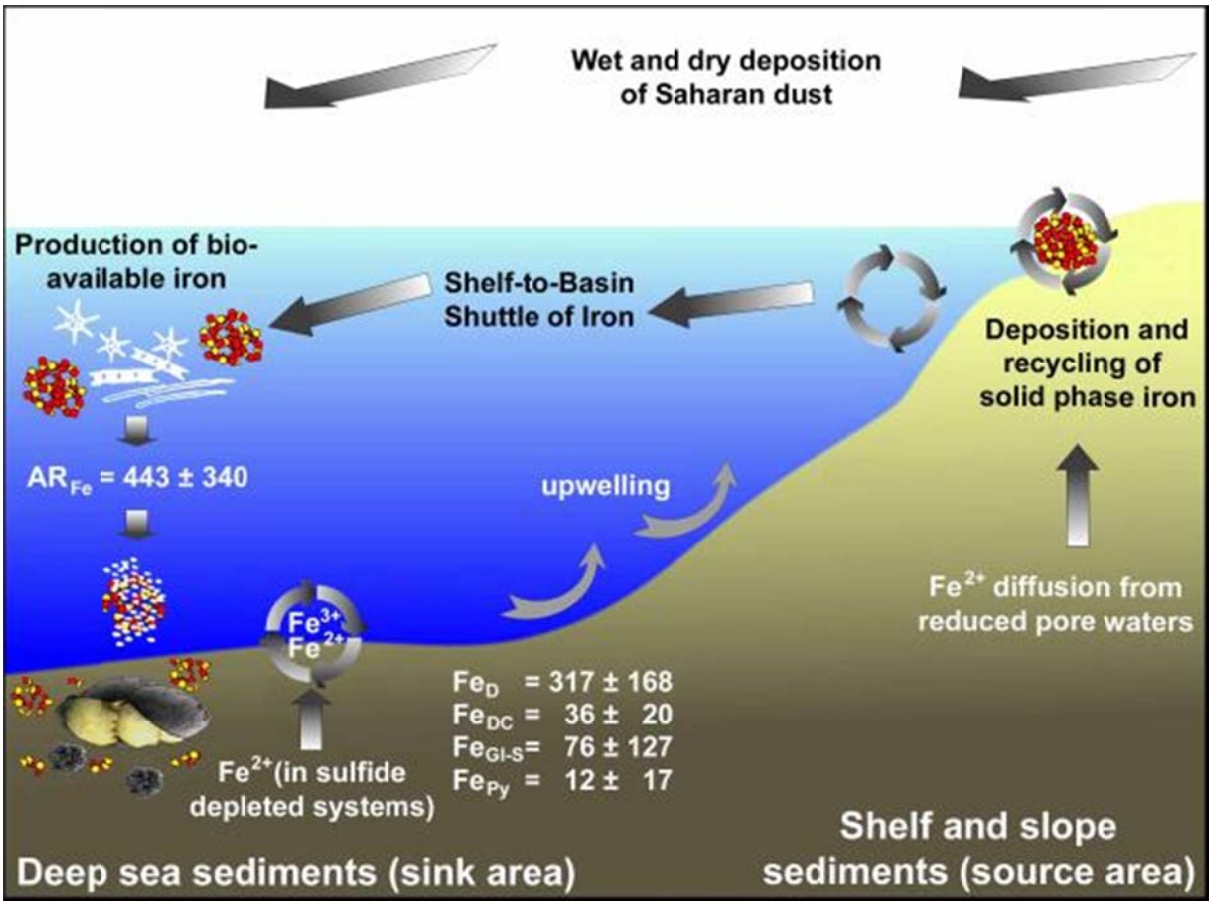

Fig. 5.4: Schematic model illustrating the marine, sedimentary iron cycle at ODP Site 959. The bulk accumulation rate of solid phase Fe, AR_{Fe}, represents the Fe input from continental source areas. The rates of Fe sequestration for the top 5 m of deep-sea sediment include the contribution of authigenic green glauconitic grains (Fe_{Gl-S}), pyrite (Fe_{Py}), detrital clay minerals (Fe_{DC}) and Fe-(oxy)hydroxides (Fe_D) to the sedimentary Fe budget. All rates are given in µmol $Fe \cdot cm^{-2} \cdot kyr^{-1}$.

5.5.2 Green-clay authigenesis as an ignored iron sink

Up to now, authigenic glauconite minerals are commonly assumed to be widely absent both in modern and ancient deep-sea sediments, or to occur in small quantities (< 1-2 wt.%; Logvinenko, 1982; Raiswell & Canfield, 2012;). Moreover, in suboxic and euxinic environments, the establishment of sulfide-dominated pore waters inhibits green-clay authigenesis by the utilization of pore water Fe^{2+} during the formation of Fe-sulfides (Passier *et al.*, 1997; Raiswell & Canfield, 1998; Poulton *et al.*, 2004). However, recent studies on the formation and distribution of green-clay both in modern and ancient ocean floor sediments have shown that glauconitization is a globally occurring phenomenon. Although glauconite minerals are not distributed homogeneously in deep-sea sediments, the green-clay fraction often accounts for about 1-10 wt.% (2-3 wt.% on average) of calcareous, fossiliferous sediments, such as those reported from the Iberian Coast, the Gulf of Guinea, the Kerguelen Plateau, the Mediterranean Sea, and the western margin of South Africa (*e.g.* Odin, 1988; Giresse *et al.*, 2004; Wigley & Compton, 2007; Baldermann *et al.*, 2013). These green-clay forming environments are characterized by a prolonged residence time at the sediment-seawater interface, and sufficient ionic exchange of Fe^{2+} and K^{+} between surrounding pore fluids and the micro-environment and precursor mineral phases from which the ferruginous green-clay forms. Even higher enrichments of authigenic green-clay – namely, 1-5 up to 30 wt.% of smectite bearing Fe(II) and Fe(III) – have been reported from hydrothermal muddy sediments of the Galapagos spreading centre, the Mid-Atlantic Ridge, the Crozet Island Archipelago, the Costa Rica Margin, the Pacific-Antarctic Ridge, and the Chile Ridge (*e.g.* Thompson *et al.*, 1985; Buatier *et al.*, 1989; Charpentier *et al.*, 2011; Cuadros *et al.*, 2011; Homoky *et al.*, 2011). At these mid-ocean ridge sites, the rate of Fe sequestration related to green-clay authigenesis can locally easily exceed 1000 μmol $Fe \cdot cm^{-2} \cdot kyr^{-1}$ (Chester, 2000). In contrast to these spatially restricted hydrothermal Fe-clay deposits, which have already been considered as a minor component of global oceanic Fe sinks (Chester, 2000), the importance of ultimate Fe uptake during the more widespread glauconitization has been overlooked, and thus its role as an important sink of Fe in modern and ancient pelagic sediments is still ignored.

5.6 Summary and conclusions

At ODP Site 959, the rate of Fe sequestration attributed to glauconitization is nearly constant and elevated throughout the uppermost 25 m of sediment (~80 μmol $Fe \cdot cm^{-2} \cdot kyr^{-1}$), and hence must be viewed as an important variable in the sedimentary iron budget, in particular when

the accompanying rate of pyrite formation is low. The latter feature leads us to suggest that Fe uptake by authigenic clay minerals was much more important on a global scale during periods of the ancient Earth (for example, in the Neoproterozoic, in the Cambrian and from the Late Jurassic to Early Cretaceous) when the seawater sulfate concentration was low (Canfield *et al.*, 2007; Poulton *et al.*, 2010; Raiswell *et al.*, 2011; Cumming *et al.*, 2013). Certainly, there are other removal mechanisms for Fe in the ocean, such as oxidation and scavenging, which operate onmuch shorter timescales and thus provide the first-order controls for the benthic Fe fluxes measured in the modern ocean (Dale *et al.*, 2015). Considering, however, that green-clay authigenesis can locally at least double the removal rate of dissolved Fe in near-subsurface pore waters compared to the burial rate of pyrite alone, it seems to be an important overlooked mechanism for reducing the pore water inventory of Fe^{2+} ions, although counted in numerical models (Elrod *et al.*, 2004; Boyd & Ellwood, 2010; Dale *et al.*, 2015), that might otherwise be available for supply to the deep ocean. Owing to the present uncertainty on benthic dissolved Fe fluxes derived from deep-sea sediments, and the poorly understood nature of the iron budget in terms of Fe removal pathways (Dale *et al.*, 2015), we call for a change in the long-standing conceptual view that ferruginous clay minerals formed during early diagenesis are of minor significance in the marine sedimentary iron cycle. Given the vast expanse of the deep-ocean basins, and the extensive occurrence of ferruginous clay minerals in ocean floor sediments, improving estimates of benthic Fe sequestration by green-clay is essential to improve our present mechanistic understanding and quantification of early diagenetic mineral reactions at the sediment-seawater interface. We conclude that, at the Ivory Coast – Ghana Marginal Ridge, green-clay authigenesis does constitute the primary mechanism of ultimate Fe sequestration and burial in this deep-water environment, and thus represents a significant authigenic sink for Fe that should be considered in both numerical and conceptual models of the past and present marine iron cycle.

5.7 Appendix chapter 5

The supplementary information to the article “Substantial iron sequestration during green-clay authigenesis in modern deep-sea sediments” by A. Baldermann, L.N. Warr, I. Letofsky-Papst & V. Mavromatis are provided in the SI Tables 5.1 to 5.4.

SI Table 1: Bulk mineralogy of ODP Hole 959C. Data marked with asterisk are from Baldermann *et al.* (2013). Mineral abbreviations: Glt = authigenic green grains (glauconite); Py = pyrite; Fh = Fe-(oxy)hydroxides; Chl = chlorite; Ilt = illite; Mnt = montmorillonite; Cal = calcite; Kln = kaolinite; Fsp = feldspar (orthoclase and albite); Qz = quartz; Ant = anatase.

Core	Section	Depth	Glt*	Py*	Fh	Chl*	Ilt*	Mnt*	Cal*	Kln*	Fsp*	Qz*	Ant*	SUM
		(mbsf)	wt.%	wt.%	wt.%	wt.%	wt.%	wt.%	wt.%	wt.%	wt.%	wt.%	wt.%	wt.%
C1H1	14-18	0.16	1.3	0.2	3.6	3	4	2	34	30	7	14	0.5	100
C1H1	81-85	0.83	4.5	0.1	2.9	2	2	2	45	23	6	12	0.4	100
C1H1	101-103	1.02	1.6	0.3	2.8	2	2	2	50	23	6	10	0.4	100
C1H1	130-134	1.32	1.1	0.2	3.8	2	3	2	37	29	7	14	0.5	100
C1H2	18-22	1.70	3.0	0.3	2.9	2	2	2	46	23	6	12	0.4	100
C2H1	68-76	3.02	4.6	0.4	2.9	2	3	2	46	22	6	11	0.4	100
C2H2	119-123	5.01	1.2	0.8	2.5	1	3	3	41	27	7	13	0.4	100
C2H5	71-75	9.03	1.4	0.9	2.3	3	4	3	29	32	7	17	0.5	100
C2H6	41-45	10.23	2.5	0.7	2.6	2	4	3	26	33	8	18	0.5	100
C2H6	80-84	10.62	1.4	0.5	2.4	2	4	4	32	30	6	17	0.5	100
C2H6	99-103	10.81	1.4	0.7	2.0	3	5	4	36	29	5	13	0.4	100
C2H6	119-123	11.01	2.8	0.8	2.7	2	4	5	25	34	6	17	0.6	100
C2H7	3-7	11.35	1.4	0.8	2.7	2	4	3	31	31	5	19	0.5	100
C2H7	17-21	11.49	2.3	1.1	2.4	2	4	3	32	31	4	18	0.5	100
C2H7	37-41	11.69	3.5	0.7	2.1	2	5	5	28	33	4	16	0.5	100
C2H7	57-61	11.89	6.0	0.8	1.3	1	3	3	41	26	5	12	0.4	100
C3H1	59-63	12.41	3.1	0.9	2.1	2	4	5	28	32	4	18	0.5	100
C3H4	4-8	16.36	1.0	1.1	2.0	3	4	2	42	26	3	15	0.4	100
C3H5	42-46	18.24	0.9	0.9	2.1	2	3	3	53	21	3	11	0.3	100
C3H6	139-143	20.71	2.0	1.2	1.6	2	3	2	49	24	4	11	0.4	100
C4H3	59-63	24.91	4.8	2.5	1.4	1	2	3	41	29	3	12	0.4	100

SI Table 2: Chemical compositions and structural formulae of authigenic clay minerals from various green grain sub-fractions separated from 0.16, 11.69 and 24.91 mbsf of ODP Hole 959C. The TEM-EDX data (Baldermann *et al.*, 2013) were combined with the TEM-EELS spectra to calculate the Fe(II)/Fe_{total} ratios.

Depth		0.16 mbsf			11.69 mbsf			24.91 mbsf	
Green grain sub-fraction	light	medium	dark	light	medium	dark	light	medium	dark
Particles analysed (n)	32	36	30	36	34	38	39	43	44
Fe(II)/Fe_{total}	0.12	0.14	0.03*	0.18	0.23	0.23	0.21	0.24	0.25
Averaged chemical composition in wt.% based on TEM-EDX									
MgO	4.0	3.7	4.2	3.8	4.1	4.2	4.4	4.4	4.2
Al_2O_3	7.6	7.1	7.3	7.5	6.5	5.2	7.1	6.1	5.2
SiO_2	61.1	61.1	59.1	61.2	59.8	58.5	60.0	58.8	58.2
K_2O	2.2	2.6	4.6	1.8	3.1	4.3	2.9	4.3	5.4
FeO	2.7	3.4	0.7	4.4	5.6	6.0	5.1	6.1	6.3
Fe_2O_3	22.0	21.6	23.3	20.5	20.1	21.4	20.0	19.9	20.3
CaO	0.4	0.5	0.8	0.8	0.8	0.4	0.5	0.4	0.4
Total	100.0	100.0	100.0	100.0	100.0	100.0	100.0	100.0	100.0
Atoms per formula unit (a.p.f.u.) based on $O_{10}(OH)_2$									
^{IV}Al	0.06	0.04	0.13	0.04	0.07	0.09	0.08	0.10	0.09
^{IV}Si	3.94	3.96	3.87	3.96	3.93	3.91	3.92	3.90	3.91
Tetrahedral charge	-0.06	-0.04	-0.13	-0.04	-0.07	-0.09	-0.08	-0.10	-0.09
^{VI}Al	0.52	0.50	0.43	0.53	0.43	0.31	0.47	0.38	0.32
$^{VI}Fe(II)$	0.15	0.18	0.04	0.24	0.31	0.33	0.28	0.34	0.35
$^{VI}Fe(III)$	1.07	1.05	1.15	1.00	0.99	1.08	0.99	0.99	1.03
^{VI}Mg	0.38	0.36	0.41	0.37	0.40	0.42	0.43	0.44	0.42
$\sum^{VI}$cations	2.12	2.09	2.03	2.14	2.13	2.14	2.17	2.15	2.12
Octahedral charge	-0.17	-0.27	-0.36	-0.19	-0.32	-0.33	-0.20	-0.33	-0.41
K	0.18	0.22	0.38	0.15	0.26	0.37	0.24	0.36	0.46
Ca	0.03	0.03	0.06	0.05	0.06	0.03	0.03	0.03	0.03
Interlayer charge	0.24	0.28	0.50	0.25	0.38	0.43	0.30	0.42	0.52

SI Table 3: Solid-phase Fe speciation data for detrital (Fe_D and Fe_{DC}) and authigenic ($Fe_{Gl\text{-}S}$ and Fe_{Py}) ferruginous mineral phases of ODP Hole 959C. Abbreviations: [1]Fe_T = bulk sediment Fe content; [2]Fe_D = dithionite-extractable Fe (i.e. Fe-(oxy)hydroxides); [3]$Fe_{Gl\text{-}S}$ = fraction of Fe attributed to authigenic green grains; [4]Fe_{Py} = fraction of Fe originally present as pyrite; [5]Fe_{DC} = boiling HCl-extractable Fe (i.e. detrital clay minerals); [6]ΔFe = difference between [1] and the sum of [2-5]; [7]ΔFe = Fe mass balance error.

Core	Section	Depth	$^{1}Fe_T$	$^{2}Fe_D$	$^{3}Fe_{Gl\text{-}S}$	$^{4}Fe_{Py}$	$^{5}Fe_{DC}$	$^{6}\Delta Fe$	$^{7}\Delta Fe$
		[mbsf]	[wt.%]	[wt.%]	[wt.%]	[wt.%]	[wt.%]	[wt.%]	[%]
C1H1	14-18	0.16	3.0	2.4	0.2	0.1	0.3	0.0	0
C1H1	81-85	0.83	2.8	1.9	0.8	0.0	0.2	-0.1	-3
C1H1	101-103	1.02	2.4	1.9	0.3	0.1	0.2	0.0	-1
C1H1	130-134	1.32	3.1	2.5	0.2	0.1	0.3	0.1	1
C1H2	18-22	1.7	2.8	1.9	0.5	0.1	0.2	0.0	1
C2H1	68-76	3.02	3.0	1.9	0.8	0.1	0.2	0.0	1
C2H2	119-123	5.01	2.2	1.6	0.2	0.2	0.2	-0.1	-3
C2H5	71-75	9.03	2.3	1.5	0.2	0.2	0.3	0.0	1
C2H6	41-45	10.23	2.8	1.7	0.4	0.2	0.3	0.2	5
C2H6	80-84	10.62	2.4	1.6	0.2	0.1	0.3	0.0	1
C2H6	99-103	10.81	2.2	1.3	0.2	0.2	0.4	0.0	0
C2H6	119-123	11.01	3.1	1.8	0.5	0.2	0.4	0.2	5
C2H7	3-7	11.35	2.8	1.8	0.2	0.2	0.3	0.2	5
C2H7	17-21	11.49	2.8	1.6	0.4	0.3	0.3	0.2	5
C2H7	37-41	11.69	2.7	1.4	0.6	0.2	0.4	0.1	3
C2H7	57-61	11.89	2.2	0.9	1.0	0.2	0.2	-0.1	-4
C3H1	59-63	12.41	2.6	1.4	0.5	0.2	0.4	0.0	1
C3H4	4-8	16.36	2.3	1.3	0.2	0.3	0.3	0.1	4
C3H5	42-46	18.24	2.2	1.4	0.2	0.2	0.3	0.2	5
C3H6	139-143	20.71	2.2	1.1	0.3	0.3	0.3	0.2	6
C4H3	59-63	24.91	2.6	0.9	0.8	0.7	0.2	0.0	0

SI Table 4: Rates of Fe supply and Fe sequestration for ODP Hole 959C. The bulk sediment accumulation rates (AR_{Sed} in $g \cdot cm^{-2} \cdot ky^{-1}$) are reported in Wagner (1998). The accumulation rates of solid phase Fe (AR_{Fe} in µmoles $Fe \cdot cm^{-2} \cdot ky^{-1}$) have been calculated for detrital (i.e. Fe_D and Fe_{DC}) and authigenic (i.e. $Fe_{Gl\text{-}S}$ and Fe_{Py}) ferruginous mineral phases. Abbreviations: $Fe_{Gl\text{-}S}$ = fraction of Fe attributed to authigenic green glauconitic grains; Fe_{Py} = fraction of Fe originally present as pyrite; Fe_D = dithionite-extractable Fe (i.e. Fe-(oxy)hydroxides); Fe_{DC} = boiling HCl-extractable Fe (i.e. detrital clay minerals).

Core	Section	Depth	$^{*}AR_{Sed}$	$ARFe$	$ARFe_{Gl\text{-}S}$	$ARFe_{Py}$	$ARFe_D$	$ARFe_{DC}$	$ARFe_{Gl\text{-}S}/ARFe_{Py}$
		[mbsf]	$[g \cdot cm^{-2} \cdot ky^{-1}]$	µM Fe $cm^{-2} \cdot ky^{-1}$	µM Fe $cm^{-2} \cdot ky^{-2}$	µM Fe $cm^{-2} \cdot ky^{-3}$	µM Fe $cm^{-2} \cdot ky^{-4}$	µM Fe $cm^{-2} \cdot ky^{-5}$	(-)
C1H1	14-18	0.16	0.928	492	36	12	391	51	3
C1H1	81-85	0.83	0.675	334	91	2	229	22	37
C1H1	101-103	1.02	0.675	287	33	11	225	23	3
C1H1	130-134	1.32	0.675	369	23	7	302	31	3
C1H2	18-22	1.70	0.785	391	72	10	273	28	7
C2H1	68-76	3.02	1.435	783	204	29	485	58	7
C2H2	119-123	5.01	1.498	595	55	59	440	58	1
C2H5	71-75	9.03	1.092	455	47	44	291	64	1
C2H6	41-45	10.23	1.092	552	85	36	337	55	2
C2H6	80-84	10.62	1.092	463	47	28	312	66	2
C2H6	99-103	10.81	1.092	424	47	37	257	81	1
C2H6	119-123	11.01	0.822	452	71	30	259	59	2
C2H7	3-7	11.35	0.822	412	36	32	266	50	1
C2H7	17-21	11.49	0.822	405	59	42	231	50	1
C2H7	37-41	11.69	0.822	404	89	27	206	61	3
C2H7	57-61	11.89	0.822	328	152	30	130	32	5
C3H1	59-63	12.41	0	0	0	0	0	0	-
C3H4	4-8	16.36	1.436	581	45	76	344	89	1
C3H5	42-46	18.24	1.190	468	33	49	290	69	1
C3H6	139-143	20.71	1.190	465	74	69	231	60	1
C4H3	59-63	24.91	1.113	520	167	131	179	38	1

Chapter 6

Conclusion remarks and future projects

The present work demonstrates that ferruginous clay mineral reactions – that cover the entire range from elevated temperatures found at mid-oceanic ridge sites to the low-temperatures of shallow-shelf and deep-sea environments – can significantly contribute to the fluxes of Fe measured in modern and ancient marine sediments. An improved understanding of the role of Fe sequestration and Fe burial attributed to green-clay authigenesis during early diagenesis is therefore essential for the identification and evaluation of the physicochemical processes and ambient (paleo)environmental controls linked to the formation and diagenesis of Fe-silicate minerals. However, up to now the importance of ferruginous clay mineral reactions has been overlooked as a central factor in the marine (sedimentary) iron cycle, and thus the estimated global fluxes between continental solid-phase Fe(III) sources and multiple authigenic mineral sinks for Fe in sediments remain biased towards the underpinned role of green-clays that form in many low-temperature environments during the early stage of marine diagenetic. The new models for glauconite mineral formation in shallow-water *versus* deep-sea sediments, and the new rates of Fe incorporation during the Fe(III)-smectite to glauconite reaction as well as during the experimental precipitation of ferrous saponite presented here should be considered in future conceptual and numerical biogeochemical models of the marine iron cycle.

(i) In order to gain a better understanding of the key factors controlling the release of dissolved Fe^{2+} to the deep ocean during the weathering of basalt at mid-oceanic ridge sites, new hydrothermal synthesis experiments are planned at variable molar Fe:Mg:Si ratios and different temperatures. $\delta^{56}Fe$, $\delta^{26}Mg$, $\delta^{30}Si$, and classical $\delta^{18}O$ and $\delta^{2}H$ isotope analysis of the reactive fluids and co-precipited ferrous saponite and Fe-(oxy)hydroxides will resolved the rate of Fe burial related to the mineral sinks *vs.* the amount of sedimentary Fe redox recycling.

(ii) The remediation of trichloroethylene (TCE)-contaminated soil solutions and groundwater by injection of nanoscale zero-valent iron (nZVI)-doped slurries containing bentonite has been recently introduced as an ecologically sustainable countermeasure. In this industrial project, the rate of TCE reduction and potential modifications of the original bentonite clay are investigated using batch experiments.

Chapter 7

Bibliography

Aller, R.C. & Blair, N.E. (2006) Carbon remineralization in the Amazon–Guianas tropical mobile mudbelt: A sedimentary incinerator. *Continental Shelf Research*, **26**, 2241-2259.

Akbulut, A. & Kadir, S. (2003) The geology and origin of sepiolite, palygorskite and saponite in Neogene lacustrine sediments of the Serinhisar-Acipayam Basin, Denizli, SW Turkey. *Clays and Clay Minerals*, **51**, 279-292.

Anderson, T.F. & Arthur, M.A. (1983) Stable isotopes of oxygen and carbon and their application to sedimentologic and palaeoenvironmental problems. Pp. 1-151 in: Stable Isotopes in Sedimentary Geology (M.A. Arthur, T.F. Anderson, I.R. Kaplan, J. Veizer and L.S. Land, editors). SEPM Short Course, Tulsa, Oklahoma, USA.

Badaut, D., Besson, G., Decarreau, A. & Rautureau, R. (1985) Occurrence of a ferrous, trioctahedral smectite in recent sediments of Atlantis II Deep, Red Sea. *Clay Minerals*, **20**, 389-404.

Bailey, S.W., Alietti, A., Brindley, G.W., Formosa, M.L.L., Jasmund, K., Konta, J., MacKenzie, R.C., Nagasawa, K., Raussell-Colom, R.A. & Zvyagin, B.B. (1980) Summary of the recommendations of the AIPEA nomenclature committee. *Clays and Clay Minerals*, **28**, 73-78.

Baldermann, A. (2010) Geochemie und Mineralogie der Smektit-Illitisierung in Glaukoniten des Nördlichen Harzvorlandes. B.Sc. Thesis, E.-M.-A. University Greifswald, Germany.

Baldermann, A. (2012) Recent glauconite formation in a deep sea environment from ODP Site 959, Ivory Coast–Ghana Marginal Ridge. Master Thesis, E.-M.-A. University Greifswald, Germany.

Baldermann, A., Deditius, A.P., Dietzel, M., Fichtner, V., Fischer, C., Hippler, D., Leis, A., Baldermann, C., Mavromatis, V., Stickler, C. & Strauss, H. (2015b) The role of bacterial

sulfate reduction during dolomite precipitation: Implications from Upper Jurassic platform carbonates. *Chemical Geology*, **412**, 1-14.

Baldermann, A., Dohrmann, R., Kaufhold, S., Nickel, C., Letofsky-Papst, I. & Dietzel, M. (2014) The Fe-Mg-saponite solid solution series – A hydrothermal synthesis study. *Clay Minerals*, **49**, 391-415.

Baldermann, A., Grathoff, G.H. & Nickel, C. (2012) Micromilieu-controlled glauconitization in fecal pellets at Oker (Central Germany). *Clay Minerals*, **47**, 513-538.

Baldermann, A., Warr, L.N., Grathoff, G.H. & Dietzel, M. (2013) The rate and mechanism of deep-sea glauconite formation at the Ivory Coast – Ghana Marginal Ridge. *Clays and Clay Minerals*, **61**, 258-276.

Baldermann, A., Warr, L.N., Letofsky-Papst, I. & Mavromatis, V. (2015) Substantial iron sequestration during green-clay authigenesis in modern deep-sea sediments. *Nature Geoscience*, **8**, 885-889.

Bekker, A., Slack, J.F., Planavsky, N., Krapež, B., Hofmann, A., Konhauser, K.O. & Rouxel, O.J. (2010) Iron formation: The sedimentary product of a complex interplay among mantle, tectonic, oceanic, and biospheric processes. *Economic Geology*, **105**, 467-508.

Bergquist, B.A., Wu, J. & Boyle, E.A. (2007) Variability in oceanic dissolved iron is dominated by the colloidal fraction. *Geochimica et Cosmochimica Acta*, **71**, 2960-2974.

Berner, R.A. (1969) Migration of iron and sulfur within anaerobic sediments during early diagenesis. *American Journal of Science*, **267**, 19-42.

Berner, R.A. (1982) Burial of organic carbon and pyrite sulfur in the modern ocean: Its geochemical and environmental significance. *American Journal of Science*, **282**, 451-473.

Blain, S., Quéguiner, B., Armand, L., Belviso, S., Bombled, B., Bopp, L., Bowie, A., Brunet, C., Brussaard, C., Carlotti, F., Christaki, U., Corbière, A., Durand, I., Ebersbach, F., Fuda, J.-L., Garcia, N., Gerringa, L., Griffiths, B., Guigue, C., Guillerm, C., Jacquet, S., Jeandel, C., Laan, P., Lefèvre, D., Monaco, C.L., Malits, A., Mosseri, J., Obernosterer, I., Park, Y.-H., Picheral, M., Pondaven, P., Remenyi, T., Sandroni, V., Sarthou, G., Savoye, N., Scouarnec, L., Souhaut, M., Thuiller, D., Timmermans, K., Trull, T., Uitz1, J., van Beek, P., Veldhuis, M., Vincent, D., Viollier, E., Vong, L. & Wagener, T. (2007) Effect of natural iron fertilization on carbon sequestration in the Southern Ocean. *Nature*, **446**, 1070-1075.

Boyd, P.W. & Ellwood, M.J. (2010) The biogeochemical cycle of iron in the ocean. *Nature Geoscience*, **3**, 675-682.

Boye, M., Nishioa, J., Croot, P., Laan, P., Timmermans, K.R., Strass, V.H., Takeda, S. & de Baar, H.J.W. (2010) Significant proportion of dissolved organic Fe complexes in fact is Fe colloids. *Marine Chemistry*, **122**, 20-27.

Breukelaar, J., Kellendonk, F.J.A. & van Santen, R.A. (1989) A process for the manufacture of synthetic saponites. European Patent 317,006.

Breukelaar, J., van Santen, R.A. & De Winter, A.W. (1990) Synthetic saponite-derivatives, a method for preparing such saponites and their use in catalytic (hydro)conversions. European Patent 398,429.

Brigatti, M.F. (1983) Relationships between composition and structure in Fe-rich smectites. *Clay Minerals*, **18**, 177-186.

Brigatti, M.F., Lugli, C., Poppi, L. & Venturelli, G. (1999) Iron-rich saponite: dissolution reactions and Cr uptake. *Clay Minerals*, **34**, 637-645.

Brown, G.C, Hughes, D.J. & Esson, J. (1973) New XRF data retrieval techniques and their application to USGS standard rocks. *Chemical Geology*, **11**, 223-229.

Buatier, M., Honnorez, J. & Ehret, G. (1989) Fe-smectite-glauconite transition in hydrothermal clays from the Galapagos Spreading Center. *Clays and Clay Minerals*, **37**, 532-541.

Burst, J.F. (1958a) Glauconite pellets: their mineral nature and applications to stratigraphic interpretations. *American Association of Petroleum Geologists Bulletin*, **42**, 310-327.

Burst, J.F. (1958b) Mineral heterogeneity in glauconite pellets. *American Mineralogist*, **43**, 481-49.

Caillère, S., Henin, S. & Esquevin, J. (1953) Synthèses à basse température de phyllite ferrifère. *Comptes Rendus de l'Academie Sciences (Paris),* **237**, 1724-1726.

Caillère, S. Oberlin, A. & Henin, S. (1954) Etude au microscope électronique de quelques silicates phylliteux obtenus par synthèses à basse température. *Clay Minerals Bulletin,* **2**, 146-156.

Caillère, S., Henin, S. & Esquevin, J. (1955) Synthèses à basse température de quelque minéraux ferrifère (silicates et oxydes). *Bulletin de la Societe Francaise de Mineralogie et Cristallographie,* **78**, 227-241.

Canfield, D. E. (1989) Reactive iron in marine sediments. *Geochimica et Cosmochimica Acta*, **53**, 619-632.

Canfield, E., Poulton, S.W. & Narbonne, G.M. (2007) Late-Neoproterozoic deep-ocean oxygenation and the rise of animal life. *Science*, **315**, 92-95.

Canfield, D.E., Thamdrup, B. & Hansen, J.W. (1993) The anaerobic degradation of organic matter in Danish coastal sediments: Iron reduction, manganese reduction, and sulfate reduction. *Geochimica et Cosmochimica Acta*, **57**, 3867-3883.

Cassar, N., Bender, M.L., Barnett, B.A., Fan, S., Moxim, W.J., Levy II, H. & Tilbrook, B. (2007) The southern ocean biological response to aeolian iron deposition. *Science*, **317**, 1067-070.

Chaerun, S.K. & Tazaki, K. (2005) How kaolinite plays an essential role in remediating oil-polluted seawater. *Clay Minerals*, **40**, 481-491.

Charpentier, D., Buatier, M.D., Jacquot, E., Gaudin, A. & Wheat, C.G. (2011) Conditions and mechanism for the formation of iron-rich montmorillonite in deep sea sediments (Costa Rica margin): Coupling high-resolution mineralogical characterization and geochemical modeling. *Geochimica et Cosmochimica Acta*, **75**, 1397-1410.

Che, C., Glotch, T.D., Bish, D.L., Michalski, J.R. & Xu, W. (2011) Spectroscopic study of the dehydration and/or dehydroxylation of phyllosilicate and zeolite minerals. *Journal of Geophysical Research*, **116**, E05007.

Chermak, J.A. & Rimstidt, J.D. (1989) Estimating the thermodynamic properties (ΔG_f and ΔH_f) of silicate minerals at 298 K from the sum of polyhedral contributions. *American Mineralogist*, **74**, 1023-1031.

Chester, R. (2000) Marine Geochemistry. 520 pp. Blackwell Science, Oxford, UK.

Chukanov, N.V., Pekov, I.V., Zadov, A.E., Chukanova, V.N. & Mökkel, S. (2003) Ferrosaponite $Ca_{0.3}(Fe^{2+},Mg,Fe^{3+})_3(Si,Al)_4O_{10}(OH)_2 \cdot 4H_2O$, the new trioctahedral smectite. *Zapiski Vserossiyskogo Mineralogicheskogo Obshchestva*, **132**, 68-74.

Coale, K.H., Johnson, K.S., Fitzwater, S.E., Michael Gordon, R., Tanner, S., Chavez, F.P., Ferioli, L., Sakamoto, C., Rogers, P., Millero, F., Steinberg, P., Nightingale, P., Cooper, D., Cochlan, E.P., Landry, M.R., Constantinou, J., Rollwagen, G., Trasvina, A. & Kudela, R. (1996) A massive phytoplankton bloom induced by an ecosystem-scale iron fertilization experiment in the equatorial Pacific Ocean. *Nature*, **383**, 495-501.

Colombié, C., Lécuyer, C. & Strasser, A. (2011) Carbon- and oxygen-isotope records of palaeoenvironmental and carbonate production changes in shallow-marine carbonates (Kimmeridgian, Swiss Jura). *Geological Magazine*, **148**, 133-153.

Corliss, J.B., Dymond, J., Gordon, L.I., Edmond, J.M., Von Herzen, R.P., Ballard, R.D., Green, K., Williams, D., Bainbridge, A., Crane, K. & Van Adel, T.H. (1979) Submarine thermal springs on Galapogos Rift. *Science*, **203**, 1073-1083.

Cornell, R.M. & Schwertmann, U. (2003) The Iron Oxides: Structure, Properties, Reactions, Occurrences and Uses. 664 pp. Wiley-VCH, Weinheim.

Craig, H. (1965) The measurement of oxygen isotope palaeotemperatures. Pp. 161-182 in: Stable Isotopes in Oceanographic Studies and Palaeotemperatures (E. Tongiorgi, editor). Consiglio Nazionale delle Richerche. Labortorio di Geologia Nucleare, Pisa, Italy.

Cuadros, J., Dekov, V.M. & Fiore, S. (2008) Crystal-chemistry of the mixed-layer sequence talc-talc-smectite-smectite from submarine hydrothermal vents. *American Mineralogist*, **93**, 1338-1348.

Cuadros, J., Dekov, V.M., Arroyo, X. & Nieto, F. (2011) Smectite formation in submarine hydrothermal sediments: samples from the HMS Challenger Expedition (1872-1776). *Clays and Clay Minerals*, **59**, 147-164.

Cuadros, J., Michalski, J.R., Dekov, V.M., Bishop, J., Fiore, S. & Dyar, M.D. (2013) Crystal-chemistry of interstratified Mg/Fe-clay minerals from seafloor hydrothermal sites. *Chemical Geology*, **360-361**, 142-158.

Cullen, J.T., Bergquist, B.A. & Moffett, J.W. (2006) Thermodynamic characterization of the partitioning of iron between soluble and colloidal species in the Atlantic Ocean. *Marine Chemistry*, **98**, 295-303.

Cumming, V.M., Poulton, S.W., Rooney, A.D. & Selby, D. (2013) Anoxia in the terrestrial environment during the late Mesoproterozoic. *Geology*, **41**, 583-586.

Dale, A.W., Nickelsen, L., Scholz, F., Hensen, C., Oschlies, A. & Wallmann, K. (2015) A revised global estimate of dissolved iron fluxes from marine sediments. *Global Biogeochemical Cycles*, **29**, article no. GB005017.

Decarreau, A. (1980) Cristallogenèse expérimentale des smectites magnésiennes: Hectorite, stévensite. *Bulletin de Minéralogie,* **103**, 579-590.

Decarreau, A. (1985) Partitioning of divalent elements between octahedral sheets of trioctahedral smectites and water. *Geochimica et Cosmochimica Acta,* **49**, 1537-1544.

Decarreau, A. & Bonnin, D. (1986) Synthesis and crystallogenesis at low temperature of Fe(III)-smectites by evolution of co-precipitated gels: Experiments in partially reducing conditions. *Clay Minerals,* **21**, 861-877.

Decarreau, A., Petit, S., Martin, F., Farges, F., Vieillard, P. & Joussein, E. (2008) Hydrothermal synthesis, between 75 and 150°C, of high-charge, ferric nontronites. *Clays and Clay Minerals*, **56**, 322-337.

Deocampo, D.M., Cuadros, J., Wing-Dudek, T., Olives, J. & Amouric, M. (2009) Saline lake diagenesis as revealed by coupled mineralogy and geochemistry of multiple ultrafine clay phases: Pliocene Olduvai Gorge, Tanzania. *American Journal of Science*, **309**, 834-868.

De Souza, R.S., De Ros, L.F. & Morad, S. (1995) Dolomite Diagenesis and Porosity Preservation in Lithic Reservoirs: Carmópolis Member, Sergipe-Alagoas Basin, Northeastern Brazil. *American Association of Petroleum Geologists Bulletin*, **79**, 725-748.

Dietzel, M. & Letofsky-Papst, I. (2002) Stability of magadiite between 20 and 100°C. *Clays and Clay Minerals*, **50**, 656-665.

Dill, H.G., Dohrmann, R. & Kaufhold, S. (2011) Disseminated and faultbound autohydrothermal ferroan saponite in Late Paleozoic andesites of the Saar-Nahe Basin, SW Germany: Implications for the economic geology of intermediate (sub)volcanic rocks. *Applied Clay Science*, **51**, 226-240.

Drits, V.A., Plançon, A., Sakharov, B.A., Besson, G., Tsipursky, S.I. & Tchoubar, C. (1984) Diffraction effects calculated for structural models of K-saturated montmorillonite containing different types of defects. *Clay Minerals*, **19**, 541-562.

Drits, V.A., Besson, G. & Muller, F. (1995) An Improved Model for Structural Transformations of Heat-Treated Aluminous Dioctahedral 2:1 Layer Silicates. *Clays and Clay Minerals*, **43**, 718-731.

Dymond, J., Corliss, J.B., Heath, G.R., Field, C.W., Dasch, E.J. & Veeh, H.H. (1973) Origin of metalliferous sediments from the Pacific Ocean. *Geological Society of America Bulletin*, **84**, 3355-3372.

Eggleton, R.A. & Fitzpatrick, R.W. (1988) New data and a revised structural model for ferrihydrite. *Clays and Clay Minerals*, **36**, 111-124.

El Albani, A., Meunier, A. & Fursich, F. (2005) Unusual occurrence of glauconite in a shallow marine lagoonal environment (Lower Cretaceous, northern Aquitaine Basin, SW France). *Terra Nova*, **17**, 537-544.

Elliott, W.C & Matisoff, G. (1996) Evolution of kinetic models for the smectite to illite transformation. *Clays and Clay Minerals*, **44**, 77-87.

Elrod, V.A., Berelson, W.M., Coale, K.H. & Johnson, K.S. (2004) The flux of iron from continental shelf sediments: A missing source for global budgets. *Geophysical Research Letters*, **31**, article no. L12307.

Epstein, S., Buchsbaum, R., Lowenstam, H.A. & Urey, H.C. (1953) Revised carbonate water isotopic temperature scale. *Geological Society America Bulletin*, **64**, 1315-1326.

Farmer, V.C., McHardy, W.J., Elsass, F. & Robert, M. (1994) *hk*-Ordering in aluminous nontronite and saponite synthesized near 90°C: Effects of synthesis conditions on nontronite composition and ordering. *Clays and Clay Minerals*, **42**, 180-186.

Fischer, R. (1991) Die Oberjura-Schichtfolge vom Langenberg bei Oker. *Arbeitskreis Paläontologie Hannover*, **19**, 21-36.

Friedman, I. & O'Neil, J.R. (1977) Compilation of stable isotope fractionation factors of geochemical interest. Chapter KK in: Data of Geochemistry (M. Fleischer, editor). Geological Survey Professional. Paper, USGS, Washington, USA.

Galliher, E.W. (1935) Glauconite genesis. *Geological Society of America Bulletin*, **46**, 1351-1356.

Garvie, L.A.J., Craven, A.J. & Brydson, R. (1994) Use of electron-energy loss near-edge fine structure in the study of minerals. *American Mineralogist*, **79**, 411-425.

Gaudin, A., Buatier, M.D., Beaufort, D., Petit, S., Grauby, O. & Decareau, A. (2005) Characterization and origin of Fe^{3+}-montmorillonite in deep water calcareous sediments (Pacific Ocean, Costa Rica margin). *Clays and Clay Minerals*, **53**, 452-465.

Giresse, P. & Wiewióra, A. (2001) Stratigraphic condensed deposition and diagenetic evolution of green clay minerals in deep water sediments on the Ivory Coast-Ghana Ridge. *Marine Geology*, **179**, 51-70.

Giresse, P., Gadel, F., Serve, L. & Barusseau, J.P. (1998) Indicators of climate and sediment-source variations at site 959: implications for the reconstructions of paleoenvironments in the Gulf of Guinea through Pleistocene times. *Proceedings of the Ocean Drilling Program, Scientific Results*, **159**, 585-603.

Giresse, P., Wiewióra, A. & Grabska, D. (2004) Glauconitization processes in the northwestern Mediterranean (Gulf of Lions). *Clay Minerals*, **39**, 57-73.

Grathoff, G.H., Moore, D.M., Hay, R.L. & Wemmer, K. (2000) Origin of illite in the lower Paleozoic of the Illinois basin: Evidence for brine migrations. *Geological Society of America Bulletin*, **113**, 1092-1104.

Grauby, O., Petit, S., Decarreau, A. & Baronnet, A. (1994) The nontronite-saponite series: An experimental approach. *European Journal of Mineralogy*, **6**, 99-112.

Greenberg, S.A. (1958) The nature of the silicate species in sodium silicate solutions. *Journal of The American Chemical Society*, **80**, 6508-6511.

Greenberg, S.A. & Price, E.W. (1957) The solubility of silica in solutions of electrolytes. *The Journal of Physical Chemistry*, **61**, 1539-1541.

Guimaraes, E.M., Velde, B., Hillier, S. & Nicot, E. (2000) Diagenetic/anchimetamorphic changes on the Proterozoic glauconite and glaucony from the Paranoa group, mid-western Brazil. *Revista Brasileira de Geociências*, **30**, 363-366.

Hanor, J.S. (1994) Physical and chemical controls on the composition of waters in sedimentary basins. *Marine and Petroleum Geology*, **11**, 31-45.

Harder, H. (1972) The role of magnesium in the formation of smectite minerals. *Chemical Geology*, **10,** 31-39.

Harder, H. (1976) Nontronite synthesis at low temperatures. *Chemical Geology*, **18**, 169-180.

Harder, H. (1978) Synthesis of iron layer silicate minerals under natural conditions. *Clays and Clay Minerals*, **26**, 65-72.

Harder, H. (1980) Synthesis of glauconite at surface temperatures. *Clays and Clay Minerals*, **28**, 217-222.

Hardie, L.A. (1996) Secular variation in seawater chemistry: An explanation for the coupled variation in the mineralogies of marine limestones and potash evaporites over the past 600 m.y. *Geology*, **24**, 279-283.

Henin, S. & Robichet, O. (1954) A study of the synthesis of clay minerals. *Clay Minerals*, **2**, 110-115.

Heuser, M., Andrieux, P., Petit, S. & Stanjek, H. (2013) Iron-bearing smectites: a revised relationship between structural Fe, *b* cell edge lengths and refractive indices. *Clay Minerals*, **48**, 97-103.

Holland, H.D., Horita, J. & Seyfried, W.E. (1996) On the secular variations in the composition of Phanerozoic marine potash evaporites. *Geology*, **24**, 993-996.

Homoky,W.B., Hembury, D.J., Hepburn, L.E., Mills, R.A., Statham, P.J., Fones, G.R. & Palmer, M.R. (2011) Iron and manganese diagenesis in deep sea volcanogenic sediments and the origins of pore water colloids. *Geochimica et Cosmochimica Acta*, **75**, 5032-5048.

Homoky, W.B., John, S.G., Conway, T. & Mills, R.A. (2013) Distinct iron isotopic signatures and supply from marine sediment dissolution. *Nature Communications*, **4**, article no. 2143.

Homoky, W.B., Severmann, S., Mills, R.A., Statham, P.J. & Fones, G.R. (2009) Pore-fluid Fe isotopes reflect the extent of benthic Fe redox recycling: Evidence from continental shelf and deep sea sediments. *Geology*, **37**, 751-754.

Horita, J., Zimmermann, H. & Holland, H.D. (2002) Chemical evolution of seawater during the Phanerozoic: Implications from the record of marine evaporates. *Geochimica et Cosmochimica Acta*, **66**, 3733-3756.

Hower, J. (1961) Some factors concerning the nature and origin of glauconite. *American Mineralogist*, **46**, 313-334.

Hower, J., Eslinger, E.V., Hower, M.E. & Perry, E.A. (1976) Mechanism of burial metamorphism of argillaceous sediments: 1. Mineralogical and chemical evidence. *Geological Society of America Bulletin*, **87**, 725-737.

Hudson, R.J.M. & Morel, F.M.M. (1990) Iron transport in marine phytoplankton: kinetics of cellular and medium coordination reactions. *Limnology and Oceanography*, **35**, 1002-1020.

Huggett, J.M. & Cuadros, J. (2010) Glauconite formation in lacustrine/palaeosol sediments, Isle of Wight (Hampshire Basin), UK. *Clay Minerals*, **45**, 35-49.

Hunger, S. & Benning, L.G. (2007) Greigite: a true intermediate on the polysulfide pathway to pyrite. *Geochemical Transactions*, **8**, 1-20.

Husinec, A. & Read, J.F. (2010) Sequence Stratigraphy, Carbon Isotopic Signature, and Dolomitization of a Late Jurassic Greenhouse Platform, Croatia. Search and Discovery Article #50345, *American Association of Petroleum Geologists (AAPG) Annual Convention and Exhibition*, 1-21.

Iler, R.K. (1979) The chemistry of silica – Solubility, Polymerization, Colloid and Surface Properties, and Biochemistry. 896 pp. Wiley-Interscience, New York.

Iriarte, P.I., Petit, S., Huertas, F.J., Fiore, S., Grauby, O., Decarreau, A. & Linares, J. (2005) Synthesis of kaolinite with a high level of Fe^{3+} for Al substitution. *Clays and Clay Minerals*, **53**, 1-10.

Jaisi, D.P., Eberl, D.D., Dong, H. & Kim, J. (2011) The formation of illite from nontronite by mesophilic and thermophilic bacterial reduction. *Clays and Clay Minerals*, **59**, 21-33.

Jasmund, K. & Lagaly, G. (1993) Tonminerale und Tone. Struktur, Eigenschaften, Anwendung und Einsatz in Industrie und Umwelt. 490 pp. Steinkopff Verlag, Darmstadt.

Jickells, T.D., An, Z.S., Andersen, K.K., Baker, A.R., Bergametti, G., Brooks, N., Cao, J.J., Boyd, P.W., Duce, R.A., Hunter, K.A., Kawahata, H., Kubilay, N., laRoche, J., Liss, P.S., Mahowald, N., Prospero, J.M., Ridgwell, A.J., Tegen, I. & Torres, R. (2005) Global iron connections between desert dust, ocean biogeochemistry, and climate. *Science*, **308**, 67-71.

Jimenez-Millan, J., Molina, J.M., Nieto, L., Nieto, M. & Ruiz-Ortis, P.A. (1998) Glauconite and phosphate peloids in Mesozoic carbonate sediments (Eastern Subbetic Zone, Betic Cordilleras, SE Spain). *Clay Minerals*, **33**, 547-559.

John, S.G., Mendez, J., Moffett, J. & Adkins, J. (2012) The flux of iron and iron isotopes from San Pedro Basin sediments. *Geochimica et Cosmochimica Acta*, **93**, 14-29.

Johnson, K.S., Coale, K.H., Elrod, V.A. & Tindale, N.W. (1994) Iron photochemistry in seawater from the equatorial Pacific. *Marine Chemistry*, **46**, 319-334.

Johnson, K.S., Elrod, V.A., Fitzwater, S.E., Plant, J.N., Chavez, F.P., Tanner, S.J., Gordon, R.M., Westphal, D.L., Perry, K.D., Wu, J. & Karl, D.M. (2003) Surface ocean-lower atmosphere interactions in the Northeast Pacific Ocean Gyre: Aerosols, iron, and the ecosystem response. *Global Biogeochemical Cycles*, **17**, article no. 1063.

Kaufhold, S. & Dohrmann, R. (2010) Stability of bentonites in salt solutions: II. Potassium chloride solution – Initial step of illitization? *Applied Clay Science*, **49**, 98-107.

Kawano, M. & Tomita, K. (1991) Dehydration and rehydration of saponite and vermiculite. *Clays and Clay Minerals*, **39**, 174-183.

Keller, L.M., Holzer, L., Wepf, R. & Gasser, P. (2011) 3D geometry and topology of pore pathways in Opalinus clay: Implications for mass transport. *Applied Clay Science*, **52**, 85-95.

Kloprogge, J.T., Komarneni, S. & Amonette, J.E. (1999) Synthesis of smectite clay minerals: A critical review. *Clays and Clay Minerals*, **47**, 529-554.

Köhler, I., Konhauser, K.O., Papineau, D., Bekker, A. & Kappler, A. (2013) Biological carbon precursor to diagenetic siderite with spherical structures in iron formations. *Nature Communications*, **4**, article no. 1741.

Kohler, E.E. & Köster, H.M. (1976) Zur Mineralogie, Kristallchemie und Geochemie kretazischer Glaukonite. *Clay Minerals*, **11**, 273-302.

Konhauser, K.O., Kappler, A. & Roden, E.E. (2011) Iron in Microbial Metabolism. *Elements*, **7**, 89-93.

Konhauser, K.O. & Urrutia, M.M. (1999) Bacterial clay authigenesis: a common biogeochemical process. *Chemical Geology*, **161**, 399-413.

Köster, H.M. (1993) Beschreibung einzelner Tonminerale. Pp. 33-89 in: *Tonminerale und Tone* (K. Jasmund & G. Lagaly, editors). Steinkopff Verlag, Darmstadt.

Köster, H.M., Ehrlicher, U., Gilg, H.A., Jordan, R., Murad, E. & Onnich, K. (1999) Mineralogical and chemical characteristics of five nontronite and Fe-rich smectites. *Clay Minerals*, **34**, 579-599.

Kuchta, L. & Fajnor, V.S. (1988) Optimal conditions for hydrothermal synthesis of saponite. *Chemicke Zvesti,* **42**, 339-345.

Lampitt, R.S., Achterberg, E.P., Anderson, T.R., Hughes, J.A., Iglesias-Rodriguez, M.D., Kelly-Gerreyn, B.A., Lucas, M., Popova, E.E., Sanders, R., Shepherd, J.G., Smythe-Wright, D. & Yool, A. (2008) Ocean fertilization: a potential means of geoengineering? *Philosophical Transactions of the Royal Society A*, **366**, 3919-3945.

Lanson, B., Lantenois, S., van Aken, P.A., Bauer, A. & Plançon, A. (2012) Experimental investigation of smectite interaction with metal iron at 80°C: Structural characterization of newly formed Fe-rich phyllosilicates. *American Mineralogist*, **97**, 864-871.

Logvinenko, N.V. (1982) Origin of glauconite in the recent bottom sediments of the ocean. *Sedimentary Geology*, **31**, 43-38.

Longuépée, H. & Cousineau, P.A. (2006) Constraints on the genesis of ferrian illite and aluminum-rich glauconite: potential impact on sedimentology and isotopic studies. *The Canadian Mineralogist*, **44**, 967-980.

MacKenzie, F.T. (2005) Sediments, Diagenesis, and Sedimentary Rocks, 7: Treatise on Geochemistry, 446 pp. Elsevier Science & Technology, USA.

Madejová, J., Bujdak, J., Gates, W.P. & Komadel, P. (1996) Preparation and infrared spectroscopic characterization of reduced-charge montmorillonite with variable Li contents. *Clay Minerals*, **31**, 233-241.

Maldonado, M.T. & Price, N.M. (2001) Reduction and transport of organically bound iron by *Thalassiosire oceanica* (Bactillariophyceae). *Journal of Phycology*, **37**, 298-309.

Martin, J.H. (1990) Glacial-interglacial CO_2 change: The iron hypothesis. *Paleoceanography*, **5,** 1-13.

Martin, J.H., Coale, K.H., Johnson, K.S., Fitzwater, S.E., Gordon, R.M., Tanner, S.J., Hunter, C.N., Elrod, V.A., Nowicki, J.L., Coley, T.L., Barber, R.T., Lindley, S., Watson, A.J., van Scoy, K., Law, C.S., Liddicoat, M.I., Ling, R., Stanton, T., Stockel, J., Collins, C., Anderson, A., Bidigare, R., Ondrusek, M., Latasa, M., Millero, F.J., Lee, K., Yao, W., Zhang, J.Z., Friederich, G., Sakamoto, C., Chavez, F., Buck, K., Kolber, Z., Greene, R., Falkowski, P., Chisholm, S.W., Hoge, F., Swift, R., Yungel, J., Turner, S., Nightingale, P., Hatton, A., Liss, P. & Tindale, N.W. (1994) Testing the iron hypothesis in ecosystems of the equatorial Pacific Ocean. *Nature*, **371,** 123-129.

Martín-Algarra, A. & Sánchez-Navas, A. (1995) Phosphate stromatolites from condensed cephalopod limestones, Upper Jurassic, southern Spain. *Sedimentology*, **42**, 893-919.

Mascle, J., Lohmann, G.P., Clift, P.D., *et al.* (1996) 9. Principal Results. *Proceedings of the Ocean Drilling Program, Initial Reports*, **159**, 297-314.

Mazur, S. & Scheck-Wenderoth, M. (2005) Constraints on the tectonic evolution of the Central European Basin System revealed by seismic reflection profiles from Northern Germany. *Netherlands Journal of Geosciences*, **84**, 389-401.

McBride, M.B. (1994) Environmental Chemistry of Soils. 416 pp. Oxford University Press, New York, USA.

McKenzie, J.A. (1981) Holocene dolomitization of calcium carbonate sediments from the coastal sabkhas of Abu Dhabi, U.A.E.: a stable isotope study. *Journal of Geology*, **89**, 185-198.

Meunier, A. & El Albani, A.E. (2007) The glauconite–Fe-illite–Fe-smectite problem: a critical review. *Terra Nova*, **19**, 95-104.

Moore, D. & Reynolds, R.C. Jr. (1997) X-Ray Diffraction and the Identification and Analysis of Clay Minerals, 378 pp. Oxford University Press, USA.

Morse, J.W. & Luther, G.W. III (1999) Chemical influences on trace metal-sulfide interactions in anoxic sediments. *Geochimica et Cosmochimica Acta*, **63**, 3373-3378.

Mudroch, A. (2001) Fischzähne aus dem Oberjura Nordwesteuropas – Systematik, Biogeochemie und Palökologie. Ph.D. thesis, University of Hannover, Germany.

Nollet, S., Hilgers, C. & Urai, J. (2005) Sealing of fluid pathways in overpressure cells: a case study from the Buntsandstein in the Lower Saxony Basin (NW Germany). *International Journal of Earth Science*, **94**, 1039-1055.

Norris, R.D. (1998) Planktonic foraminifer biostratigraphy: eastern equatorial Atlantic. *Proceedings of the Ocean Drilling Program, Scientific Results*, **159**, 445-479.

Odin, G.S. (1982) How to measure glaucony ages. Pp. 387-403 in: Numerical Dating in Stratigraphy (G.S. Odin, editor). John Wiley & Sons, Chichester, West Sussex, UK.

Odin, G.S. (1988) Green Marine Clays, 445 pp. Elsevier, Amsterdam.

Odin, G.S. & Fullagar, P.D. (1988) Geological significance of the glaucony facies. Pp. 295-332 in: Green Marine Clays (G.S. Odin, editor). Elsevier, Amsterdam.

Odin, G.S. & Matter, A. (1981) De glauconiarum origine. *Sedimentology*, **28**, 611-641.

Odom, E. (1976) Microstructure, mineralogy and chemistry of Cambrian glauconite pellets and glauconite, central U.S.A. *Clays and Clay Minerals*, **24**, 232-238.

Ojakangas, R.W. & Keller, W.D. (1964) Glauconitization of rhyolite sand grains. *Journal of Sedimentary Petrology*, **34**, 84-90.

Parekh, P., Follows, M.J. & Boyle, E. (2004) Modeling the global iron cycle. *Global Biogeochemical Cycles*, **18**, article no. GB1002.

Parthasarathy, G., Choudary, B.M., Sreedhar, B., Kunwar, A.C. & Srinivasan, R. (2003) Ferrous saponite from the Deccan Trap, India, and its application in adsorption and reduction of hexavalent chromium. *American Mineralogist*, **88**, 1983-1988.

Passier, H.F.,Middelburg, J.J., de Lange, G.J. & Böttcher, M.E. (1997) Pyrite contents, microstructures, and sulfur isotopes in relation to formation of the youngest eastern Mediterranean sapropel. *Geology*, **25**, 519-522.

Pevear, D.R. (1999) Illite and hydrocarbon exploration. *Proceedings of the National Academy of Sciences of the United States of America*, **96**, 3440-3446.

Pilskaln, C.H. & Honjo, S. (1987) The fecal pellet fraction of biogeochemical particle fluxes to the deep sea. *Global Biogeochemical Cycles*, **1**, 31-48.

Porter, S., Vanko, D.A. & Ghazi, A.M. (2000) Major and trace element compositions of seconddary clays in basalts altered at low temperature, eastern flank of the Juan de Fuca Ridge. *Proceedings of the Ocean Drilling Program, Scientific Results*, **168**, 149-157.

Post, J.L. (1984) Saponite from near Ballarat, California. *Clays and Clay Minerals*, **32**, 147-153.

Posth, N.R., Canfield, D.E. & Kappler, A. (2014) Biogenic Fe(III) minerals: From formation to diagenesis and preservation in the rock record. *Earth Science Reviews*, **135**, 103-121.

Poulton, S.W. & Canfield, D.E. (2011) Ferruginous Conditions: A Dominant Feature of the Ocean through Earth`s History. *Elements*, **7**, 107-112.

Poulton, S.W., Fralick, P.W. & Canfield, D.E. (2010) Spatial variability in oceanic redox structure 1.8 billion years ago. *Nature Geoscience*, **3**, 486-490.

Poulton, S.W., Krom, M.D. & Raiswell, R. (2004) A revised scheme for the reactivity of iron (oxyhydr)oxide minerals towards dissolved sulfide. *Geochimica et Cosmochimica Acta*, **68**, 3703-3715.

Poulton, S.W. & Raiswell, R. (2002) The low-temperature geochemical cycle of iron: From continental fluxes to marine sediment deposition. *American Journal of Science*, **302**, 774-805.

Poulton, S.W. & Raiswell, R. (2005) Chemical and physical characteristics of iron oxides in riverine and glacial meltwater sediments. *Chemical Geology*, **218**, 203-221.

Price, G.D. & Sellwood, B.W. (1994) Palaeotemperatures indicated by Upper Jurassic (Kimmeridgian-Tithonian) fossils from Mallorca determined by oxygen isotope composition. *Palaeogeography, Palaeoclimatology, Palaeoecology*, **110**, 1-10.

Pryor, W.A. (1975) Biogenic Sedimentation and Alteration of Argillaceous Sediments in Shallow Marine Environments. *Geological Society of America Bulletin*, **86**, 1244-1254.

Pytte, A.M. & Reynolds, R.C. (1988) The thermal transformation of smectite to illite. Pp. 133-140 in: Thermal History of Sedimentary Basins (N.D. Naeser and T.H. McCulloh, editors). Springer, USA.

Raiswell, R. (2011a) Iceberg-hosted nanoparticulate Fe in the Southern Ocean: Mineralogy, origin, dissolution kinetics and source of bioavailable Fe. *Deep Sea Research I*, **58**, 1364-1375.

Raiswell, R. (2011b) Iron transport from the continents to the open oceans: The aging-rejuvenation cycle. *Elements*, **7**, 101-106.

Raiswell, R. & Canfield, D.E. (1998) Sources of iron for pyrite formation in marine sediments. *American Journal of Science*, **298**, 219-245.

Raiswell, R. & Canfield, D.E. (2012) The iron biogeochemical cycle past and present. *Geochemical Perspectives*, **1**, 1-222.

Raiswell, R., Reinhard, C.T., Derkowski, A., Owens, J., Bottrell, S.H., Anbar, A.D. & Lyons, T.W. (2011) Formation of syngenetic and early diagenetic iron minerals in the late Archean Mt. McRae Shale, Hamersley Basin, Australia: New insights on the patterns, controls and paleoenvironmental implications of authigenic mineral formation. *Geochimica et Cosmochimica Acta*, **75**, 1072-1087.

Raiswell, R. Tranter, M., Benning, L.G., Siegert, M., De´ath, R., Huybrechts, P. & Payne, P. (2006) Contributions from glacially derived sediment to the global iron oxyhydroxide cycle: Implications for iron delivery to the oceans. *Geochimica et Cosmochimica Acta*, **70**, 2765-2780.

Ramachandran, V.S., Paroli, R.M., Beaudoin, J.J. & Delgado, A.H. (2002) Handbook of Thermal Analysis of Construction Materials. 680 pp. Noyes Publications, New York.

Rameil, N. (2008) Early diagenetic dolomitization and dedolomitization of Late Jurassic and earliest Cretaceous platform carbonates: A case study from the Jura Mountains (NW Switzerland, E France). *Sedimentary Geology*, **212**, 70-85.

Rao, V.P., Thamban, M. & Lamboy, M. (1995) Verdine and glaucony facies from surface sediments of the eastern continental margin of India. *Marine Geology*, **127**, 105-113.

Reinhold, C. (1998) Multiple episodes of dolomitization and dolomite recrystallization during shallow burial in Upper Jurassic shelf carbonates: eastern Swabian Alb, southern Germany. *Sedimentary Geology*, **121**, 71-95.

Reitsema, R.H. (1980) Dolomite and nahcolite formation in organic rich sediments: isotopically heavy carbonates. *Geochimica et Cosmochimica Acta*, **44**, 2045-2049.

Rohrssen, M.K. (2007) Siderite-magnetite oxygen isotope fractionation: A potential iron mineral biosignature. B.Sc. Thesis, Carleton College, Northfield, Minnesota, USA.

Russell, J.D. (1979) Infrared spectroscopy of ferrihydrite: Evidence for the presence of structural hydroxyl groups. *Clay Minerals*, **14**, 109-114.

Russell, J.D. & Fraser, A.R. (1994) Infrared methods. Pp. 11-67 in: *Clay Mineralogy: Spectroscopic and Chemical Determinative Methods* (M.J. Wilson, editor). Chapman & Hall, London.

Sandler, A., Nathan, Y., Eshet, Y. & Raab, M. (2001) Diagenesis of trioctahedral clays in a Miocene to Pleistocene sedimentary-magmatic sequence in the Dead Sea Rift, Israel. *Clay Minerals*, **36**, 29-47.

Schiffman, P. & Staudigel, H. (1995) The smectite to chlorite transition in a fossil seamount hydrothermal system: the Basement Complex of La Palma, Canary Islands. *Journal of Metamorphic Geology*, **13**, 487-498.

Schulz, H.D. & Zabel, M. (2006) Marine Geochemistry, 574 pp. Springer, Berlin.

Severmann, S., Lyons, T.W., Anbar, A., McManus, J. & Gordon, G. (2008) Modern iron isotope perspective on the benthic iron shuttle anf the redox evolution of ancient oceans. Geology, 36, 487-490.

Severmann, S., McManus, J., Berelson,W.M. & Hammond, D.E. (2010) The continental shelf benthic iron flux and its isotope composition. *Geochimica et Cosmochimica Acta*, **74**, 3984-4004.

Środoń, J. & Eberl, D.D. (1984) Illite. Pp. 495-544 in: Micas (S.W. Bailey, editor). Reviews in Mineralogy, Mineralogical Society of America, USA.

Stille, P. & Clauer, N. (1994) The process of glauconitization: chemical and isotopic evidence. *Contributions to Mineralogy and Petrology*, **117**, 253-262.

Strickler, M.E. & Ferrell, R.E. Jr. (1990) Fe substitution for Al in glauconite with increasing diagenesis in the first Wilcox sandstone (Lower Eocene), Livingston Parish, Lousiana. *Clays and Clay Minerals*, **38**, 69-76.

Sunda, W.G. (2001) Bioavailability and Bioaccumulation of Iron in Seawater. Pp. 41-84 in: The Biogeochemistry of Iron in Seawater (D.R. Turner & K.A. Hunter, editors). Wiley, New York, USA.

Taylor, K.G., Hudson-Edwards, K.A., Bennett, A.J. & Vishnyakov, V. (2008) Early diagenetic vivianite [$Fe_3(PO_4)_2 \cdot 8H_2O$] in a contaminated freshwater sediment and insights into zink uptake: A μ-EXAFS, μ-XANES and Raman study. *Applied Geochemistry*, **23**, 1623-1633.

Taylor, K.G. & Konhauser, K.O. (2011) Iron in Earth Surface Systems: A Major Player in Chemical and Biological Processes. *Elements*, **7**, 83-88.

Taylor, K.G. & Macquaker, J.H.S. (2011) Iron Minerals in Marine Sediments Record Chemical Environments. *Elements*, 7, 113-118.

Templeton, A.S. (2011) Geomicrobiology of Iron in Extreme Environments. *Elements*, **7**, 95-100.

Theng, B.K.G. & Yuan, G. (2008) Nanoparticles in the soil environment. *Elements*, **4**, 395-399.

Thompson, G., Mottl, M.J. & Rone, P.A. (1985) Morphology, mineralogy and chemistry of hydrothermal deposits from the Tag Area, 26°N Mid-Atlantic Ridge. *Chemical Geology*, **49**, 243-257.

Tipping, E. (2002) Cation Binding by Humic Substances. Cambridge University Press, Cambridge, UK.

Tischendorf, G., Förster, H.-J., Gottesmann, B. & Rieder, M. (2007) True and brittle micas: composition and solid-solution series. *Mineralogical Magazine*, **71**, 285-320.

Tsipursky, S.I. & Drits, V.A. (1984) The distribution of octahedral cations in the 2:1 layers of dioctahedral smectites studied by oblique texture electron diffraction. *Clay Minerals*, **19**, 177-192.

Tucker, M.E. & Wright, V.P. (1990) Carbonate Sedimentology, 496 pp. Blackwell Science Inc., Oxford.

Turekian, K.K. (1968) Oceans, 120 pp. Prentice Hall, Englewood Cliffs, New York, USA.

Van Aken, P.A., Liebscher, B. & Styrsa, V.J. (1998) Quantitative determination of iron oxidetion states in minerals using Fe $L_{2,3}$-edge electron energy-loss near-edge structure spectroscopy. *Physics and Chemistry of Minerals*, **25**, 323-327.

Van der Lubbe, T., Richter, U. & Knötschke, N. (2009) Velociraptorine dromaeosaurid teeth from the Kimmeridgian (Late Jurassic) of Germany. *Acta Palaeontologica Polonica*, **54**, 401-408.

Veizer, J. & MacKenzie, F.T. (2005) Evolution of sedimentary rocks. Pp. 369-704 in: Sediments, Diagenesis, and Sedimentary Rocks (F.T. MacKenzie, editor). Elsevier Science & Technology, USA.

Velde, B. (1992) Introduction to clay minerals: Chemistry, origin, uses and environmental significance. 198 pp. Chapman and Hall, London.

Voigt, T., von Eynatten, H. & Franzke, H.-J. (2004) Late Cretaceous unconformities in the Subhercynian Cretaceous Basin (Germany). *Acta Geologica Polonica*, **54**, 673-694.

Wagner, T. (1998) Pliocene-Pleistocene deposition of carbonate and organic carbon at Site 959: Paleoenvironmental implications for the eastern equatorial Atlantic of the Ivory Coast/Ghana. *Proceedings of the Ocean Drilling Program, Scientific Results*, **159**, 557-574.

Warr, L.N. & Grathoff, G. (2012) Geoscientific applications of particle detection and imaging techniques with special focus on the monitoring clay mineral reactions. Pp. 667-683 in: Handbook of Particle Detection (C. Grupen and I. Buvat, editors). Springer, Berlin.

Warr, L.N., Perdrial, J.N., Lett, M.-C., Heinrich-Salmeron, A. & Khodja, M. (2009) Clay mineral-enhanced bioremediation of marine oil pollution. *Applied Clay Science*, **46**, 337-345.

Warren, J. (2000) Dolomite: occurrence, evolution and economically important associations. *Earth Science Reviews*, **52**, 1-81.

Weber, J.N. & Smith, F.G. (1961) Rapid determination of calcite-dolomite ratios in sedimentary rocks. *Journal of Sedimentary Petrology*, **31**, 130-132.

Weaver, C.E. & Pollard, L.D. (1973) The Chemistry of Clay Minerals, 213 pp. Elsevier, Amsterdam, London, New York.

Wiewióra, A., Giresse, P., Petit, S. & Wilamowski, A. (2001) A deep-water glauconitization process on the Ivory Coast – Ghana Marginal Ridge (ODP Site 959): Determination of Fe^{3+}-rich montmorillonite in green grains. *Clays and Clay Minerals*, **49**, 540-558.

Wigley, R.A. & Compton, J.S. (2007) Oligocene to Holocene glauconite phosphorite grains from the Head of the Cape Canyon on the western margin of South Africa. *Deep Sea Research II*, **54**, 1375-1395.

Wildman, W.E., Whittig, L.D. & Jackson, M.L. (1971) Serpentine stability in relation to formation of iron-rich montmorillonite in some California soils. *American Mineralogist*, **56**, 587-602.

Wolters, F. & Emmerich, K. (2007) Thermal reactions of smectites – Relation of dehydroxilation temperature to octahedral structure. *Thermochimica Acta*, **462**, 80-88.

Wu, J., Boyle, E.A., Sunda, W.G. & Wen, L. (2001) Soluble and colloidal iron in oligotrophic North Atlantic and North Pacific. *Science*, **293**, 847-849.

Zolla, V.,Freyria, F.S., Sethi, R. & Di Molfetta, A. (2009) Hydrogeochemical and Biological Processes Affecting the Long-term Performance of an Iron-Based Permeable Reactive Barrier. *Journal of Environmental Quality*, **38**, 897-908.